University of Alberta

Geotechnical Analysis of Flow Slides, Debris Flows, and Related Phenomena

by

Xiaobo Wang

A thesis submitted to the Faculty of Graduate Studies and Research
in partial fulfillment of the requirements for the degree of

Doctor of Philosophy
in
Geotechnical Engineering

Department of Civil and Environmental Engineering

Edmonton, Alberta
Spring 2008

Library and
Archives Canada

Published Heritage
Branch

395 Wellington Street
Ottawa ON K1A 0N4
Canada

Bibliothèque et
Archives Canada

Direction du
Patrimoine de l'édition

395, rue Wellington
Ottawa ON K1A 0N4
Canada

Your file Votre référence
ISBN: 978-0-494-45620-0
Our file Notre référence
ISBN: 978-0-494-45620-0

NOTICE:
The author has granted a non-exclusive license allowing Library and Archives Canada to reproduce, publish, archive, preserve, conserve, communicate to the public by telecommunication or on the Internet, loan, distribute and sell theses worldwide, for commercial or non-commercial purposes, in microform, paper, electronic and/or any other formats.

The author retains copyright ownership and moral rights in this thesis. Neither the thesis nor substantial extracts from it may be printed or otherwise reproduced without the author's permission.

AVIS:
L'auteur a accordé une licence non exclusive permettant à la Bibliothèque et Archives Canada de reproduire, publier, archiver, sauvegarder, conserver, transmettre au public par télécommunication ou par l'Internet, prêter, distribuer et vendre des thèses partout dans le monde, à des fins commerciales ou autres, sur support microforme, papier, électronique et/ou autres formats.

L'auteur conserve la propriété du droit d'auteur et des droits moraux qui protège cette thèse. Ni la thèse ni des extraits substantiels de celle-ci ne doivent être imprimés ou autrement reproduits sans son autorisation.

In compliance with the Canadian Privacy Act some supporting forms may have been removed from this thesis.

While these forms may be included in the document page count, their removal does not represent any loss of content from the thesis.

Conformément à la loi canadienne sur la protection de la vie privée, quelques formulaires secondaires ont été enlevés de cette thèse.

Bien que ces formulaires aient inclus dans la pagination, il n'y aura aucun contenu manquant.

Canada

Abstract

Debris flows and granular flow slides incorporate a broad range of sediment-fluid mixture flows that are intermediate between dry rock avalanches and hyperconcentrated flows. This study provides a comprehensive examination of the state of the art in constitutive and numerical modeling of dense granular flows. Emphasis is placed on granular deposit flows with high solid concentration.

The terminology for debris flows and related phenomena is reviewed within the context of existing classifications of landslides, particularly the classification of landslides of the flow type. Constitutive laws widely used in debris flow modeling are critically examined with information found in the literature and data from field observations, laboratory experiments, and theoretical analyses. Based on a comprehensive review of existing analytical approaches to debris flow runout predictions, a new analytical model based on energy conservation and considering internal energy dissipation is formulated. The new analytical model is developed to improve understanding of fundamental aspects in modeling of dense granular flows and to provide practitioners with simple, reliable mobility analysis of flow slides and debris flows.

The post-failure deformation behavior of liquefaction flow slides is simulated using the new analytical model. Liquefied shear strengths in terms of undrained strength and bulk friction angle are back-calculated for ten flow slide cases according to cohesive and frictional soil behavior models. Results from back-analyses provide evidence that a useful representation of liquefied shear strength can be obtained through dynamic analysis based on energy conservation within the framework of the Coulomb friction model.

The concepts of steady-state deformation, the collapse surface, and sliding-surface liquefaction are used to interpret post-failure deformation behavior and mobility of rapid landslides. The new analytical model is used to simulate undrained granular flows mobilized from landslides on natural slopes. The analyses indicate that back-calculated bulk friction angles appear to be in agreement with the results from undrained ring-shear tests. Using the Coulomb friction model as a constitutive law, dynamic analysis developed in this study is capable of simulating post-failure deformation behavior of rapid landslides on natural slopes.

Acknowledgement

The author expresses gratitude to Professor D.H. Chan and Professor N.R. Morgenstern for supervising this study.

Professor Chan provided the author with learning opportunities and research materials to accomplish this study. His guidance, understanding, insightful discussions, and support throughout this research are greatly appreciated.

Professor Morgenstern suggested this topic, granted a generous amount of time and intellectual effort in problem-solving discussions, and offered emotional help and encouragement. Many books, research articles, and technical reports reviewed in this study were delivered or suggested to the author by Professor Morgenstern. The development of the analytical model for dense granular flows from an energy perspective originates from stimulating discussions with Professor Morgenstern. During the final stages of this study, Professor Morgenstern spent many weekends helping the author revise and finalize the thesis. His kindness, patience, and support have made this work a pleasant and satisfying research experience for the author. It is the author's hope that the quality of this thesis reflects the quality of the guidance he was offered.

The author is indebted to Professor P. Steffler for contributions to the formulation of the analytical model that was developed as part of the thesis and for the numerical solution of the model. His interest and insight on this topic proved most valuable. The author appreciates the assistance given by Professor O. Hungr at the University of British Columbia who provided the latest version of the DAN-W program. The author is also indebted to Professor Hungr for reading the thesis and for making many suggestions to improve the thesis. The author benefited immensely from many of Professor Hungr's comments and suggestions. The author wants to thank Dr. S.M. Olson for discussions and clarifications on the kinetic analysis approach. Thanks are also extended to the Geotechnical Engineering Office of Hong Kong for providing data and technical reports of many case studies on debris flows.

The author had many fruitful discussions with fellow graduate students at the University of Alberta. Thanks go to Jason Stianson for his friendship, generous support, and willingness to discuss technical and nontechnical issues with the author.

The Geotechnical Engineering Group at the University of Alberta provided a supportive and friendly environment for the author. Special thanks are due to Sally Petaske for her support throughout the course of this research.

Finally, the author is deeply grateful to his wife Junxia, daughter Bonnie, and son Boris for their patience, understanding, love, and strength. They have sacrificed more to this thesis than could be described on these pages. Their love and support have been and always will be an invaluable part of the author's life.

Table of Contents

Chapter 1 Introduction 1

1.1 Introduction to Debris Flow Modeling 1

1.2 Historical Development of Constitutive Modeling of Debris Flows 3

1.3 Historical Development of Numerical Modeling of Debris Flows 5

1.4 Scope of the Study 8

1.5 Outline of Thesis 8

Chapter 2 Terminology and Definitions for Debris Flows 10

2.1 Introduction 10

2.2 Classification of Flow-Like Landslides 10

2.3 Classification of Sediment-Water Flows 13

2.4 Debris Flow Size Classification 14

2.5 Discussion and Conclusion 15

Chapter 3 Constitutive Modeling of Debris Flows 23

3.1 Introduction 23

3.2 The Newtonian Fluid Model 23

3.3 The Non-Newtonian Fluid Model 25

3.4 The Dilatant Fluid Model 29

3.5 The Coulomb Friction Model 31

3.6 The Coulomb Viscous Model 33

3.7 The Voellmy Fluid Model 34

3.8 Discussion of Shear Resistance in Dense Granular Flows 37

3.8.1 Yield Strength 37

3.8.2 Rate Dependence 39

3.8.3 Constitutive Equation for Modeling Dense Granular Flow 41

3.9 Conclusion 43

Chapter 4 Numerical Modeling of Debris Flows 50

4.1 Introduction 50

4.2 Empirical Relationships for Debris Flows 50

4.3 The Sliding Block Model 54

4.4 The Depth-Averaged Model 57

4.4.1 Derivation of the General Depth-Averaged Equations 58

4.4.2 Determination of Basal Resistance in Depth-Averaged Models 64

4.5 Discussion 74

4.6 Conclusion 76

Chapter 5 A Slice-Based Model with Internal Energy Dissipation 90

5.1 Introduction 90

5.2 The Slice-Based Model 91

5.3 Numerical Schemes for Debris Flow Simulation 94

5.3.1 The Finite Difference Method 94

5.3.2 The Finite Element Method 95

5.3.3 The Discrete Element Method 97

5.3.4 Smoothed Particle Hydrodynamics 99

5.4 Formulation of the Slice-Based Model with Internal Energy Dissipation. 100

5.4.1 Mechanical Energy Equations 101

5.4.2 Derivation of Governing Equations Based on the Conservation of Energy 103

5.4.3 Effects of Slope Curvature on Motion of Liquefaction Flow Slides and Debris Flows 105

5.4.4 Comparison with Previous Mathematical Models 106

5.5 A Numerical Scheme for the Analytical Model Based on Energy Considerations 108

5.6 Model Verification and Numerical Experiments 114

5.7 Conclusions 115

Chapter 6 The Dynamic Analysis of Liquefaction Flow Slides 121

6.1 Introduction 121

6.2 Liquefaction Flow and Liquefied Shear Strength 121

6.3 Methods of Estimating Liquefied Shear Strength from Case Studies 124

6.4 Procedures for the Dynamic Analysis of Liquefaction Flow Slides 127

6.5 Case Histories of Liquefaction Flow Slides 128

6.6 Liquefied Shear Strength from the Dynamic Analysis of Liquefaction Flow Slide Case Histories 130

6.7 Liquefied Shear Strength from Kinetic Analysis Using the Sliding Block Model 131

6.8 Discussion of Results 133

6.8.1 Effects of a Constitutive Model 134

6.8.2 Comparison of Liquefied Shear Strengths Estimated Using Different Approaches 135

6.8.3 Coefficient of Bulk Friction in Liquefaction Flows 136

6.8.4 Sources of Uncertainty in Dynamic Analysis 137

6.9 Conclusions 138

Chapter 7 Dynamic Analysis of Debris Flows on Natural Slopes 151

7.1 Introduction 151

7.2 Liquefaction and Debris Flow-Triggering Mechanism 153

7.2.1 Steady-State Line, Collapse Surface and Debris Flow Initiation 153

7.2.2 Natural Comminution and Sliding-Surface Liquefaction 157

7.3 Dynamic Analysis of the Tsukidate Landslide 159

7.3.1 Field and Experimental Investigations of the Tsukidate Landslide ... 159

7.3.2 Numerical Modeling of the Tsukidate Landslide 161

7.4 Dynamic Analysis of the Takarazuka Landslide 161

7.5 Dynamic Analysis of the Hiegaesi Landslide 162

7.6 Conclusions 164

Chapter 8 Conclusions and Recommendations 182

8.1 Summary 182

8.2 Conclusion 187

8.3 Recommendations for Future Studies 188

References 191

Appendix A Numerical Algorithm and Model Verification 214

A.1 Numerical Algorithm 214

A.2 Code Verification 217

A.3 Model Verification 223

A.3.1 Dam-Break Sand Flow 223

A.3.2 Simulation of granular slumping on a horizontal plane 228

A.3.2 Runout Analysis of Tailing Dam Break 234

Appendix B Case Histories of Liquefaction Flow Slides and Dynamic Analyses ... 236

B.1 A Flow Slide in the Lower San Fernando Dam 236

B.1.1 Historical Information of the Lower San Fernando Flow Slide 236

B.1.2 Stability Analyses of the Lower San Fernando Flow Slide 238

B.1.3 Dynamic Analysis of the Lower San Fernando Flow Slide 240

B.1.4 Kinetic Analysis of the Lower San Fernando Flow Slide 241

B.2 A Flow Slide in the North Dike of the Wachusett Dam 249

B.2.1 Historical Information of the Wachusett Flow Slide 249

B.2.2 Stability Analysis of the Wachusett Flow Slide 250

B.2.3 Dynamic Analysis of the Wachusett Flow Slide 251

B.2.4 Kinetic Analysis of the Wachusett Flow Slide 252

B.3 A Flow Slide in the Calaveras Dam 259

B.3.1 Historical Information of the Calaveras Flow Slide 259

B.3.2 Stability Analysis of the Calaveras Flow Slide 260

B.3.3 Dynamic Analysis of the Calaveras Flow Slide 261

B.3.4 Kinetic Analysis of the Calaveras Flow Slide 261

B.4 A Flow Slide in the Fort Peck Dam 267

B.4.1 Historical Information of the Fort Peck Flow Slide 267

B.4.2 Stability Analysis of the Fort Peck Flow Slide 268

B.4.3 Dynamic Analysis of the Fort Peck Flow Slide 269

B.4.4 Kinetic Analysis of the Fort Peck Flow Slide 269

B.5 A Flow Slide in a Roadway Embankment on Lake Ackerman 275

B.5.1 Historical Information of the Lake Ackerman Flow Slide 275

B.5.2 Stability Analysis of the Lake Ackerman Flow Slide 276

B.5.3 Dynamic Analysis of the Lake Ackerman Flow Slide 276

B.5.4 Kinetic Analysis of the Lake Ackerman Flow Slide 277

B.6 A Flow Slide in the Highway Embankment at Koda Numa 286

B.6.1 Historical Information of the Koda Numa Flow Slide 286

B.6.2 Stability Analysis of the Koda Numa Flow Slide 286

B.6.3 Dynamic Analysis of the Koda Numa Flow Slide 287

B.6.4 Kinetic Analysis of the Koda Numa Flow Slide 287

B.7 A Flow Slide in the Railway Embankment of the Uetsu-Line 295

B.7.1 Historical Information of the Uetsu-Line Flow Slide 295

B.7.2 Stability Analysis of the Uetsu-Line Flow Slide 295

B.7.3 Dynamic Analysis of the Uetsu-Line Flow Slide 296

B.7.4 Kinetic Analysis of the Uetsu-Line Flow Slide 296

B.8 A Flow Slide in the Shibecha-Cho Embankment 305

B.8.1 Historical Information of the Shibecha-Cho Flow Slide 305

B.8.2 Stability Analysis of the Shibecha-Cho Flow Slide 305

B.8.3 Dynamic Analysis of the Shibecha-Cho Flow Slide 306

B.8.4 Kinetic Analysis of the Shibecha-Cho Flow Slide 306

B.9 A Flow Slide in the Route 272 Embankment 314

B.9.1 Historical Information of the Route 272 Flow Slide 314

B.9.2 Stability Analysis of the Route 272 Flow Slide.................................314

B.9.3 Dynamic Analysis of the Route 272 Flow Slide 315

B.9.4 Kinetic Analysis of the Route 272 Flow Slide 315

B.10 A Flow Slide in the Hachiro-Gata Embankment.......................................323

B.10.1 Historical Information of the Hachiro-Gata Flow Slide..................323

B.10.2 Stability Analysis of the Hachiro-Gata Flow Slide 323

B.10.3 Dynamic Analysis of the Hachiro-Gata Flow Slide 324

B.10.4 Kinetic Analysis of the Hachiro-Gata Flow Slide 324

List of Tables

Table 2-1 Landslide velocity scale (Modified from Cruden and Varnes 1996) 17

Table 2-2 Classification of slope movements (Cruden and Varnes 1996) 17

Table 2-3 Classification of landslides proposed by the EPOCH project (Dikau et al. 1996) 18

Table 2-4 Classification of landslides of flow type (Modified from Hungr et al. 2001) 19

Table 2-5 Rheological classification of sediment-water flows (Modified from Pierson and Costa 1987) 21

Table 2-6 Size classification of debris flows (Jacob 2005) 22

Table 3-1 Velocities for flow of a Newtonian fluid down a slope 44

Table 3-2 Velocities for flow of a Bingham fluid down a slope 44

Table 3-3 Velocities for flow of a Herschel-Bulkley fluid down a slope 45

Table 3-4 Velocities for flow of a dilatant fluid down a slope 45

Table 3-5 Velocities for flow of a generalized viscoplastic fluid down a slope 46

Table 3-6 Summary of reported shear strength and viscosity for a mixture of water and fine-grained sediment 47

Table 4-1 Parameters for correlations between the tangent of travel angle and landslide volume 78

Table 4-2 Parameters for correlations between the tangent of travel angle and the slope angle (Data from Hunter and Fell 2003) 79

Table 4-3 Empirical relationships for debris flows (Data from Rickenmann 1999) ... 80

Table 4-4 Empirical equations for long-runout landslides (Data from Legros 2002). 81

Table 4-5 Liquefied shear strength from kinetic analysis of liquefaction flows (Data from Olson and Stark 2002) ... 82

Table 4-6 Depth-averaged equations in orthogonal curvilinear coordinate systems .. 83

Table 5-1 Dynamic analysis of liquefaction flow slides with DAN-W ... 116

Table 5-2 Mathematical models for debris flow simulation based on the conservation of momentum ... 117

Table 6-1 Summary of liquefaction flow slide case histories ... 140

Table 6-2 Liquefaction flow slide analysis with the cohesive model ... 141

Table 6-3 Liquefaction flow slide analysis with the frictional model ... 142

Table 6-4 Kinetic analysis of liquefaction flow slides with the sliding block model 143

Table 6-5 Coefficient of bulk friction and liquefied shear strength ratio ... 144

Table 7-1 Properties of soil sample from source area of the Tsukidate landslide 165

List of Figures

Figure 3-1 Velocity profile for flow of a Newtonian fluid down a slope 48

Figure 3-2 Velocity profile for flow of a non-Newtonian fluid down a slope 48

Figure 3-3 Debris flow deposit thickness versus yield strength for different slopes (Data from Iverson 2003) 49

Figure 4-1 Definitions of travel angle and travel distance 85

Figure 4-2 Tangent of travel angle (H/L) versus landslide volume 85

Figure 4-3 Sliding block model with energy line for frictional material 86

Figure 4-4 Definitions of variables for depth-averaged model in Cartesian coordinates (Modified from Denlinger and Iverson 2004) 86

Figure 4-5 Sketch of the curvilinear coordinate system 87

Figure 4-6 Curvilinear coordinate system used for two-dimensional Savage-Hutter model (Modified from Wang et al. 2004) 87

Figure 4-7 Two-dimensional debris flow with Cartesian coordinates 88

Figure 4-8 Two-dimensional non-Newtonian flow with Cartesian coordinates 88

Figure 4-9 Shape factor (β) versus rheological index (η) for different ratio of shear depth to total flow depth 89

Figure 4-10 Shear stress distribution for Bingham fluid flowing down an inclined plane with slope angle of θ 89

Figure 5-1 Forces acting on a single slice in the slice-based model 118

Figure 5-2 Typical motion of a slice 118

Figure 5-3 Uniform deformation assumed 119

Figure 5-4 Slices and notations used for the slice-based model 119

Figure 5-5 Coefficients of lateral earth pressure based on the Savage-Hutter definition 120

Figure 6-1 Typical undrained response of loose sands in monotonic loading, creep, and cyclic loading 145

Figure 6-2 Travel path of the center of gravity in the sliding block model 146

Figure 6-3 Acceleration versus time in analysis with the sliding block model 146

Figure 6-4 Velocity versus time in analysis with the sliding block model 147

Figure 6-5 Displacement versus time in analysis with the sliding block model 147

Figure 6-6 Geometries of the North Dike of the Wachusett Dam based on field observation 148

Figure 6-7 Geometries of the North Dike flow slide based on dynamic analysis with the cohesive model 149

Figure 6-8 Geometries of the North Dike flow slide based on dynamic analysis with the friction model 150

Figure 7-1 Typical isotropically consolidated undrained test on loose sand (Modified from Sladen et al. 1985a) 166

Figure 7-2 Mohr circles for rainfall-induced debris flows (Modified from Anderson and Sitar 1995) 167

Figure 7-3 Field stress path in $p'-q$ plane for rainfall-induced debris flows 167

Figure 7-4 Steady-state lines for soils with different coefficients of uniformity

(Modified from De Matos 1988): (a) Deviator stress versus void ratio; (b) Effective minor principal stress versus void ratio 168

Figure 7-5 Changes in steady-state line associated with natural comminution 169

Figure 7-6 Grain size distribution for samples in shear-ring tests (Data from Sassa 2000) 170

Figure 7-7 Grain size distribution for samples of a landslide associated with sliding-surface liquefaction (Data from Sassa 2000) 170

Figure 7-8 Location of Tsukidate landslide and the earthquake epicenter (After Wang et al. 2005) 171

Figure 7-9 Views of the Tsukidate landslide (After Fukuoka et al. 2004): (a) Oblique front view; (b) Oblique side view; (c) View from the toe of the Tsukidate landslide 171

Figure 7-10 Configuration of displaced materials and location of sampling sites (After Uzuoka et al. 2005) 172

Figure 7-11 Gain-size distribution of soil samples taken from the Tsukidate landslide (Data from Uzuoka et al. 2005) 172

Figure 7-12 Contour map of the Tsukidate landslide area after the earthquake (After Wang et al. 2005) 173

Figure 7-13 Cross section of the Tsukidate landslide along A-A' in Figure 7-12 (After Wang et al. 2005) 174

Figure 7-14 Longitudinal cross section of the Tsukidate landslide used for dynamic analysis 174

Figure 7-15 Post-failure profile of the Tsukidate landslide based on dynamic analysis

.... 175

Figure 7-16 Front velocity profile of the Tsukidate landslide based on dynamic analysis 175

Figure 7-17 Plan view of the Takarazuka landslide (after Sassa 2000) 176

Figure 7-18 Longitudinal cross section of the Takarazuka landslide used for dynamic analysis 177

Figure 7-19 Post-failure profile of the Takarazuka landslide simulated using dynamic analysis with the friction model 178

Figure 7-20 Front velocity profile of the Takarazuka landslide based on dynamic analysis 178

Figure 7-21 The Hiegaesi landslide (After Sassa 2000): (a) Photograph of the landslide; (b) Sketch of the landslide in plan; (c) Longitudinal cross section of the landslide. P: observation pit; S1, S2 and S3: sampling sites. 179

Figure 7-22 Grain size distributions of soil samples from the sliding zone and the displaced mass of the Hiegaesi landslide (Data from Sassa 2000) 180

Figure 7-23 Sliding surface and pre-failure slope geometry of the Hiegaesi landslide 180

Figure 7-24 Post-failure geometry of the Hiegaesi landslide based on dynamic analysis 181

Figure 7-25 Front velocity profile of the Hiegaesi landslide based on dynamic analysis 181

Figure A.1 Flow chart of dynamic analysis based on energy consideration 216

Figure A.2 Simple debris flow case for code verification 217

Figure A.3 Flow profiles at 0.2 s interval from hand calculation 220

Figure A.4 Flow profiles at 0.2 s interval from computer simulation 220

Figure A.5 Velocities on boundary 2, 3, and 4 from hand calculation (_H) and computer simulation (_C) 221

Figure A.6 Displacements on boundary 2, 3, and 4 from hand calculation (_H) and computer simulation (_C) 221

Figure A.7 Heights on boundary 2, 3, and 4 from hand calculation (_H) and computer simulation (_C) 222

Figure A.8 Initial geometry of dam break problem 224

Figure A.9 Simulation of dam-break sand flow with friction model ($\phi = \phi_b = 30^\circ$). 225

Figure A.10 Simulation of dam-break sand flow with friction model ($\phi = \phi_b = 20^\circ$) 226

Figure A.11 Simulation of dam-break sand flow with friction model ($\phi = \phi_b = 10^\circ$)227

Figure A.12 Definition of the mean angle of dispose 227

Figure A.13 Simulation of granular spreading mass with initial aspect ratio of 3.2 and height of 3.2 m 230

Figure A.14 Simulation of granular spreading mass with initial aspect ratio of 3.2 and height of 6.4 m 231

Figure A.15 Simulation of granular spreading mass with initial aspect ratio of 3.2 and height of 9.6 m 232

Figure A.16 Nondimensional final profiles of granular slumps with the same initial aspect ratio of 3.2 (normalized with respect to L) 233

Figure A.17 Tailing dam break analysis based on dynamic analysis with purely cohesive model 235

Figure B.1 Cross sections of the Lower San Fernando Dam after earthquake (Modified Castro et al. 1992) 242

Figure B.2 Schematic reconstruction of failed cross section of the Lower San Fernando Dam (Modified Castro et al. 1992) 243

Figure B.3 Geometries of the Lower San Fernando flow slide based on field observations 244

Figure B.4 Geometries of the Lower San Fernando flow slide based on dynamic analysis with the cohesive model 245

Figure B.5 Geometries of the Lower San Fernando flow slide based on dynamic analysis with the friction model 246

Figure B.6 Travel path of the centroid of the Lower San Fernando flow slide 247

Figure B.7 Centroid velocity versus time for the Lower San Fernando flow slide .. 247

Figure B.8 Centroid displacement versus time for the Lower San Fernando flow slide 248

Figure B.9 Pre-failure cross section of the North Dike of the Wachusett Dam (Modified from Olson et al. 2000) 253

Figure B.10 Pre- and post-failure geometries of the North Dike of the Wachusett Dam (Modified from Olson et al. 2000) 253

Figure B.11 Geometries of the North Dike of the Wachusett Dam based on field observation 254

Figure B.12 Geometries of the Wachusett flow slide based on dynamic analysis with the cohesive model 255

Figure B.13 Geometries of the Wachusett flow slide based on dynamic analysis with the friction model 256

Figure B.14 Travel path of the centroid of the Wachusett flow slide 257

Figure B.15 Centroid velocity versus time for the Wachusett flow slide 257

Figure B.16 Centroid displacement versus time for the Wachusett flow slide 258

Figure B.17 Pre- and post-failure geometries of the Calaveras Dam (Modified from Olson 2001) 262

Figure B.18 Pre- and post-failure geometries of the Calaveras Dam used for dynamic analysis 262

Figure B.19 Geometries of the Calaveras flow slide based on dynamic analysis with the cohesive model 263

Figure B.20 Geometries of the Calaveras flow slide based on dynamic analysis with the friction model 264

Figure B.21 Travel path of the centroid of the Calaveras flow slide 265

Figure B.22 Centrod velocity versus time for the Calaveras flow slide 265

Figure B.23 Centroid displacement versus time for the Calaveras flow slide 266

Figure B.24 Pre- and post-failure geometries of the Fort Peck Dam (Modified from Olson 2001) 270

Figure B.25 Pre- and post-failure geometries of the Fort Peck Dam used for dynamic analysis 270

Figure B.26 Geometries of the Fort Peck flow slide based on dynamic analysis with the cohesive model 271

Figure B.27 Geometries of the Port Peck flow slide based on dynamic analysis with the friction model 272

Figure B.28 Travel path of the centroid of the Fort Peck flow slide 273

Figure B.29 Centroid velocity versus time for the Fort Peck flow slide 273

Figure B.30 Centroid displacement versus time for the Fort Peck flow slide 274

Figure B.31 Location of trucks at the time of failure of the Ackerman Lake road embankment (After Hryciw et al. 1990) 278

Figure B.32 Failure of the embankment on Ackerman Lake (After Hryciw et al. 1990) 278

Figure B.33 Pre- and post-failure cross section of the embankment on Ackerman Lake (After Hryciw et al. 1990) 279

Figure B.34 Pre-failure geometries of the Lake Ackerman embankment used for yield shear strength analyses (Modified from Olson 2001) 279

Figure B.35 Post-failure geometries of the Lake Ackerman embankment used for liquefied shear strength analyses (Modified from Olson 2001) 280

Figure B.36 Post-failure geometries of the Lake Ackerman embankment used for kinetic analysis (Modified from Olson 2001) 280

Figure B.37 Geometries of the Lake Ackerman flow slide used for dynamic analysis 281

Figure B.38 Geometries of the Lake Ackerman flow slide based on dynamic analysis with the cohesive model 282

Figure B.39 Geometries of the Lake Ackerman flow slide based on dynamic analysis with the friction model 283

Figure B.40 Travel path of the centroid of the Lake Ackerman flow slide 284

Figure B.41 Centroid velocity versus time for the Lake Ackerman flow slide 284

Figure B.42 Centroid displacement versus time for the Lake Ackerman flow slide 285

Figure B.43 Pre- and post-failure cross section of the embankment at Koda Numa (Modified from Olson 2001) 288

Figure B.44 Pre-failure geometries of the Koda Numa embankment used for yield shear strength analyses (Modified from Olson 2001) 288

Figure B.45 Post-failure geometries of the Koda Numa embankment used for liquefied shear strength analyses (Modified from Olson 2001) 289

Figure B.46 Post-failure geometries of the Koda Numa embankment used for kinetic analyses (Modified from Olson 2001) 289

Figure B.47 Geometries of the Koda Numa flow slide used for dynamic analysis .. 290

Figure B.48 Geometries of the Koda Numa flow slide based on dynamic analysis with the cohesive model 291

Figure B.49 Geometries of the Koda Numa flow slide based on dynamic analysis with the friction model 292

Figure B.50 Travel path of the centroid of the Koda Numa flow slide 293

Figure B.51 Centroid velocity versus time for the Koda Numa flow slide 293

Figure B.52 Centroid displacement versus time for the Koda Numa flow slide 294

Figure B.53 Pre- and post-failure cross section of the embankment of the Uetsu-Line

(Modified from Olson 2001) 298
Figure B.54 Pre-failure geometries of the Uetsu-Line embankment used for yield shear strength analyses (Modified from Olson 2001) 298
Figure B.55 Post-failure geometries of the Uetsu-Line embankment used for liquefied shear strength analyses (Modified from Olson 2001) 299
Figure B.56 Post-failure geometries of the Uetsu-Line embankment used for kinetic analyses (Modified from Olson 2001) 299
Figure B.57 Geometries of the Uetsu-Line flow slide used for dynamic analysis ... 300
Figure B.58 Geometries of the Uetsu-Line flow slide based on dynamic analysis with the cohesive model 301
Figure B.59 Geometries of the Uetsu-Line flow slide based on dynamic analysis with the friction model 302
Figure B.60 Travel path of the centroid of the Uetsu-Line flow slide 303
Figure B.61 Centroid velocity versus time for the Uetsu-Line flow slide 303
Figure B.62 Centroid displacement versus time for the Uetsu-Line flow slide 304
Figure B.63 Damage of the embankment during the Kushiro-Oki earthquake (After Olson 2001) 307
Figure B.64 Cross sections along four profiles in Figure B.63 (After Olson 2001). 307
Figure B.65 Pre-failure geometries of the Shibecha-Cho embankment used for yield shear strength analyses (Modified from Olson 2001) 308
Figure B.66 Post-failure geometries of the Shibecha-Cho embankment used for liquefied shear strength analyses (Modified from Olson 2001) 308
Figure B.67 Post-failure geometries of the Shibecha-Cho embankment used for kinetic

analyses (Modified from Olson 2001) 309

Figure B.68 Geometries of the Shibecha-Cho flow slide used for dynamic analysis 309

Figure B.69 Geometries of the Shibecha-Cho flow slide based on dynamic analysis with the cohesive model 310

Figure B.70 Geometries of the Shibecha-Cho flow slide based on dynamic analysis with the friction model 311

Figure B.71 Travel path of the centroid of the Shibecha-Cho flow slide 312

Figure B.72 Centroid velocity versus time for the Shibecha-Cho flow slide 312

Figure B.73 Centroid displacement versus time for the Shibecha-Cho flow slide ... 313

Figure B.74 Pre- and post-failure geometry of the Route 272 flow slide (After Olson 2001) 316

Figure B.75 Pre-failure geometries of the Route 272 embankment used for yield shear strength analyses (Modified from Olson 2001) 316

Figure B.76 Post-failure geometries of the Route 272 embankment used for liquefied shear strength analyses (Modified from Olson 2001) 317

Figure B.77 Post-failure geometries of the Route 272 embankment used for kinetic analyses (Modified from Olson 2001) 317

Figure B.78 Geometries of the Route 272 flow slide used for dynamic analysis..... 318

Figure B.79 Geometries of the Route 272 flow slide based on dynamic analysis with the cohesive model 319

Figure B.80 Geometries of the Route 272 flow slide based on dynamic analysis with the friction model 320

Figure B.81 Travel path of the centroid of the Route 272 flow slide 321

Figure B.82 Centroid velocity versus time for the Route 272 flow slide 321

Figure B.83 Centroid displacement versus time for the Route 272 flow slide 322

Figure B.84 Pre- and post-failure geometry of the Hachiro-Gata flow slide (After Olson 2001) 325

Figure B.85 Pre-failure geometries of the Hachiro-Gata embankment used for yield shear strength analyses (Modified from Olson 2001) 325

Figure B.86 Post-failure geometries of the Hachiro-Gata embankment used for liquefied shear strength analyses (Modified from Olson 2001) 326

Figure B.87 Post-failure geometries of the Hachiro-Gata embankment used for kinetic analyses (Modified from Olson 2001) 326

Figure B.88 Geometries of the Hachiro-Gata flow slide used for dynamic analysis 327

Figure B.89 Geometries of the Hachiro-Gata flow slide based on dynamic analysis with the cohesive model 328

Figure B.90 Geometries of the Hachiro-Gata flow slide based on dynamic analysis with the friction model 329

Figure B.91 Travel path of the centroid of the Hachiro-Gata flow slide 330

Figure B.92 Centroid velocity versus time for the Hachiro-Gata flow slide 330

Figure B.93 Centroid displacement versus time for the Hachiro-Gata flow slide 331

Chapter 1

Introduction

1.1 Introduction to Debris Flow Modeling

Debris flow is an extremely rapid flow of a highly concentrated mixture of water and predominantly coarse granular material. The composition of a typical debris flow is a poorly sorted, sediment-water mixture that commonly contains more than 50 percent solid by volume. The constituent sediment usually varies widely in size, from clay particles to boulders of several meters in diameter. Debris flows are caused by changes in effective stresses due to variations of external force or pore pressure. Gravity is the main driving force mobilizing initially stable deposits. Intense precipitation, reshaping of slopes by erosion or construction, alternate freezing and thawing, earthquake, and volcanic eruptions are important causative agents of debris flows. Because of high flow velocities, large impact forces, long runout distance, and poor temporal predictability, debris flows are among the most dangerous and destructive natural hazards (Jakob and Hungr 2005; Johnson and Rodine 1984). Debris flow hazards have severe social, economic, and environmental consequences in mountainous environments, particularly on alluvial fans where settlements and infrastructure have been built.

In recent decades, comprehensive field and laboratory observations have led to great theoretical and practical advances in understanding the mechanisms of debris flow processes. This understanding has aided in recognizing debris flow hazard potential and has helped to decrease the loss of life and property caused by debris flow disasters. The number of research articles in scientific journals and conferences is enormous and increases each year. Debris flow literature (Armanini and Michiue 1997; Chen 1997; Costa and Wieczorek 1987; Jakob and Hungr 2005; Rickenmann and Chen 2003; Wieczorek and Naeser 2000) has significantly contributed to theoretical studies and practical applications of debris flow science. However, the underlying physics of debris flow remains poorly understood. To take efficient measures against debris flow damages, scientists and engineers face difficulties obtaining well-founded engineering predictions of debris flow mobility which is essential information for both hazard assessment and preventive design.

The complicated nature of debris flows and the difficulties in conducting reliable laboratory tests and in situ observations account for the current status in debris flow studies. On the one hand, debris flows are extremely complex in their physical behavior and demand subtle theoretical descriptions and mathematical models. On the other hand, examinations of the validity of debris flow simulation models against field observations are often difficult or impossible because of dangers involved with in situ experimental campaigns, uncontrollable geophysical conditions, and unpredictable time and locations of debris flow events (Hutter 2005). Laboratory tests of debris flows of reduced size can be performed under well-defined and well-controlled conditions. However, debris flows are known to be scale-dependent and runout distance is greatly influenced by the rate of pore pressure dissipation. The significance of scale effects raises questions regarding the application of experimental observations to predicting debris flow behavior in practice. Because of these difficulties in experimental tests and field observations, numerical modeling has become an important and promising alternative in debris flow studies. Compared with laboratory and field observations, numerical modeling is capable of generating information on debris flow mobility quickly and efficiently.

Modeling of debris flows requires a constitutive model to describe the behavior of water-sediment mixtures. Debris flow is multiphase on a microscopic scale. The solid phase typically consists of discrete clasts; the interstitial fluid consists of water, suspended fine particles, and possibly entrained gas. From an energy perspective, momentum exchange and energy dissipation are involved in instantaneous collisions, sustained rolling and sliding of particles, deformation of interstitial fluid, and strong interactions between solid and fluid phases. A variety of constitutive relationships from highly theoretical models to simple semi-empirical ones have been formulated for analyzing debris flow behavior. Even though highly theoretical models have general validity, most of them are too complicated to implement in practice. Simple equations based on semi-empirical models can easily be implemented but are often limited to a narrow range of application due to lack of adaptability. Therefore, the selection of appropriate constitutive equations has been one of the major issues in debris flow simulations.

Highly mobile soil flows can be produced by the failures of constructed fill slopes, waste dumps, road embankments, tailing dams, and hydraulic fill dams (Morgenstern 1978, 2001; Seed 1968). Detailed studies of these flow slides indicate that soils involved in the flows are characterized by strain-softening behavior. High runout mobility is the result of static or dynamic liquefaction of the strain softening soils (Dawson et al. 1998; Hungr et al. 2002; Olson 2001; Olson et al. 2000; Seed 1968). The liquefaction flow slides of soil structures triggered by either monotonic or cyclic loading are not usually classified as debris flows. However, laboratory experiments performed on samples from debris flow deposits show that natural sediment involved in debris flows behaves like a strain softening soil (Fukuoka et al. 2004; Sassa 2000). Despite apparent differences in source material and slope geometry there are similarities in failure mechanism and post-failure deformation behavior between liquefaction flow slides and natural debris flows (Fell et al. 2000; Hungr et al. 2002; Morgenstern 1978; Pastor et al. 2002). For this reason, formulations of constitutive behavior and analytical models have much in common for all such flow phenomena.

1.2 Historical Development of Constitutive Modeling of Debris Flows

When formulating a constitutive model for granular flows, the work of Bagnold (1954) should be considered. He conducted experiments on dense mixtures of neutrally buoyant, cohesionless, solid spherical particles suspended in a Newtonian fluid, using concentric cylinder rheometers. Bagnold measured the shear and normal forces for grain-fluid mixtures with a wide range of solid concentrations (volume concentration varied from 0.13 to 0.62) and introduced the concept of dispersive stress. The dispersive stress is defined as the stress which is generated by grain collisions and is additional to the normal stress exerted by the intergranular fluid. Bagnold's experiments and analyses demonstrated that shear and normal stresses vary linearly with the shear rate when the effects of interstitial fluid viscosity dominate in a macro-viscous regime, and vary quadratically with shear rate when grain collisions dominate in a grain inertial regime.

The concept of dispersive pressure proposed by Bagnold (1954) has a major influence on the subsequent formulation of debris flow constitutive models, particularly the models developed by Japanese researchers. Takahashi (1978, 1980, 1991) assumed that debris flows are mechanically identical to granular flows and that flowing resistances are associated with collisions among particles. Using Bagnold's (1954) dilatant fluid model, Takahashi (1978, 1980, 1991) derived equations for debris flow modeling and extensively applied them to all stages of the debris flow process, from initiation through deposition. Takahashi's model is essentially identical to Bagnold's dilatant fluid model except that the numerical constants in Takahashi's model are determined on the basis of flume testing results.

Johnson (1970) and Johnson and Rodine (1984) proposed Bingham and Coulomb viscous models for debris flow simulations based on observations of small experimental debris flows and of natural debris flow deposits. The total resistance in the Coulomb viscous model is expressed as a combination of yield, frictional and viscous resistances. The Coulomb viscous model has been applied to explain mechanisms of the formation of relatively rigid upper plugs within a flow and the transport of large clasts in debris flows (Johnson 1970; Johnson and Rodine 1984). Johnson (1996) developed the viscous-inertial model for analyzing granular flows with a wide range of solid concentrations. The viscous-inertial model combines the Coulomb viscous model for macro-viscous flows and Bagnold's dilatant fluid model for grain flows.

Chen (1987, 1988a, 1988b) and Chen and Ling (1996) extended Bagnold's model and proposed a generalized viscoplastic fluid model by incorporating the Mohr-Coulomb yield criterion into the original dilatant fluid model (Bagnold 1954). The shear resistance in the generalized viscoplastic fluid model consists of a yield strength and a dynamic resistance. The yield strength is independent of shear rate and determined from an extended form of the Mohr-Coulomb law. The dynamic resistance is shear rate dependent and determined from the generalized Bagnold (1954) equations.

Hungr and Morgenstern (1984a, 1984b) conducted a series of experimental tests on granular flows with a wide range of velocities. The experimental results indicated that the Coulomb relationship between shear and normal stresses is valid in both slow- and rapid-moving granular flows. The validity of the Coulomb friction law in a moving granular mass flow has been further substantiated with laboratory experiments on rock fragments (Cagnoli and Manga 2004). Because of the well-grounded validity and easy numerical implementation, the Coulomb friction law has been the most widely used constitutive model for the numerical analysis of debris flows (Cagnoli and Manga 2004; Gray et al. 1999; Iverson 1997; Iverson and Vallance 2001; Iverson and Denlinger 2001; Iverson et al. 2004; McDougall and Hungr 2004, 2005; Wang et al. 2004; Wieland et al. 1999).

1.3 Historical Development of Numerical Modeling of Debris Flows

Mathematical modeling of granular flows was originally introduced by Savage and Hutter (1989, 1991). Starting from the mass and momentum conservation equations for flow on a rough inclined plane, and using the depth averaging process and making scaling arguments, Savage and Hutter (1989) derived the one-dimensional, depth-averaged equations for the shallow free surface flow of dry granular materials. The model assumes that a moving granular mass behaves as a cohesionless Coulomb frictional material and the relationship between shear and normal stresses on internal and rough bounding surfaces obeys the Coulomb friction law. Multi-dimensional extensions of the Savage-Hutter model have been formulated for analyzing dry granular flows over complex topography (Denlinger and Iverson 2004; Gray et al. 1999; Iverson and Denlinger 2001; Pudasaini and Hutter 2003; Pudasaini et al. 2005a, 2005b; Wang et al. 2004). The Savage-Hutter model and its generalized versions have been tested against laboratory experiments of rapid granular flows over a wide variety of bed topographies (Chiou et al. 2005; Greve and Hutter 1993; Hutter and Koch 1991; Hutter et al. 1995; Iverson et al. 2004; Kelfoun and Druitt 2005; Wieland et al. 1999). Theoretical predictions were found to be in good agreement with experimental measurements. The Savage-Hutter model and its various generalized versions have been established as the leading models in the area of dry granular flow analysis. However, their broad applications are limited to modeling of dry granular flows over the simple topography analyzed in most laboratory experiments.

Hungr (1995) formulated a continuum model for the analysis of rapid flow-like landslides. Based on the model, a dynamic analysis program (DAN) has been developed and applied to debris flows (Hungr 1995; Hungr and Evans 2004; Hungr et al. 2002). Later, McDougall and Hungr (2004, 2005) extended the model of Hungr (1995) for analyzing debris flows over three-dimensional topography. This model embraces a wide range of constitutive formulation.

Iverson (1997) and Iverson and Denlinger (2001) introduced Coulomb mixture theory and derived governing equations for a wide spectrum of grain-fluid mixture flows based on two-phase analysis. The Coulomb mixture model assumes that solids and interstitial fluids in debris flows behave constitutively as Coulomb frictional materials and Newtonian viscous materials, respectively. A negligible velocity difference between solid and fluid and constant mixture density is assumed by the authors (Iverson 1997; Iverson and Denlinger 2001) to simplify continuity and momentum equations. Advection-diffusion equations are postulated to describe pore pressure changes in response to the movement of solids (Iverson and Denlinger 2001).

Pitman and Le (2005) proposed a two-fluid model for granular flows of the mixture of solid particles and fluid. Continuity and momentum equations are explicitly formulated for both solid and fluid phases in the two-fluid model. Interactions between particles and fluid are taken into account in the model with a velocity-dependent force. Together with constitutive assumptions and boundary conditions, the continuity and momentum equations can be applied to the analysis of debris flows. The two-fluid model does not make use of the assumption that fluid and solid have identical velocities in the Coulomb mixture model (Iverson 1997; Iverson and Denlinger 2001). The velocities for solid and fluid phases can be determined separately.

The original Savage-Hutter model accounts only for the deformation of dry granular materials. The effect of pore pressure due to the presence of interstitial fluid is missing. In dry granular flows, the effect of interstitial fluid is negligible. However, debris flow mobility is known to be dependent on the pore pressure of the interstitial fluid. The effect of fluid is of importance in debris flow runout predictions. Pudasaini et al. (2005b) extended the Savage-Hutter model for debris flow simulation by including pore pressures in the model. The extended model has been applied to analyzing debris flow flume tests, and good agreement is obtained between theoretical predictions and experiments (Pudasaini et al. 2005b). However, the pore pressures are not predicted; they are merely assumed by employing an advection-diffusion equation similar to those proposed by Iverson and Denlinger (2001) and Savage and Iverson (2003).

Depth-averaged continuum equations can be derived by the integration of continuity and momentum equations for an incompressible flowing medium over flow depth. The derivation of depth-averaged equations for debris flow modeling is based on the assumption that horizontal length scales are much greater than flow depth. This assumption allows the complex three-dimensional problem to be solved with substantially reduced computational effort. However, the depth averaging process sacrifices flow details in the dimension normal to the flow direction (Steffler and Jin 1993). With uniform velocity distribution over the flow depth, depth-averaged models neglect the effects of internal flow dynamics on debris flow simulations.

1.4 Scope of the Study

Debris flow modeling demands appropriate constitutive and numerical models. Although a variety of constitutive and numerical models have been developed in debris flow studies, rigorous testing of these proposed models is still lacking. This study provides a comprehensive examination of the state of the art in debris flow modeling. The objectives of the study are to determine if suitable constitutive and numerical models exist or could be developed for debris flows, which would provide practitioners with simple, reliable predictions of the potential flow extent. Considering the issues discussed above regarding debris flow simulation, the present research work involved the following areas:

(1) Review of the available literature on debris flow terminology, and on constitutive and numerical modeling;

(2) Investigation of constitutive models of debris flows and the methods for obtaining model parameters;

(3) Examination of depth-averaged models in debris flow simulation and of bed shear relationships used in these models;

(4) Development of a new analytical model based on energy conservations and including the effects of internal energy dissipation;

(5) Application of the new analytical model to field cases with sufficient detail available to permit comparisons between predicted and observed behavior.

1.5 Outline of Thesis

As mentioned earlier in this chapter, the prime objective of this research is to provide practitioners with simple and practical procedures to predict the potential extent of debris flows and related phenomena. The studies undertaken to achieve this objective are described in subsequent chapters:

Chapter 2 presents an overview of the classification systems and terminology of sediment-water flows. Emphasis is placed on classifying flow-like landslides.

Chapter 3 contains critical investigations of the constitutive relationships in debris flow modeling. The validity and applicability of constitutive laws are examined from the perspective of debris flow simulations.

Chapter 4 deals with depth-averaged models in debris flow simulation. The depth-averaged governing equations are formulated in detail. Bottom shear relationships used in debris flow analyses are discussed as well.

Chapter 5 describes the formulation of a new analytical model for debris flows. The new model is based on energy conservations and accounts for the effects of internal energy dissipation due to flow deformation. A numerical solution is developed for the implementations of the model in debris flow analysis.

Chapter 6 describes applications of the proposed model to well-documented liquefaction flow slide case histories. The validity of the new model is tested by comparing theoretical predictions with observed behaviors.

Chapter 7 investigates the trigger mechanism for debris flows on natural slopes, particularly debris flows mobilized from landslides. Case histories of debris flows on natural slopes are analyzed using the new model. Applicability of the model is examined by comparing shear strengths back-calculated from dynamic analyses with the results from ring-shear tests.

Chapter 8 contains the major conclusions of the work and makes recommendations for further research.

Chapter 2

Terminology and Definitions for Debris Flows

2.1 Introduction

Debris flows are often classified as flow-like landslides. Many different landslide classification systems have been developed for specific purposes. Classification is often based on how much emphasis is placed on a particular aspect of the problem or on observations in specific regions. The scope of their application is thus often limited to the corresponding objective. Improper use of these classifications can cause problems in understanding and communication between researchers and practitioners. An unambiguous and agreed-upon definition of debris flow is essential for communication and idea exchange among researchers and engineers in the debris flow field. This chapter focuses on classifications of flow-like mass movement and definitions of debris flow. Two types of classification are examined: one is based on the kind of material and the type and rate of movement; the other is based on constitutive properties of the materials involved in the movement. The limitations and strengths of various classifications are discussed and the classification appropriate to debris flow research is recommended.

2.2 Classification of Flow-Like Landslides

The terminology proposed in the early landslide classification by Sharpe (1938) greatly influenced ensuing classifications of flowing mass movement. Sharpe used relative velocity and sediment concentration as two primary factors in the classification. Rapid flow-like landslides were categorized as earthflow, mudflow, and debris avalanche. If grain size criteria proposed by Cruden and Varnes (1996) are used, the debris avalanche in the classification of Sharpe (1938) is identical to the debris flow in the classification of Cruden and Varnes (1996).

The landslide classification by Varnes (1978) and its modification by Cruden and Varnes (1996) are the most widely adopted classification systems in North America. Distinctions between various types of landslides are primarily based on the types of movement and kinds of materials in the classification of Cruden and Varnes. The types of landslide movement include fall, topple, slide, spread, and flow. The post-failure velocities of displaced masses are divided into seven classes (Table 2-1). The types of materials involved in slope movement are categorized as rock and engineering soils which are further divided into debris and earth on the basis of soil composition. Earth describes a soil in which less than 20 percent of the particles are larger than 2 mm. Debris is defined as a soil containing a significant proportion of coarse material, with more than 20 percent of the particles larger than 2 mm. Table 2-2 presents the classification of landslides proposed by Cruden and Varnes (1996).

The comprehensive classification of slope movements by Hutchinson (1988) is based primarily on the morphology of slope. Slope movements are divided into eight main classes, i.e., rebound, creep, sagging of mountain slopes, landslides, flow-like debris movements, topples, falls, and complex slope movements. Each major type of slope movement is further subdivided according to movement mechanism, type of material and rate of movement. Debris flow, a subtype of flow-like debris movement, denotes the very-to-entirely rapid flow of wet debris. In the classification of Hutchinson (1988), hillslope debris flow and channelized debris flow are distinguished by the existence of an established channel.

The classification of landslides developed by the EPOCH (1991-1993) project (The Temporal Occurrence and Forecasting of Landslides in the European Community, Contact No. 90 0025) is commonly used in Europe (Dickau et al. 1996). The classification is based on material type (e.g., rock, debris, soil), principal mechanisms of movement (e.g., fall, topple, slide, flow, complex), and degree of disruption of the displaced materials. Landslide types classified according to this classification scheme are shown in Table 2-3. Debris and soil in Table 2-3 are distinguished by the particle size of the materials moved. Soil describes materials with particle size finer than 2 mm. Debris is material coarser than 2 mm and usually describes an assortment of material including clasts incorporated into a matrix. Within this classification, debris flow denotes the down-slope movement of the mixtures of fine material, coarse material, and water.

Hungr et al. (2001) presented a systematic classification for flow-like landslides. The classification takes account of material properties, mechanism, velocity of movement, and the existence of an established channel. The landslide materials are divided into sorted and unsorted materials. Sorted materials include gravel, sand, silt, and clay. Unsorted materials include debris, earth, mud, peat, and rock. Debris is a loose material of low plasticity such as that produced by mass-wasting processes, weathering, glacial transport, or human activity (Hungr et al. 2001). Based on the material components and other criteria, flow-like landslides are divided into ten types as shown in Table 2-4 (Hungr et al. 2001).

According to Table 2-4, debris flow can be distinguished from other types of landslides on the basis of material composition, moisture content, velocity of movement and peak discharge, and the existence of established channels. For instance, the distinction between debris flows and mud flows is primarily based on the type and size of materials moved. Debris flows are distinguished from debris avalanches by the presence of a confined channel. Debris flood and debris flows are distinguished by the latter possessing relatively high sediment concentration and peak discharge.

Post-failure velocity of landslides is an important parameter for landslide hazard evaluation. The rate-of-movement scale proposed by Cruden and Varnes (1996) is adopted in the above definitions of flow-like landslides. According to the velocity classification in Table 2-1, debris flow, debris avalanche, mud flow, and rock avalanche are among the extremely rapid class and capable of causing severe economic and social consequences (Hungr et al. 2001).

2.3 Classification of Sediment-Water Flows

The constitutive behavior of mixtures of water and sediment is primarily governed by solid concentration and deformation rate. Pierson and Costa (1987) proposed a classification for sediment-water flows based on rheological behavior and characteristics of flows. Using sediment concentration and velocity as criteria, Pierson and Costa (1987) proposed four types of sediment-water flows: normal stream flow, hyperconcentrated stream flow, slurry flow, and granular flow (Table 2-5). Exact positions of rheological boundaries in Table 2-5 depend on the magnitude of the yield strength of mixtures, which is controlled by sediment concentration as well as sediment composition and particle-size distribution. The acquisition of measurable yield strength due to increase of sediment concentration corresponds to the transition from normal stream flow to hyperconcentrated flow. The dramatic increase in yield strength due to increase of sediment concentration coincides with the transition from hyperconcentrated stream flow to slurry flow. Transition from slurry flow to granular flow begins when the sediment concentration increases to the point where flowing behavior of the mixture is predominantly controlled by contacts and collisions of grains. According to Pierson and Costa (1987), slurry flow is the most appropriate term for debris flow within the rheological classification. Depending on material properties, water content, and dominant resistances involved in the flow, a debris flow can be either a viscous or an inertial slurry flow.

Rheological classification of sediment-water flows proposed by Coussot and Meunier (1996) are primarily based on solid concentration and the type of materials moved. Sediment-water flows are classified into four main types: stream flows, hyperconcentrated flows, debris flows, and landslides. Debris flow is defined as a single viscous material flow undergoing large homogeneous deformations without significant changes in mechanical properties. Cousot and Meunier (1996) pointed out that debris flow is an intermediate type between hyperconcentrated flow and landslide. Debris flows are distinguished from hyperconcentrated flows and landslides based mainly on sediment concentration, flowing, and deposit characteristics. Debris flows are further subdivided into two main types based on the rheological properties of materials: muddy debris flows and granular debris flows.

Jan and Shen (1997) pointed out that fluid viscosity, turbulence, particle sliding friction, and particle collision have effects on momentum exchange in debris flows. Six flow regimes are proposed for debris flows based on their constitutive behaviors: friction regime, collision regime, friction-collision regime, macro-viscous regime, viscoplastic regime, and visco-plastic-collisional regime. In the friction regime, momentum exchange of debris flows arises primarily from the mutual contact between particles and momentum exchange due to interstitial fluid is negligible. In the collision regime, momentum exchange of debris flow is mainly transferred by particle collisions. In the friction-collisional regime, momentum exchange of debris flow caused by both particle friction and particle collisions is significant. Debris flows in the macro-viscous regime can be treated as generalized Newtonian fluids with effective viscosity being dependent on fluid property, temperature, and sediment concentration. Debris flows in the viscoplastic regime have a finite yield strength and flow as Newtonian fluids if the yield strength is exceeded. The yield strength of debris flows in the viscoplastic regime consists of cohesion and friction provided by fine-grained matrix and coarse particles, respectively. In the visco-plastic-collisional regime, interactions of larger particles and fluid viscosity may play significant roles in momentum exchange in debris flows. The shear resistance mobilized includes yield, viscous, collision, and turbulent stress components. This classification is complex and speculative. It has not found much application.

2.4 Debris Flow Size Classification

Jakob (2005) presented a size classification for debris flows based on total volume, peak discharge, and area inundated by debris. Emphasis is placed on the hazard assessment for a debris flow-prone terrain. The volume of debris flows plays a dominant role in the classification because peak discharge and inundation area are determined primarily by their correlations with total volume. Muddy debris flows and granular debris flows are distinguished in the classification and corresponding empirical equations are used to calculate peak discharge and area inundated. Table 2-6 presents the size classification of debris flows and corresponding potential consequences of each class from the perspective of hazard assessment.

2.5 Discussion and Conclusion

The classifications described above can be divided into two categories: qualitative classifications (Sharpe 1938; Cruden and Varnes 1996; Hutchinson 1988; Hungr et al. 2001) based on style and rate of movement, type of material moved, and flow features; and quantitative classifications (Pierson and Costa 1987; Coussot and Meunier 1996; Jan and Shen 1997) based on physical and rheological properties of flowing masses.

The application of quantitative classifications generally requires very good knowledge of material behavior, as well as initial and boundary conditions. Some of the classifications focus exclusively on the dynamic modeling of debris flows (e.g., Jan and Shen 1997) and parameters required for the classifications can only be determined by well-controlled laboratory experiments. Quantitative classifications, therefore, are suitable for studying well-documented case histories in which rheological properties of materials are well defined.

Field observations demonstrate that debris flows are characterized as highly heterogeneous (Phillips and Davies 1991; Iverson 1997; Hungr 2001). Depending on the solid concentration and external driving forces, a debris flow can behave in very different ways mimicking a solid or liquid even in different phases of the same flow event. Quantitative classifications cannot take into consideration such heterogeneity and changes in rheological properties of debris flows. The validity of quantitative classifications is therefore very questionable, since practical debris flows are by no means the idealized fluid flows the classifications assume. In addition to this basic criticism, the quantitative classifications are not readily applicable in a debris flow-prone terrain in practice, since many of quantities required for the classifications are extremely difficult to measure or estimate reliably.

The qualitative classifications of Cruden and Varnes (1996), Hutchinson (1988), and Hungr et al. (2001) are based on a wide variety of factors which include the kind of material, type and rate of movement, water content, liquefaction behavior of source materials, and the presence of a confined channel. Most of the information required can be easily obtained through geotechnical investigations. Compared with quantitative classification, qualitative classification is more practical and suitable for hazard prediction and risk assessment in a debris flow-prone terrain. Among qualitative classifications, the classification of flow-like landslides proposed by Hungr et al. (2001) is the latest version for flows of geotechnical materials. Based on classifications of landslides with a broad meaning by Hutchinson (1988) and Cruden and Varnes (1996), the classification of Hungr et al. (2001) focuses on landslides of the flow type and approaches the subject from a geotechnical point of view. Consequently, the classification of Hungr et al. (2001) is followed in this research and the corresponding terminology is used.

Table 2-1 Landslide velocity scale (Modified from Cruden and Varnes 1996)

Velocity Class	**Description**	**Velocity (mm/sec)**	**Typical Velocity**
7	Extremely rapid	$> 5\times10^{3}$	> 5 m/second
6	Very rapid	$5\times10^{1} \sim 5\times10^{3}$	3 m/minute ~ 5 m/second
5	Rapid	$5\times10^{-1} \sim 5\times10^{1}$	1.8 m/hour ~ 3 m/minute
4	Moderate	$5\times10^{-3} \sim 5\times10^{-1}$	13 m/month ~ 1.8 m/hour
3	Slow	$5\times10^{-5} \sim 5\times10^{-3}$	1.6 m/year ~ 13 m/month
2	Very slow	$5\times10^{-7} \sim 5\times10^{-5}$	16 mm/year ~ 1.6 m/year
1	Extremely slow	$< 5\times10^{-7}$	< 16 mm/year

Table 2-2 Classification of slope movements (Cruden and Varnes 1996)

Type of Movement	**Type of Material**		
	Bedrock	**Engineering Soils**	
		Predominantly Coarse	**Predominantly Fine**
Fall	Rock fall	Debris fall	Earth fall
Topple	Rock topple	Debris topple	Earth topple
Slide	Rock slide	Debris slide	Earth slide
Spread	Rock spread	Debris spread	Earth spread
Flow	Rock flow	Debris flow	Earth flow

Table 2-3 Classification of landslides proposed by the EPOCH project (Dikau et al. 1996)

Type of Movement		Type of Material		
		Rock	**Debris**	**Soil**
Fall		Rock fall	Debris fall	Soil fall
Topple		Rock topple	Debris topple	Soil topple
Slide	Rotational	Single	Single	Single
		Multiple	Multiple	Multiple
		Successive	Successive	Successive
	Translational	Block slide	Block slide	Slab slide
	Planar	Rock slide	Debris slide	Mudslide
Lateral spreading		Rock spreading	Debris spread	Soil spreading
Flow		Rock flow	Debris flow	Soil flow
Complex		e.g., Rock avalanche	e.g., Flow slide	e.g., Slump-earth flow

Table 2-4 Classification of landslides of flow type (Modified from Hungr et al. 2001)

Material	**Water Content**[a]	**Special Condition**	**Velocity**	**Name**
Silt, sand, gravel, and debris	Dry, moist or saturated	- No excess pore-pressure - Limit volume	Various	Non-liquefied sand (silt, gravel, debris) flow[c]
Silt, sand, debris, and weak rock	Saturated at rupture surface	- Liquefiable material - Constant water content	Extremely rapid	Sand (silt, debris, rock) flow slide[d]
Sensitive clay	At or above liquid limit	- Liquefaction in situ - Constant water content	Extremely rapid	Clay flow slide[e]
Peat	Saturated	-Excess pore-pressure	Slow to very rapid	Peat flow[f]
Clay or earth	Near plastic limit	- Slow movements - Plug flow (sliding)	Less than rapid	Earth flow[g]
Debris	Saturated	- Established channel - Increased water content	Extremely rapid	Debris flow[h]
Mud	At or above liquid limit	- Fine grained debris flow	Greater than very rapid	Mud flow[i]
Debris	Free water present	- Flood	Extremely rapid	Debris flood[j]
Debris	Partly or fully saturated	- No established channel - Relatively shallow, steep source	Extremely rapid	Debris avalanche[k]
Fragmented rock	Various, mainly dry	- Intact rock at source - Large volume[b]	Extremely rapid	Rock avalanche[l]

[a] Water content of the source material in the vicinity of rupture surface at the time of failure.

[b] Volume greater than 10,000 m^3 approximately.

[c] Non-liquefied sand (silt, gravel, or debris) flow is a flow-like movement of loose dry or moist, sorted or unsorted granular material, without significant excess pore-pressure.

[d] Sand (silt, debris, weak rock) flow slide is a very rapid to extremely rapid flow of sorted or unsorted granular material on moderate slopes, involving excess pore-pressure or liquefaction of material originating from the landslide source.

[e] Clay flow slide is a very rapid to extremely rapid flow of liquefied sensitive clay at or close to its original water content.

[f] Peat flow is a slow to very rapid flow-like movement of saturated peat, involving high pore-pressures.

[g] Earth flow is a rapid or slower, intermittent flow-like movement of plastic, clayey earth.

[h] Debris flow is a very rapid to extremely rapid flow of saturated non-plastic debris in a steep channel. The plasticity index of material involved is less than 5 percent.

[i] Mud flow is a very to extremely rapid flow of saturated plastic debris in a channel, involving significantly greater water content relative to the source

material. The plasticity index of material involved is greater than 5 percent.

[j] Debris flood is a very rapid, surging flow of water, heavily charged with debris, in a steep channel.

[k] Debris avalanche is a very rapid to extremely rapid shallow flow of partially or fully saturated debris on a steep slope, without confinement in an established channel.

[l] Rock avalanche is an extremely rapid, massive flow-like motion of fragmented rock from a large rock slide or rock fall.

Table 2-5 Rheological classification of sediment-water flows (Modified from Pierson and Costa 1987)

Fluid Type	Newtonian	Non-Newtonian		
Interstitial Fluid	Water	Water + Fines		Water + Air + Fines
Flow Category	Stream flow		Slurry flow	Granular flow
Flow Behavior	Liquid		Plastic	

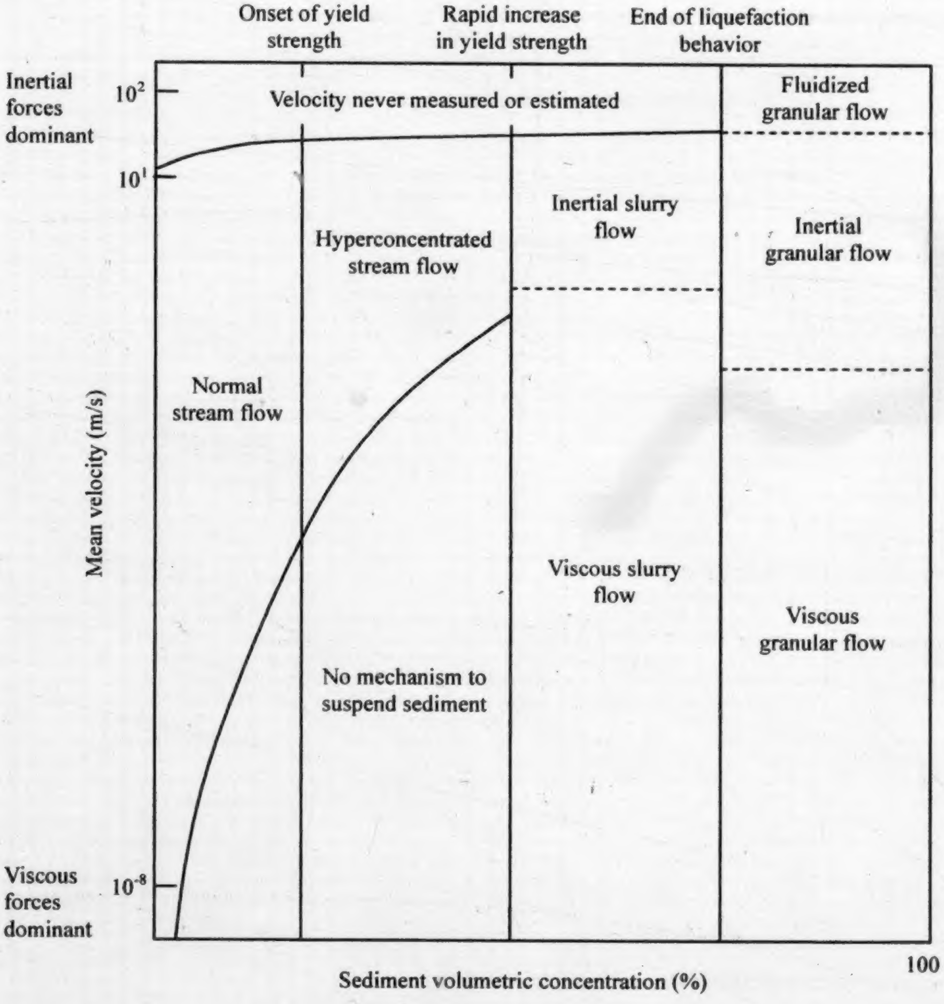
Onset of yield strength
Rapid increase in yield strength
End of liquefaction behavior
Inertial forces dominant
10^2
10^1
10^{-8}
Viscous forces dominant
Mean velocity (m/s)
Velocity never measured or estimated
Fluidized granular flow
Hyperconcentrated stream flow
Inertial slurry flow
Inertial granular flow
Normal stream flow
Viscous slurry flow
Viscous granular flow
No mechanism to suspend sediment
100
Sediment volumetric concentration (%)

Table 2-6 Size classification of debris flows (Jacob 2005)

Size Class	**Volume (m^3)**	**Potential Consequences**
1	$< 10^2$	Very localized damage; known to have killed forestry workers in small gullies; damage to small buildings
2	$10^2 \sim 10^3$	Could bury cars, destroy a small wooden building, break trees, block culverts, derail trains
3	$10^3 \sim 10^4$	Could destroy larger buildings, damage concrete bridge piers, block or damage highways and pipelines
4	$10^4 \sim 10^5$	Could destroy parts of villages, destroy sections of infrastructure corridors or bridges; could block creeks
5	$10^5 \sim 10^6$	Could destroy parts of towns, destroy forests up to several square kilometers, block creeks and small rivers
6	$10^6 \sim 10^7$	Could destroy towns, obliterate valleys or fans up to several tens of square kilometers, dam rivers
7	$10^7 \sim 10^8$	Could destroy parts of cities, obliterate valleys or fans up to several tens of square kilometers, dam large rivers
8	$10^8 \sim 10^9$	Could destroy cities, inundate large valleys up to 100 square kilometers, dam large rivers
9	$10^9 \sim 10^{10}$	Vast and complete destruction over hundreds of square kilometers
10	$> 10^{10}$	Vast and complete destruction over hundreds of square kilometers

Chapter 3

Constitutive Modeling of Debris Flows

3.1 Introduction

The modeling and prediction of debris flow behavior require that an appropriate constitutive law be defined. Debris flow properties depend on a variety of factors, such as suspended solid concentration, particle size distribution, particle shape, frequency and intensity of particle-to-particle friction and collision, cohesive property of interstitial fluid, and pore pressure. Field observation and experimental tests indicate that the behavior of debris flow is too complex to be characterized quantitatively on a microscopic scale. For simplicity, debris flow is usually treated as the movement of an apparent fluid. Many constitutive models have been proposed to describe the rheological properties of the equivalent fluid based on observed or assumed behavior. Interstitial fluid viscosity, turbulence, particle sliding, and collision have long been regarded key features in momentum exchange in debris flows. According to dominant factors in debris flow momentum exchange, constitutive models of debris flow can be classified as: Newtonian fluid model, non-Newtonian fluid model, dilatant fluid model, Coulomb frictional model, Coulomb viscous model, and Voellmy fluid model. The assumptions, validity, and applicability of these models will be discussed in this chapter.

3.2 The Newtonian Fluid Model

The Newtonian fluid model can be used to describe the flow of sediment-water mixtures only if the solid concentration is low and solid phase effects can be expressed by equivalent effective viscosity. The relation between shear stress and shear rate for a Newtonian fluid is given by:

$$\tau = \mu \frac{du}{dz} \tag{3.1}$$

where τ is the shear stress, μ is effective viscosity, and du/dz is shear rate.

Neither particle interactions nor cohesion of the fluid matrix are considered explicitly in Newtonian fluid models. The Newtonian fluid model, therefore, can be used to simulate debris flow only if the solid concentration is below a certain limit. The value of this threshold depends not only on fluid properties and temperature but also on chemical, physical, and mineralogical properties of the solid and its grain size distribution. Jan and Shen (1997) mentioned that a granular-fluid mixture could be treated as a generalized Newtonian fluid with effective viscosity depending on the fluid viscosity and sediment concentration until the volume sediment concentration exceeds nine percent.

The requisite of low sediment concentration makes the Newtonian fluid model of limited application for debris flow modeling. According to the classification by Hungr et al. (2001), a typical debris flood is similar to a water flood and has relatively lower sediment concentration. The Newtonian fluid model appears to be applicable to modeling of debris floods. Hunt (1994) simulated dam-break floods by using Newtonian fluid models. Theoretical predictions showed close agreement with laboratory observations. Rickenmann (1991) conducted experiments on fine material, hyperconcentrated flows and found that the Newtonian fluid can describe this kind of slurry flow in the range of the Reynolds number below 10. The velocity profile and depth-averaged velocity of a steady, one-dimensional, uniform Newtonian fluid down an inclined plane (Figure 3-1) are summarized in Table 3-1. In the table, θ is the inclined angle of the plane, h is the flow depth, u_s is the velocity at free surface, and $\bar{u}$ is the depth-averaged velocity and is defined as

$$\bar{u} = \frac{\int_0^h u\,dz}{h} \tag{3.2}$$

3.3 The Non-Newtonian Fluid Model

The non-Newtonian fluid model describes the flow regime where the viscosity of the fluid varies with shear rate. A wide variety of nonlinear relations between shear stress and shear rate have been developed for non-Newtonian fluids. Among them, the Bingham model, the Herschel-Bulkley model, and the quadratic model have been applied to simulating debris flow behavior.

The Bingham model (linear, viscoplastic model) describes the behavior of initially solid-like material that does not flow until some critical shear stress (yield strength) has been reached, beyond which the material flows in a Newtonian manner. The Bingham model has a simple form and can be treated easily in analytical calculation. For this reason, it has been most widely used for defining the rheological properties of fine-grained slurries, compared with other non-Newtonian fluid models. In one-dimensional form, the relationship between shear stress and shear rate for a Bingham fluid is:

$$\begin{aligned} &\frac{du}{dz} = 0 && \textit{for} \quad \tau < \tau_0 \\ &\tau = \tau_0 + \mu\frac{du}{dz} && \textit{for} \quad \tau > \tau_0 \end{aligned} \tag{3.3}$$

where τ_0 is the yield strength.

Application of the Bingham constitutive law to debris flow modeling is based on the assumptions that deformations of the fine-grained matrix governs the macroscopic behavior of the total mixture and that dynamic effects of grain collision, friction, pore-pressure fluctuations, and formation and destruction of the coarse particle network are either negligible or are collectively manifested as approximately Bingham behavior (Phillips and Davies 1991; Major and Pierson 1992; Whipple 1997; Pierson 2005). These assumptions are most reasonable for fine-grained, matrix-rich mudflows and slurry flows. Therefore, it is possible that the Bingham model is appropriately applied only to the mudflows and flows of fine-grained slurries analyzed in most experimental studies. Application of the Bingham model to more granular debris flows should be treated with caution (Whipple 1997).

Laboratory rheological studies of fine-grained slurries have demonstrated a dependence of apparent yield strength and viscosity on debris flow texture and sediment concentration (Phillips and Davies 1991; Major and Pierson 1992). In general, experimental tests have demonstrated that (1) sediment concentration affects the magnitude of yield strength and viscosity of fine-grained slurries, but does not alter general Bingham-like behavior; for a given grain size distribution, yield strength and viscosity are correlated with sediment concentration; (2) apparent viscosity and yield strength are shear rate dependent and extremely sensitive to sediment concentration; both yield strength and viscosity increase by over an order of magnitude over a narrow range of sediment concentration; and (3) for a given sediment concentration, flows with a larger proportion of fines have higher yield strengths and apparent viscosities.

Application of the Bingham plastic model to the analyses of debris flows has been carried out by many investigators. Mei and Yuhi (2001) numerically simulated Bingham fluid flow in a shallow channel using depth-averaged governing equations. Han and Wang (1996) and Huang and Garcia (1997) modeled dam-break debris flows using the Bingham model to describe the relationship between stress and strain rate. Chen and Lee (2002) analyzed several landslides in Hong Kong with the Bingham model. Jin and Fread (1999) used the Bingham model to simulate mud and debris flow. Jeyapalan et al. (1983a, 1983b) divided failure flows of mine tailing dams into laminar and turbulent flow. The Bingham plastic rheological model was used to describe the rheological behavior of flowing materials from tailing dam failures. The theoretical predictions were tested using a series of flume experiments and good agreement was achieved between predictions and observations. The Bingham model was also used for modeling flow slides caused by failure of tailing dams (Pastor et al. 2002). The velocities of a steady, one-dimensional flow of Bingham fluid down an inclined plane (Figure 3-2) are summarized in Table 3-2 where μ and τ_0 are constant.

It has been found that fine-grained slurries have shear thinning properties, i.e., viscosity decreases gradually with an increase in shear rate. The Bingham plastic model may overestimate the true shear strength of this type of material. A

Herschel-Bulkley model (nonlinear viscoplastic model) has been proposed to simulate shear thinning behaviors of water-sediment mixtures (Coussot et al. 1998; Imran et al. 2001; Huang and Garcia 1997). The relationship between shear stress and the rate of strain for a Herschel-Bulkley model is:

$$\begin{aligned} &\frac{du}{dz} = 0 && for \quad \tau < \tau_0 \\ &\tau = \tau_0 + \mu_\eta \left(\frac{du}{dz} \right)^\eta && for \quad \tau > \tau_0 \end{aligned} \tag{3.4}$$

where μ_η is the consistency index, and η is the flow-behavior index.

Coussot et al. (1998) indicated that the Herschel-Bulkley model is applicable to simulating natural debris flows with a fines (<40 μm) fraction higher than 10 percent. A wide range of rheometric tests, including inclined plane tests, large-scale rheometer tests, and field tests, have been conducted to determine rheological parameters for the Herschel-Bulkley model. It has been shown that the Herschel-Bulkley model is capable of fitting experimental data with $\eta = 1/3$. Table 3-3 summarizes the velocities for debris flow with constitutive behavior defined by the Herschel-Bulkley model.

O'Brien and Julien (1985) and Julien and Lan (1991) proposed a quadratic rheological model as a constitutive law for hyperconcentrated sediment flows. The total shear stress in the quadratic rheological model involves four different types of stress: (1) yield stress, (2) viscous stress, (3) turbulent stress, and (4) dispersive stress. Yield stress accounts for the cohesive nature of the fine-grained mixture. Viscous stress describes the contribution of fluid-particle viscosity to total shear stress. Turbulent and dispersive stresses result from flow turbulence and particle collisions, respectively. When expressed in terms of shear rates, yield stress is independent of the velocity gradient, viscous stress varies linearly with the velocity gradient, and turbulent and dispersive stresses increase with the second power of the velocity gradient. The relationship between shear stress and shear rate for the quadratic rheological model is:

$$\begin{aligned} &\frac{du}{dz} = 0 && for \quad \tau < \tau_0 \\ &\tau = \tau_0 + \mu\frac{du}{dz} + \xi\left(\frac{du}{dz}\right)^2 && for \quad \tau > \tau_0 \end{aligned} \tag{3.5}$$

where ξ is a turbulent-dispersive parameter. In equation (3.5), the first term describes the yield strength due to cohesion. The second term accounts for viscous stress. The third term, turbulent-dispersive stress, combines effects of turbulence and effects of dispersive stress induced by collisions between sediment particles. The turbulent-dispersive parameter is dependent on a variety of material properties including mass density, mixing length, sediment size, linear sediment concentration, and impact coefficients. O'Brien and Julien (1988) measured the rheological properties of natural silt and clay mudflow deposits from the Colorado Rocky Mountains. Best-fitted quadratic curves have been obtained by regression analysis of experimental results. The magnitudes of yield stress and viscosity are found to be exponential functions of the volumetric sediment concentration. Julien and Lan (1991) tested the quadratic model against a variety of experimental data. The quadratic model showed reasonable agreement with experimental results.

Yield strength is a very important property in non-Newtonian fluid models. In general, yield strength results form the cohesion of fine-grained materials in debris flows. As a consequence, application of the non-Newtonian constitutive equation requires that debris flow materials contain a significant volume of fine-grained sediment. Reexamination of experimental studies on non-Newtonian models indicates that many tests focused on the behavior of fine-grained slurries with sediment volumetric concentration around 0.5 (O'Brien and Julien 1988; Julien and Lan 1991; Major and Pierson 1992). The increase in content of coarse material alters the constitutive behavior of slurries causing the bulk rheological behavior to deviate from the non-Newtonian ideal. Therefore, non-Newtonian fluid models appear to be applicable to simulating the flow behavior of some clay flow slides and peat flows, according to the classification proposed by Hungr et al. (2001).

3.4 The Dilatant Fluid Model

The dilatant fluid model is based on the concepts of dispersive stress introduced by Bagnold in 1954. Bagnold (1954) conducted a series of tests on dense mixtures of neutrally buoyant, cohesionless, solid spherical particles suspended in a Newtonian fluid. Shear and normal stresses were measured in Bagnold's tests using concentric cylinder rheometers.

Volume solid concentration of the mixtures varied from 0.13 to 0.62. Three flow regimes are identified based on experimental results and physical arguments: macroviscous regime, grain-inertia regime, and transmission regime. Bagnold's experiments and analyses demonstrate that shear and normal stresses change linearly with the shear rate when the effects of interstitial fluid viscosity dominate in the macro-viscous regime and vary quadratically with the shear rate when grain collisions dominate in the grain-inertia regime. To explain flow behavior in the grain-inertia regime, Bagnold proposed the concept of dispersive pressure, which is generated by grain collisions and is additional to the normal stress exerted by the interstitial fluid. The expressions for shear stress and normal stress in the grain-inertia regime are:

$$\tau = a_i \rho_s \lambda^2 d^2 \left(\frac{du}{dz}\right)^2 \sin\phi_d \tag{3.6}$$

$$\sigma = a_i \rho_s \lambda^2 d^2 \left(\frac{du}{dz}\right)^2 \cos\phi_d \tag{3.7}$$

where a_i is a numerical constant, ρ_s is the grain density, $\lambda = \frac{1}{(C_m/C)^{1/3} - 1}$ is the linear concentration, C and C_m are solid volumetric concentration and maximum possible volume concentration (0.74 for uniform spheres), respectively, d is grain diameter, and ϕ_d is the dynamic angle of internal friction. Table 3-4 shows the velocity profile, surface velocity, and average velocity for a one-dimensional flow of dilatant fluid down a slope.

The concept of dispersive stress developed from Bagnold's experiments serves as the theoretic basis for Takahashi's analyses of debris flows. Equations (3.6) and (3.7) were adopted by Takahashi (1978, 1980, 1991) and Takahashi et al. (1992) to investigate debris flow characteristics: velocity profile, debris flow discharge, solid concentration, particle distribution, and deposit thickness. As a consequence, the debris flow model developed by Takahashi is essentially identical to Bagnold's dilatant fluid model except that the different values of a_i are determined from experimental data. Bagnold found from his experiments that a_i remains constant and is equal to 0.042 for the inertial flow regime. Very large values of a_i (ranging from 0.35 to 0.5) have to be adopted by Takahashi to obtain reasonable agreement between predicted velocity and observations (Takahashi 1980).

In an attempt to formulate a more general constitutive law for debris flows, Chen (1987, 1988a, 1988b, 1996) proposed a generalized viscoplastic fluid model by incorporating the Mohr-Coulomb yield criterion into Bagnold's dilatant fluid model. The total shear strength in the generalized viscoplastic fluid model consists of a rate-dependent part and a rate-independent part. The yield strength is independent of shear rate and determined from an extended form of the Mohr-Coulomb law. The dynamic resistance is shear rate dependent and determined from generalized equations derived by Bagnold (1954). The normal stress and shear stress for the one-dimensional generalized viscoplastic model are:

$$\tau = c\cos\phi + p\sin\phi + \mu_1\left(\frac{du}{dz}\right)^{\eta} \tag{3.8}$$

$$\sigma = p + \mu_2\left(\frac{du}{dz}\right)^{\eta} \tag{3.9}$$

where τ and σ are total shear and normal stresses, respectively, c is cohesion, ϕ is the angle of internal friction, p is mean normal pressure which is rate-independent, μ_1 and μ_2 are consistency and cross-consistency indices, respectively, and η is the flow-behavior index. Summation of the first two terms on the right-hand side of equation (3.8) represents yield strength, $\tau_0 = c\cos\phi + p\sin\phi$. The values of c and ϕ

are rate-independent. The value of η may vary from 1 to 2 as the flow changes from a macroviscous regime to a grain-inertia regime. The consistency index and cross-consistency index are determined by:

$$\mu_1 = a_1 \rho_s^{\eta-1} d^{2(\eta-1)} \mu_w^{2-\eta} C_m^{-\frac{B}{K}} \left(1-KC\right)^{-\frac{B}{K}} \tag{3.10}$$

$$\mu_1 = a_2 \rho_s^{\eta-1} d^{2(\eta-1)} \mu_w^{2-\eta} C_m^{-\frac{B}{K}} \left(1-KC\right)^{-\frac{B}{K}} \tag{3.11}$$

in which a_1 and a_2 are numerical constants, μ_w is the viscosity of interstitial fluid, C_m is the maximum possible sediment concentration, C is the sediment concentration, B is a gross factor describing effects of the variation of particle size, shape, rheological properties, deformability, and orientation of the dispersed particles; K is a gross factor describing effects of space-filling, sedimentation volume, and self-crowding; and $\frac{B}{K}$ represents a gross factor describing the interaction effect of colliding particles. The velocity profile, surface velocity, and depth-averaged velocity are shown in Table 3-4 for a generalized viscoplastic model.

The generalized viscoplastic model takes account of three major rheological properties of debris flows: (1) dilatancy of the sediment-water mixture, (2) yield stress determined by the Mohr-Coulomb criterion, and (3) the effect of the viscosity of intergranular fluid. Despite its general validity, many parameters required by the generalized viscoplastic model are difficult to determine. Chen (1988b) attempted to define parameters for the generalized viscoplastic model based on experimental studies of granular flows. However, the generalized viscoplastic model appears to be too complicated to be useful in practice.

3.5 The Coulomb Friction Model

Many experiments indicate that granular mass flow behaves as a Coulomb frictional material and that the relationship between shear stress and normal stress at the base obeys the Coulomb frictional law:

$$\tau = \sigma \tan\phi \tag{3.12}$$

where σ and τ denote normal stress and shear stress, respectively, and ϕ is the frictional angle.

Laboratory flume experiments and ring shear tests have been carried out by Hungr and Morgenstern (1984a, 1984b) to investigate the flow behavior of granular materials at high shear rate and high normal stress. Tests were performed on coarse sand, mixtures of sand and rock flour, polystyrene beads, and sand submerged in water. Residual strength envelopes were obtained in terms of shear stress versus normal stress. Experimental results were well represented by straight linear strength envelopes with zero cohesion, demonstrating a Coulomb friction behavior with a constant frictional angle. Rate and normal stress effects on shear strengths have not been observed over a great range of velocity and material characteristics.

Laboratory experiments on granular flows of rock fragments by Cagoli and Manga (2004) also show that granular mass flows do not behave as either Bingham fluids or Bagnold dilatant grain flows. The experimental results suggest the relationship between shear and normal stress obeys the Coulomb friction law at the base of granular mass flows. The shear stress does not depend on the shear rate in granular flows. Because of the well-grounded validity and easy numerical implementation, the Coulomb friction law has been widely used as a constitutive equation in debris flow modeling.

Savage and Hutter (1989) formulated the depth-averaged model for dry granular flows down an inclined plane assuming shear stress and normal stress at the base of flows obeying the Coulomb friction law. After the pioneering work of Savage and Hutter, the Coulomb friction model has been widely applied to the analyses of rapid granular mass flows (Hutter and Koch 1991; Greve and Hutter 1993; Greve et al. 1994; Wieland et al. 1999; Gray et al. 1999; Wang et al. 2004; Pudasaini et al. 2005a, 2005b). A survey of the literature indicates that many case histories have been successfully analyzed using the Coulomb friction model. Flow slides in Rocky Mountain coal mine waste dumps were back-analyzed using a dynamic analysis program (Hungr 1995) with a friction model. The back-calculated friction angle varies in the range of 10° to

24 (Golder Associates Ltd. 1995). Pastor et al. (2002) simulated flowslides caused by failures of tailing dams and mine waste dumps with the sliding mass being described as a frictional material. Chen and Lee (2000) carried out numerical simulations of debris flows in Hong Kong using the frictional model. Kelfoun and Druitt (2005) simulated the Socompa rock avalanche in Chile using depth-averaged flow equations and a frictional constitutive law.

The macroscopic constitutive response of materials subjected to the Coulomb friction law is determined by the overall frictional performance of the mass. Sliding and rolling between particles have strong effects upon the level of bulk Coulomb friction and consequently upon the macroscopic strength of water-sediment mixtures. Application of the Coulomb frictional model requires persistent mutual contact between particles and formation of force chains on a microscopic scale. Therefore, the Coulomb friction model is appropriate to granular flows with substantially high sediment concentration, in which particles sustain contact as they slide relative to one another, and material constitutive properties are primarily dependent on the force network of coarse particles within the flow and the nature of contacts between particles. These granular flows include non-liquefied sand flow, sand flow slide, debris flow, debris avalanche, and rock avalanche, according to the classification by Hungr et al. (2001).

3.6 The Coulomb Viscous Model

The resistance of a Coulomb viscous flow is a combination of the yield strength and viscosity of the slurry in the interstices of the coarse, granular phase. The Coulomb viscous model includes Coulomb's equation and a term with a viscosity coefficient. The yield strength consists of cohesion and friction parts (Johnson and Rodine 1984). The frictional part in yield strength is proportional to the normal stress acting on the shear plane. For one-dimensional flow, the constitutive equations of the Coulomb viscous model are:

$$\frac{du}{dz} = 0, \qquad \tau < \tau_c + \sigma \tan \phi \tag{3.13}$$

$$\tau = \tau_c + \sigma \tan \phi + \mu \frac{du}{dz}, \quad \tau > \tau_c + \sigma \tan \phi \tag{3.14}$$

where τ_c is the cohesive strength, σ is normal stress, ϕ is the internal friction angle, and μ is viscosity.

In the Coulomb viscous model, the Coulomb frictional equation can be expressed as total yield stress, $\tau_0 = \tau_c + \sigma \tan \phi$. This suggests that velocity characteristics of the Coulomb viscous fluid are similar to those of a Bingham fluid (Table 3-2). Therefore, the Coulomb viscous model and the Bingham model are generally classified as viscoplastic models by many researchers. However, these two models reflect different mechanical behavior of flows. The yield strength of a Bingham fluid arises mainly from cohesion of the interstitial fluid; interaction between particles is negligible. In the Coulomb viscous model, the friction part has significant effects on the total yield strength. The determination of total flow resistance of a Coulomb viscous fluid requires taking account of the effects of particle contact friction. The Coulomb viscous model has been applied to explain mechanisms of the formation of relatively rigid upper plugs and the transport of large clasts in debris flows (Johnson and Rodine 1984).

3.7 The Voellmy Fluid Model

The Voellmy fluid model has been used by engineers for many years (Korner 1980; Bartelt et al. 1999) in modeling snow avalanche motion. Rooted in the theory of open-channel flow, the Voellmy model assumes that the shear resistance at the base of an avalanche is given by the sum of a Coulomb-type friction and a turbulence term that varies with the square of the flow velocity:

$$\tau = \sigma \tan \phi + \gamma \frac{u^2}{\xi} \tag{3.15}$$

where τ and σ are shear and normal stresses, ϕ is the friction angle, u is longitudinal velocity, γ is the unit weight of material and ξ is a turbulence coefficient with the dimension of acceleration.

The frictional coefficient $\tan\phi$ and turbulence coefficient ξ in equation (3.15) depend on material properties and the roughness of the flow surface, respectively. The magnitude of these parameters can be determined by back-analysis of historical avalanche events. Case history studies indicate the parameters in the Voellmy model tend to vary over a wide range for different avalanche paths and different snow and terrain conditions (Lang et al. 1985; Barbolini et al. 2000).

According to the classification proposed by Hungr et al. (2001), debris avalanche and rock avalanche are very similar to snow avalanche within the framework of granular flows. Researchers are thus led in a natural way to use the Voellmy fluid model as a constitutive law for analyzing debris avalanches, rock avalanches, and related phenomena (Korner 1976; Evans et al. 2001; Hungr and Evans 1996, 2004; Hungr et al. 2002). Hungr (1995) developed a dynamic analysis program (DAN) for the mobility analysis of rapid flow slides, debris flows, and avalanches. The Voellmy fluid model is embedded in DAN as one of the constitutive laws to define material properties. Flowslides in Rocky Mountain coal mine waste dumps were back-analyzed using DAN with the friction model and the Voellmy model (Golder Associates Ltd. 1995; Hungr et al. 2002). Compared with the friction model, the Voellmy model was found to be more appropriate for the flow slides in which a significant amount of fully liquefied sandy gravel materials were involved (Hungr et al. 2002). The Voellmy model and friction model have been widely used for back-analyzing debris flows on natural terrain in Hong Kong (Hungr 1998; Ayotte and Hungr 1998, 2000; Lo and Chau 2003). Results of the back-analyses indicate that the friction model can adequately simulate open-slope debris flows, while the Voellmy model is more appropriate to simulate long-runout, channelized debris flows. Hungr and Evans (1996) and Evans et al. (2001) analyzed a number of case histories of rock avalanches using DAN with different constitutive laws. The constitutive laws considered include the Bingham model, the friction model, and the Voellmy model. Compared with the friction and Voellmy models, the Bingham model tends to overestimate flow velocities and the degree of longitudinal spreading of the avalanches. Both friction and Voellmy models are able to simulate the runout distance of avalanches quite well. However, similar to the Bingham model, the friction model has a tendency to overestimate flow velocities and to produce an excessively thin debris distribution at the front of avalanche deposits. In general, the Voellmy model provides the best agreement between calculations and field observations in terms of debris spreading, distribution, and velocity profiles.

The Voellmy model is purely phenomenological and the model formulation is primarily based on observations of real avalanches (Bartelt et al. 1999). Parameters in the Voellmy model cannot be measured independently. Parameter magnitudes have to be determined by back-analyzing historical avalanche events. Since flow resistance depends on two parameters in the Voellmy model, an infinite number of combinations of parameters can be used to obtain a given runout distance for an avalanche event. Each pair of parameters produces a different velocity profile. An appropriate choice of a unique pair can only be made if there are some independent velocity observations available along the debris flow path. However, very few well-documented rock avalanches or debris flows have been found to have adequate velocity measurements such that reliable calibration of the Voellmy model parameters can be carried out.

Observations of snow avalanches indicate that granular flows are obviously different from turbulent water flows. As corroborated by recent large chute experiments with snow (Kern et al. 2004), turbulence has not been generally found in flowing granular materials (Salm 2004). The shear resistance as a result of turbulence is lacking in experimental evidence when attempts are made to apply the Voellmy model to granular flows. On the other hand, tests performed on granular flows show that shear resistance is independent of flow velocity and that the Coulomb friction law is commonly valid in granular mass flows (Hungr and Morgenstern 1984a, 1984b; Cagoli and Manga 2004). On a microscopic scale, the mean free path of particles in debris flow is very small and the relative motion of particles is restricted by the viscosity of the interstitial fluid and the friction between particles. Debris flow particles generally have restitution coefficients close to zero. Debris flow constitutive behaviors based on experimental and field observations cannot justify the assumption that turbulence exists in debris flows. Application of the Voellmy model in granular flows requires an alternative explanation of the turbulence friction in the model. In the original Voellmy model, derivation of the equation for computing runout distance of an avalanche is based on the balance of energy (McClung 1983; Perla et al. 1980). It is possible that the turbulence term in the Voellmy model may arise out of the loss of kinetic energy in granular flows which is not accounted for by the energy dissipation due to basal frictional resistance.

3.8 Discussion of Shear Resistance in Dense Granular Flows

The constitutive models developed for flows of sediment-water mixtures range from the simple Newtonian fluid model to highly theoretical generalized viscoplastic fluid models. Successful interpretation, modeling, and prediction of debris flow behavior require the choice of appropriate constitutive models and correct determination of model parameters. However, it is often difficult to decide which model gives a true description of the debris flow. In many cases, the decision is made by trial and error. Most constitutive equations described so far involve two important parts – yield strength which is rate-independent and viscous stress or dispersive stress which is rate-dependent. Contributions of yield strength and viscous stress to gross shear strength of dense granular flows are discussed in the following sections.

3.8.1 Yield Strength

Rheological investigations of fine-grained slurries indicate that such mixtures behave like non-Newtonian fluids and yield strength must be exceeded before flow occurs. Many rheometric measurements have been conducted to determine yield strength. Phillips and Davies (1991) studied rheological properties of debris flow deposits using a 30^0 inverted cone-and-plate viscometer with a diameter of 2 m. Test results indicate that the fine-grained debris flow deposit behaves as a viscoplastic material and the full-scale debris flow deposit (complete mixture of coarse and fine particles) behaves as a dilatant plastic material. Major and Pierson (1992) conducted rheological tests on slurries consisting of clay, silt, and sand from a natural debris flow deposit by using concentric-cylinder viscometers. Experimental results suggested that slurries exhibit general Bingham fluid behavior. Yield strength and plastic viscosity of the model is very sensitive to sediment concentration. Coussot et al. (1998) indicated the Herschel-Bulkley model is capable of fitting experimental tests on fine suspensions with $\eta = 1/3$. Parsons et al. (2001) performed a series of laboratory experiments on fine-grained slurries in a 10 meter long flume. It was observed that slurries predominantly exhibited non-Newtonian (shear-thinning or Bingham) fluid behavior with finite yield strength. The increase of clay content makes slurries behave in a more Bingham-like fashion. Table 3-6 summarizes the reported yield strength and viscosity determined from experiments on mixtures of water and fine-grained sediments.

Laboratory investigations of debris flow constitutive properties have mainly focused on the behaviors of mixtures ranging from clay slurries to dense suspensions of idealized particles. A typical debris flow, however, contains sediment with particle size ranging from clay to boulders, volumetric concentration greater than 0.6, and shear rates ranging from 0 to 10 s^{-1}. As a consequence, the applicability of experimental findings to the mechanics of natural debris flow remains uncertain because of limited sample volume, the exclusion of coarser particles, and the range of shear rates used in the tests. Table 3-6 shows that yield strength ranges from about 10 to 400 Pa for the fine-grained slurries analyzed in most experimental studies. The deposit thickness of a Bingham material on a slope can be determined using the one-dimensional limit equilibrium equation for an infinite slope:

$$h = \frac{\tau}{\gamma \sin\theta} \tag{3.16}$$

where h is the thickness of debris flow deposit, τ is yield strength, and γ is the unit weight of debris flow.

Figure 3-3 shows the relationship between thickness of debris flow deposit and shear strength for different slopes. For slopes greater than 5^0, deposits with strengths less than 400 Pa should be no thicker than 0.2 m. This prediction conflicts with field observations of debris flow deposits, which are commonly meters in thickness even on steep slopes (Iverson 2003). The discrepancy between yield strength of fine-grained slurries measured in the laboratory and yield strength determined from field observations of debris flow deposits indicates that the viscoplastic yield strength of the interstitial fluid accounts for only a small amount of total debris flow shear resistance. The contribution of yield strength to flow resistance is negligible in modeling coarse-grained debris flows.

3.8.2 Rate Dependence

The dispersive stress concept developed from Bagnold's experiments has had significant influence on subsequent studies of granular flows. The quadratic relationship between shear stress from particle interactions and shearing rate is adopted in the formulation of many constitutive models. These models include the quadratic model, Takahashi's model, and the dilatant fluid model. The first critical review on Bagnold's 1954 experiment was presented by Hunt et al. (2002). After reexamination of the experimental shear stress, Hunt et al. (2002) found that the shear stress in the grain-inertia regime depends on the shear rate to the power of 1.5 instead of the quadratic dependence on shear rate as claimed by Bagnold. Their investigation of the dimensions of the experimental facility in the Bagnold experiments indicated that end effects and boundary conditions have significant influence on Bagnold's stress measurements. Hunt and coworkers then conducted a boundary-layer analysis of experimental results using finite element methods. The particle-fluid mixture is simulated as a Newtonian fluid with a corrected viscosity dependent on the solid concentration. The simulations showed that changes from the macro-viscous to the grain-inertia regime suggested by Bagnold actually correspond to a variation from a linear shear flow to a flow dominated by the boundary layer along the rotating end walls. Hunt et al. (2002) concluded that the quadratic relationship between normal or shear stresses and shear rate in the inertial regime measured by Bagnold (1954) was flawed owing to the neglect of geometric effects of the experimental facility. This has not been widely recognized in the literature and the findings make constitutive models based on dispersive stress concepts suspect.

Laboratory experiments carried out by Hungr and Morgenstern (1984a, 1984b) suggested the validity of the Coulomb friction law in granular mass flows. The shear stress in the Coulomb equation is independent of shearing rate. Cagoli and Manga (2004) conducted experimental studies on dry granular flows of rock fragments. Their experimental results provided evidence to substantiate the conclusion (Hungr and Morgenstern 1984a, 1984b) that the bulk constitutive behavior of granular flows can be described by using the Coulomb friction model.

To investigate the effect of strain-rate and viscosity on granular flows, large-scale ring-shear tests were conducted on dry glass beads and glycerin-saturated glass beads (Sassa 1988, 2000). No effect of strain rate was observed in either dry or glycerin-saturated granular flows. The tests also showed that the viscous shear resistance in a flow of glass beads saturated with glycerin was negligible compared with frictional resistance mobilized in the flow. It is worth noting that the viscosity of glycerin used in the tests was 1500 times greater than that of water. Sassa (2000) thus concluded that the influence of shear velocity (strain rate) is not important in granular flows of practical interest such as debris flows and fast moving landslides. Shear resistance mobilized after failure and during motion is proportional to effective normal stress and regulated by the friction law. Constitutive laws in terms of strain rate such as the non-Newtonian fluid model and the dilatant fluid model cannot appropriately define the shear resistance mobilized in natural dense granular flows.

A series of large-scale experiments was conducted at the U.S. Geological Survey flume to study the mechanics of debris flows (Iverson 1997; Major 1997, 2000; Major and Iverson 1999). Debris flow thickness, basal total normal stress, and basal pore water pressure were measured in the experiments. The experimental data revealed that high pore-fluid pressures exist during debris flow motion. The sustained high pore pressures cause a reduction of shear strength of debris and thereby increase the mobility of debris flows. The flume experiments also demonstrated that intergranular friction and basal friction dominate the mechanical behavior of debris flows. Coulomb friction in a debris flow is mediated by variable pore-fluid pressure according to the effective stress principle (Terzaghi 1943). When effects of pore-fluid pressure are considered, the Coulomb friction model is suitable for determining flow resistance of a water-saturated debris flow (Iverson and Denlinger 2001; Savage and Iverson 2003). Quantitative data from experiments at the U.S. Geological Survey debris flow flume reinforce the validity of the Coulomb friction law in the dense granular flows investigated in this study.

The shear-rate dependent resistance might become significant in the granular flows with extremely high velocity such as debris avalanches, or in granular flows with low solid concentration such as debris flood. A number of constitutive models have been proposed and applied to simulation of those types of granular flows, which is not explored in this study.

3.8.3 Constitutive Equation for Modeling Dense Granular Flow

Field observations and laboratory experiments indicate that constitutive behavior of debris flow is sensitive to changes in sediment concentration, grain size, and grain-size distribution (Phillips and Davies 1991; Major and Pierson 1992). Large-scale flume experiments show that the coarse particles within a debris flow tend to accumulate at the flow front as a result of grain-size segregation and form a high-resistance, coarse-grained debris flow head, which is pushed by a low-resistance, liquefied debris flow body consisting of fine sediment (Major 1997; Iverson 1997, 2003; Hungr 2000). The composition of a natural debris flow can change even in different phases of the same flow as a consequence of deposition, material entrainment, and gain or loss of water content (Evans et al. 2001; Hungr and Evans 2004). Although a natural debris flow may start as a dense granular flow whose shear resistance can be characterized adequately by the Coulomb friction law, it may subsequently develop into a hyperconcentrated sediment flow because of the sensitivity of the constitutive behavior of debris flows to changes in mixture composition. Non-Newtonian fluid models such as the Bingham, the Herschel-Bulkley or the quadratic model can be appropriately applied to the hyperconcentrated flow (O'Brien and Julien 1988; Julien and Lan 1991; Laigle and Coussot 1997; Pierson 2005).

The accurate volume concentration needed to differentiate between a hyperconcentrated flow and a debris flow depends on properties of sediment grains and interactions between solid and fluid phases and is not always predictable. However, laboratory experiments conducted for the calibration of the quadratic model indicate that a hyperconcentrated flow has a volume concentration ranging from 20 percent to 55 percent by volume (O'Brien and Julien 1988). Reexamination of debris flow case histories which have been successfully back-analyzed using the quadratic fluid model shows that the volume concentration in these cases is not more than 55 percent (O'Brien et al. 1993; Mikos et al. 2006). However, debris flows analyzed in this study are limited to the flow of dense coarse-grained sediment-water mixtures with solid concentrations greater than the upper bound of the hyperconcentrated flow (50 to 60 percent by volume). This lower bound of sediment concentration for debris flows appears to be consistent with the classifications of granular flows from a geotechnical engineering standpoint. Such classifications include those proposed by Varnes (1978), Cruden and Varnes (1996), and Hungr et al. (2001). On the other hand, field investigations have demonstrated that some natural debris flows may experience considerable temporal and spatial variations in constitutive behavior due to material entrainment and changes in water content. Successful back-analysis of these case histories requires that different constitutive laws be used correctly to take account of variations in the flow resistance mobilized in different motion phases of a debris flow event (Hungr and Evans 2004; McDougall et al. 2006). These complex debris flow events are excluded from the case history back-analyses in this study so that a specific constitutive law can be appropriately applied to describing debris flow behavior from initiation through deposition.

3.9 Conclusion

The gross strength of water-sediment mixtures is dependent on the cohesive strength, viscosity, and even turbulence of a fluid phase and on the frictional strength of a granular phase. If the sediment concentration is sufficiently small so that interactions among clasts are negligible, normal stress has little effect on the strength of the mixture and the strength of the mixture is essentially determined by the fluid phase (cohesive strength, viscosity, and possible turbulence). If the sediment concentration is high enough and grains touch one another, granular force chains provide a considerable amount of frictional strength. The magnitude of frictional strength depends on the effective normal stress and the angle of contact friction.

It should be emphasized that materials involved in debris flows are very complex and are not open for an exact mechanical-mathematical treatment. However, field observations and experimental studies of debris flows with high solid concentration suggest that:

(1) Friction between coarse particles has significant effects on total flow resistance. Shear resistance due to yield strength of interstitial fluid is much smaller than frictional shear resistance of granular particles.

(2) Applicability of rheometric results to mechanics of debris flows is questionable because of limited sample volume, removal of coarse particles, and the range of shear rate used in the experiments.

(3) Experimental investigations on granular flows with high solid concentration indicate that shear stress is independent of shear rate. Turbulence has not been found in experimental geophysical granular flows.

(4) From a geotechnical engineering perspective, the Coulomb friction law satisfactorily describes the bulk shear resistance mobilized in the practical dense granular flows investigated in this study.

Table 3-1 Velocities for flow of a Newtonian fluid down a slope

Velocities	**Expressions**
Velocity profile	$u = \frac{\rho g h^2 \sin\theta}{\mu}\left[\frac{z}{h} - \frac{1}{2}\left(\frac{z}{h}\right)^2\right]$
Surface velocity	$u_s = \frac{1}{2}\frac{\rho g h^2 \sin\theta}{\mu}$
Average velocity	$\overline{u} = \frac{1}{3}\frac{\rho g h^2 \sin\theta}{\mu} = \frac{2}{3}u_s$

Table 3-2 Velocities for flow of a Bingham fluid down a slope

Velocities	**Expressions**
Velocity profile	$u = \frac{\rho g {h_0}^2 \sin\theta}{\mu}\left[\frac{z}{h_0} - \frac{1}{2}\left(\frac{z}{h_0}\right)^2\right] \quad for \quad 0 \le z \le h_0$
Surface velocity	$u_s = \frac{\rho g {h_0}^2 \sin\theta}{2\mu} \quad for \quad h_0 \le z \le h$
Average velocity	$\overline{u} = \frac{\rho g {h_0}^2 \sin\theta}{\mu}\left(\frac{1}{2} - \frac{1}{6}\frac{h_0}{h}\right) = \left(1 - \frac{1}{3}\frac{h_0}{h}\right)u_s$

Table 3-3 Velocities for flow of a Herschel-Bulkley fluid down a slope

Velocities	**Expressions**
Velocity profile	$u = \frac{\eta}{\eta+1}\left[\frac{\rho g h_0{}^{\eta+1}\sin\theta}{\mu_\eta}\right]^{1/\eta}\left[1-\left(1-\frac{z}{h}\right)^{\eta+1/\eta}\right] \quad for \quad 0 \le z \le h_0$
Surface velocity	$u_s = \frac{\eta}{\eta+1}\left[\frac{\rho g h_0{}^{\eta+1}\sin\theta}{\mu_\eta}\right]^{1/\eta} \quad for \quad h_0 \le z \le h$
Average velocity	$\overline{u} = \frac{n}{n+1}\left(1-\frac{\eta}{2\eta+1}\frac{h_0}{h}\right)\left[\frac{\rho g h_0{}^{\eta+1}\sin\theta}{\mu_\eta}\right]^{1/\eta} = \left(1-\frac{\eta}{2\eta+1}\frac{h_0}{h}\right)u_s$

Table 3-4 Velocities for flow of a dilatant fluid down a slope

Velocities	**Expressions**
Velocity profile	$u = \frac{2}{3}\sqrt{\frac{\rho g \sin\theta}{\alpha}}\left[h^{3/2} - (h-z)^{3/2}\right], \quad \alpha = a_i \rho_s \lambda^2 d^2 \sin\phi_d$
Surface velocity	$u_s = \frac{2}{3}\sqrt{\frac{\rho g \sin\theta}{\alpha}} h^{3/2}$
Average velocity	$\overline{u} = \frac{2}{5}\sqrt{\frac{\rho g \sin\theta}{\alpha}} h^{3/2} = \frac{3}{5} u_s$

Table 3-5 Velocities for flow of a generalized viscoplastic fluid down a slope

Velocities	**Expressions**
Velocity profile	$u=\frac{\eta}{\eta+1}\left[\frac{\alpha\rho g h_0^{\eta+1}\sin\theta}{\mu_\eta}\right]^{1/\eta}\left[1-\left(1-\frac{z}{h}\right)^{\eta+1/\eta}\right] \quad for \quad 0\leq z\leq h_0$ $\alpha=\frac{1-\cot\theta\sin\phi}{1-\frac{\mu_2}{\mu_1}\sin\phi}$
Surface velocity	$u_s=\frac{\eta}{\eta+1}\left[\frac{\alpha\rho g h_0^{\eta+1}\sin\theta}{\mu_\eta}\right]^{1/\eta} \quad for \quad h_0\leq z\leq h$
Average velocity	$\overline{u}=\frac{n}{n+1}\left(1-\frac{\eta}{2\eta+1}\frac{h_0}{h}\right)\left[\frac{\alpha\rho g h_0^{\eta+1}\sin\theta}{\mu_\eta}\right]^{1/\eta}=\left(1-\frac{\eta}{2\eta+1}\frac{h_0}{h}\right)u_s$

Table 3-6 Summary of reported shear strength and viscosity for a mixture of water and fine-grained sediment

Materials	**Parameters**			**Reference**
	C_v or C_w	$\tau_0(Pa)$	$\mu(Pa\cdot s^{\eta})$	
Fine-grained natural debris flow deposit	C_w=0.75~0.83	15~300	0.4~240 $\eta=1$	Phillips and Davies 1991
Fine-grained natural debris flow deposit	C_v=0.44~0.66	10~400	0.2~30 $\eta=1$	Major and Pierson 1992
Clay-water mixture	—	4~20	1.4~3.5 $\eta=\frac{1}{3}$	Laigle and Coussot 1997
Fine suspension	C_v=0.3~0.45	40~100	12~24 $\eta=\frac{1}{3}$	Coussot et al. 1998
Fine-grained slurries	C_v=0.35~0.55	40~70	7~30 $\eta=0.4\sim0.7$	Persons et al. 2001
		14~125	0.7~5 $\eta=1$	

Note: C_v, volumetric sediment concentration; C_w, concentration by weight of sediment; τ_0, yield strength; μ, viscosity; η, flow-behavior index ; $\eta=1$, Bingham fluid; —, data not available.

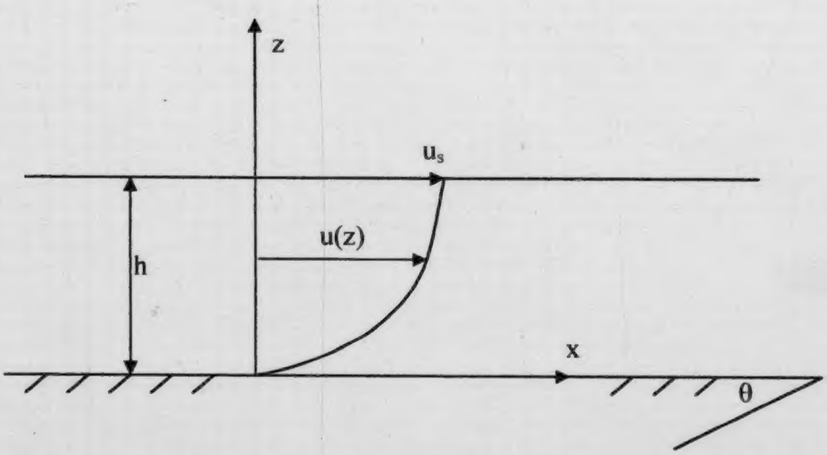

Figure 3-1 Velocity profile for flow of a Newtonian fluid down a slope

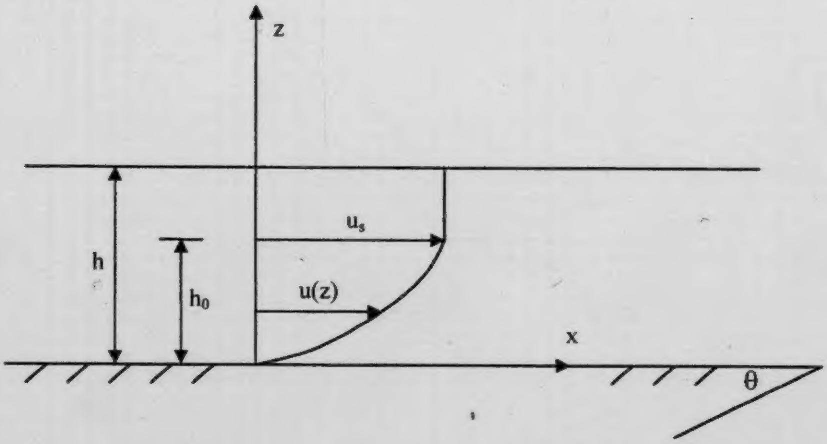
z
u_s
h
h_0
u(z)
x
θ

Figure 3-2 Velocity profile for flow of a non-Newtonian fluid down a slope

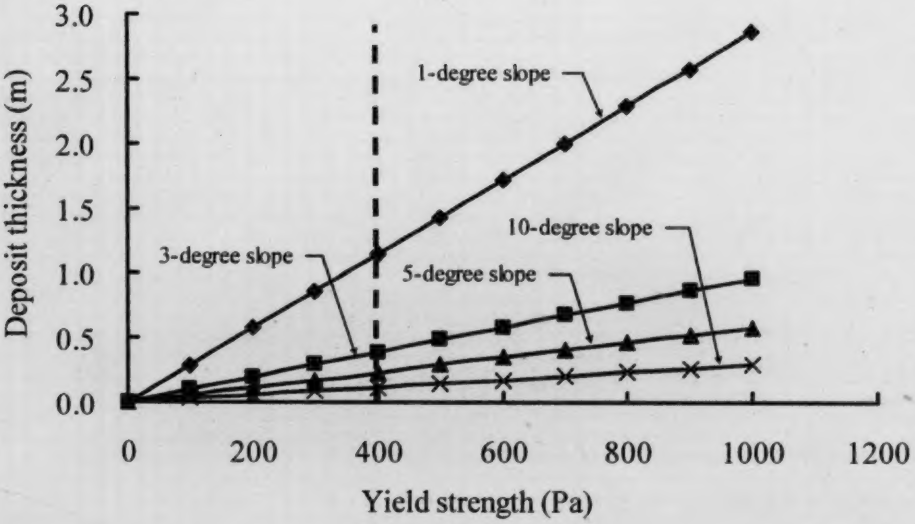

Figure 3-3 Debris flow deposit thickness versus yield strength for different slopes (Data from Iverson 2003)

Chapter 4

Numerical Modeling of Debris Flows

4.1 Introduction

In order to perform a hazard assessment and eventually to design protective measures against debris flows, it is necessary to estimate important parameters such as potential debris volume, mean flow velocity, peak discharge, and runout distance. Approaches to studying debris flow mobility by field and laboratory observations have limitations due to the unpredictability of time and location of occurrences, dangers involved with observations, and experimental restrictions upon grain size and sample volume. Empirical or analytical methods, however, do not involve such difficulties and can be utilized to provide parameters required for debris flow hazard assessment and mitigative designs. Empirical methods are based on field observations and on the regression analyses between parameters affecting the mobility of debris flows. Analytical methods include two categories: sliding block models and continuum models. Sliding block models describe the motion of debris flow as a dimensionless body moving down the profile of the path. Continuum models simulate water-sediment mixtures of debris flow as an equivalent fluid for which rheological properties are expected to describe the bulk behavior of prototype debris flows. In this chapter, empirical methods, sliding block models and continuum models will be discussed in the context of debris flow simulations. Emphasis will be placed on the depth-averaged model which is the continuum model predominantly used in debris flow modeling.

4.2 Empirical Relationships for Debris Flows

The travel distance and the travel angle are well-known parameters that express mobility of rapid landslides in empirical methods (as shown in Figure 4-1). The travel distance (*L*) is the horizontal projection of the line connecting the crown of the landslide source and the toe of the landslide deposit. The travel angle (α) is the slope of the line connecting the landslide crest and the deposit toe. Figure 4-1 indicates that the tangent of the travel angle can be expressed as:

$$\tan\alpha = \frac{H}{L} \tag{4.1}$$

where H is the vertical drop of the landslide. The tangent of the travel angle has been considered as a measure of the relative mobility of rapid landslides and as the equivalent of the coefficient of friction (Scheidegger 1973; Hsu 1975). Plots of the equivalent coefficient of friction versus the volume of a rapid landslide suggest that the travel angle decreases as the volume of sliding mass increases (Scheidegger 1973; Hsu 1975; Golder Associates Ltd. 1992, 1995; Corominas 1996; Finlay et al. 1999; Hunter and Fell 2003). The trend of reduction of travel angle with increase of volume was initially observed for rock avalanches with volumes greater than 0.5×10^6 m^3 (Scheidegger 1973; Hsu 1975). Further studies with rapid landslides having a great range of volumes show that highly mobile landslides of all sizes experience a continuous reduction of travel angle with volume increase (Corominas 1996; Legros 2002; Hunter and Fell 2003). Figure 4-2, the ratio of H over L (tangent of the travel angle) versus volume of landslide, is based on the database from Hunter and Fell (2003). It can be seen in Figure 4-2 that H/L decreases with an increase in landslide volume. Similar figures have been obtained based on landslide inventories investigated by Scheidegger (1973), Hsu (1975), Corominas (1996), and Finlay et al. (1999). The relationships between travel angle and landslide volume suggested by these figures can be expressed as:

$$\log(\tan\alpha) = \log\left(\frac{H}{L}\right) = A + B\log(V) \tag{4.2}$$

where A and B are constants, and V is the landslide volume. Parameters A and B in equation (4.2) can be determined by regression analysis of the landslide data. Scheidegger (1973) conducted analysis of 33 rapid, catastrophic landslides. The values of A and B calculated by the least squares regression method are 0.62419 and -0.15666, respectively. The correlation coefficient is 0.82. Corominas (1996) investigated 204 landslides of all sizes and demonstrated that the travel angle is dependent not only on the size of landslide, but on the type of movement and on topographic constraints and obstacles on the sliding path. The mobile landslides are classified in four groups: rockfalls, translational slides, earthflows and mudslides, and debris flows. Constraints on sliding paths are divided into four categories based primarily on topographic characteristics of the path: channelized, deflected, obstructed, and unobstructed. Individual relationships between travel angle and volume of landslides are proposed for various types of landslides and sliding paths (Table 4-1). Hunter and Fell (2003) analyzed 350 rapid landslides in steep natural slopes and constructed cut and fill slopes. The mobility of the landslide is assessed from the type of slope, failure mechanisms, slope geometry, sliding volume, and confinement of travel paths. Empirical equations for predicting the travel angle of landslides in natural slopes and coal waste spoil piles have been proposed:

$$\tan\alpha = \frac{H}{L} = A + B\tan\theta \tag{4.3}$$

where θ is the downslope angle below the source area, and A and B are constants dependent on the type of landslide, soil materials, and confinement of sliding path. Table 4-2 summarizes the parameters in equation (4.3) based on the database from Hunter and Fell (2003). For landslides in cut slopes of dilative soil and weathered rock, the tangent of the travel angle is estimated by:

$$\tan\alpha = \frac{H}{L} = 0.78\sqrt{\tan\theta_{cut}} \tag{4.4}$$

where θ_{cut} is the cut slope angle. For landslides in loose fill slopes of silty sands to sandy silts with low clay content, the correlation between the tangent of the travel angle and the sliding volume can be expressed as:

$$\tan\alpha = \frac{H}{L} = 0.67V^{-0.882} \tag{4.5}$$

where V is the volume of the landslide.

Rickenmann (1999) presented an overview of empirical relationships (Table 4-3) that have been proposed to estimate peak discharge, mean flow velocity, and travel distance. The applicability of the proposed equations is investigated with available field and experimental data. Comparisons between predicted and observed data indicate a considerable scatter. Legros (2002) analyzed the mobility of 203 long-runout landslides and concluded that the runout distance of a highly mobile landslide depends primarily on the volume. Correlation equations for runout distance versus volume, tangent of travel versus volume, and area of deposit versus volume have been proposed based on the best power fits of datasets (Table 4-4).

The volume-change model has been developed for predicting debris flow runout distance in the Queen Charlotte Islands, British Columbia (Fannin and Wise 2001). Starting from the initial failure volume, the model describes volume changes due to entrainment and deposition along the path of movement. The travel distance is determined when cumulative flow volume diminishes to zero. Three types of flow behaviors are identified in the model: unconfined flow, confined flow, and transition flow. Regression equations for volume changes along the path of movement have been established from 131 debris flow events in the Queen Charlotte Islands. The volume entrained or deposited is calculated based on the path characteristics (reach length, width, and confinement), flow behavior, slope angle, and incoming flow volume.

Empirical methods provide a useful means for predicting the post-failure mobility of landslides. Simplicity is the main advantage of empirical approaches because they do not address material rheological properties or mechanics of movement. However, there is an inherent limitation in empirical methods: the quality of model prediction is highly dependent on the database used for model development. Due to the complexity of actual debris flow processes and difficulties obtaining well-documented debris flow cases, empirical models making use of available data sets for the different processes are highly approximate. There is a lack of agreement among researchers and among general correlation relationships for the prediction of debris flow runout because of the uncertainty and variability of the data sets used to formulate empirical equations.

As indicated by Rickenmann (1999), Legros (2002), and Hunter and Fell (2003), comparisons between predicted values from empirical models and observations exhibit poor fit and considerable scatter. The weak correlation between parameters describing debris flow mobility is the result of limited consideration of factors which have significant effects on debris flow dynamics. These factors include the mechanism of failure, material rheology, channel constraints, obstacles on the flow path, and inaccuracy in the estimate of flow volume. Empirical relationships are typically derived from regional databases of field observation. As a consequence, application of the equations is restricted to similar soil and terrain conditions.

4.3 The Sliding Block Model

The sliding block model describes movement of the centroid of the debris flow mass by a dimensionless block along a curved path (Figure 4-3). The resultant force acting on the block is a result of the gravity driving force and movement resistance. Movement resistance depends on material rheological properties. Motion of the block is described by Newton's second law:

$$F = ma \tag{4.6}$$

where F is the resultant force, m is the sliding mass, and a is acceleration. If the Coulomb frictional law is applicable to granular flows, the resultant force is defined by $F = mg\cos\theta(\tan\theta - \tan\phi)$ and the acceleration of the sliding block is calculated from equation (4.6):

$$a = g\cos\theta(\tan\theta - \tan\phi) \tag{4.7}$$

where g is gravitational acceleration, θ is the local slope on the sliding path, and ϕ is the internal friction angle. If the initial condition (initial velocity) and boundary condition (profile of the slide path) are known, velocity and displacement of the block can be determined by integration of equation (4.7) along the path of movement.

The energy-line method (Korner 1980) is the sliding block model in terms of energy. The total energy of a sliding block consists of potential energy (elevation) and kinetic energy (velocity). The change of kinetic energy is equal to the work of the net force acting on the block:

$$d\left(\frac{mv^2}{2}\right) = F \cdot dS \tag{4.8}$$

where S is the displacement along the slide path. For the Coulomb frictional material, $F = mg\cos\theta\left(\tan\theta - \tan\phi\right)$. The change of kinetic energy can be expressed as:

$$d\left(\frac{mv^2}{2}\right) = F \cdot dS = mg\left(\Delta h - \Delta x \tan\phi\right) \tag{4.9}$$

where h is the vertical displacement and x is the horizontal displacement. Equation (4.9) indicates that the energy line for friction material, the line with elevation above the sliding path equal to $\frac{v^2}{2g}$, is a straight line having the slope of the frictional angle to the horizontal (Figure 4-3). For materials described with other constitutive equations, such as the Voellmy model, the energy line is curved and concave (Korner 1980; Hungr et al. 2005).

Hutchinson (1986) took into consideration the effects of pore pressure on the movement of flow slides and developed a sliding-consolidation model. The model assumes that high excessive pore water pressure exists at the initiation stage of flow slides as a result of undrained loading or liquefaction. Under the influence of high pore water pressure at the base, the failure material accelerates and slides downslope. During this process, the basal excess pore pressure dissipates successively due to consolidation of the sliding mass. As the pore pressure decreases, the resistance acting on the sliding surface increases and decelerates the sliding mass until it is brought to rest. The sliding-consolidation model has been applied to studying the 1966 flow slide at Aberfan, South Wales.

Sassa (1988) pointed out that the bulk friction angle in the sliding block model is the result of the combination of internal friction angle of the sliding mass and the pore pressure during motion. From the perspective of geotechnical engineering, an improved sliding block model was introduced by estimating the bulk friction angle with the internal friction angle and pore water pressure:

$$\tan\phi_a = \left(1 - r_u\right)\tan\phi \tag{4.10}$$

where ϕ_a is the bulk friction angle, r_u is the ratio between pore water pressure and total normal stress, and ϕ is the internal friction angle. The improved sliding block model has been applied to mobility studies of the Ontake debris avalanche and the Jizukiyama landslide (Sassa 1988).

Application of the sliding block model to back-calculating shear strengths of liquefaction flows is known as kinetic analysis (Davis et al. 1988; Olson 2001). The liquefaction flow is simplified as rigid body movement in the analysis and the travel of the centroid of the sliding mass is assumed in the calculation. The initial and final positions of the centroid and its travel path are specified. The centroid positions are determined by surveying pre- and post-liquefaction geometries. The travel path of the center of gravity is described simply by a mathematical function; its parameters are computed from the coordinates of the initial and final positions of the center of gravity and curvatures at those points. Because the information about centroid travel in liquefaction flow cases is difficult to obtain, various assumptions are adopted in the kinetic analysis. Davis et al. (1988) used a hyperbola to fit the travel path of the center of gravity in the Lower San Fernando Dam kinetic analysis. After examining some flow slide case histories, Olson (2001) concluded that a cubic polynomial provides a better approximation of the centroid travel path. Using cubic polynomials, Olson (2001) estimated liquefied shear strengths from ten liquefaction flow case records. In the analyses, the driving force is computed from the weight of the sliding mass and the curvature of the prescribed travel path of the center of gravity, while the resistance is calculated from the length of the failure surface and the shear strength assigned to it. The acceleration is then computed from the resultant force and moving mass:

$$a = \frac{W \sin\theta - s_u L}{m} \tag{4.11}$$

where W is the weight of the failure mass, θ is the slope of the travel path of failure mass center of gravity, s_u is the mobilized shear strength, and L is the length of the failure surface. Velocities and displacements are subsequently determined by integrating acceleration with respect to time. The liquefied shear strength is obtained when the assigned value yields results fitting the observed movement of the center of gravity reasonably well at the moment that the centroid velocity is equal to zero. Table 4-5 summarizes the liquefied shear strengths back-calculated form the liquefaction flow case histories using kinetic analysis (Olson 2001; Olson and Stark 2002).

4.4 The Depth-Averaged Model

Because of the complicated rheological properties of debris flows, solving the fully dynamic equations for such unsteady, nonuniform flows is still not possible. The continuum model simulates debris flow as the flow of an equivalent fluid, with rheological properties that describe the bulk behavior of the prototype debris flow event. The bulk rheological properties of an equivalent fluid combine the contributions from particles, interstitial fluid, and interactions between solid phase and fluid phase.

In fluid mechanics, the differential form of the conservation laws for mass and momentum, applicable at a point, are the basis of most continuum simulations. The depth-averaged technique is commonly applied to the derivation of governing equations, which are obtained by integrating the mass and momentum conservation equations over the depth of the flow in a specific coordinate system. The depth averaging process can substantially reduce the complexity of computational effort and make simulation of debris flows over complex topography practical. However, the depth-averaged process sacrifices flow details over the vertical dimension and only the mean velocity in the flow direction and the mean depth are available from the computational results (Steffler and Jin 1993). As a consequence, these equations are valid only for horizontal length scales greater than the channel depth.

Application of the depth-averaged model to debris flows includes two steps: (1) establish governing equations and choose a basal resistance expression; (2) validate the model by comparing computational results with experimental data or field measurements. When choosing a basal resistance expression, analyses of the rheological properties of debris flow material, i.e., the constitutive equations, are taken into account.

4.4.1 Derivation of the General Depth-Averaged Equations

The depth-averaged flow equations are also known as shallow water equations or Saint Venant equations. The essential point for the formulation of depth-averaged equations is that the vertical dimension of flows is much smaller than any typical horizontal length scale. This is the necessary condition to apply depth-averaged equations to various situations.

4.4.1.1 Assumptions

The derivation of depth-averaged flow equations is based on the following assumptions:

(1) typical flow depth is much smaller than the down- and cross-slope length of the flow;

(2) uniform velocity distribution is in the vertical direction without dominant secondary flow effects;

(3) there is hydrostatic pressure distribution;

(4) fluid is incompressible;

(5) the bed slope is small;

(6) there is negligible shear stress at the free surface.

4.4.1.2 Governing Equations

In Cartesian coordinate system with Eulerian description, the equations of mass and momentum conservation for free surface flow of a granular material along a gently varying slope (Figure 4-4) can be written as:

$$\frac{\partial u_i}{dx_i} = 0 \tag{4.12}$$

$$\rho\left(\frac{\partial u_i}{\partial t} + u_j \frac{\partial u_i}{\partial x_j}\right) = \rho g_i - \frac{\partial \tau_{ji}}{\partial x_j} \tag{4.13}$$

where u_i denotes the velocity component in the x_i direction, ρ is density, g_i denotes the component of gravity acceleration in the x_i direction, and τ_{ij} denotes components of the stress tensor.

4.4.1.3 Kinematic Boundary Conditions

If the equation of a boundary surface in Figure 4-4 is $f(x_i,t)=0$, the coordinates of any fluid particle on the boundary must continuously satisfy this equation. Suppose that in a small interval of time δt, a particle moves along the boundary over a short distance whose elements are δx_i. Since its new position must satisfy the equation of the boundary surface, the change $\delta f(x_i,t)$ must be zero. Thus the following equation must be satisfied at all points on a boundary surface (except at points of discontinuity in the flow pattern):

$$\frac{\partial f(x_i,t)}{\partial t}+u_i\frac{\partial f(x_i,t)}{\partial x_i}=0 \tag{4.14}$$

The basal surface is expressed as $f_b(x_i,t)=z-z_b=0$ and the boundary condition is:

$$u_b\frac{\partial z_b}{\partial x}+v_b\frac{\partial z_b}{\partial y}-w_b=0 \tag{4.15}$$

Boundary conditions at the free surface with the function $f_s(x_i,t)=z-(z_b+h)=0$ can be written as:

$$\frac{\partial(z_b+h)}{\partial t}+u_s\frac{\partial(z_b+h)}{\partial x}+v_s\frac{\partial(z_b+h)}{\partial y}-w_s=0 \tag{4.16}$$

where u, v, and w denote velocities in x, y, and z directions, respectively, subscripts b and s indicate variables at bottom or on free surface, and h is flow depth.

4.4.1.4 Leibnitz's Rule

Leibnitz's rule, equation (4.17), shows how to differentiate an integral in which the integrand ψ and the limits of integration α and β are functions of the variable χ with respect to which the integral is differentiated (Hildebrand 1976):

$$\frac{\partial}{\partial \chi}\int_{\alpha}^{\beta}\psi(\chi,\xi)d\xi=\int_{\alpha}^{\beta}\frac{\partial \psi(\chi,\xi)}{\partial \chi}d\xi+\psi(\chi,\beta)\frac{\partial \beta}{\partial \chi}-\psi(\chi,\alpha)\frac{\partial \alpha}{\partial \chi} \tag{4.17}$$

which is valid for all values of $\chi\in[a,b]$ when ψ and $\frac{\partial \psi}{\partial \chi}$ are continuous for $a\le\chi\le b$ and $\alpha\le\xi\le\beta$, and also $\frac{\partial \alpha}{\partial \chi}$ and $\frac{\partial \beta}{\partial \chi}$ are continuous in (a,b).

4.4.1.5 The Depth-Averaging Process

Integration of the continuity equation (4.12) over the flow depth with the use of Leibnitz's rule to interchange the order of integration and differentiation gives:

$$\frac{\partial}{\partial x}\int_{z_b}^{z_b+h}udz-u_s\frac{\partial(z_b+h)}{\partial x}+u_b\frac{\partial z_b}{\partial x}+\frac{\partial}{\partial y}\int_{z_b}^{z_b+h}vdz-v_s\frac{\partial(z_b+h)}{\partial y}+v_b\frac{\partial z_b}{\partial y}+w_s-w_b=0$$

Introducing boundary conditions (4.15) and (4.16), and definition of $\overline{\varphi}=\frac{1}{h}\int_{z_b}^{z_b+h}\varphi dz$, where φ represents any variable in the equations, the continuity equation reduces to:

$$\frac{\partial h}{\partial t}+\frac{\partial(h\overline{u})}{\partial x}+\frac{\partial(h\overline{v})}{\partial y}=0 \tag{4.18}$$

Rewriting the momentum equations (4.13) in the x direction gives:

$$\rho\left[\frac{\partial u}{\partial t}+\frac{\partial(u^2)}{\partial x}+\frac{\partial(uv)}{\partial y}+\frac{\partial(uw)}{\partial z}\right]=\rho g_x-\left(\frac{\partial \tau_{xx}}{\partial x}+\frac{\partial \tau_{yx}}{\partial y}+\frac{\partial \tau_{yz}}{\partial z}\right) \tag{4.19}$$

Integrating each item on both sides of equation (4.19) from the bed to the free surface with the use of Leibnitz's rule gives:

$$\rho\int_{z_b}^{z_b+h}\frac{\partial u}{\partial t}dz=\rho\left[\frac{\partial}{\partial t}\int_{z_b}^{z_b+h}udz-u_s\frac{\partial(z_b+h)}{\partial t}+u_b\frac{\partial z_b}{\partial t}\right]$$

$$\rho\int_{z_b}^{z_b+h}\frac{\partial(u^2)}{\partial x}dz=\rho\left[\frac{\partial}{\partial x}\int_{z_b}^{z_b+h}(u^2)dz-(u^2)_s\frac{\partial(z_b+h)}{\partial x}+(u^2)_b\frac{\partial z_b}{\partial x}\right]$$

$$\rho\int_{z_b}^{z_b+h}\frac{\partial(uv)}{\partial y}dz=\rho\left[\frac{\partial}{\partial y}\int_{z_b}^{z_b+h}(uv)dz-(uv)_s\frac{\partial(z_b+h)}{\partial y}+(uv)_b\frac{\partial z_b}{\partial y}\right]$$

$$\rho\int_{z_b}^{z_b+h}\frac{\partial(uw)}{\partial z}dz=\rho\left[(uw)_s-(uw)_b\right]$$

$$\int_{z_b}^{z_b+h}\frac{\partial\tau_{xx}}{\partial x}dz=\frac{\partial}{\partial x}\int_{z_b}^{z_b+h}\tau_{xx}dz-(\tau_{xx})_s\frac{\partial(z_b+h)}{\partial x}+(\tau_{xx})_b\frac{\partial z_b}{\partial x}$$

$$\int_{z_b}^{z_b+h}\frac{\partial\tau_{yx}}{\partial y}dz=\frac{\partial}{\partial y}\int_{z_b}^{z_b+h}\tau_{yx}dz-(\tau_{yx})_s\frac{\partial(z_b+h)}{\partial y}+(\tau_{yx})_b\frac{\partial z_b}{\partial y}$$

$$\int_{z_b}^{z_b+h}\frac{\partial\tau_{zx}}{\partial z}dz=(\tau_{zx})_s-(\tau_{zx})_b$$

$$\int_{z_b}^{z_b+h}\rho g_x dz=\rho g_x h$$

With consideration of boundary conditions and the assumption that shear stresses on the free surface are negligible, combining the above equations results in the depth-integrated momentum equation in the x direction:

$$\rho\left[\frac{\partial(h\bar{u})}{\partial t}+\frac{\partial\left(h\overline{u^2}\right)}{\partial x}+\frac{\partial(h\overline{uv})}{\partial y}\right]=$$

$$\rho g_x h-\frac{\partial(h\bar{\tau}_{xx})}{\partial x}-\frac{\partial(h\bar{\tau}_{yx})}{\partial y}+\left[(\tau_{zx})_b-(\tau_{xx})_b\frac{\partial z_b}{\partial x}-(\tau_{yx})_b\frac{\partial z_b}{\partial y}\right]$$

Introducing the basal shear resistance $\tau_{bx}=-(\tau_{zx})_b+(\tau_{xx})_b\frac{\partial z_b}{\partial x}+(\tau_{yx})_b\frac{\partial z_b}{\partial y}$, the depth-averaged momentum equation in the x direction reduces to:

$$\rho\left[\frac{\partial(h\bar{u})}{\partial t}+\frac{\partial\left(h\overline{u^2}\right)}{\partial x}+\frac{\partial(h\overline{uv})}{\partial y}\right]=\rho g_x h-\frac{\partial(h\bar{\tau}_{xx})}{\partial x}-\frac{\partial(h\bar{\tau}_{yx})}{\partial y}-\tau_{bx} \qquad (4.20)$$

Applying the same procedure to the momentum equation in the y and z directions, the corresponding depth-averaged momentum equations are derived:

$$\rho\left[\frac{\partial(h\overline{v})}{\partial t}+\frac{\partial(h\overline{uv})}{\partial x}+\frac{\partial\left(h\overline{v^2}\right)}{\partial y}\right]=\rho g_y h-\frac{\partial\left(h\overline{\tau}_{xy}\right)}{\partial x}-\frac{\partial\left(h\overline{\tau}_{yy}\right)}{\partial y}-\tau_{by} \tag{4.21}$$

$$\rho\left[\frac{\partial(h\overline{w})}{\partial t}+\frac{\partial(h\overline{uw})}{\partial x}+\frac{\partial(h\overline{vw})}{\partial y}\right]=\rho g_z h-\frac{\partial\left(h\overline{\tau}_{xz}\right)}{\partial x}-\frac{\partial\left(h\overline{\tau}_{yz}\right)}{\partial y}-\tau_{bz} \tag{4.22}$$

in which:

$$\tau_{by}=-\left(\tau_{zy}\right)_b+\left(\tau_{xy}\right)_b\frac{\partial z_b}{\partial x}+\left(\tau_{yy}\right)_b\frac{\partial z_b}{\partial y} \quad \text{, and} \quad \tau_{bz}=-\left(\tau_{zz}\right)_b+\left(\tau_{xz}\right)_b\frac{\partial z_b}{\partial x}+\left(\tau_{yz}\right)_b\frac{\partial z_b}{\partial y}$$

In depth-averaged models, stress calculations are established by simplification of the vertical momentum equation (4.22). Nondimensional analysis with the shallowness assumption indicates that the forces associated with changes of momentum in the z direction are negligible relative to the weight of the sliding mass (Savage and Hutter 1989; Gray et al. 1999). Neglecting the vertical flow acceleration leads to the following normal stress distribution in the z direction:

$$\left(\tau_{zz}\right)_b=\rho g_z h \tag{4.23}$$

$$\tau_{zz}=\rho g_z\left(z_b+h-z\right) \tag{4.24}$$

Equations (4.23) and (4.24) indicate that the normal stress varies hydrostatically in the vertical direction. The depth averaged stresses, therefore, reduce to:

$$\overline{\tau}_{ij}=\begin{pmatrix}\frac{1}{2}\rho g_z h & 0 & 0\\ 0 & \frac{1}{2}\rho g_z h & 0\\ 0 & 0 & \frac{1}{2}\rho g_z h\end{pmatrix} \tag{4.25}$$

The depth-averaged model assumes that horizontal velocities are approximately constant over the depth. The observations of strongly localized thin shear layers in field and laboratory granular flows justify such assumptions (Savage and Hutter 1989). The uniform velocity distribution along the flow depth implies that $\overline{u_i u_j}=\overline{u}_i\cdot\overline{u}_j$. Therefore, the depth averaged continuity and momentum equations reduce to:

$$\frac{\partial h}{\partial t}+\frac{\partial(h\bar{u})}{\partial x}+\frac{\partial(h\bar{v})}{\partial y}=0 \tag{4.26}$$

$$\rho\left[\frac{\partial(h\bar{u})}{\partial t}+\frac{\partial(h\bar{u}^2)}{\partial x}+\frac{\partial(h\bar{u}\cdot\bar{v})}{\partial y}\right]=\rho g_x h-\rho g_z h\frac{\partial h}{\partial x}-\tau_{bx} \tag{4.27}$$

$$\rho\left[\frac{\partial(h\bar{v})}{\partial t}+\frac{\partial(h\bar{u}\cdot\bar{v})}{\partial x}+\frac{\partial(h\bar{v}^2)}{\partial y}\right]=\rho g_y h-\rho g_z h\frac{\partial h}{\partial y}-\tau_{by} \tag{4.28}$$

Contrary to the classical shallow water problems, the motion of debris flows usually takes place on steep slopes and curved beds. In these cases, the flow velocities are parallel to the bed rather than horizontal, as assumed in shallow water equations. The significant slope and curved surface influences debris flow dynamics and should be incorporated in the governing equations. After the pioneering work by Savage and Hutter (1989), a curvilinear reference system is commonly established in the formulation of the depth-averaged governing equations to incorporate such effects (Savage and Hutter 1991; Greve et al. 1994; Gray et al. 1999). In curvilinear reference systems, as shown in Figure 4-5, the local coordinates are oriented so that x and y are tangent to the bed surface and the z direction is normal to the bed surface. The unit vectors in x, y, and z directions are orthogonal. In a curvilinear coordinate system, derivation of depth-averaged equations takes account of effects of surface curvature by incorporating a centrifugal force into momentum conservation equations. Table 4-6 summarizes governing equations with curvilinear coordinate systems. Detailed derivation of these governing equations is described in references listed in Table 4-6.

Practical application of the depth-averaged equations (4.26) to (4.28) requires that stress terms on the right-hand sides of the equations are specified. During that process, the rheological behavior of debris has to be defined and introduced into the depth-averaged equations. Formulations of the relationship between shear stress and shear rate in equations (4.27) and (4.28) determine the performance of the depth-averaged models in practical applications.

4.4.2 Determination of Basal Resistance in Depth-Averaged Models

Implementation of depth-averaged equations to debris flow modeling requires the selection of appropriate constitutive models which can be used to define flow resistance in the governing equations. Non-Newtonian fluid and Coulomb frictional constitutive laws are often used to describe material properties in depth-averaged models due to the simplicity of their practical implementation. In the case that material properties are specified by the non-Newtonian fluid model, the stress terms in depth-averaged equations are expressed from the perspective of hydraulic engineering. Bingham, Herschel-Bulkley, and quadratic fluid models are among the non-Newtonian fluid models often used by hydraulic engineers in debris flow modeling. In the case of the Coulomb friction law specified for material properties, the stresses are determined from the perspective of geotechnical engineering. Concepts of coefficients of lateral pressure from soil mechanics are introduced into debris flow simulation to take into consideration the deformation state of the flowing mass.

The following formulation of basal resistance relations is carried out for debris flow modeling with material properties specified by a variety of rheological models, including the Bingham model, the Herschel-Bulkley model, the quadratic fluid model, and the Coulomb friction model. Figure 4-7 is the reference sketch for two-dimensional debris flows with Cartesian coordinates.

4.4.2.1 Basal Resistance Based on the Bingham and Herschel-Bulkley Models

Consider a two-dimensional, unsteady debris flow down a relatively small slope at an angle with respect to the horizontal, as shown in Figure 4-8. The motion of the debris flow is governed by the continuity and momentum equations:

$$\frac{\partial u}{\partial x}+\frac{\partial w}{\partial z}=0 \qquad (4.29)$$

$$\frac{\partial u}{\partial t}+\frac{\partial\left(u^2\right)}{\partial x}+\frac{\partial(uw)}{\partial x}=g\sin\theta-\frac{1}{\rho}\frac{\partial\tau_{xx}}{\partial x}-\frac{1}{\rho}\frac{\partial\tau_{zx}}{\partial z} \tag{4.30}$$

$$\frac{\partial w}{\partial t}+\frac{\partial(uw)}{\partial x}+\frac{\partial\left(w^2\right)}{\partial x}=g\cos\theta-\frac{1}{\rho}\frac{\partial\tau_{xz}}{\partial x}-\frac{1}{\rho}\frac{\partial\tau_{zz}}{\partial z} \tag{4.31}$$

where ρ is the bulk density of debris, and g is the acceleration due to gravity. The kinematic and stress boundary conditions are:

$$u_b\frac{\partial z_b}{\partial x}-w_b=0\text{, at }z=z_b \tag{4.32}$$

$$\frac{\partial h}{\partial t}+u_s\frac{\partial\left(z_b+h\right)}{\partial x}-w_s=0\text{, at }z=z_b+h \tag{4.33}$$

The shallowness assumption is valid, i.e., the characteristic flow depth is very small relative to the characteristic flow length and the flow depth varies relatively slowly in the longitudinal direction. Nondimensional analysis indicates that the normal stress in the z direction is approximated as hydrostatic and equation (4.31) reduces to:

$$\tau_{xx}=\tau_{zz}=\rho g\cos\theta\left(z_b+h-z\right) \tag{4.34}$$

Depth-averaged governing equations are obtained by integrating equations (4.29) and (4.30) from the bed ($z=z_b$) to the free surface ($z=z_b+h$):

$$\frac{\partial h}{\partial t}+\frac{\partial(h\bar{u})}{\partial x}=0 \tag{4.35}$$

$$\frac{\partial(h\bar{u})}{\partial t}+\frac{\partial\left(\beta h\bar{u}^2\right)}{\partial x}=gh\sin\theta-gh\cos\theta\frac{\partial h}{\partial x}-\frac{\tau_{bx}}{\rho} \tag{4.36}$$

where $\bar{u}=\frac{\int_{z_b}^{z_b+h}u\,dz}{h}$ is the depth-averaged velocity, τ_{bx} is the basal flow resistance depending on rheological properties of debris, and $\beta=\frac{\int_{z_b}^{z_b+h}u^2dz}{h\bar{u}^2}$ is the shape factor dependent on the vertical profile of velocity in the z direction.

The Herschel-Bulkley model is the more general form of the Newtonian and Bingham models. The constitutive equations for the Herschel-Bulkley model are expressed as:

$$\frac{du}{dz}=0 \qquad for \quad \tau<\tau_0$$
$$\tau=\tau_0+\mu_\eta\left(\frac{du}{dz}\right)^\eta \qquad for \quad \tau>\tau_0 \tag{4.37}$$

where τ_0 is the yield strength, μ_η is the consistency index, and η is the flow-behavior index. The Herschel-Bulkley model reduces to the Bingham model when η equals 1 and to the Newtonian model when η equals 1 and τ_0 equals 0. The existence of yield strength in the Herschel-Bulkley model indicates that two fluid regions exist in the flow domain of a Herschel-Bulkley fluid: the unsheared plug zone with uniform velocity u_p, where yield strength is greater than shear stress (the layer of $z_b+h_0\le z\le z_b+h$ in Figure 4-8), and sheared layer ($z_b\le z\le z_b+h_0$ in Figure 4-8) where velocity varies from 0 to u_p as z increases from z_b to z_b+h_0. The boundary between shear and plug layers in Figure 4-8 is determined by the yield condition:

$$\tau_{zx}=\rho g\left(h-h_0\right)\sin\theta=\tau_0 \quad \text{at} \quad z=z_b+h_0 \tag{4.38}$$

Equations (4.37) and (4.38) combine with the hydrostatic approximation of stresses in the z direction to give the following velocity distribution for the flow of the Herschel-Bulkley fluid in Figure 4-8:

$$u=\begin{cases} u_p & z_b+h_0\le z\le z_b+h \\ \left[1-\left(1-\frac{z}{h_0}\right)^{\eta+1/\eta}\right]u_p & z_b\le z\le z_b+h_0 \end{cases} \tag{4.39}$$

where $u_p=\frac{\eta}{\eta+1}\left[\frac{\rho g h_0^{\eta+1}\sin\theta}{\mu_\eta}\right]^{1/\eta}$. The depth-averaged velocity and bed shear stress are:

$$\bar{u}=\frac{1}{h}\int_{z_b}^{z_b+h}u\,dz=\left(1-\frac{\eta}{2\eta+1}\frac{h_0}{h}\right)u_p=\left[1-\frac{\eta}{2\eta+1}\frac{h_0}{h}\left(1-\frac{\tau_0}{\rho g h\sin\theta}\right)\right]u_p \tag{4.40}$$

$$\tau_{bx}=\tau_0+\mu_\eta\left(\frac{du}{dz}\right)^\eta_{z=z_b}=\tau_0+\mu_\eta\left(\frac{\eta+1}{\eta}\frac{u_p}{h_0}\right)^\eta \tag{4.41}$$

The shape factor β in equation (4.36) is determined by

$$\beta = \frac{\int_{z_b}^{z_b+h} u^2 dz}{h(\bar{u})^2} = \frac{h\int_{z_b}^{z_b+h} u^2 dz}{\left(\int_{z_b}^{z_b+h} udz\right)^2} = \frac{1 - \frac{\eta(4\eta+3)}{(2\eta+1)(3\eta+2)}\frac{h_0}{h}}{\left(1 - \frac{\eta}{2\eta+1}\frac{h_0}{h}\right)^2} \tag{4.42}$$

The relationship between shape factor β, and flow-behavior index η, is demonstrated in Figure 4-9 for a variety of the ratio of shear depth to total depth of flow. As indicated by Figure 4-9, the shape factor increases with the increase of the ratio of the shear depth to total flow depth. In the case of a thin shear layer near the sliding surface (e.g., $\frac{h_0}{h} \le 0.3$), as indicated by Savage and Hutter (1989), the shape factor is approximated to be 1 and the depth-averaged governing equations for a Herschel-Bulkley flow reduce to:

$$\frac{\partial h}{\partial t} + \frac{\partial(h\bar{u})}{\partial x} = 0 \tag{4.43}$$

$$\frac{\partial(h\bar{u})}{\partial t} + \frac{\partial(h\bar{u}^2)}{\partial x} = gh\sin\theta - gh\cos\theta\frac{\partial h}{\partial x} - \frac{\tau_{bx}}{\rho} \tag{4.44}$$

$$\bar{u} = \frac{1}{h}\int_{z_b}^{z_b+h} udz = \left(1 - \frac{\eta}{2\eta+1}\frac{h_0}{h}\right)u_p = \left[1 - \frac{\eta}{2\eta+1}\frac{h_0}{h}\left(1 - \frac{\tau_0}{\rho gh\sin\theta}\right)\right]u_p \tag{4.45}$$

$$\tau_{bx} = \tau_0 + \mu_\eta\left(\frac{du}{dz}\right)_{z=0}^{\eta} = \tau_0 + \mu_\eta\left(\frac{\eta+1}{\eta}\frac{u_p}{h_0}\right)^{\eta} \tag{4.46}$$

$$u_p = \frac{\eta}{\eta+1}\left[\frac{\rho g h_0^{\eta+1}\sin\theta}{\mu_\eta}\right]^{1/\eta} \tag{4.47}$$

The flow behavior index ~~η~~ equals to 1 for a Bingham fluid. Substituting η with 1 in equations (4.45) to (4.47) gives corresponding depth-averaged equations for Bingham flow:

$$\frac{\partial h}{\partial t} + \frac{\partial(h\bar{u})}{\partial x} = 0 \tag{4.48}$$

$$\frac{\partial(h\bar{u})}{\partial t}+\frac{\partial(h\bar{u}^2)}{\partial x}=gh\sin\theta-gh\cos\theta\frac{\partial h}{\partial x}-\frac{\tau_{bx}}{\rho} \tag{4.49}$$

$$\bar{u}=\frac{1}{h}\int_{z_b}^{z_b+h}u\,dz=\left(1-\frac{1}{3}\frac{h_0}{h}\right)u_p=\left[1-\frac{1}{3}\frac{h_0}{h}\left(1-\frac{\tau_0}{\rho gh\sin\theta}\right)\right]u_p \tag{4.50}$$

$$\tau_{bx}=\tau_0+\mu_1\left(\frac{du}{dz}\right)_{z=0}=\tau_0+2\mu_1\frac{u_p}{h_0} \tag{4.51}$$

$$u_p=\frac{1}{2}\frac{\rho gh_0^2\sin\theta}{\mu_1} \tag{4.52}$$

Pastor et al. (2004) proposed a simple solution to approximate the basal resistance force of a Bingham flow. For a simple shear flow over an inclined plane with a slope angle of θ, equilibrium analysis indicates that the distribution of shear stress varies linearly with the depth, from 0 at the free surface to $\tau_{bx}=\rho gh\sin\theta$ at the bed, as shown in Figure 4-10. The velocity profile is obtained by integrating constitutive equations (4.53) and (4.54) for a Bingham fluid:

$$\begin{aligned}&\frac{du}{dz}=0 && \tau<\tau_0\\ &\tau=\tau_0+\mu_1\frac{du}{dz} && \tau>\tau_0\end{aligned} \tag{4.53}$$

$$\tau=\tau_{bx}\left(1-\frac{z}{h}\right) \tag{4.54}$$

The velocity distribution is parabolic in the shear layer and constant in the plug region:

$$u=\begin{cases}\dfrac{\tau_{bx}h_0^2}{2\mu h} & z_b+h_0\le z\le z_b+h\\[2ex] \dfrac{\tau_{bx}}{\mu h}\left(h_0z-\dfrac{z^2}{2}\right) & z_b\le z\le z_b+h_0\end{cases} \tag{4.55}$$

The depth-averaged velocity is obtained by integrating equation (4.55) over flow depth:

$$\bar{u}=\frac{1}{h}\int_0^h u\,dz=\frac{\tau_{bx}h}{6\mu}\left(1-\frac{\tau_0}{\tau_{bx}}\right)^2\left(2+\frac{\tau_0}{\tau_{bx}}\right) \tag{4.56}$$

The bottom shear stress is determined by solving equation (4.56), which is related to the averaged depth velocity $\bar{u}$. An approximation solution has been proposed for practical implementation of equation (4.56) in debris flow modeling (Hungr 1995; Pastor et al. 2004).

4.4.2.2 Basal Resistance Based on the Quadratic Fluid Model

The quadratic rheological model developed by O'Brien and Julien (1985) and Julien and Lan (1991) has been used as a constitutive law for a great range of hyperconcentrated flows. The relationship between shear stress and shear rate for the quadratic rheological model is:

$$\begin{aligned} &\frac{du}{dz}=0 && for \quad \tau<\tau_0 \\ &\tau=\tau_0+\mu\frac{du}{dz}+\xi\left(\frac{du}{dz}\right)^2 && for \quad \tau>\tau_0 \end{aligned} \tag{4.57}$$

where ξ is a turbulent-dispersive parameter dependent on a variety of material properties including mass density, mixing length, sediment size, linear sediment concentration and impact coefficients. Application of the quadratic model to analyze mud and debris flows is carried out using the FLO-2D program (O'Brien 2003).

FLO-2D is a volume conservation program. The overland flow or flow through the segments of channels is simulated by motion of the flowing mass through a series of elements in FLO-2D. The flow propagation is dependent on topography and flow resistance. The depth-averaged governing equations in the FLO-2D program (O'Brien 2003) are:

Continuity equation:

$$\frac{\partial h}{\partial t}+\frac{\partial(h\bar{u})}{\partial x}+\frac{\partial(h\bar{v})}{\partial y}=i \tag{4.58}$$

Momentum equations:

$$S_{fx}=S_{0x}-\frac{\partial h}{\partial x}-\frac{\bar{u}}{g}\frac{\partial\bar{u}}{\partial x}-\frac{\bar{v}}{g}\frac{\partial\bar{u}}{\partial y}-\frac{1}{g}\frac{\partial\bar{u}}{\partial t} \tag{4.59}$$

$$S_{fy} = S_{0y} - \frac{\partial h}{\partial y} - \frac{\bar{u}}{g}\frac{\partial \bar{v}}{\partial x} - \frac{\bar{v}}{g}\frac{\partial \bar{v}}{\partial y} - \frac{1}{g}\frac{\partial \bar{v}}{\partial t} \tag{4.60}$$

where h is the flow depth, $\bar{u}$ and $\bar{v}$ are depth-averaged velocity components in x and y directions, i is excess rainfall intensity, S_{fx} and S_{fy} are friction slope components along x and y directions, S_{0x} and S_{0y} are natural bed slopes, and g is gravity acceleration.

The total friction slope S_f is the sum of the yield slope S_y, the viscous slope S_v, and the turbulent-dispersive slope S_{td}. The yield slope is written as a function of the yield strength. Viscous and turbulent-dispersive slope terms are written in terms of depth-averaged velocities:

$$S_f = S_y + S_v + S_{td} \tag{4.61}$$

$$S_y = \frac{\tau_0}{\gamma_m h} \tag{4.62}$$

$$S_v = \frac{K\eta}{8\gamma_m}\frac{V}{h^2} \tag{4.63}$$

$$S_{td} = \frac{n_{td}^2 V^2}{h^{4/3}} \tag{4.64}$$

where γ_m is the specific weight of the sediment mixture, K is the resistance parameter for laminar flow, n_{td} is the flow resistance coefficient equivalent to Manning's n-value, and V denotes the depth-averaged velocity equal to $\bar{u}$ and $\bar{v}$ in the x and y directions, respectively. To estimate dispersive effects in debris flows, n_{td} is approximated as the exponential function of the traditional turbulent resistance n-value:

$$n_{td} = n_t b e^{mC_v} \tag{4.65}$$

where n_t is the turbulent n-value, C_v is sediment volumetric concentration, b is a coefficient with a value of 0.0538, and m is an exponent with a value of 6.0896.

The yield stress τ_0 and the viscosity η are computed using exponential functions of sediment concentration based on studies of O'Brien and Julien (1985) and Julien and Lan (1991):

$$\eta = \alpha_\eta e^{\beta_\eta C_v} \tag{4.66}$$

$$\tau = \alpha_\tau e^{\beta_\tau C_v} \tag{4.67}$$

where α_η, β_η, α_τ, and β_τ are empirical coefficients.

Substitution of equations (4.61) to (4.67) into (4.58) to (4.60) gives differential governing equations for debris flow simulations in the FLO-2D program:

$$\frac{\partial h}{\partial t} + \frac{\partial (h\overline{u})}{\partial x} + \frac{\partial (h\overline{v})}{\partial y} = i \tag{4.68}$$

$$\frac{\partial h}{\partial x} + \frac{\overline{u}}{g}\frac{\partial \overline{u}}{\partial x} + \frac{\overline{v}}{g}\frac{\partial \overline{u}}{\partial y} + \frac{1}{g}\frac{\partial \overline{u}}{\partial t} + \frac{\alpha_\tau e^{\beta_\tau C_v}}{\gamma_m h} + \frac{K(\alpha_\eta e^{\beta_\eta C_v})}{8\gamma_m}\frac{\overline{u}}{h^2} + \frac{(n_t b e^{mC_v})^2 \overline{u}^2}{h^{4/3}} - S_{0x} = 0 \tag{4.69}$$

$$\frac{\partial h}{\partial y} + \frac{\overline{u}}{g}\frac{\partial \overline{v}}{\partial x} + \frac{\overline{v}}{g}\frac{\partial \overline{v}}{\partial y} + \frac{1}{g}\frac{\partial \overline{v}}{\partial t} + \frac{\alpha_\tau e^{\beta_\tau C_v}}{\gamma_m h} + \frac{K(\alpha_\eta e^{\beta_\eta C_v})}{8\gamma_m}\frac{\overline{v}}{h^2} + \frac{(n_t b e^{mC_v})^2 \overline{v}^2}{h^{4/3}} - S_{0y} = 0 \tag{4.70}$$

4.4.2.3 Basal Resistance Based on the Coulomb Friction Model

The Coulomb friction law without cohesion is the best-tested model for rapid, dense, granular flows. Experiments demonstrate that Coulomb-like proportionality between intergranular shear stresses and normal stresses is evident in rapid, dense, granular flows (Hungr and Morgenstern 1984a, 1984b; Savage and Hutter 1989; Iverson and Vallance 2001; Denlinger and Iverson 2004). Applicability of the cohesionless Coulomb equation extends beyond the quasi-static flow regime in which grains sustain contacts as they slide relative to one another and particles interact exclusively through mutually persistent frictional contacts among particles. The basic form of the Coulomb friction equation with zero cohesion is:

$$\tau = \sigma \tan \phi \tag{4.71}$$

where σ and τ denote normal stress and shear stress, repectively, and ϕ is the frictional angle.

Because of the shallowness assumption, the normal stress in the z direction can be approximated as hydrostatic. The normal stress at the bed is then determined by the overburden of the flow depth:

$$\tau_{zz} = \rho g \cos\theta \left(z_b + h - z\right) \tag{4.72}$$

$$\left(\tau_{zz}\right)_{z=z_b} = \rho g h \cos\theta \tag{4.73}$$

The basal shear stress can be calculated using the Coulomb friction law. The longitudinal pressure in the x direction is related to normal pressure in the z direction through the coefficients of lateral pressure. The coefficient of lateral pressure is defined as the ratio of the longitudinal pressure to the normal pressure

$$K = \frac{\tau_{xx}}{\tau_{zz}} \tag{4.74}$$

where K is a coefficient of lateral pressure. An active or passive state of stress is dependent on whether an element of material is elongated or compressed during a downslope motion. The equation for lateral pressure coefficients can be derived from the Mohr stress circle and the Coulomb failure envelope (Savage and Hutter 1989; Iverson 1997):

$$K_a = 2\frac{1-\sqrt{1-\cos^2\phi \sec^2\phi_b}}{\cos^2\phi} - 1 \quad for \quad \frac{\partial \bar{u}}{\partial x} > 0 \tag{4.75}$$

$$K_p = 2\frac{1+\sqrt{1-\cos^2\phi \sec^2\phi_b}}{\cos^2\phi} - 1 \quad for \quad \frac{\partial \bar{u}}{\partial x} < 0 \tag{4.76}$$

$$\sec^2\phi_b = 1 + \tan^2\phi_b \tag{4.77}$$

where K_a and K_p are coefficients of active and passive lateral pressure, respectively, ϕ is the internal frictional angle, and ϕ_b is the basal frictional angle. Combining all these equations, the depth-averaged governing equations for two-dimensional debris flow with the Coulomb frictional model as constitutive equations reduce to:

$$\frac{\partial h}{\partial t} + \frac{\partial \left(h\bar{u}\right)}{\partial x} = 0 \tag{4.78}$$

$$\frac{\partial(h\bar{u})}{\partial t}+\frac{\partial(h\bar{u}^2)}{\partial x}=gh\sin\theta-\left(K_{a/p}\right)gh\cos\theta\frac{\partial h}{\partial x}-\operatorname{sgn}(\bar{u})\,gh\cos\theta\tan\phi_b \qquad (4.79)$$

where $-\operatorname{sgn}(\bar{u})$ indicates that basal resistance has the opposite direction to the sliding velocity. The depth-averaged momentum equation (4.79) can be written in Lagrangian form by using $\frac{d\bar{u}}{dt}=\frac{\partial\bar{u}}{\partial t}+\bar{u}\frac{\partial\bar{u}}{\partial x}$:

$$\frac{d\bar{u}}{dt}=g\sin\theta-\left(K_{a/p}\right)g\cos\theta\frac{\partial h}{\partial x}-\operatorname{sgn}(\bar{u})\,g\cos\theta\tan\phi_b \qquad (4.80)$$

Equations (4.78) to (4.80) are governing equations for single phase cohesionless granular flows over simple sliding surfaces. It is worth noting that effects of surface curvature are neglected in the equations.

The multi-dimensional extension of simple depth-averaged equations has been proposed for the analysis of dry granular flows across complicated three-dimensional terrains (Gray et al. 1999; Pudasaini and Hutter 2003; Wang et al. 2004; Denlinger and Iverson 2004; Pudasaini et al. 2005a). Effects of slope curvature are taken into account by using a curvilinear coordinate system and incorporating a centrifugal force into momentum conservation equations. The depth-averaged model for granular flows containing interstitial fluid has been formulated by including effects of pore fluid pressure on flow dynamics (Hungr 1995; Iverson and Denlinger 2001; McDougall and Hungr 2004, 2005; Pudasaini et al. 2005b; Pitman and Le 2005). The formulation of governing equations for the Coulomb mixture theory (Iverson and Denlinger 2001) is based on the assumption that the solid in water-saturated granular flows behaves as a Coulomb granular material and interstitial fluid behaves as a viscous Newtonian fluid. An advective diffusion equation is proposed to describe the changes in pore water pressures (Denlinger and Iverson 2001). A two-phase model developed by Pitman and Le (2005) can simulate the velocities of solid and fluid phases in the solid-fluid mixture flows. A drag term describes the interactions between solid and fluid in the governing equation. The advanced two-phase models (Iverson and Denlinger 2001; Pitman and Le 2005) are complex and have not found much practical application.

The single phase depth-averaged governing equations have been applied to simulating debris avalanches, debris flows, and other types of fast landslides. Good agreement has been achieved between model predictions and experimental or field observations (Bertolo and Wieczorek 2005; Hungr and Evans 1996, 1997; Iverson et al. 2004; Hungr et al. 2005; Kelfoun and Druitt 2005). As a consequence, a depth-averaged model with the Coulomb friction law as the constitutive equation has been established as one of the leading models for debris flow simulations.

4.5 Discussion

Prediction of the post-failure mobility of liquefaction flow slides, debris flows, debris avalanches, and other types of flow-like landslides can be conducted using empirical methods, sliding block models and depth-averaged models. The empirical method is very simple and can provide a useful means of predicting post-failure travel distance (or the travel distance angle). Very useful empirical models can be developed for regional and type-specified flow-like landslides provided that large and good-quality databases are available. However, the application of empirical correlations to field data results in considerable scatter due to the complexity of the debris flow process and uncertainty involved in the establishment of empirical equations. Uncertainties in the empirical model are associated with the accuracy of the data which is primarily dependent on the quality of the maps and profiles provided by the referenced authors, and the consistency among authors in describing the same landslide case. Review of empirical models indicates that most relationships established so far can only provide an order of magnitude estimate of some debris flow parameters, but are not capable of giving accurate predictions of values required for protective designs (Rickenmann 1999). The empirical approach does not take into consideration the type of material flowing, mechanisms of failure, travel path confinement, ground water, and geology of the study regions. Therefore, the application of empirical equations is limited to regions where geological and climatic conditions are similar to those from which the equations were derived.

The sliding block model delineates the motion of the sliding mass as a rigid dimensionless block. The velocity and runout distance of the centroid of the post-failure material are determined by assigning appropriate bulk rheological properties and travel path in the block model. Forces acting on the block consist of the gravity driving force and basal resistance. The resistance is exclusively dependent on the rheological properties specified for the failure material. Frictional and Voellmy models are the most widely used constitutive law for the block model. Improved sliding models have been created by taking into consideration the effects of pore water pressure (Hutchinson 1986; Sassa 1988). The kinetic analysis is the application of the sliding block model to the estimation of liquefied shear strength (Davis et al. 1988; Olson 2001; Olson and Stark 2002). The cohesive model is specified as a constitutive equation and the length of failure surface is required to determine resistance acting on the sliding block in the kinetic analysis. The sliding block model can not account for the confinement of travel path and lateral spreading of the failure materials. The sliding block model, therefore, can only provide a very crude approximation of the debris flow process.

Depth-averaged equations provide the most advanced model for debris flow simulations. Predictions of the velocity field, lateral spreading, and longitudinal runout distance of debris flows are obtained by solving the depth-averaged governing equations with the appropriate constitutive law. The derivation of depth-averaged equations for debris flow modeling is based on the shallowness assumption, i.e., that the longitudinal length scales much greater than flow depth. The depth-averaging process substantially reduces computational efforts and makes possible the practical simulation of debris flows over complex topography. The depth averaging process, however, sacrifices flow details in the dimension normal to flow direction. With uniform velocity distribution over the flow depth, depth-averaged models are not capable of accounting for the effects of internal flow dynamics on debris flow simulations.

The constitutive behavior of materials is incorporated into the depth-averaged model through simplified basal flow resistance formulations. The complicated mixture of flowing sediment and water is represented by a simplified equivalent fluid with particular rheological characteristics (Hungr 1995). Iverson (1997), Iverson and Denlinger (2001), and Pitman and Le (2005) presented a two-phase formulation of the depth-averaged model for water-saturated granular flows. In the two-phase model, the behavior of granular materials is governed by the Coulomb friction law and assumptions are made to describe the interactions between solid and fluid phases Due to the difficulties involved in the implementation of two-phase theory, the application of these formulations is still limited to the analysis of experimental granular flows over simple topography. Practical applications of depth-averaged models require specification of the appropriate constitutive law for an equivalent fluid. The Bingham model, the Herschel-Bulkley model, and the Coulomb frictional model are commonly used in debris flow simulations. Studies indicate that estimated travel distance and velocity from depth-averaged models are sensitive to the constitutive laws and parameters defining the models that are used in the numerical analysis (Bertolo and Wieczorek 2005; Naef et al. 2006). Generally, there are no procedures directly based on experimental tests to determine the representative bulk properties of debris. Consequentely, the constitutive model and corresponding parameters have to be determined by the back-analyses of real cases. It is well known that constitutive performance of sediment-water mixtures is governed by many factors, among which sediment concentration and solid material properties are key elements.

4.6 Conclusion

Investigation of debris flow numerical modeling indicates that:

(1) Applications of simple empirical relationships established so far lead to results with considerable scatter. Constitutive properties of debris are not fully taken into account in the derivation of empirical equations. Compared with the analytical models, the empirical models possess limited applicability and generality in debris flow hazard assessment and protective designs.

(2) The sliding block model simplifies mass movement as a rigid body motion. Lateral and longitudinal spreading of failure materials is not accounted for in the model.

Predictions based on the sliding block model provide a crude approximation of debris flows.

(3) The depth-average models are capable of providing detailed predictions of flowing velocity, lateral spreading, and longitudinal travel distance of debris flows. The constitutive properties of materials are incorporated in the depth-averaged governing equations combined with bed flow resistance.

(4) Energy dissipation due to particle sliding, collision, and interactions between solid and fluid phases is not explicitly accounted for in current depth-averaged models. The accuracy of prediction can be improved by incorporating internal deformations into the debris flow simulation model.

Table 4-1 Parameters for correlations between the tangent of travel angle and landslide volume

Landslide Type	**Sliding Path**	*A*	*B*	**Reference**
Rockfalls	All	0.62419	-0.15666	Scheidegger 1973
All landslides	All	-0.047	-0.085	Corominas 1996
Rockfalls	All	0.210	-0.109	
	Obstructed	0.231	-0.091	
	Deflected	1.078	-0.233	
	Unobstructed	0.1671	-0.119	
Translational slides	All	-0.159	-0.068	
	Obstructed	-0.133	-0.057	
	Unobstructed	-0.143	-0.080	
Debris flows	All	-0.012	-0.105	
	Obstructed	-0.049	-0.108	
	Channelized	-0.077	-0.109	
	Unobstructed	-0.031	-0.102	
Earthflows and mudflows	All	-0.214	-0.070	
	Unobstructed	-0.220	-0.138	

Notes: Regression equation is $\log(\tan\alpha) = \log\left(\frac{H}{L}\right) = A + B\log(V)$, where α is travel angle, H is vertical drop, L is travel distance, and V is landslide volume measure in m^3.

Table 4-2 Parameters for correlations between the tangent of travel angle and the slope angle (Data from Hunter and Fell 2003)

Slope Type	**Soil Type**	**Sliding Path**	A	B
Natural slope	Silty sands and sandy clay with gravel and boulders, low clay content	Unconfined	0.087	0.77
		Partly confined	0.086	0.69
		Confined	0.147	0.54
Waste spoil pile	Coal mine waste spoil, sandy gravel, low fines content and loose dumped	All	0.16	0.54
		Confined, all	0.13	0.57
		Confined, highly mobile	0.14	0.35
		Unconfined	0.17	0.59

Notes: Regression equation is $\tan\alpha = \frac{H}{L} = A + B\tan\theta$, where α is travel angle, H is vertical drop, L is travel distance, and θ is downslope angle below the source area.

Table 4-3 Empirical relationships for debris flows (Data from Rickenmann 1999)

Parameters	Flow Type	Empirical Equations
Peak discharge	Granular debris flows (Japan)	$Q_p = 0.135V^{0.780}$
	Muddy debris flows (Japan)	$Q_p = 0.0188V^{0.790}$
	Merapi volcano (Indonesia)	$Q_p = 0.00558V^{0.831}$
	Sakurajima volcano (Japan)	$Q_p = 0.00135V^{0.870}$
	Landslide dam failures	$Q_p = 0.293V_w^{0.56}$
	Glacial dam failures	$Q_p = 0.0163V_w^{0.64}$
Mean flow velocity	Newtonian laminar flow	$U = \frac{1}{3}\frac{\rho g H^2 S}{\mu}$
	Dilatant gain shearing flow	$U = \frac{2}{3}\xi H^{3/2} S$
	Newtonian turbulent flow (Manning-Strickler equations)	$U = \frac{1}{n} H^{2/3} S^{1/2}$
	Newtonian turbulent flow (Chezy equations)	$U = C H^{1/2} S^{1/2}$
	Empirical equation	$U = C_1 H^{0.3} S^{1/2}$
Travel distance	Debris flows (Swiss Alps)	$L = 1.9V^{0.16} H_e^{0.83}$

C, Chezy coefficient; C_1, constant determined from regression analysis; g, gravitational acceleration; H, flow depth; H_e, elevation difference between the starting point and the lowest point of deposition; L, travel distance; n, Manning coefficient; Q_p, peak discharge; S, channel slope; U, mean flow velocity; V, debris flow volume; V_w, volume of water behind a dam; ρ, debris flow density; μ, dynamic viscosity of debris flows; ξ, coefficient for dilatant shearing flow.

Table 4-4 Empirical equations for long-runout landslides (Data from Legros 2002)

Parameters	**Landslide Type**	**Empirical Equations**
Tangent of travel angle	Nonvolcanic landslides	$\frac{H}{L} = 0.16V^{-0.15}$
	Volcanic landslides	$\frac{H}{L} = 0.11V^{-0.19}$
	Martian landslides	$\frac{H}{L} = 0.42V^{-0.19}$
	Submarine landslides	$\frac{H}{L} = 0.03V^{-0.09}$
Travel distance	Nonvolcanic landslides	$L = 8V^{0.25}$
	Volcanic landslides	$L = 15.6V^{0.39}$
	Martian landslides	$L = 6.2V^{0.34}$
	Submarine landslides	$L = 18V^{0.33}$
	Debris flows	$L = 235V^{0.39}$
Deposit area	Volcanic landslides	$A = 55V^{0.87}$
	Martian landslides	$A = 6.1V^{0.70}$
	Debris flows	$A = 230V^{0.76}$

A, area of landslide deposit; H, vertical drop of landslide; L, travel distance; V, landslide volume.

Table 4-5 Liquefied shear strength from kinetic analysis of liquefaction flows (Data from Olson and Stark 2002)

Case History		Liquefied Shear Strength (kPa)		
No.	**Name**	**Best Estimate**	**Lower Bound**	**Upper Bound**
1	Calaveras Dam	34.5	28.7	37.8
2	Fort Peck Dam	27.3	16.8	34.0
3	Lower San Fernando Dam	18.7	15.8	21.8
4	Wachusett Dam	16.0	10.4	19.1
5	Hachiro-Gata Embankment	2.0	1.0	3.2
6	Koda Numa Embankment	1.2	—	—
7	Lake Ackerman Embankment	3.9	3.4	4.7
8	Route 272 Embankment	4.8	3.0	5.7
9	Shibecha-Cho Embankment	5.6	3.9	8.3
10	Uetsu-Line Embankment	1.7	—	—

Note: —, data not available.

Table 4-6 Depth-averaged equations in orthogonal curvilinear coordinate systems

Governing Equation	References	Comments
$\frac{\partial h}{\partial t}+\frac{\partial}{\partial x}\left(h\overline{u}\right)=0$ $\frac{du}{dt}=\frac{\partial\overline{u}}{\partial t}+\overline{u}\frac{\partial\overline{u}}{\partial t}=\sin\zeta-\tan\phi\,\mathrm{sgn}\left(\overline{u}\right)\left(\cos\zeta+\lambda\kappa\overline{u}^{2}\right)-\varepsilon K\cos\zeta\frac{\partial h}{\partial x}$	Savage and Hutter 1991	Nondimensional
$\frac{\partial h}{\partial t}+\frac{\partial}{\partial x}\left(h\overline{u}\right)=0$ $\rho\frac{du}{dt}=\rho\left(\frac{\partial\overline{u}}{\partial t}+\overline{u}\frac{\partial\overline{u}}{\partial t}\right)=\rho g\sin\zeta-\tan\phi\,\mathrm{sgn}\left(\overline{u}\right)\left(\rho g\cos\zeta+\rho\frac{\overline{u}^{2}}{r}\right)-K\frac{\partial}{\partial x}\left(\frac{1}{2}\rho gh^{2}\cos\zeta\right)$	Greve and Hutter 1993	Dimensional
$\frac{\partial h}{\partial t}+\frac{\partial\left(h\overline{u}\right)}{\partial x}+\frac{\partial\left(h\overline{v}\right)}{\partial y}=0$ $\frac{d\overline{u}}{dt}=\sin\zeta-\tan\phi\frac{\overline{u}}{\sqrt{\overline{u}^{2}+\overline{v}^{2}}}\left(\cos\zeta+\lambda\kappa\overline{u}^{2}\right)-\varepsilon K_{x}\cos\zeta\frac{\partial h}{\partial x}$ $\frac{d\overline{v}}{dt}=-\tan\phi\frac{\overline{v}}{\sqrt{\overline{u}^{2}+\overline{v}^{2}}}\left(\cos\zeta+\lambda\kappa\overline{u}^{2}\right)-\varepsilon K_{y}\cos\zeta\frac{\partial h}{\partial y}$	Greve, Koch and Hutter 1994	Nondimensional

Table 4.6 (continued)

Governing Equation	References	Comments
$\frac{\partial h}{\partial t}+\frac{\partial(h\overline{u})}{\partial x}+\frac{\partial(h\overline{v})}{\partial y}=0$ $\frac{\partial}{\partial t}(h\overline{u})+\frac{\partial}{\partial x}(h\overline{u}^2)+\frac{\partial}{\partial y}(h\overline{u}\overline{v})=h\sin\zeta-\frac{\overline{u}}{\sqrt{\overline{u}^2+\overline{v}^2}}h\tan\phi(\cos\zeta+\lambda\kappa\overline{u}^2)-\varepsilon h\cos\zeta\frac{\partial z_b}{\partial x}-\frac{\partial}{\partial x}\left(\frac{\beta_x h^2}{2}\right)$ $\frac{\partial}{\partial t}(h\overline{v})+\frac{\partial}{\partial x}(h\overline{u}\overline{v})+\frac{\partial}{\partial y}(h\overline{v}^2)=-\frac{\overline{v}}{\sqrt{\overline{u}^2+\overline{v}^2}}h\tan\phi(\cos\zeta+\lambda\kappa\overline{u}^2)-\varepsilon h\cos\zeta\frac{\partial z_b}{\partial y}-\frac{\partial}{\partial y}\left(\frac{\beta_y h^2}{2}\right)$ $\beta_x=\varepsilon\cos\zeta K_x$ and $\beta_y=\varepsilon\cos\zeta K_y$	Wang, Hutter and Pudasaini 2004	Nondimensional, curvilinear coordinate system presented in Figure 4-6.

Note: $\varepsilon=\frac{H}{L}$, where H is typical depth and L is typical spread of flow; $\lambda=\frac{L}{R}$, where R is typical radius of curvature of the sliding surface; r, radius of the curvature of sliding surface; κ, curvature of the sliding surface; $\overline{u}$, depth-averaged velocity in the x direction; $\overline{v}$, depth-averaged velocity in the y direction; ρ, material density; h, flow depth; ϕ, frictional angle; m, mass of material; ζ, slope angle; z_b, elevation of the sliding surface; K, coefficient of lateral pressure; K_x, coefficient of lateral pressure in the x direction; K_y, coefficient of lateral pressure in the y direction.

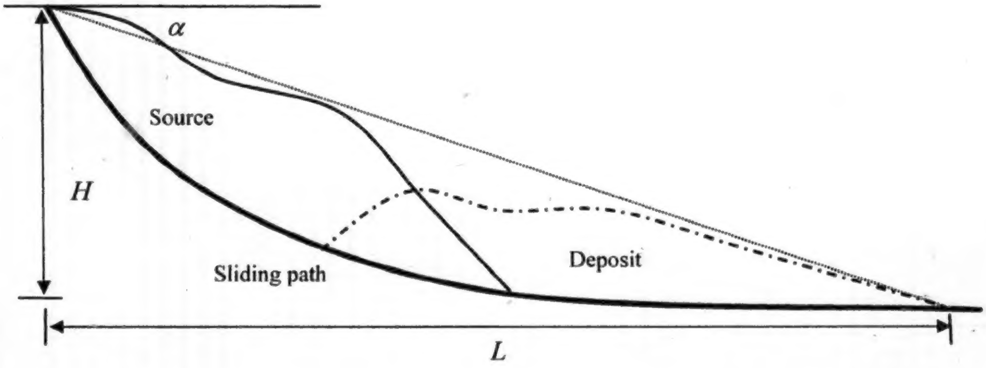
α
Source
H
Sliding path
Deposit
L

Figure 4-1 Definitions of travel angle and travel distance

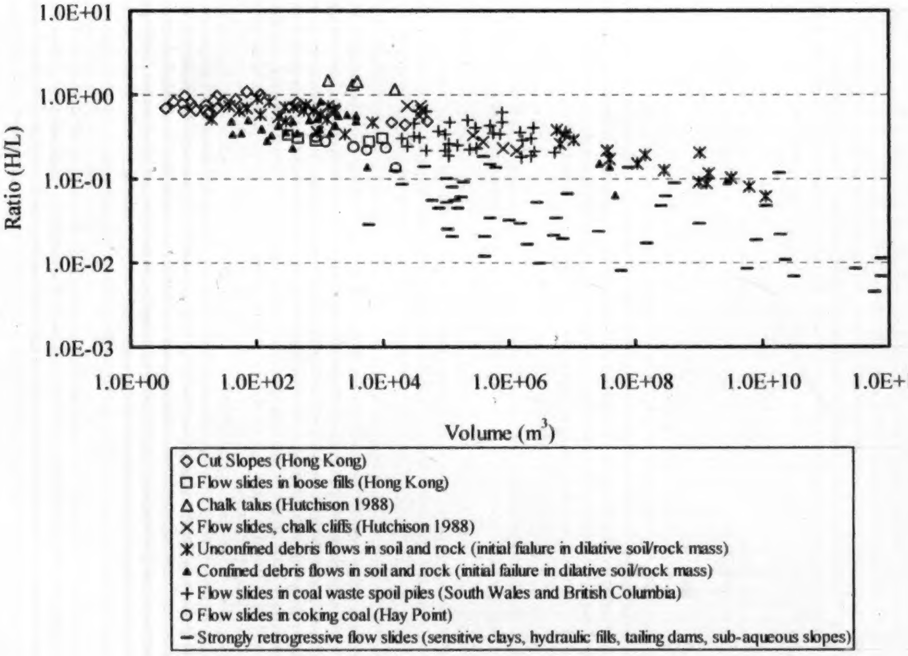

Figure 4-2 Tangent of travel angle (H/L) versus landslide volume

(Data from Hunter and Fell 2003)

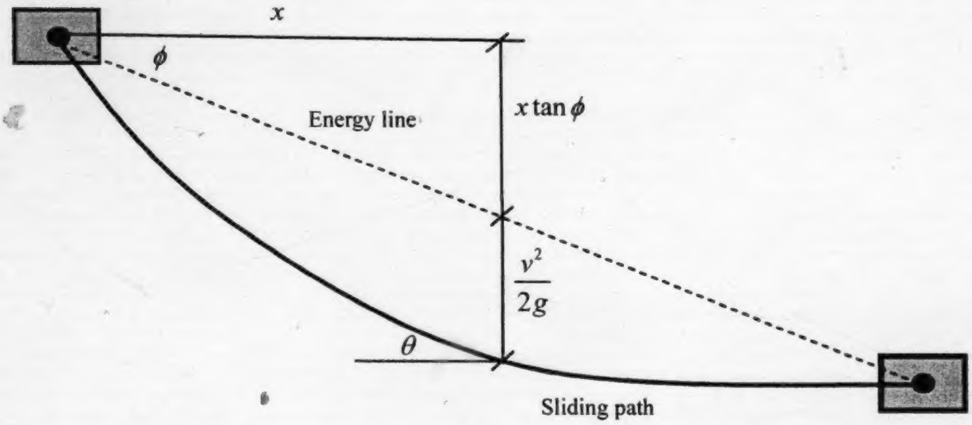
x
ϕ
Energy line
$x\tan\phi$
$\frac{v^2}{2g}$
θ
Sliding path

Figure 4-3 Sliding block model with energy line for frictional material

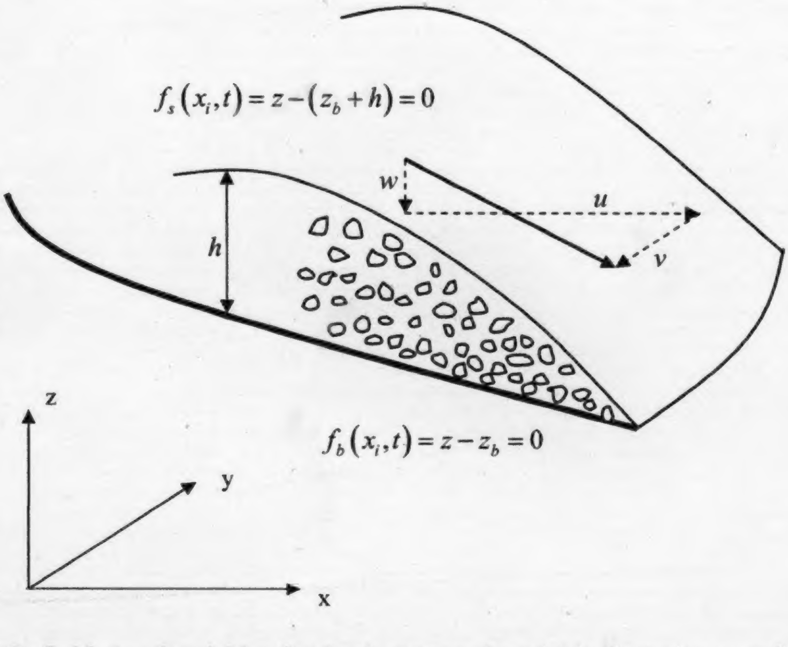
$f_s(x_i,t)=z-(z_b+h)=0$
w
u
h
v
$f_b(x_i,t)=z-z_b=0$
z
y
x

Figure 4-4 Definitions of variables for depth-averaged model in Cartesian coordinates (Modified from Denlinger and Iverson 2004)

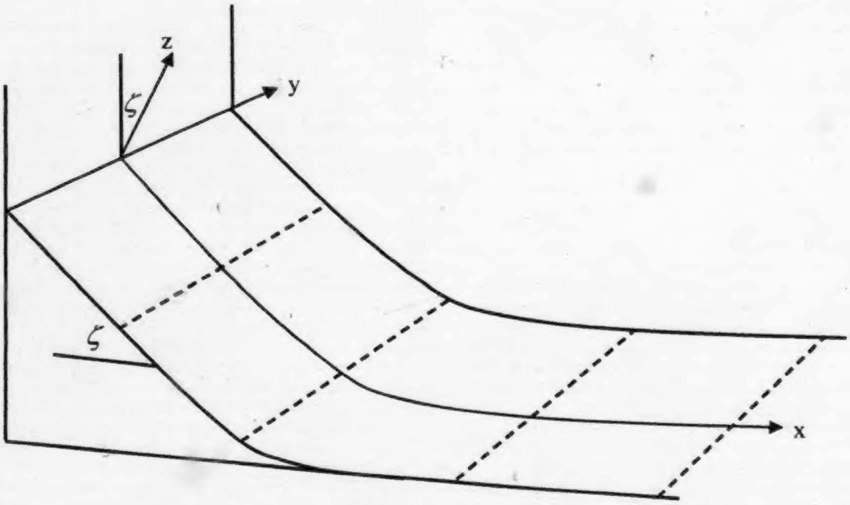

Figure 4-5 Sketch of the curvilinear coordinate system

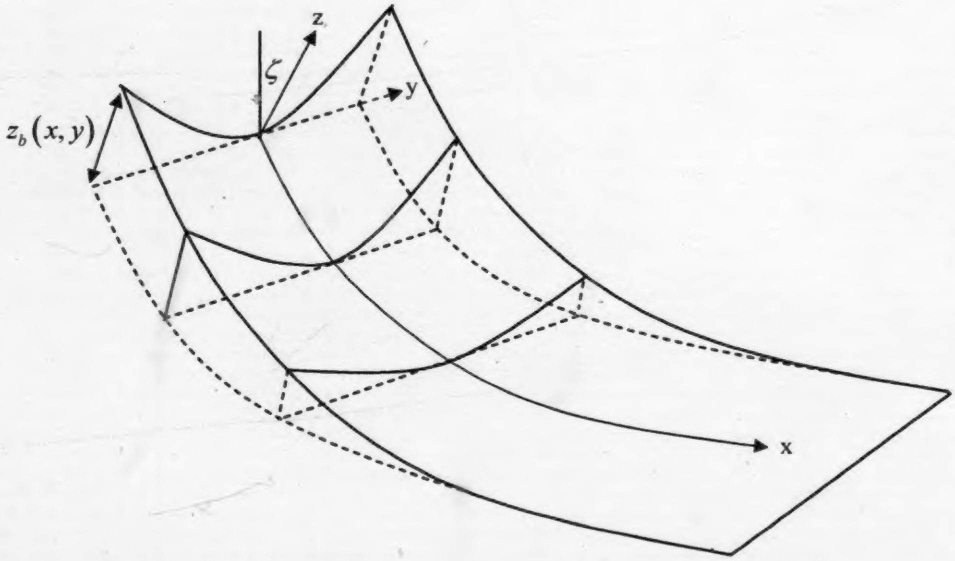

Figure 4-6 Curvilinear coordinate system used for two-dimensional Savage-Hutter model (Modified from Wang et al. 2004)

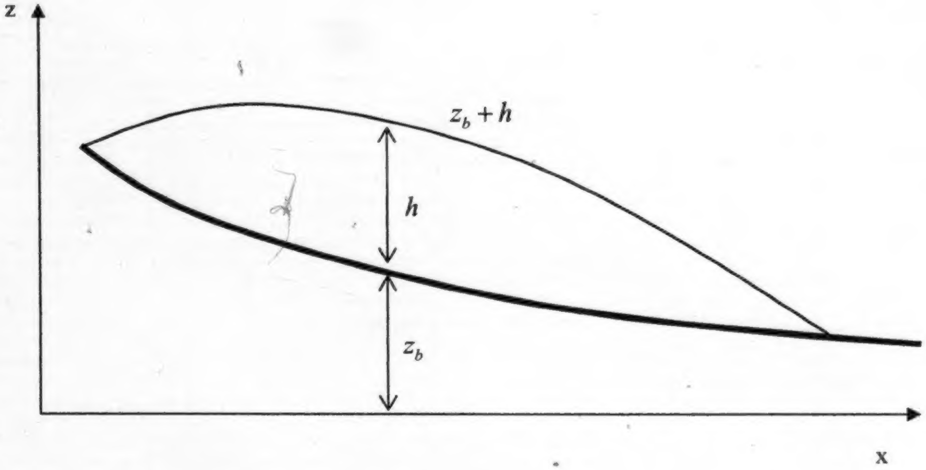

Figure 4-7 Two-dimensional debris flow with Cartesian coordinates

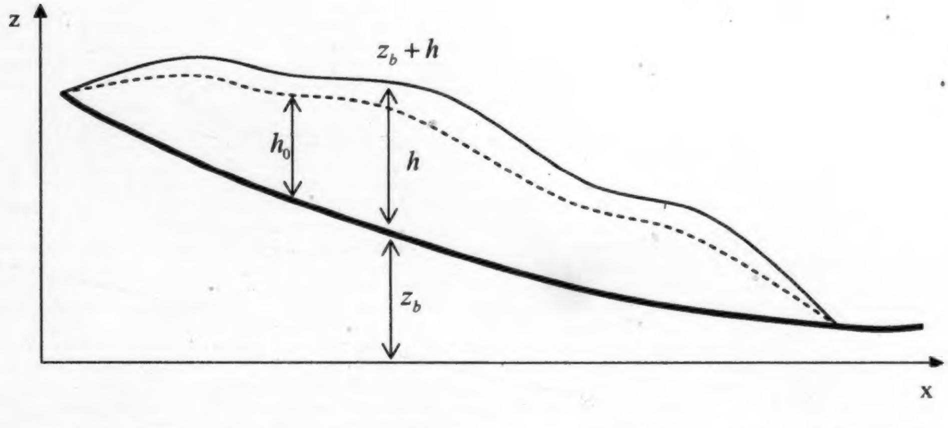
z
$z_b + h$
h_0
h
z_b
x

Figure 4-8 Two-dimensional non-Newtonian flow with Cartesian coordinates

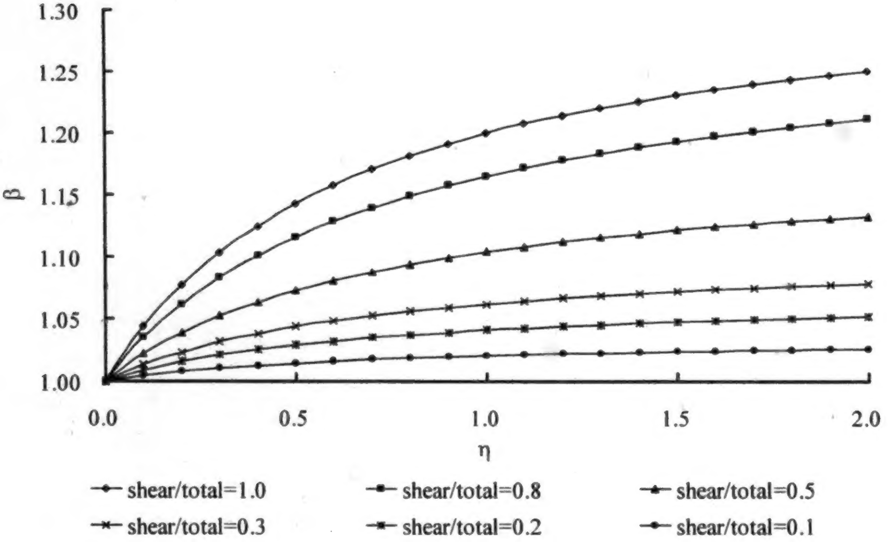

Figure 4-9 Shape factor (β) versus rheological index (η) for different ratio of shear depth to total flow depth

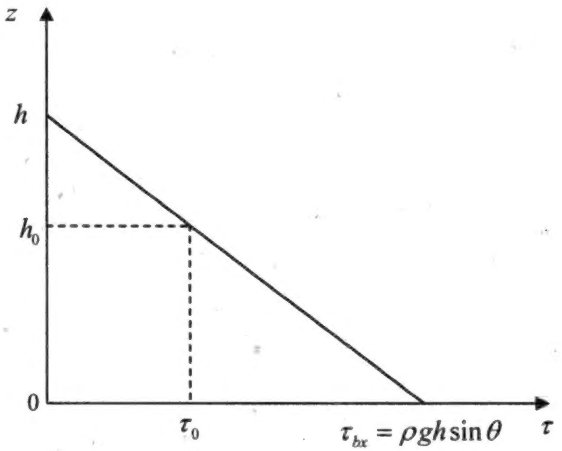
z
h
h_0
0
τ_0
$\tau_{bx} = \rho g h \sin\theta$
τ

Figure 4-10 Shear stress distribution for Bingham fluid flowing down an inclined plane with slope angle of θ

Chapter 5

A Slice-Based Model with Internal Energy Dissipation

5.1 Introduction

Depth-averaged equations have been dominantly applied to modeling debris avalanches, debris flows, and other types of fast moving landslides. Constitutive properties of debris are incorporated into governing equations through a basal flow resistance, which is expressed in terms of averaged velocities when the Bingham and Herschel-Bulkley models are selected and in terms of hydrostatic overburden stress and the coefficient of internal friction when the Coulomb frictional law is used. As observed in the formulation of depth-averaged equations, uniform velocity is assumed and the energy dissipation in depth-averaged models is primarily caused by basal resistance. It is well known that the flows of highly concentrated sediment-water mixtures, such as liquefaction flow slides, and debris flows, consume kinetic energy not only through basal frictional resistance, but also through collision and friction among grains, and interactions between solid phase and fluid phase. However, due to the complexity and difficulties involved in simulating these mechanisms, the effects of internal energy dissipation on the dynamics of debris flow are usually not specifically considered in debris flow simulations.

In this chapter, a slice-based model with internal energy dissipation is formulated on a macroscopic scale. Formulation of the governing equations is based on the conservation law for energy. Compared with the existing depth-averaged slice-based models, terms related to deformation work and internal energy dissipation are introduced into the governing equations. The numerical method for practical implementation of the governing equations is presented following the model formulation.

5.2 The Slice-Based Model

Slice-based dynamic analysis has been developed and successfully used in studies of fast moving gravitational flows such as rapid landslides, debris flows, and liquefaction flow slides (Hungr 1995; Tinti et al. 1997; Miao et al. 2001; Kwan and Sun 2006). In the slice-based model, the flowing mass is represented by an ensemble of connected slices (2 dimensions) or blocks (3 dimensions) which are subjected to gravitational forces, basal resistance, and internal force. While sliding down over the specified sliding surface, the slices interact with each other, consequently dissipating energy along their base and exchanging momentum between individual slices. The shapes of slices are able to change as flow develops but total volume is conserved and no mass can penetrate between slices. Newton's laws of motion are employed to define the relationship between slice movement and forces acting on it. A Lagrangian specification is generally adopted to easily locate positions of slices at certain time points. The initial dimension of sliding mass and topography of the sliding path have to be specified in a slice-based model. In practice, the required information can be obtained by field investigations with a combination of stability analysis and empirical judgment. The runout distance and velocities from field observations can be used to test against simulation results and to calibrate input parameters of the model.

The models proposed by Hungr (1995), Tinti et al. (1997), Miao et al. (2001), and Kwan and Sun (2006) are all momentum-based methods. A general survey of the momentum-based models indicates that the computation of gravity driving force and bottom resistance has very similar expressions in these models. It is the formulation of internal force that distinguishes one method from the other.

Hungr (1995) presented a dynamic model (DAN) for the runout analysis of rapid landslides. DAN is based on an explicit solution of the Saint Venant equations with the integration of a variety of constitutive relationships which have been widely applied to debris flow modeling. The displaced materials of a landslide are represented by a number of boundary elements and mass elements. Formulation of the governing equations is based on the principle of momentum conservation for the boundary elements. Mass conservation is applied to the mass elements to calculate changes in flow depth and internal deformation within the landslide. Flow resistance along the sliding surface is determined using the constitutive law specified in an analysis. The resultant longitudinal pressure acting on the boundary element is determined by the product of the hydrostatic pressure gradient of the equivalent fluid and a lateral pressure coefficient (Hungr 1995). The value of the lateral pressure coefficient is dependent on the coefficients of active and passive earth pressure, the stiffness coefficient, and average tangential strain of the mass elements. Initially, unit value is used as lateral pressure coefficient for each element. The magnitude of lateral coefficient is then increased or decreased by a value equal to the product of the incremental strain times a stiffness coefficient. The lateral coefficient can vary between the minimum and maximum values which correspond to active and passive earth pressure coefficients specified. Hungr (2003) proposed that the values of the active and passive earth pressure can be determined based on internal frictional strength of the sliding material by using the equation formulated by Savage and Hutter (1989).

An improved debris mobility model (DMM) has been presented recently by Kwan and Sun (2006). The improved DMM is based on the model for the dynamic analysis of rapid landslides (DAN) developed by Hungr (1995). Enhanced DMM eliminates the limitation of the rectangular channel assumed in DAN. The formulation of flow resistance in DMM is based on the whole wetted perimeter of the flow channel. In consequence, the calculation can be conducted to simulate debris flow in channels of varying cross-sectional profiles along the flow path. For simplicity, the cross section of the flow channel is approximated as a trapezoid in the modified DMM formulation. Calculation of internal forces in DMM is based on the hydrostatic gradient and the lateral pressure coefficient which is dependent on the local internal deformation state of the landslide. The method proposed by Hungr (1995) is used in DMM to calculate coefficient of lateral earth pressure. The total flow resistance consists of resistances developed at the bottom and on the two side slopes of the channel. The bottom resistance is estimated using the same procedure as in the original formulation of DAN

(Hungr 1995) and material properties are described by the Voellmy model. The resistances on side slopes are based on the weight of the sliding mass above the side slopes. The force calculation is applied to the boundary elements in the original DAN formulation and the volume of mass elements is incorporated only into the calculation of slice height. Formulations of the forces in DMM are based on the real volume of sliding mass. Compared with the original DAN model, the improved DMM incorporates real volumes of mass blocks into the formulation of the forces and provides a more realistic landslide mobility analysis. Applications of DMM and DAN to modeling of rapid landslides in Hong Kong show that very similar front velocities are predicted by both models. The back-calculated strengths from DAN are greater than those determined from the improved DMM due to incorporation of resistances on the side slopes in the DMM model.

Tinti et al. (1997) expressed internal force in terms of an interaction coefficient, which is dependent on the dynamic state of the slices and the instantaneous distance between slice centers. The value of the interaction coefficient varies between 0 and 1, which represent two limits for interslice actions. When the interaction coefficient equals 0, interacting slices have the same post-interaction velocities irrespective of their pre-interaction states and slices move as if they adhered to one another; this is the maximum possible interaction. When the interaction coefficient equals 1, the slices conserve their pre-interaction velocities as if no interaction took place. The interaction coefficient can be expressed as a function in terms of interaction intensity, deformability parameter, and shape parameter (Tinti et al. 1997).

Miao et al. (2001) proposed a sliding block model for the runout analysis of rapid landslides. The model starts with the limit equilibrium assessment and incorporates mass dynamics and soil deformation into the calculation of slide mass movement. In the sliding block model, the slide mass is divided into a series of slices. Forces acting on a single slice consist of gravity, basal resistance, and interactions between slices. The initial interslice forces are determined by limit equilibrium analysis using the method of unbalanced thrust, in which the resultant interslice force is assumed to be parallel to the base of the preceding slice and acts at the midpoint of the height of the slice. The critical state corresponding to the unit factor of safety is considered as the initial state. Initial accelerations are computed based on initial unbalanced forces. As long as the mass movement is triggered, the interslice forces are determined based on the deformation energy. The calculation of deformation energy is based on the macroscopic deformation of the slices and bulk deformation modulus. For slices in a tensile state, the deformation energy vanishes and the interslice force is assumed to be zero. The basal shear resistance is determined based on the overburden normal force with the Coulomb frictional law, similar to the procedures used by other slide block models. Application of the sliding block model to two rapid landslides in China (Miao et al. 2001) indicated that the sliding block model results in a very large fluctuation in the velocity field simulated within very short periods of time. This is caused by the assumption that interslice forces vanish as soon as the slice is in a tensile state.

5.3 Numerical Schemes for Debris Flow Simulation

Numerical methods employed in debris flow simulations include the finite difference method (FDM), the finite element method (FEM), the discrete element method (DEM), and the method based on smoothed particle hydrodynamics (SPH). Formulations of these numerical models are outlined below, with a discussion of their applications to debris flow runout analyses. Based on the numerical methods available, an easily-implemented Lagrangian numerical approach is proposed following the formulation of the slice-based model with internal energy dissipation.

5.3.1 The Finite Difference Method

The finite difference method (FDM) is perhaps the most commonly used numerical method for modeling debris avalanches, debris flows, and other types of rapid landslides. In the finite difference approach, the continuous problem domain is replaced by a finite difference grid. The derivatives are approximated by the differences defined at neighbouring grid points, and the governing partial differential equations are represented by a set of algebraic equations in terms of unknowns at the grid points. The solution of the system equation is obtained after imposing the necessary initial and boundary conditions. The FDM has the advantage of being very easy to interpret physically, and has been used to develop a wide variety of numerical schemes to solve unsteady flow, particularly one-dimensional flow.

The Lagrangian moving mesh finite-difference scheme proposed by Savage and Hutter (1989) has been widely applied to simulate granular flows. In the Lagrangian scheme, the debris body is discretized into a number of material cells, which move and deform with the motion of debris. The mass of each material cell is conserved during motion and the mean height of the cell can be determined based on the material volume and boundary locations. Good agreement has been achieved between observations of experimental chute flows and theoretical predictions from the Savage-Hutter model with the Lagrangian scheme (Savage and Hutter 1989; Wieland et al. 1999; Tai et al. 2002). In the Lagrangian scheme, explicit artificial numerical diffusion is required to maintain numerical stability. However, the incorporation of artificial numerical diffusion deteriorates the quality of resolution. To avoid introduction of numerical oscillations and to maintain numerical diffusion as small as possible, the nonoscillatory central (NOC) difference scheme, a high-resolution Eulerian finite difference approach, has been formulated for the simulation of granular avalanches and debris flows (Tai et al. 2002; Wang et al. 2004; Pudasaini et al. 2005a, 2005b).

5.3.2 The Finite Element Method

In the finite element method (FEM), the problem domain is divided into an assemblage of small regions (finite elements) of standard shapes (triangle, quadrilateral, tetrahedral, etc.). The elements have nodes defined on the element boundary (at the vertices and/or on the sides) or within the element. Interpolation functions, usually polynomial, are used to approximate the partial differential equations over each element and to formulate local element equations representing the behavior of the elements. According to topological relations between the nodes and elements, the local elemental equations are then assembled into the global equations. Information required in the problem domain is obtained by solving the global equations with properly defined initial and boundary conditions. The FEM has the flexibility to handle material heterogeneity, nonlinearity, and complex boundary conditions. Nonuniform discretizations are easily implemented in the FEM so that elements can be concentrated in the areas of interest, allowing for optimization of computational effort. By varying the functions used to interpolate the solution over the elements, a variety of numerical schemes may be readily implemented and tested. As a consequence, the FEM has been established as the most widely applied numerical method across a wide variety of science and engineering fields.

Within the FEM context, the Lagrangian-Galerkin finite element method (Chen and Lee 2000, 2002), the combined Eulerian-Lagrangian finite element method (Crosta et al. 2003; Crosta et al. 2005), and the two-step Taylor-Galerkin algorithm (Pastor et al. 2002; Quecedo and Pastor 2003; Quecedo et al. 2004) have been used to solve the depth-averaged governing equations for flow slides, mudflows, debris flows, and rapid landslides. Despite the simplicity and easy implementation of the Lagrangian FEM, the finite element mesh is subjected to large displacements and deformations due to the long runout distance and wide spreading to be simulated. The large displacements and deformations lead to a highly distorted mesh. As a consequence, the calculated results deteriorate. For the Eulerian-Lagrangian method, the finite element mesh does not distort and accurate calculation is obtained. However, considerable computation cost is required to implement the Eulerian-Lagrangian finite element method. The Taylor-Galerkin algorithm can be considered as the FEM counterpart of the Lax-Wendroff procedure in the FDM. It consists of a higher order expansion of the time derivative, followed by the spatial discretization of the resulting equation using the conventional Galerkin weighting method. The general Taylor-Galerkin procedure requires calculation of the derivatives of the flux tensor and source vector relative to the vector of unknowns for each element in the mesh and a number of multiplications. To avoid the large computation memory required and the time-consuming operations involved in a general Taylor-Galerkin method, a two-step algorithm has been developed and used to solve shallow water equations (Quecedo and Pastor 2003). The two-step Taylor-Galerkin algorithm presents a good compromise between simplicity of the formulation and accuracy of the results and has been used to solve advection-dominated problems such as dam break and the propagation of rapid landslides (Pastor et al. 2002; Quecedo and Pastor 2003; Quecedo et al. 2004).

5.3.3 The Discrete Element Method

The discrete element method (DEM) is based on the Lagrangian approach of simulating the motion of a granular mass by microscopic particles. In the DEM, the flowing mass is discretized into an assembly of particles. The interaction forces between particles are determined based on the relative displacement of particle contacts. Interactions and external forces acting on the particles subsequently affect their dynamics. The trajectory of each particle is described by using Newton's second law, which defines fundamental relationships between the movement of particles and the forces acting on them. During a small computation time step, the interaction force and acceleration of each particle are assumed to be constant, while velocity varies linearly. Particle position is evaluated at regular time intervals. On a macroscopic scale, the flowing behavior is described in terms of the motion of individual particles.

The DEM has been used to investigate a wide variety of slope failures and the mobility of long runout landslides (e.g., Campbell et al. 1995; Okura et al. 2000a, 2000b). Campbell et al. (1995) carried out large-scale landslide runout analyses using discrete particle simulation. The landslides were discretized into assemblages of two-dimensional discs (ranging from 5000 to 1,000,000). The inter-particle force in the direction normal to the contact point was simulated as a coupled spring and dashpot connected in parallel. The particle surfaces were allowed to overlap slightly and the degree of overlap compressed the spring, thereby applying an elastic force. The dashpot dissipated some of the kinetic energy of the particles and thus made the contact inelastic. The two particles interacted as a damped spring-mass system as long as they remained in contact. A similar spring with a frictional slider connected the particles in the direction tangential to the point of contact. The slider limited the amount of tangential force that could be transmitted. Each of the constituent particles was subjected to contact forces with other particles and externally imposed gravitational forces. The motion of particles was governed by Newton's second law.

The runout distance, flow mechanism, and correlations between flow mobility and volume of rockfalls were investigated by Okura et al. (2000a, 2000b) using the discrete particle model. The rockfall was simulated as the flow of dry and nonviscous granular materials and a rigid and frictional collision model was formulated. The magnitude of interaction between particles was dependent on the properties of restitution and kinetic friction acting on the contact. Numerical simulations indicated that the high mobility of large-scale rockfalls and the positive correlation between runout distance and the volume of the rockfall were a result of internal collisions between particles.

A mathematical model using DEM has been proposed to simulate two-phase granular flow (Asmar et al. 2003). The flow domain is discretized into cells which are smaller than the scale of variation of macroscopic flow properties but larger than the particle size. The solid phase is simulated as soft, polydisperse spheres. The contact forces between particles consist of elastic, cohesion, friction, and damping forces, as determined by a conventional spring-dashpot-slider model. The motion of fluid is governed by local, averaged Navier-Stokes equations. The fluid properties are averaged in the cell using a volume weighted function. Coupling between fluid and solid phases is achieved through the fluid inter-phase force which is computed based on the fluid drag force acting on particles. DEM has also been used to simulate dry granular flows in laboratory flume tests (Valentino et al. 2004). Analyses indicate that proper determination of the material properties required in DEM simulation is difficult. Deformation behavior and the mobility of debris flows have proven to be associated with changes in pore pressures within displaced materials. Notwithstanding considerable advances in DEM, there are no appropriate models to describe effects of pore pressure on a microscopic scale. As a consequence, DEM has not found much application in practical debris flow analyses.

5.3.4 Smoothed Particle Hydrodynamics

Smoothed particle hydrodynamics (SPH) is a particle-based mesh-free method. SPH was originally developed for simulating astrophysical problems and has later been extended to model a wide range of engineering problems (Monaghan 1992). SPH uses particles as interpolation points to represent materials at discrete locations. The particles carry all the computational information and form the computational frame used for spatial discretization to solve the partial differential equations describing mass and momentum balance in fluid dynamics. Within the SPH context, the motion of a continuum is represented with the motion of a large number of particles. Formulation of SPH is based on the interpolation method which allows any function to be expressed in terms of its values at a set of particles. Using a specifically selected interpolating kernel that approximates a delta function, the partial differential equations can be transformed into corresponding integral forms.

SPH formulation involves kernel approximation and particle approximation. In the kernel approximation, a function is approximated by its integral interpolant, which is defined as the integration of the multiplication of the function and a smoothing kernel function (Monaghan 1992). The kernel approximation gives an estimate of each dependent field variable. In the particle approximation, the integral interpolant at a particle is approximated by summation of the volume-weighted contributions from all the neighboring particles within the region controlled by the smoothing length. Approximations of spatial derivatives are evaluated in terms of the function values at particles by transforming the differential operation on the function into an operation on the smoothing kernel function specified. SPH is a simple and straightforward numerical procedure with the advantages of being Lagrangian, mesh-free, and easily implemented. As a consequence, SPH can easily trace material interface, free surfaces, and moving boundaries.

One-dimensional dam-break flow has been computed using smoothed particle hydrodynamics (Wang and Shen 1999). In one-dimensional dam-break simulations, particles are defined as vertical slices having properties of mass, velocity, and depth.

The Gaussian function is selected as the kernel function. Simulations indicate that SPH is especially appropriate for modeling problems with sharp moving fronts. In SPH simulations, individual particles continuously adjust length and depth according to the varying flow conditions. Sharp discontinuities in the flow can easily be captured and accurately simulated. A three-dimensional numerical model for the dynamic analysis of flow slides, debris flows, and avalanches has been formulated by McDougall and Hungr (2004). Using the SPH method, the model is based on a Lagrangian solution of depth-averaged equations generalized for the flow of earth materials. The numerical scheme proposed permits large displacement without mesh distortion and facilitates simulations of rapid landslides over complex topographies. The model has been tested against laboratory flume experiments and real case histories of rapid landslides. Recently, a material entrainment algorithm has been proposed and incorporated into the dynamic model to simulate bulk behavior of rapid landslides entraining substantial path material (McDougall and Hungr 2005).

5.4 Formulation of the Slice-Based Model with Internal Energy Dissipation

The depth-averaged model is established by integrating the mass and momentum conservation equations in differential form over the flow depth with the use of Leibnitz's law. The constitutive property of debris is incorporated into the depth-averaged governing equations in terms of the basal frictional resistance. Integration of the differential form of the conservation laws over the flow depth considerably reduces the computational cost required in rapid landslide runout analysis. Formulation of the governing equation in curvilinear coordinates provides a more realistic modeling of debris flow over complex topographies. However, the depth-averaging process sacrifices internal deformation details with the approximation of uniform velocity over the thickness of flow. The Coulomb frictional law has been widely employed to compute basal shear resistance for depth-averaged models in debris flow simulations. The magnitude of resistance is determined by the product of overburden normal stress and coefficient of basal friction $\tan\phi_b$.

The slice-based model incorporates the effects of internal deformation on the flow dynamics using either the interaction coefficient (Tinti et al. 1997) or deformation energy (Miao et al. 2001). The interslice force proposed in the slice-based model is primarily dependent on the magnitude of deformation and the dynamic state of the slices. However, application of the slice-based model to rapid landslide simulation is either difficult or impractical owing to the great uncertainties involved in the formulation of the interslice force and the determination of model input parameters required. For instance, the significant fluctuation in velocity field predicted by the model of Miao et al. (2001) is mainly caused by inappropriate computation of the interaction force in terms of deformation energy.

A slice-based model incorporating internal energy dissipation is formulated below. The formulation of a new model is mainly based on the conservation of energy of a slice during the motion, and the deformation work and energy dissipation are specifically considered in the mechanical energy equations.

5.4.1 Mechanical Energy Equations

The rate of change of the kinetic energy of a material volume can be written as the sum of three parts (Aris 1962):

(1) the rate at which the body forces do work, i.e., change in potential energy;

(2) the rate at which the surface stresses do work; and

(3) the rate at which the internal stresses do work, i.e., change in internal energy due to deformation.

The kinetic energy equation for a unit volume mass is given by:

$$\rho\frac{d}{dt}\left(\frac{1}{2}u_i u_i\right)=\rho g_i u_i+\frac{\partial}{\partial x_j}\left(u_i\tau_{ij}\right)-\tau_{ij}e_{ij} \tag{5.1}$$

Where ρ is the density of fluid, $u_i u_i = u_1^2+u_2^2+u_3^2$ is kinetic energy per unit volume, τ_{ij} are components of the stress tensor, e_{ij} are components of the strain rate tensor,

u_i is the component of the velocity vector in the x_i direction, and ρg_i is the body force per unit volume in the x_i direction.

An integral form of the mechanical energy equation can be derived by integrating each term in equation (5.1) over a material volume or a slice of a landslide body V. Using Gauss' theorem, equation (5.1) in the Lagrangian system becomes:

$$\frac{d}{dt}\int_V \left(\frac{1}{2}\rho u_i u_i\right) dV = \int_V \rho g_i u_i dV + \int_A u_i \tau_{ij} dA_j - \int_V \tau_{ij} e_{ij} dV \tag{5.2}$$

Each term in equation (5.2) is a time rate of change: the first term is the rate of the kinetic energy of a material volume, the second term is the rate of total work done by the body force acting on a material volume, the third term represents the total work done by the forces acting on the surface of a material volume, and the forth term represents the rate of energy dissipation due to deformation of a material volume. The description of the third term is obvious because $\tau_{ij} dA_j$ is the surface force in the i direction and $u_i \tau_{ij} dA_j$ is the scalar product of the force with the velocity vector. The deformation work includes two parts: the work due to volume expansion and the work due to irreversible deformation. For an incompressible fluid, the work due to volume expansion is zero and the deformation work represents irreversible kinetic energy dissipation. Thus, the term $\int_V \tau_{ij} e_{ij} dV$ represents a rate of loss of kinetic energy and a gain of internal energy due to deformation of the volume.

The body force can be represented as the gradient of a scalar potential gz. The rate of work done by body forces can be taken to the left-hand side of equation (5.2) and can be interpreted as a change in the potential energy. For an incompressible fluid, ρ is constant and the mass within a material volume can be determined by:

$$m = \int_V \rho dV \tag{5.3}$$

and equation (5.2) can be rewritten as:

$$\frac{d}{dt}\left(\frac{1}{2} m \overline{u}_i^2 + mgz_W\right) = \int_A u_i \tau_{ij} dA_j - \int_V \tau_{ij} e_{ij} dV \tag{5.4}$$

Where $\overline{u}_i$ is the average velocity component of a material volume, and z_W is elevation of the center of gravity of the flowing mass. The left-hand side of the equation (5.4) represents the rate of change of mechanical energy (the sum of kinetic energy and potential energy).

5.4.2 Derivation of Governing Equations Based on the Conservation of Energy

The sliding mass is divided into a series of contiguous slices, as shown in Figure 5-1. Forces acting on a slice of width b and height h are shown in Figure 5-2. In this figure:

W denotes the weight of the slice;

P denotes the interslice force;

T denotes the shear force acting along the base of the slice;

N denotes the normal force;

b denotes the width of the slice;

h denotes the height of the slice;

m denotes the mass of the slice;

$\overline{u}$ denotes the mean velocity of the slice along the base of the slice;

θ denotes the inclination of the base of the slice with respect to the horizontal;

Subscript k denote the slice number; and

Subscripts L and R denote properties on the left and right sides a slice.

With the assumption that the interslice frictional forces between slices are zero, the rate of total work done by the surface forces in equation (5.4) is given by:

$$\int_A u_i \tau_{ij} dA_j = P_L \overline{u}_L \cos\theta_L - P_R \overline{u}_R \cos\theta_R - T\overline{u} \tag{5.5}$$

where θ_L and θ_R are inclinations between velocities and corresponding interslice forces acting on the left and right sides of the boundary.

The rate of change of total potential energy of a slice in equation (5.4) can be expressed as the sum of the rate of potential energy changes due to the displacement and deformation of the slice, as shown in Figure 5-2:

$$\frac{d}{dt}(mgz_w) = \frac{d}{dt}(mgz_{w1}) + \frac{d}{dt}(mgz_{w2}) \tag{5.6}$$

$$m = \rho bh \tag{5.7}$$

where $\frac{d}{dt}(mgz_{w1})$ represents the rate of change of potential energy due to displacement of the center of the gravity, $\frac{d}{dt}(mgz_{w2})$ represents the rate of the change of the potential energy due to deformation of the slice, and ρ is the mean density of the sliding mass. Thus:

$$\frac{d}{dt}(mgz_{W1}) = -mg\overline{u}\sin\theta \tag{5.8}$$

$$\frac{d}{dt}(mgz_{W2}) = -\frac{1}{2}mghe_{zz} \tag{5.9}$$

where e_{zz} is the mean vertical strain rate of a slice defined in Figure 5-3.

Using equations (5.5) to (5.9), equation (5.4) becomes:

$$\frac{d}{dt}\left(\frac{1}{2}m\overline{u}^2\right) = mg\overline{u}\sin\theta + \frac{1}{2}mghe_{zz} + P_L\overline{u}_L\cos\theta_L - P_R\overline{u}_R\cos\theta_R - T\overline{u} - \int_V \tau_{ij}e_{ij}dV \tag{5.10}$$

Summing both sides of equation (5.10) for all slices (k = 0 to n in Figure 5-4) gives the rate of change of the kinetic energy of the overall sliding mass:

$$\frac{d}{dt}\left(\sum_{k=0}^{n}\frac{1}{2}m_k\overline{u}_k^2\right) = \sum_{k=0}^{n} m_k g\left[\overline{u}_k\sin\theta_k + \frac{1}{2}(he_{zz})_k\right] - \sum_{k=0}^{n}T_k\overline{u}_k - \sum_{k=0}^{n}\int_{V_k}\tau_{ij}e_{ij}dV_k \tag{5.11}$$

It is easy to show that the rate of work done by interslice forces is cancelled out in the proceeding derivation. Equation (5.11) states that the rate of the change of kinetic energy of a sliding mass is equal to the sum of the rate of potential energy change, the rate of work done by resistance force along the base of sliding mass, and the rate of deformation work.

5.4.3 Effects of Slope Curvature on Motion of Liquefaction Flow Slides and Debris Flows

The motion of liquefaction flow slides and debris flows usually takes place on slopes with curved sliding surfaces. Significant slope and surface curvature influence flow dynamics and should be incorporated in the governing equations. Depth-averaged equations formulated in curvilinear coordinate systems (Savage and Hutter 1991; Greve et al. 1994; Gray et al. 1999; Siviglia and Cantelli 2005) show that consideration of slope curvature incorporates centrifugal forces into momentum conservation equations. A centrifugal force normal to a sliding surface does not directly contribute to momentum in the direction parallel to the sliding surface. However, incorporation of a centrifugal force changes the magnitude of forces normal to the sliding surface. For frictional material, resistance acting on the base of a slice is dependent on the normal force. Changes in shear resistance due to variations in normal forces have effects on the momentum equation along the slope. The same conclusion applies to the energy equation. The centrifugal force, which is perpendicular to the velocity vector, does not contribute to the energy equations directly. Changes in forces normal to the slope, however, have effects on changes in kinetic energy through basal resistance.

The magnitude of the centrifugal force can be calculated by:

$$F_c = \kappa m \bar{u}^2 = m \frac{\bar{u}^2}{r} \tag{5.12}$$

where κ is slope curvature, defined as the rate of change in the angle of the tangent with the arc length of the slope, r is the radius of curvature, and $\bar{u}$ is the mean velocity parallel to the slope.

Practical observations of sliding surfaces of liquefaction flow slides and debris flows analyzed in this study indicated that large curvatures may exist in source areas. During the initiation stage, displaced materials move with small velocities in source areas. The resultant centrifugal force is not significant, as indicated by equation (5.12). Sliding masses with higher velocities beyond source areas may also experience small centrifugal forces because of small curvatures or large radii of local, curved sliding surface; this applies to the cases in this study. A sliding mass with a high velocity passing a sharp bend in the sliding surface engenders considerable centrifugal force. However, this force often lasts for a very short period of time and its contribution to the change in kinetic energy is limited. As a consequence, the effects of curvature on the motion of flow slides and debris flows can be neglected from a practical point of view. Effects of bottom curvature on mudflow dynamics have been studied by Siviglia and Cantelli (2005) using a curvilinear coordinate reference system. Their study indicated that curvature of slope tends to increase the pressure relative to the hydrostatic distribution, but deviations are negligible as long as the assumption of shallowness is satisfied.

DAN-W program has been used to study the effects of the centrifugal forces on the motion of the liquefaction flow slides analyzed in this study. For each case, two dynamic analyses were carried out and runout distance was calculated using same parameters. The effects of the centrifugal forces are included in one simulation but excluded in another. The runout distance and maximum velocities calculated for 10 cases of liquefaction flow slides are shown in the Table 5-1. Results from DAN-W analysis in Table 5-1 agree with the conclusion aforementioned: centrifugal forces have negligible influences on the back-analysis of liquefaction flow slides carried out in this thesis.

5.4.4 Comparison with Previous Mathematical Models

Flow slides, and debris flows generally exhibit pervasive, fluid-like deformation. Morgenstern (1978) has previously drawn attention to the class of problems associated with mobile flows in a variety of geological and geomorphological settings. He concluded with the observations that characterization of mobile soil and rock flows and the design of protective structures should proceed using principles of fluid mechanics. The fundamental equations of debris flow dynamics can be formulated based on the following universal laws of conservation in fluid mechanics: conservation of mass, conservation of momentum, and conservation of energy. A literature survey indicates that mathematical models for debris flow simulations are often formulated based on the conservation laws of mass and momentum, as summarized in Table 5-2.

As noted by Morgenstern in 1978, large volumes of soil or rock can become fluidized by virtue of energy transfer mechanisms following instability. Iverson et al. (1997) provided an extended discussion on mobilization of debris flows from landslides and noted that three processes are involved in the mobilization: (a) widespread Coulomb failure within sediment mass, (b) partial or complete soil liquefaction by high pore-fluid pressure, and (c) conversion of landslide translational energy to internal vibrational energy. These processes operate simultaneously and synergistically in many circumstance and change of pore-fluid pressues and conversion of energy are crucial compoents in debris flow mobilization and evolution. Derivation of governing equation (5.10) is based on energy consideration and idealization of complex energy transfer mechanisms involved in mobilization, motion, and deposition of flow slides, and debris flows. Within the framework of universal energy conservation law, energy dissipation due to internal deformation is integrated into geotechnical analysis of granular flows explicitly. Based on conservation laws of mass and energy, the analytical model developed in this chapter provides new insight into quantitative analysis of granular flows in geotechnical settings.

Examination of current slice-based models in debris flow analysis, as presented in the following sections, indicates that the mass conservation is generally applied to individual slices separated by plane boundaries. During flow development, it is assumed that no mass can penetrate between slices. It is evident that this assumption neglects effects of mixing and any energy dissipation associated with mixing process in debris flows. In the new analytical model, however, the internal energy dissipation term in equation (5.10) appears to provide a pseudo way of accounting for the mixing effects.

5.5 A Numerical Scheme for the Analytical Model Based on Energy Considerations

Depth-averaged governing equations can be solved using either a Lagrangian or an Eulerian scheme. Two numerical, finite difference methods – one Lagrangian the other Eulerian – have been tested against flume experiments on dry granular flows (Savage and Hutter 1989). Simulations indicated that the Eulerian scheme based on the upwind flux correction method gave poor predictions of experimental avalanches with general initial profiles. The Lagrangian finite difference approach (Savage and Hutter 1989, 1991) was found to be simple, efficient, and reliable for the granular rapid flow problem which involves a free surface, dry bottom, and moving boundaries. The approach is based on a Lagrangian, moving mesh, finite difference scheme in which the flowing material is divided into quadrilateral cells in two dimensions or triangular prisms in three dimensions. Boundary locations are determined for each time step. The depth of a cell is calculated from cell volume and boundary locations. Numerical simulations of flume experiments on dry granular flows showed very good agreement between theoretical predictions and observation data (Savage and Hutter 1989, 1991; Wieland et al. 1999).

Hungr (1995) formulated equations for the motion of rapid landslides along a specified path and subsequently developed a dynamic analysis program (DAN). The sliding mass in DAN is divided into a number of blocks contacting each other. The blocks are capable of deforming freely while retaining fixed volumes of material. The effect of curvature is accounted for by including the contribution of the centrifugal force into the normal force calculation. DAN incorporates seven widely accepted constitutive models for the calculation of basal resistance. The rheological properties of the sliding mass are allowed to change at different positions along the sliding path.

Tinti et al. (1997), Miao et al. (2001), and Kwan and Sun (2006) formulated slice-based models for modeling rapid landslides. The numerical method proposed for solving the governing equations is the Lagrangian finite difference approach similar to that used by Savage and Hutter (1989) and Hungr (1995). Following the procedures of Savage and Hutter (1989) and Hungr (1995), the Lagrangian finite difference scheme is presented below for solving the equations of the slice-based model with internal energy dissipation.

In the Lagrangian scheme, the sliding mass is discretized into a number of slices, as shown in Figure 5-1. In Figure 5-4, $(h_c)_k$, $(x_c)_k$, $(x_b)_k$, and $(x_b)_{k+1}$ denote the average depth, center location, and boundaries of slice k, respectively. Mass conservation of slice k during the landslide motion indicates:

$$\frac{d}{dt}(V_k)=0 \tag{5.13}$$

where V_k is the volume of slice k. The mean depth of slice at time t can thus be determined by:

$$(h_c)_k^t=\frac{V_k}{(x_b)_{k+1}^t-(x_b)_k^t} \tag{5.14}$$

Solution of the governing equations of rapid landslides requires determining the positions of the boundaries of each slice at time t. The basic loop of the numerical scheme assumes that all the variables involved in the calculation at $t+\Delta t$ are known from previous time t, where Δt is time step-size. In the framework of the Lagrangian finite difference scheme, the governing equation (5.10) can be written as:

$$\frac{E_k^{t+\Delta t}-E_k^t}{\Delta t}=\dot{W}_k^t \tag{5.15}$$

$$E_k=\frac{1}{2}m_k\overline{u}_k^2 \tag{5.16}$$

$$\dot{W}_k=m_kg\overline{u}_k\sin\theta_k+\frac{1}{2}m_kgh_k\left(e_{zz}\right)_k+\left(P_L\overline{u}_L\cos\theta_L\right)_k-\left(P_R\overline{u}_R\cos\theta_R\right)_k-T_k\overline{u}_k-\int_{V_k}\tau_{ij}e_{ij}dV \tag{5.17}$$

where E_k is the kinetic energy of slice k, $\dot{W}_k$ is the sum of the rate of the work done by body force, surface force, and energy dissipation due to deformation of slice k. E_k and $\dot{W}_k$ are determined from equations (5.16) and (5.17), respectively.

The constitutive law and assumptions regarding interslice forces and deformation work are required for calculating the rate of work in equation (5.17). The basal shear resistance can be determined based on the constitutive laws for materials. For Mohr-Coulomb materials, the basal resistance along the base of the slice can be expressed as:

$$T_k = \tau A_k = \left(c + \sigma \tan \phi_b\right) A_k = cA_k + N_k \tan \phi_b \tag{5.18}$$

where T_k and N_k are shear resistance and normal force acting on the base of slice k, A_k is basal area of slice k, τ is shear stress, c is cohesion, σ is normal stress, and ϕ_b is basal friction angle.

Equation (5.18) is a generalized form of the Mohr-Coulomb equation. In this study, either a purely cohesive or a frictional model is used as a constitutive law in back-analyses of liquefaction flow slides (Chapter 6) and debris flows (Chapter 7). It is evident that if the friction angle is equal to 0 ($\phi_b = 0$), equation (5.18) reduces to the purely cohesive model; if the cohesive strength is equal to 0 ($c = 0$), equation (5.18) reduces to the frictional model.

In debris flow simulations, lateral pressure can be approximated as a product of hydrostatic pressure and the coefficient of lateral pressure if the frictional model is used as a constitutive law. With interslice shear forces ignored, lateral pressure can be written as:

$$\left(P_L\right)_k = \frac{\left(K_L\right)_k \gamma \left(h_b\right)_k^2}{2} \tag{5.19}$$

$$\left(P_R\right)_k = \frac{\left(K_R\right)_k \gamma \left(h_b\right)_{k+1}^2}{2} \tag{5.20}$$

where $\gamma = \rho g$ is the unit weight of sliding mass, $\left(h_b\right)_k$ and $\left(h_b\right)_{k+1}$ are flow depths on the left and right sides of slice k (Figure 5-4), and $\left(K_L\right)_k$ and $\left(K_R\right)_k$ are the lateral earth pressure coefficients on the left and right sides of slice k. The lateral stress coefficient can be active, passive or static based on local strain rate (velocity gradient) of a slice in the longitudinal direction. Equations proposed by Savage and Hutter (1989) have been commonly used for calculating the coefficients of lateral earth pressure in the analysis of dense granular flows. The derivation of Savage-Hutter equations on lateral stresses assumes Coulomb failure occurs simultaneously along the bed and within the sliding mass. Therefore, the definition of the Savage-Hutter coefficients is considered to be more general than those of Rankine lateral earth pressure coefficients used in classical soil mechanics. Examination of the Savage-Hutter equations indicates that the coefficient of active earth pressure is greater than unity if value of basal friction angle is close to that of the internal friction angle (Figure 5-5). This is physically impossible. On the other hand, localized thin shear layers is generally assumed in the the depth-averaged models (Savage and Hutter 1989) and the contribution to the magnitude of lateral stress from internal materials appears to be more significant than that from the materials of the thin shear zone along the bed.

In this analysis, the active or passive state of stress on the left side of a slice is dependent on whether the slice is expending or contracting. The values of the lateral stress coefficients are calculated using the Rankine equation:

$$(K_L)_k = \begin{cases} \dfrac{1-\sin\phi}{1+\sin\phi} = \tan^2\left(45-\dfrac{\phi}{2}\right) & \left(\dfrac{\partial u}{\partial x}\right)_k > 0 \\ 1 & \left(\dfrac{\partial u}{\partial x}\right)_k = 0 \\ \dfrac{1+\sin\phi}{1-\sin\phi} = \tan^2\left(45+\dfrac{\phi}{2}\right) & \left(\dfrac{\partial u}{\partial x}\right)_k < 0 \end{cases} \tag{5.21}$$

where ϕ is the internal friction angle.

For a purely cohesive material, internal friction angle is equal to 0 and lateral earth pressure coefficient is equal to 1. Total lateral forces calculated using the Rankine theory are:

$$(P_L)_k = \begin{cases} \dfrac{1}{2}\gamma(h_b)_k^2 - 2c(h_b)_k & \left(\dfrac{\partial u}{\partial x}\right)_k > 0 \\ \dfrac{1}{2}\gamma(h_b)_k^2 & \left(\dfrac{\partial u}{\partial x}\right)_k = 0 \\ \dfrac{1}{2}\gamma(h_b)_k^2 + 2c(h_b)_k & \left(\dfrac{\partial u}{\partial x}\right)_k < 0 \end{cases} \tag{5.22}$$

According to equation (5.22), the calculated horizontal force is negative when a slice is in the active state and $(h_b)_k < \frac{4c}{\gamma}$. Because tensile stresses occur rarely in soils, equation (5.22) is modified to take the tensile crack into account:

$$(P_L)_k = \begin{cases} \frac{1}{2}\gamma(h_b)_k^2 & \left(\frac{\partial u}{\partial x}\right)_k \geq 0 \\ \frac{1}{2}\gamma(h_b)_k^2 + 2c(h_b)_k & \left(\frac{\partial u}{\partial x}\right)_k < 0 \end{cases} \tag{5.23}$$

Deformation of the slice is simplified as a pure shear deformation, as shown in Figure 5-3. The deformation work rate is approximated by:

$$\int_{V_k} \tau_{ij} e_{ij} dV = (\bar{\tau}_{xx}\bar{e}_{xx} + \bar{\tau}_{zz}\bar{e}_{zz})_k \, b_k \, (h_c)_k \tag{5.24}$$

where $(\bar{e}_{xx})_k = -\frac{\partial}{\partial x}(u\cos\theta)_k = -\frac{(u_R\cos\theta_R - u_L\cos\theta_L)_k}{b_k}$ is the mean strain rate. Following the conventions of stress and strain representation usually adopted in geotechnical engineering, negative signs have been introduced in order that compressive stresses and compressive strains are positive quantities.

For an incompressible fluid:

$$\bar{e}_{xx} + \bar{e}_{zz} = 0 \tag{5.25}$$

$\bar{\tau}_{xx}$ and $\bar{\tau}_{zz}$ are mean horizontal and vertical stresses, respectively,

$$(\bar{\tau}_{zz})_k = \frac{\gamma(h_c)_k}{2} \tag{5.26}$$

For a frictional material, lateral stresses are computed from:

$$(\bar{\tau}_{xx})_k = K_k(\bar{\tau}_{zz})_k \tag{5.27}$$

where

$$K_k = \frac{(K_L)_k + (K_R)_k}{2} \tag{5.28}$$

For a purely cohesive material, coefficient of lateral earth pressure is equal to 1 and average lateral stresses inside slice k can be calculated by:

$$(\bar{\tau}_{xx})_k = \begin{cases} (\bar{\tau}_{zz})_k & \left(\dfrac{\partial u}{\partial x}\right)_k \geq 0 \\ (\bar{\tau}_{zz})_k + 2c & \left(\dfrac{\partial u}{\partial x}\right)_k < 0 \end{cases} \tag{5.29}$$

Using equations (5.16) to (5.29), the kinetic energy of slice k at time $t+\Delta t$ can be determined:

$$E_k^{t+\Delta t} = E_k^t + \dot{W}_k^t \Delta t \tag{5.30}$$

The center velocity of a slice at time $t+\Delta t$ is:

$$(u_c)_k^{t+\Delta t} = \sqrt{\frac{2E_k^{t+\Delta t}}{m_k}} \tag{5.31}$$

The boundary velocity is approximated as:

$$(u_b)_k^{t+\Delta t} = \frac{(u_c)_{k-1}^{t+\Delta t} + (u_c)_k^{t+\Delta t}}{2} \tag{5.32}$$

Displacement of slice boundary is:

$$(x_b)_k^{t+\Delta t} = (x_b)_k^t + \frac{(u_b)_k^t \cos\theta_k^t + (u_b)_k^{t+\Delta t} \cos\theta_k^{t+\Delta t}}{2} \Delta t \tag{5.33}$$

where $(x_b)_k^t$ and $(x_b)_k^{t+\Delta t}$ are x coordinates of boundaries of slice k at time t and $t+\Delta t$, respectively.

The height of slice k at $t+\Delta t$ is computed by:

$$(h_c)_k^{t+\Delta t} = \frac{V_k}{\left[(x_b)_{k+1}^{t+\Delta t} - (x_b)_k^{t+\Delta t}\right]}, \quad (h_b)_k^{t+\Delta t} = \frac{(h_c)_{k-1}^{t+\Delta t} + (h_c)_k^{t+\Delta t}}{2} \tag{5.34}$$

$$(h_b)_0^{t+\Delta t} = 0, \quad (h_b)_n^{t+\Delta t} = 0 \tag{5.35}$$

where V_k is the volume of slice k, $(h_b)_k^{t+\Delta t}$ is the height of the left boundary of slice k at $t+\Delta t$, and $(h_c)_k^{t+\Delta t}$ is the central height of slice k at $t+\Delta t$.

At time $t=0$, the velocities and kinetic energy of slices are equal to zero. The acceleration of slice i can be determined from momentum conservation:

$$m_k \frac{d\bar{u}_k}{dt} = m_k g \sin\theta_k - T_k + (P_L - P_R)_k \cos\theta_k \tag{5.36}$$

The velocities and displacements of slices during the first time step can be calculated as long as accelerations are obtained from equation (5.36). The motion of each slice can then be determined using equations of energy conservation with the Lagrangian difference scheme presented above. The computation proceeds until the maximum slice velocity is under the velocity threshold specified. It is worthwhile to note that the dynamic model based on energy consideration assumes that lateral pressure and basal resistance on individual slices are known and defined by the Rankine and Mohr-Coulomb equations. The momentum equilibrium of overall sliding mass is not examined during the calculation. As a consequence, the dynamic analysis using the new analytical model can not converge on the static case since kinematics is not being considered in the formulation and the internal force distribution implicit as calculated in the static case differ from that assumed in the model. The velocity of threshold plays a key role in terminating the computation. Based on the classification of flow-like landslides (Hungr et al. 2001), the value of 0.05 m/s is used as velocity threshold in the analyses of case histories of flow slides and debris flows, which are among the extremely rapid class.

5.6 Model Verification and Numerical Experiments

Precision and performance of the slice-based model and numerical method presented in previous sections have been tested by following numerical experiments: (1) code verification has been conducted by comparing model prediction with hand calculation of a simple debris flow case; (2) the physical reality of the model has been tested by simulations of granular dam-break problems; (3) the model has then been tested by comparing numerical predictions with experimental results of granular slumping on a horizontal plane; (4) the applicability of the model is evaluated by simulating a tailing dam break with purely plastic model.

A complete description of these experiments, together with a complete set of comparisons between model predictions and experimental results, is presented in Appendix A. Appendix A also describes details of the discretization process and implementation of the numerical algorithm for solving the governing equations of the slice-based model with internal energy dissipation.

5.7 Conclusions

(1) A slice-based model is proposed to simulate debris flows, liquefaction flow slides, and other types of rapid landslides in a more realistic manner. The model is formulated based on universal conservation laws of mass and energy.

(2) Effects of deformation work and internal energy dissipation on debris flow dynamics is taken into consideration explicitly in the proposed model.

(3) The investigation of numerical methods applied to modeling rapid landslides indicates that the Lagrangian finite difference scheme is simple, efficient, and reliable for the one-dimensional flow problem which involves a free surface, dry bottom, and moving boundaries.

(4) The Lagrangian finite difference approach is formulated to solve the governing equations for the runout analysis of rapid landslides. The terms due to deformation work in debris flow are incorporated into the formulation to account for the effects of internal energy dissipation.

Table 5-1 Dynamic analysis of liquefaction flow slides with DAN-W

Case History		Centrifugal Forces Included			Centrifugal Forces Excluded		
No.	**Name**	**ϕ(°)**	**v_{max} (m/s)**	**Runout (m)**	**ϕ (°)**	**v_{max}(m/s)**	**Runout (m)**
1	Calaveras Dam	11	15.3	212.9	11	15.1	209.0
2	Fort Peck Dam	6.2	24.3	493.3	6.2	24.2	492.9
3	Lower San Fernando Dam	20	9.9	48.6	20	11.3	52.6
4	Wachusett Dam	12	12.6	104.9	12	12.4	104.0
5	Hachiro-Gata Embankment	16.5	3.8	8.0	16.5	3.8	8.1
6	Koda Numa Embankment	10	5.1	20.4	10	6.1	20.5
7	Lake Ackerman Embankment	31	10.3	11.9	31	11.0	13.2
8	Route 272 Embankment	16	9.0	24.4	16	8.8	27.4
9	Shibecha-Cho Embankment	19	6.7	24.3	19	6.6	23.6
10	Uetsu-Line Embankment	8.5	12.0	93.8	8.5	11.8	93.1

Note: Same value (ϕ) is used for internal and basal friction angles.

Table 5-2 Mathematical models for debris flow simulation based on the conservation of momentum

Model	Governing Equation	References	Comments
Savage-Hutter	$\frac{\partial h}{\partial t}+\frac{\partial}{\partial x}(h\overline{u})=0$ $\frac{d\overline{u}}{dt}=\sin\theta-\cos\theta\tan\phi\,\mathrm{sgn}(\overline{u})-\varepsilon K\cos\theta\frac{\partial h}{\partial x}$	Savage and Hutter 1989	Variables in governing equations are nondimensional.
DAN	$\frac{d\overline{u}}{dt}=g\sin\theta-\frac{\tau}{\rho h}-gK\frac{dh}{dx}\cos\theta$	Hungr 1995, Hungr et al. 2005	Governing equation is derived from momentum conservation of boundary blocks.
Block-based	$m\frac{d\overline{u}}{dt}=W\sin\theta-W\cos\theta\tan\phi+m\frac{\overline{u}_{post}-\overline{u}_{pre}}{\Delta t}$	Tinti et al. 1997	$\overline{u}_{pre}$ and $\overline{u}_{post}$ are pre- and post-interaction velocities of slice.
Sliding block	$m\frac{d\overline{u}}{dt}=W\sin\theta-T+P_L\cos(\theta_L-\theta_R)-P_R$	Miao et al. 2001	Calculation of P is based on deformation energy.

Note: $\varepsilon=\frac{H}{L}$, where H is typical depth and L is typical spread of flow; W, gravity force; P, lateral pressure force; T, shear resistance on base; τ, shear stress; ρ, material density; m, material mass; h, flow depth; ϕ, frictional angle; θ, slope angle; Δt, time interval during which internal interaction occurs; K, coefficient of lateral pressure.

Subscripts L and R denote properties on the left and right sides of a slice.

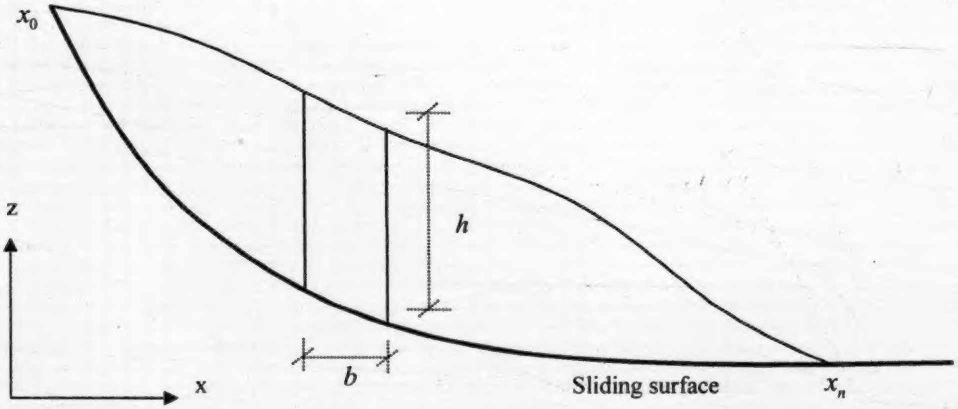
x_0
z
x
h
b
Sliding surface
x_n

Figure 5-1 Forces acting on a single slice in the slice-based model

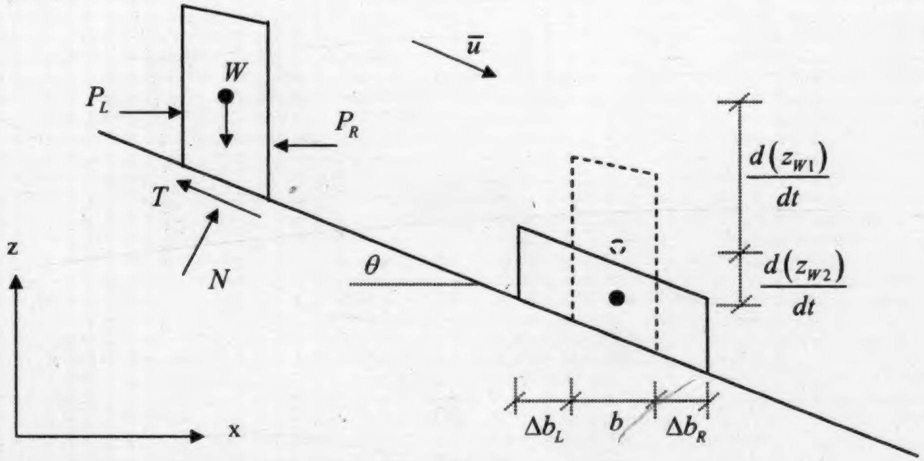
$\overline{u}$
W
P_L
P_R
T
N
z
x
θ
$\frac{d(z_{W1})}{dt}$
$\frac{d(z_{W2})}{dt}$
Δb_L
b
Δb_R

Figure 5-2 Typical motion of a slice

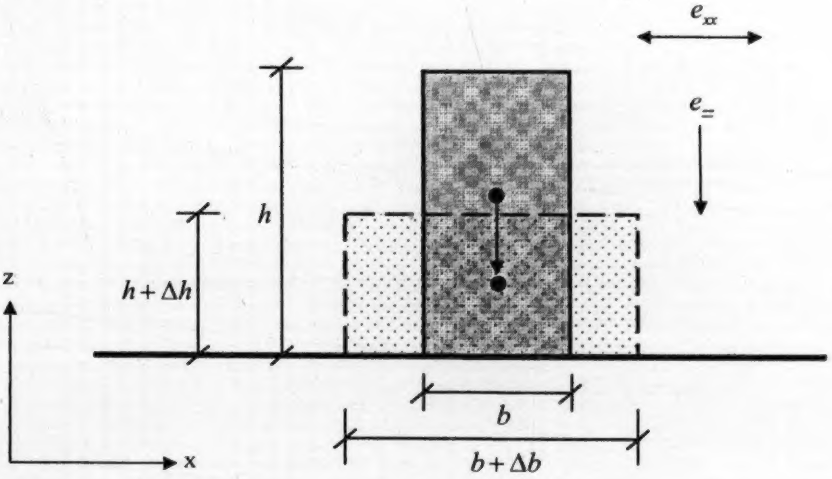
e_{xx}
e_{zz}
h
z
$h+\Delta h$
b
x
$b+\Delta b$

Figure 5-3 Uniform deformation assumed

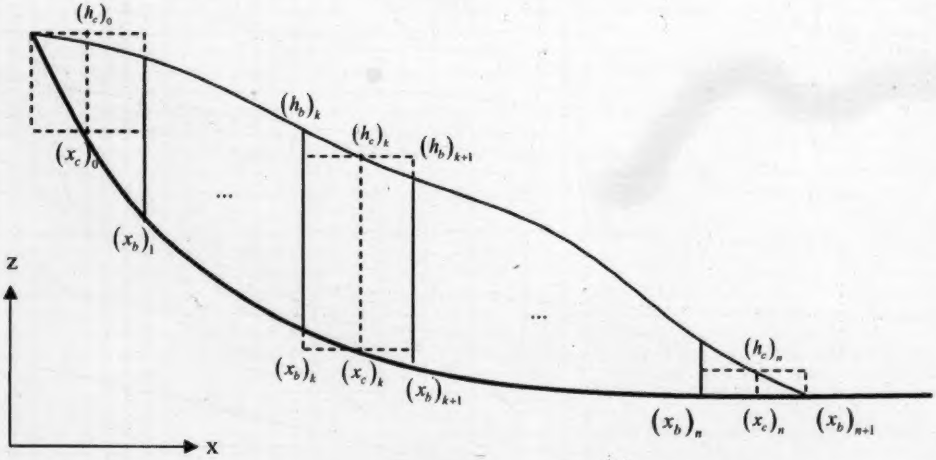
$(h_c)_0$
$(h_b)_k$
$(h_c)_k$
$(h_b)_{k+1}$
$(x_c)_0$
...
$(x_b)_1$
z
...
$(h_c)_n$
$(x_b)_k$
$(x_c)_k$
$(x_b)_{k+1}$
$(x_b)_n$
$(x_c)_n$
$(x_b)_{n+1}$
x

Figure 5-4 Slices and notations used for the slice-based model

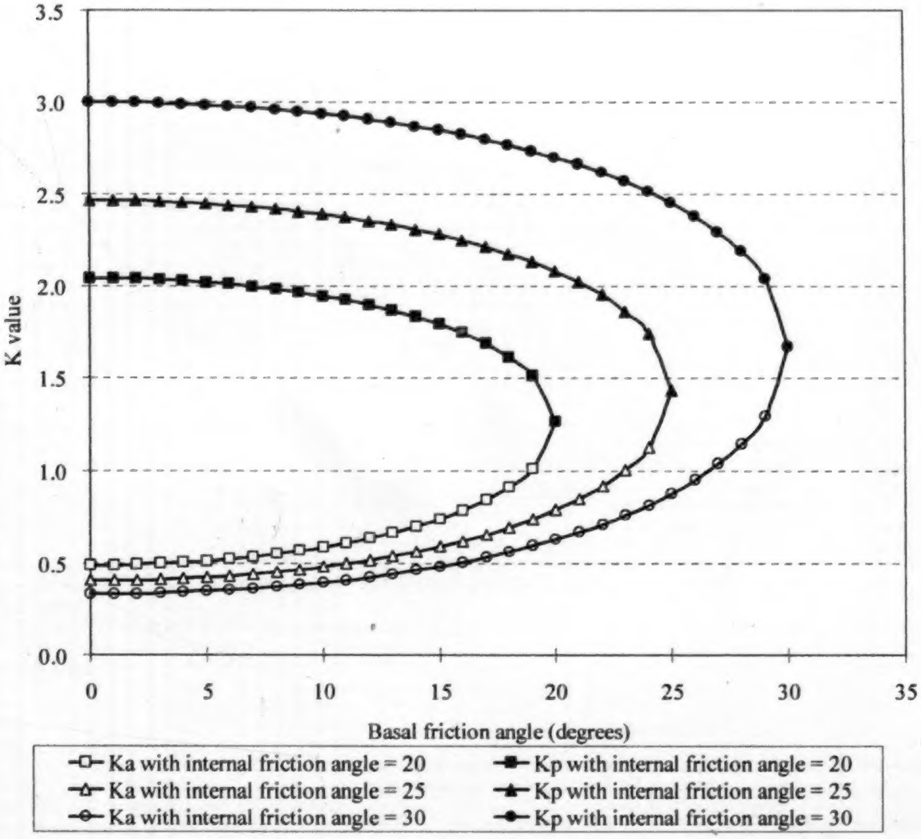

Figure 5-5 Coefficients of lateral earth pressure based on the Savage-Hutter definition

Chapter 6

The Dynamic Analysis of Liquefaction Flow Slides

6.1 Introduction

The slice-based model based on energy conservation has been formulated for debris flow modeling. The formulation is based on the depth-averaged model (Savage and Hutter 1989; Hungr 1995) and slice-based models (Tinti et al. 1997; Miao et al. 2001; Kwan and Sun 2006). An easily-implemented, simple, and efficient numerical approach has been proposed to solve the governing equations of the slice-based model developed in this thesis. In this chapter, liquefaction flow slide case histories are back analyzed using the new analytical model. Liquefied shear strengths are evaluated for ten well-documented liquefaction flow case histories. First, a definition of liquefied shear strength is given and the most commonly used methods for assessing the values of liquefied shear strength are reviewed. Then, procedures for implementing slice-based dynamic analysis to estimate liquefied shear strength are described. Improvements in assessing liquefied shear strength from dynamic analysis are demonstrated.

6.2 Liquefaction Flow and Liquefied Shear Strength

Liquefaction flow is a strain-softening behavior of contractive soils under undrained conditions. Figure 6-1 presents the typical undrained response of loose soils with strain-softening behavior when they are subjected to monotonic loading, creep, and cyclic loading. The figure shows that there is a sudden decrease in the soil strength after liquefaction is triggered. This loss of strength is related to the development of high pore pressures that reduce effective stress in the soil. Liquefaction failure of saturated soils can occur if drainage is impeded or if the rate of generation of excess pore water pressure is sufficiently higher than its dissipation (Casagrande 1936; Castro 1969; Eckerley 1990; Sasitharan 1994; Spence and Guymer 1997; Wang and Sassa 2001). Sasitharan (1994) demonstrated that flow slides and liquefaction of loose material can be initiated under both drained and undrained loading when the stress path attempts to cross the collapse surface (Sladen et al. 1985a). As illustrated in Figure 6-1, the yield strength is defined as the peak shear strength available during undrained loading and the liquefied shear strength is the shear strength mobilized at large deformation after liquefaction is triggered (Olson 2001).

Liquefaction can occur in both natural and man-made deposits (Morgenstern 2001). An inherent characteristic common to all soils susceptible to liquefaction is that the soil structure is loose, contractive, and collapsible during undrained loading. As a result of disturbance, a large loss in undrained strength occurs as a portion of the load once supported by the soil structure is transferred onto the pore fluid. If a slope is composed of a significant amount of strain softening soil and the in situ gravitational shear stresses are larger than the ultimate state strength, a liquefaction flow slide can occur if the stress state in the slope reaches the collapse surface. The trigger mechanism for the liquefaction flow slide can be cyclic, such as earthquake loading, monotonic, such as a rise in groundwater level, heavy rainfall, or rapid undrained loading (Sasitharan 1994). Liquefaction flow slides can have catastrophic consequences because they occur suddenly, with little or no warning, and the high mobility of materials in the liquefied state can threaten distant people and property (Morgenstern 2001). Liquefaction and liquefaction flow slides have been recognized as contributions to earthquake-induced catastrophes for many years (Terzaghi 1956; Morgenstern 1967; Seed 1968; Ishihara 1993).

To evaluate post-liquefaction stability and performance of soil structures, the liquefied shear strength is required and is a dominant input to post-liquefaction evaluation. In dam design, for instance, assessment of liquefaction potential involves significant issues of cost and public safety. If a large quantity of loose sand is involved in dam construction, an estimation of the liquefied shear strength of sand during and after an earthquake is the key to evaluating the potential hazard associated with the loss of containment capacity of a dam. The understanding of liquefaction and the mechanics of subsequent flow slides also has a bearing on many problems of practical interest such as stability of waste dumps, debris flows, mechanics of submarine landslides, and stability of artificial islands (Morgenstern 2001).

In soil mechanics a considerable amount of practical and theoretical work has been devoted to understanding and predicting liquefaction and liquefaction flow slides (Casagrande 1936; Poulos et al. 1985; Sladen et al. 1985a, 1985b; Seed 1987; Castro et al. 1985, 1992; Stark and Mesri 1992; Ishihara 1993; Sasitharan et al. 1993, 1994). There are two schools of thought with respect to the estimation of liquefied shear strength of sand: one is based on steady-state concepts utilizing laboratory testing results, the other is based on case history studies by correlating liquefied shear strength with field test results, primarily soil penetration resistance. The former builds on methods proposed by Poulos et al. (1985), Konrad and Watts (1995), Fear and Robertson (1995), and others, while the latter relies on methods presented by Seed (1987), Stark and Mesri (1992), and Ishihara (1993). Olson (2001) critically reviewed these methods and presented a comprehensive assessment of the state of the art. Olson's studies indicated that laboratory-based approaches are limited to large, high-risk projects because sampling undisturbed sand is costly in practice and many factors may influence test results in the laboratory (Olson 2001). The studies at Duncan Dam (Byrne et al. 1994) provide an example of the use of undisturbed sampling for evaluating the liquefaction potential of a dam in practice. Recognizing the limitations of the laboratory-testing approach, Olson (2001) and Olson and Stark (2002) summarized in detail well-documented liquefaction failure cases and reevaluated liquefied shear strengths. The correlation between liquefied shear strength of sand and in situ penetration resistance was updated based on these analyses.

6.3 Methods of Estimating Liquefied Shear Strength from Case Studies

The relationship between liquefied shear strength and soil penetration resistance – standard penetration test (SPT) or cone penetration test (CPT) – has been widely used to evaluate mobilized shear strength during a liquefaction event. Back-analyses of liquefaction case histories with sufficient information provides the most practical means for developing the corresponding relationship between liquefied shear strength and SPT or CPT. Liquefied shear strengths are back-calculated using limit equilibrium analysis of the post-liquefaction geometry of the sliding mass or by kinetic analysis in which the kinetics of failure are taken into account. Seed (1987) presented a chart showing a relationship between liquefied shear strength and the clean sand equivalent SPT resistance. The chart was used to estimate the undrained strength of liquefied sand from SPT penetration resistance. The Seed (1987) chart was obtained by back-analyzing a number of liquefaction flow slides and lateral spreads. Limit-equilibrium stability analyses of post-failure slope geometry are conducted to determine the liquefied shear strengths mobilized during liquefaction flow slides and lateral spreads. For a given case, the value of shear strength in the assumed liquefied soil was varied and the factor of safety was calculated. The liquefied shear strength was obtained when a factor of safety of unity was achieved in the stability analysis of post-failure slope geometry.

Davis et al. (1988) proposed an approach to estimate liquefied shear strength from liquefaction case histories with consideration of the dynamics of the failure. It has been illustrated that use of the post-failure cross section to estimate the strength mobilized during liquefaction is not appropriate because the dynamics of failure are not taken into account. Limit equilibrium analysis of post-failure geometry, without considering the effect of the dynamics during a flow slide, can result in the back-calculated shear strength being considerably lower than the value of shear strength actually mobilized during the failure. The limit equilibrium analyses of the post-failure geometry, therefore, were considered to provide lower-bound estimates of liquefied shear strength.

Olson (2001) used both simplified and rigorous post-failure stability analyses and kinetic analysis to back-calculate liquefied shear strength for 33 case histories. The simplified and rigorous post-failure stability analyses are essentially limit equilibrium approaches. The kinetic analysis is modified from a method first presented by Davis et al. (1988). Effects of the dynamics of the failure on back-calculated shear strength are taken into account in kinetic analysis. These approaches are described in detail in Olson's work and are only briefly reviewed here.

Simplified stability analysis is used for cases with limited information. The analysis assumes that the ground surface is parallel to the sliding surface during the flow slide and the mobilized shear strength is equal to the liquefied shear strength at the time the flowing mass comes to rest. Liquefied shear strength is estimated from the depth of sliding materials and the slope of the sliding surface, which are obtained from field investigation of the post-failure geometry.

A more rigorous stability analysis can be performed if sufficient information is available about post-liquefaction geometry. The procedure is a slope stability analysis that applies a constant liquefied shear strength ratio to assign variable shear strengths to the liquefied zone along the sliding surface. The liquefied strength ratio is defined as the liquefied shear strength normalized by the pre-failure vertical effective stress (Olson and Stark 2002). The shear strength ratio is varied in the analysis and the factor of safety is calculated. The liquefied shear strength ratio is obtained when the factor of safety is equal to one. This method was modified from a similar method first adopted by Seed (1987).

Kinetic analysis is based on Newton's laws of motion. The sliding mass is simplified as rigid body movement in the analysis and the travel of the centroid of the sliding mass is assumed in the calculation. The initial and final positions of the centroid and its travel path are specified. Centroid positions are determined by surveying pre- and post-liquefaction geometries. The travel path of the center of gravity is described simply by a mathematical function; its parameters are computed from the coordinates of the initial and final positions of the center of gravity and curvatures at those points.

Because accurate information about centroid travel in liquefaction flow cases is difficult to obtain, various assumptions are adopted in kinetic analysis. Davis et al. (1988) used a hyperbola to fit the travel path of the center of gravity in the Lower San Fernando Dam kinetic analysis. After examining some flow slide case histories, Olson (2001) concluded that a cubic polynomial provides a better approximation of a centroid travel path. Using cubic polynomials, Olson (2001) estimated liquefied shear strengths from ten liquefaction flow case records. In those analyses, the driving force is computed from the weight of the sliding mass and curvature of the travel path of the center of gravity, while the resistance is calculated from the length of the failure surface and the shear strength assigned to it. The acceleration is then computed from the resultant force and moving mass. Velocities and displacements are subsequently determined by integrating acceleration with respect to time. The liquefied shear strength is obtained when the assigned value yields results fitting the observed movement of the center of gravity reasonably well at the moment that the centroid velocity is equal to zero.

Calculation of resistance in kinetic analysis assumes that the shear strength of liquefied sand is fully mobilized along the entire failure surface during liquefaction flow development, i.e., from initiation to deposition. A constant length of the failure surface was adopted to calculate the resistance in Davis's kinetic analysis of the Lower San Fernando Dam flow (Davis et al. 1988). In Olson's recent valuable work (Olson 2001), the length of the failure surface used to calculate the resistance force varies with time:

$$L_t = L_0 + \frac{D_t}{D_f}(L_f - L_0) \tag{6.1}$$

where L_t is the length of the failure surface at time t, L_0 is the length of the initial failure surface, L_f is the length of the final failure surface, D_t is the distance traveled by the centroid at time t, and D_f is the total travel distance of the centroid. The above assumptions are not always valid in reality. For instance, only a small portion of the failure mass is moving both initially and in the final stage of liquefaction flow. The liquefied shear strength along portions at rest during the overall motion is not mobilized.

6.4 Procedures for the Dynamic Analysis of Liquefaction Flow Slides

To estimate the liquefied shear strength from liquefaction flow case histories, the following information is necessary:

(1) Pre-failure cross section of the embankment structures, type of soil, and soil profile;

(2) Pre-failure deformation behavior and driving shear stresses, which are dependent on the gravity of the soils and ground water levels in situ;

(3) Failure surface and post-failure deformation behavior. The failure surface can be obtained through field investigation of post-failure configuration of sliding mass with the combination of the stability analysis of pre-failure slope geometry;

(4) Constitutive behavior of the soil in each zone along the failure surface for the appropriate loading condition; in general, undrained loading is critical for a stain-softening soil susceptible to flow liquefaction.

Dynamic analysis of liquefaction flows using the slice-based model can be accomplished through the following procedures: site characterization, identification of sliding surface, and estimation of averaged liquefied shear strength; these are briefly described below.

Site characterization Geotechnical properties of the liquefied mass involved in flow slides are investigated on the basis of case history records. Runout distance of liquefaction flow is estimated by examining pre- and post-liquefaction geometries.

Identification of sliding surface Post-liquefaction geometry combined with other available information is used to identify the sliding path. Pre-liquefaction geometry and sliding path are input as the initial geometric model and flow path for ensuing dynamic analyses.

Estimation of average liquefied shear strength A series of dynamic analyses is conducted by adjusting shear strengths with the cohesive or frictional model. The best estimation of liquefied shear strength is achieved by matching simulation results with those observed in the field. Because few case history records have information about flow duration and velocity of the liquefied mass, the agreement is based mainly on the observed runout distance and distribution of deposits.

6.5 Case Histories of Liquefaction Flow Slides

Liquefaction case histories provide the primary means to understand the mechanisms of liquefaction and to verify theoretical and laboratory assessments of liquefied shear strength. With respect to liquefaction flow slides, a limited number of well-documented case histories are available because of the rarity of liquefaction flows and the difficulties in obtaining field observations on which analyses can be based. Seed (1987) collected a number of cases that can be used to estimate liquefied shear strength from SPT penetration resistance. Seed (1987) constructed a chart to show the relationship between liquefied shear strength and SPT penetration resistance. The Seed (1987) chart was updated by Seed and Harder (1990) based on results of the back-analyses of 17 case histories of liquefaction flows and lateral spreads. These databases (Seed 1987; Seed and Harder 1990) provide a basis for estimating liquefied shear strength or liquefied strength ratio from CPT or SPT penetration resistance. Since Seed's original work in 1987, many improved relationships for assessing liquefied shear strength have been proposed based on the back-analyses of this limited database of case histories (Seed and Harder 1990; Stark and Mesri 1992; Olson and Stark 2002). Wride et al. (1999) reexamined the databases developed by Seed (1987), Seed and Harder (1990), and others, and pointed out that alternative explanations for some of the case histories could result in higher design strengths for denser soils.

Olson (2001) and Olson and Stark (2002) developed a comprehensive liquefaction analysis procedure using results of the back-calculation of 33 liquefaction flow case histories. These 33 liquefaction case histories involved a wide range of liquefaction failures and a variety of soils including loss clean sands, silty sands, sandy silts, and tailings sands. Despite a number of practical difficulties and uncertainties involved in the analysis, it has been shown that the liquefied shear strength ratio increases with an increase in normalized standard and cone penetration resistances. The proposed relationship between liquefied strength ratio and penetration resistance exhibits considerably less scatter than the relationships previously proposed (Seed 1987; Seed and Harder 1990; Stark and Mesri 1992). The CPT- or SPT-based chart and corresponding equations were updated to provide a more accurate estimation of the liquefied shear strength ratio from CPT or SPT penetration resistances. In general, the improved relationships (Olson 2001; Olson and Stark 2002) predict values of liquefied strength ratio greater than those previously proposed. Among 33 liquefaction flow case histories, ten cases have sufficient information to incorporate the effects of kinetics into stability analysis. The stability analyses considering kinetics of failure are carried out for the ten case histories. Analysis indicated that the effect of kinetics on the back-calculation of liquefied strength ratio is important for embankments or slopes greater than 10 meters in height.

In the study reported here, ten liquefaction case histories with sufficient flow information are analyzed using the slice-based dynamic model. Table 6-1 summarizes the essential information for individual case histories. The type of structure, materials involved, triggering mechanisms, pre- and post-failure geometries, and major references for each case are included in Table 6-1. Descriptions of the case histories and detailed analyses are presented in Appendix B. Case history descriptions are primarily based on the works by Seed (1987), Seed and Harder (1990), Stark and Mesri (1992), Fear (1996), and Olson (2001) as well as original references, and are not repeated here. Uncertainty associated with parameters in Table 6-1 is due to lack of detailed information; the single value assigned to each parameter for each case history is the best estimation from available data.

6.6 Liquefied Shear Strength from the Dynamic Analysis of Liquefaction Flow Slide Case Histories

The back-analyses of case histories of liquefaction flow slides were conducted using the analytical model developed in Chapter 5. Model calibration for dynamic analysis of debris flows has been proposed by Ayotte and Hungr (2000) and Bertolo and Wieczorek (2005). In liquefaction flow slide analysis a similar calibration procedure is followed. A specific constitutive model is first selected to define flow resistance in a liquefaction flow slide. Selection of the constitutive law should take account of the results of laboratory and field testing on the liquefaction flow deposits. Model parameters are then adjusted until the runout characteristics simulated by the dynamic analysis reasonably fit those observed in the field. Agreement between model simulation and field observation is evaluated mainly based on runout distance, material distribution, and velocity profiles. Most liquefaction flow slides lack velocity records, therefore total runout distance and material distribution act as critical indices in model evaluation.

Olson (2001) back-calculated liquefied shear strengths for case histories in Table 6-1 by using stability analysis with failure kinetics incorporated. According to the equations used to calculate the mobilized shear resistance in the kinetic analysis, the liquefied shear strength is given by the constitutive law for a purely cohesive material:

$$\tau = c \tag{6.2}$$

where c is a constant shear strength, the undrained shear strength.

To compare the liquefied shear strengths back-calculated from a dynamic analysis with those from a kinetic analysis (Olson 2001), the cohesive model is used as a constitutive law for flow resistance mobilized in a liquefaction flow slide. Detailed analyses are presented in Appendix B. The calculated liquefied shear strengths from dynamic analyses are summarized in Table 6-2. Liquefied shear strengths calculated by Olson (2001) using kinetic analysis are also included in Table 6-2.

Experiments on granular mass flows indicate that the relationship between normal stress and shear stresses in a granular flow conforms to the Coulomb friction law

(Hungr and Morgenstern 1984a, 1984b; Sassa 1988, 2000; Cagoli and Manga 2004; Iverson and Vallance 2001). The Coulomb friction model can also be applied to describe the constitutive behavior of liquefied soils in a dynamic analysis. Accurate evaluation of pore pressure in granular flows is very difficult, if not impossible. For this reason, total stress instead of effective stress is used in the dynamic analysis to avoid the evaluation of pore pressure and stress history effects. The bulk friction angle is used to calculate the shear resistance in a liquefaction flow slide. The coefficient of bulk friction is defined as the ratio of mobilized shear resistance to total normal stress (Sassa 1988, 2000) and the bulk friction angle is related to the internal friction angle by including a pore pressure ratio (Hungr and Evans 1996):

$$\tan\phi_a = (1 - r_u)\tan\phi \tag{6.3}$$

where ϕ_a is the bulk friction angle, ϕ is the internal friction angle of granular material, and r_u is the pore pressure ratio, defined as the ratio of pore pressure to total normal stress in soil mechanics.

The bulk friction angles mobilized in liquefaction flow slides are back-calculated from dynamic analysis with the Coulomb friction model as a constitutive law. For each case, the bulk friction angle back-calculated using the analytical model based on energy conservation is presented in Table 6-3. Detailed calculations are described in Appendix B.

6.7 Liquefied Shear Strength from Kinetic Analysis Using the Sliding Block Model

Kinetic analyses of liquefaction flow slide case histories (Davis et al. 1988; Olson 2001) and sliding block analyses of mobile landslides (Fell et al. 2000; Hungr et al. 2005) are based on the same principle: the motion of a sliding mass is approximated as the movement of a rigid block using Newton's second law of motion. The movement of the block represents the motion of the centroid of the sliding mass. Forces acting on the block consist of the driving force of gravity and the resistance along the sliding surface.

Calculation of the basal resistance involves assumptions of the constitutive behavior of displaced materials. A cohesive model has been applied to the analysis of liquefaction flows by Davis (1988) and Olson (2001). In landslide mobility analysis, friction and Voellmy models have often been used as constitutive laws to calculate basal resistance (Scheidegger 1973; Fell et al. 2000; Hungr et al. 2005). Back-analysis of liquefaction flow slides or landslides using sliding-block analysis requires that the travel path of the centroid of the sliding mass be specified. Because the accurate description of centroid positions is not possible in most liquefaction flows or landslides, case history back-analysis using the sliding block model often entails a simplified mathematical function to describe the travel path of the center of gravity. Olson (2001) back-calculated liquefied shear strengths for ten liquefaction flow slide cases by using cubic polynomials to describe the centroid travel path. In the analyses, the basal resistance is determined using the cohesive model as a constitutive law and the driving force is computed from the weight of the sliding mass and the curvature of the prescribed travel path of the centroid.

The friction model can be used as a constitutive law for liquefaction flow slide analysis (Hungr and Morgenstern 1984a, 1984b; Sassa 1988, 2000; Iverson and Vallance 2001). The acceleration of the block is calculated from the gravity driving force and the shear resistance along the base:

$$a = \frac{W \sin\theta - W \cos\theta \tan\phi}{m} \tag{6.4}$$

where W is the weight of the failure mass, θ is the slope angle of the travel path of the centroid of the failure mass, ϕ is the friction angle, and m is the mass of displaced materials. Velocities and displacements are subsequently determined by integrating acceleration with respect to time.

In this study, the liquefaction flow case histories in Table 6-1 are back-analyzed using the sliding block model with the Coulomb equation as a constitutive law. Motion of the centroid in a liquefaction flow is described by a third order polynomial equation, similar to that used by Olson (2001). The back-calculated friction angle is obtained when the assigned value yields results fitting the observed movement of the center of gravity reasonably well at the moment when the centroid velocity is equal to zero. For illustrative purposes, Figure 6-2 shows a typical travel path of a centroid of displaced materials. Acceleration, velocity, and displacement of the centroid in a kinetic analysis using the sliding block model are presented in Figure 6-3, Figure 6-4, and Figure 6-5, respectively. Together with the dynamic analysis, Appendix B presents the calculation for each case in detail. Table 6-4 summarizes the friction angles for liquefaction flow case histories back-calculated using the sliding block model. The bulk friction from dynamic analysis with internal energy dissipation is also included in Table 6-3.

6.8 Discussion of Results

Case history studies suggest that dynamic analysis has several advantages over kinetic analysis for the back-calculation of liquefied shear strength. These advantages include:

(1) The initial shape of the liquefaction flow slide is accounted for in dynamic analysis in an accurate manner by dividing the sliding mass into a number of slices.

(2) Dynamic analysis allows the selection of a variety of material constitutive models to determine the basal resistance. Different rheological properties can be assigned to the moving mass at different positions of the sliding path; this facilitates analysis of complex liquefaction flow slide cases such as those with dramatic soil changes along the sliding path.

(3) Resistance of liquefaction flow can be calculated with various constitutive models; this makes it possible to study liquefaction flow case histories from a variety of perspectives.

(4) Deformation of the sliding mass can be simulated because of slice interactions which cause momentum exchange between slices and change in the shape of slices.

(5) The final shape of the liquefaction flow is simulated in dynamic analysis. Calibration of a constitutive model and input parameters can be carried out by comparison of distribution of debris in the field and simulated post-liquefaction geometry.

(6) Detailed movement information throughout the liquefaction flow slide is available from dynamic analysis.

(7) If velocity estimations are available, velocity profiles provide additional information which can be used to verify the validity and reliability of dynamic analysis.

6.8.1 Effects of a Constitutive Model

The effects of constitutive models on dynamic analysis can be evaluated by comparing computational results with field observations in terms of runout distance, deposit distribution, and velocity profiles. For each dynamic analysis, the runout distance predicted has to be matched reasonably with the field observation so that the liquefied shear strength can be determined. Comparison of mass spreading and velocity become the most important criteria in the evaluation of constitutive model behavior. An analysis of the flow slide of the North Dike of the Wachusett Dam is given here for illustrative purposes. Figure 6-6 shows the pre- and post-liquefaction geometries used for the back-analysis of the North Dike flow slide. The geometries in Figure 6-6 are based on comprehensive case studies conducted by a number of investigators (Olson et al 2000; Olson 2001). Figure 6-7 and Figure 6-8 are post-liquefaction geometries produced by dynamic analysis with the cohesive and frictional models, respectively.

Comparison of post-liquefaction geometries in Figure 6-7 and Figure 6-8 reveals that the cohesive model yields a final mass distribution with a blunt front and the friction model generally produces a tapered post-liquefaction geometry. With constant shear strength, the cohesive model tends to predict deposition even on steep slopes close to the source area and leaves a thin mantle behind the main deposit area, while the friction model does not have such a tendency. Hungr and Evans (1996) back-analyzed 23 rock avalanche case histories using the Bingham model, the frictional model, and the Voellmy model. The results demonstrate that the frictional model produces thin deposition in the distal part and the Bingham model with high yield strength tends to exaggerate the longitudinal spreading of debris. Dynamic analysis using the cohesive model with internal energy dissipation appears to perform similar to that using DAN with the Bingham model. Although both the cohesive model and the frictional model can simulate runout distance reasonably well, the frictional model predicts material deposition more realistically.

6.8.2 Comparison of Liquefied Shear Strengths Estimated Using Different Approaches

Back-calculated shear strengths for the cohesive model and the frictional model are summarized in Table 6-2 and Table 6-3, respectively. Comparison with the results based on the stability and kinetic analyses provides a practical way to evaluate the reliability of the values of liquefied shear strengths estimated from the dynamic analyses. As one of most studied and best-defined liquefaction flow slides, the Lower San Fernando Dam flow slide is used below to demonstrate this procedure.

The limit equilibrium analysis of the initial failure surface of the Lower San Fernando Dam indicated that average driving shear stress values in the lower zone of the hydraulic fill shell is about 46 kPa (Castro et al. 1985), within the range of 40.7 to 50.3 kPa (Castro et al. 1992). Comprehensive investigation of the liquefaction failure of the Lower San Fernando Dam by Seeds et al. (1989) showed the driving shear stress in the hydraulic fill was about 38.3 to 43.1 kPa. The very large displacement of the failure materials in the Lower Sand Fernando Dam indicates that the liquefied shear strength mobilized in the flow was considerably less than the lower bounds of the above estimates for the driving stress based on the limit equilibrium analysis: if the liquefied shear strength is larger than the pre-failure static driving shear stress, liquefaction flow slide cannot be initiated (Poulos et al. 1985; Poulos 1988; Olson 2004).

The liquefied shear strength of 25 kPa back-calculated from the analytical model based on energy conservation appears to be consistent with the driving shear stress determined from stability analysis of initial failure geometry. For the liquefaction flow slide in the Lower San Fernando Dam, comparison with the liquefied shear strength obtained using other methods indicates that liquefied shear strength falls toward the upper end of the estimates based on the stability analysis of the post-failure slope configuration, for instance, from 14.4 to 23.9 kPa by Seed et al. (1989) and from 7.2 to 12 kPa by Castro et al. (1992), and toward the lower end of the estimates from laboratory testing combined with the steady state concept, for instance, from 29.2 to 38.8 kPa by Castro et al. (1992) and 38.3 kPa by Seed et al.(1989). In general, the liquefied shear strength based on dynamic analysis with consideration of internal energy dissipation shows reasonable agreement with values obtained from kinetic analyses with post-failure motion included; for instance, 18.7 kPa with a range of 15.8 to 21.8 kPa by Olson (2001) and 24.4 kPa by Davis et al. (1988).

6.8.3 Coefficient of Bulk Friction in Liquefaction Flows

The resistance in a liquefaction flow can be evaluated using the concept of bulk friction (Sassa 2000). Bulk friction represents the shear resistance mobilized during the motion of dense granular flows such as fast moving landslides, liquefaction flow slides. The coefficient of bulk friction is the tangent of the bulk friction angle which can be back-calculated using the dynamic analysis of case histories. Liquefaction flow is essentially the frictional behavior of contractive soils due to an increase of pore water pressure during rapid loading (Poulos 1981; Ishihara 1993; Olson 2001), and the liquefied shear strength of loose cohesionless soils at steady state is often assumed to be proportional to the major principal effective stress after consolidation. The liquefied strength ratio which is defined as the liquefied shear strength normalized by the pre-failure vertical effective stress is commonly used to estimate liquefied shear strength from field testing. The coefficient of bulk friction and the liquefied strength ratio appear to play equivalent roles in relation to the estimation of the liquefied shear strength. The coefficient of bulk friction and the liquefied strength ratio for ten liquefaction flow slide case histories back-calculated using dynamic analysis and kinetic analysis (Olson 2001; Olson and Stark 2002) is presented in Table 6.5. It is evident that the liquefied shear strength calculated using dynamic analysis with internal energy dissipation is considerably greater than that obtained from kinetic analysis, although the two ratios are not related fundamentally.

Kinetic analysis of liquefaction flow case histories using the sliding block model has been conducted in this study. The Coulomb equation is used to determine the basal resistance in the kinetic analysis. The travel path of the center of gravity in a liquefaction flow is approximated by a third polynomial, following the procedure adopted by Olson (2001). Values of bulk friction angles back-calculated from the dynamic and kinetic analyses of liquefaction flows are presented in Table 6-4. The table shows that values of liquefied shear strength back-calculated from case histories generally agree whether arrived at by kinetic analysis or by dynamic analysis with internal energy dissipation. Laboratory experiments and field observations indicate that liquefied soil behaves like a Coulomb-type material. In that respect, the bulk friction angle back-calculated from the case history study using dynamic analysis with internal energy dissipation provides a useful strength parameter for practical liquefaction evaluation.

6.8.4 Sources of Uncertainty in Dynamic Analysis

For a given liquefaction flow slide case history, the following sources of uncertainty are involved in the calculation of liquefied shear strength using dynamic analysis: (1) the mass of liquefied soil; (2) the location of the sliding surface; (3) the shear strength of nonliquefied soils; (4) field observations of runout distance and mass distribution; (5) computation of internal energy dissipation.

The mass of liquefied soil and its distribution are of primary importance in estimating the liquefied shear strength. The runout distance estimated from post-liquefaction geometry has to be matched in each dynamic analysis to obtain liquefied shear strength. The mass distribution is also used to evaluate constitutive model performance by comparing simulation results with field observations. Location of the sliding surface used in the dynamic analysis is mainly based on the slope stability analysis and analysis of post-liquefaction geometry (Olson 2001). To minimize the uncertainty involved in back-calculated shear strength, only well-documented liquefaction case histories were selected for this study.

The concept of equivalent fluid (Hungr 1995) is used in dynamic analysis. A value for liquefied shear strength is obtained based on evaluation of the bulk behavior of liquefied soils; the heterogeneity of the soils is not taken into account in the analysis. Computation of internal energy dissipation is based on the assumption that pure shear deformation occurs during all stages of a liquefaction flow and a liquefied soil behaves like a Coulomb-type material. The Coulomb equation is used in the calculation of internal energy dissipation. The equations used for calculating the internal energy dissipation are only approximations for the variations in internal energy dissipation during the development of liquefaction flow. However, most liquefaction flow slides back-analyzed in this study experienced large displacements; this tends to reduce the heterogeneity of soils after liquefaction has been achieved and to bring the liquefied soils to a steady-state condition (Castro 1969; Poulos 1981; Morgenstern 2001). Liquefied shear strength back-calculated using dynamic analysis thus provides a reasonable estimation of the undrained resistance of soils which have experienced large deformations and reached a steady state.

6.9 Conclusions

Ten liquefaction flow case histories have been reinvestigated using the dynamic analysis approach. The liquefied shear strengths were estimated by obtaining reasonable agreement of runout distance and material distribution between the model and that observed in the field. The slice interaction and large deformation simulated by dynamic analysis make it possible to reconstruct the development of liquefaction flows. Details of the runout distance and velocity profiles of the liquefied materials calculated from dynamic simulation provide practitioners with important information for their mitigative designs.

The constitutive law for shear resistance has a significant influence on material distribution in a dynamic analysis. Compared with the cohesive model, the friction model provides a better fit between simulation and field observation in terms of deposit distribution. Bulk friction angles back-calculated from dynamic analyses of liquefaction flow cases can be used to evaluate the mobility of soil structures after liquefaction is triggered.

The post-failure deformation behavior of liquefaction flow slides is simulated using the analytical model incorporating internal energy dissipation. Liquefied shear strengths in terms of undrained strength and bulk friction angle are back-calculated for ten flow slide cases. Comparative studies of results back-analyzed using different methods provide evidence that representation of liquefied shear strength can be obtained through dynamic analysis within the framework of the Coulomb friction model.

Table 6-1 Summary of liquefaction flow slide case histories

Case History		Type of Structure	Materials	Trigger	Pre-failure		Post-failure		References
No.	**Name**				**Height^a (m)**	**Angle (°)**	**Runout^b (m)**	**Angle^c (°)**	
1	Calaveras	Hydraulic fill dam	Silty sands to sandy silts	Construction	57.6	17.3	205.8	6.0	Hazen 1920; Olson 2001
2	Fort Peck	Hydraulic fill dam	Fine to medium sands	Construction	57.1	12.3	508.4	3.5	Middelbrooks 1942; Olson 2001
3	Lower San Fernando	Hydraulic fill dam	Silty sands to sandy silts	Earthquake	33.7	21.7	45.0	13.4	Seed et al. 1975
4	Wachusett	Zoned earth fill dam	Fine sand	Reservoir filling	26.8	23.7	97.5	8.3	Olson et al. 2000
5	Hachiro-Gata	Road embankment	Fine sand	Earthquake	3.7	19.2	8.6	9.7	Olson 2001
6	Koda Numa	Road embankment	Silty sand	Earthquake	2.5	29.9	19.4	5.7	Olson 2001; Fear 1996
7	Lake Ackemam	Road embankment	Fine to medium sand	Vibration	7.8	21.1	10.7	14.0	Olson 2001
8	Route 272	Road embankment	Silty sand	Earthquake	7.7	34.1	25.6	8.2	Olson 2001
9	Shibecha-Cho	Road embankment	Silty sand	Earthquake	9.3	30.8	23.5	11.7	Olson 2001
10	Uetsu-Line	Railway embankment	Fine to medium sand	Earthquake	8.3	24.2	96.9	4.1	Olson 2001; Fear 1996

[a] Pre-failure slope height is the vertical distance from the crest to the toe of the initial slope.

[b] Runout is the horizontal distance from the toe of the original slope to the toe of the displaced mass.

[c] Travel angle is the angle between a horizontal line and the line connecting the crest of the source area with the toe of the displaced mass.

Table 6-2 Liquefaction flow slide analysis with the cohesive model

Case History		**Dynamic Analysis with Internal Energy Dissipation**			**Kinetic Analysis (Olson 2001)**		
No.	**Name**	**Liquefied Shear Strength (kPa)**	**v_{max} (m/s)**	**Runout (m)**	**Liquefied Shear Strength (kPa)**		
					Best Estimate	**Lower Bound**	**Upper Bound**
1	Calaveras Dam	32.6	25.6	202.6	34.5	28.7	37.8
2	Fort Peck Dam	24.5	25.1	509.9	27.3	16.8	34.0
3	Lower San Fernando Dam	25.0	23.7	46.8	18.7	15.8	21.8
4	Wachusett Dam	16.2	15.5	102.8	16.0	10.4	19.1
5	Hachiro-Gata Embankment	3.0	11.3	8.0	2.0	1.0	3.2
6	Koda Numa Embankment	0.6	5.4	19.7	1.2	—	—
7	Lake Ackerman Embankment	5.5	8.5	10.4	3.9	3.4	4.7
8	Route 272 Embankment	5.6	7.1	25.8	4.8	3.0	5.7
9	Shibecha-Cho Embankment	8.0	8.1	22.1	5.6	3.9	8.3
10	Uetsu-Line Embankment	1.8	15.7	98.3	1.7	—	—

Note: v_{max}, maximum velocity; —, data not available.

Table 6-3 Liquefaction flow slide analysis with the frictional model

Case History		**Dynamic Analysis with Internal Energy Dissipation**		
No.	**Name**	**ϕ (°)**	**v_{max} (m/s)**	**Runout (m)**
1	Calaveras Dam	8.1	9.9	204.2
2	Fort Peck Dam	5.0	17.1	509.2
3	Lower San Fernando Dam	11.0	8.3	45.3
4	Wachusett Dam	9.5	10.8	100.8
5	Hachiro-Gata Embankment	10.6	2.1	9.2
6	Koda Numa Embankment	7.4	4.4	18.6
7	Lake Ackerman Embankment	11.5	2.1	11.4
8	Route 272 Embankment	11.0	6.3	25.1
9	Shibecha-Cho Embankment	12.0	4.9	23.1
10	Uetsu-Line Embankment	6.0	9.4	95.9

Table 6-4 Kinetic analysis of liquefaction flow slides with the sliding block model

Case History		**Bulk friction Angle ϕ (°)**	
No.	**Name**	**Kinetic Analysis with the Sliding Block Model**	**Dynamic Analysis with Internal Energy Dissipation**
1	Calaveras Dam	8.0	8.1
2	Fort Peck Dam	4.0	5.0
3	Lower San Fernando Dam	11.5	11.0
4	Wachusett Dam	10.4	9.5
5	Hachiro-Gata Embankment	9.5	10.6
6	Koda Numa Embankment	5.0	7.4
7	Lake Ackerman Embankment	8.3	11.5
8	Route 272 Embankment	10.5	11.0
9	Shibecha-Cho Embankment	15.8	12.0
10	Uetsu-Line Embankment	3.3	6.0

Table 6-5 Coefficient of bulk friction and liquefied shear strength ratio

Case history		**Dynamic Analysis**		**Kinetic Analysis (Olson 2001)**	
No.	**Name**	$\phi(^\circ)$	$\tan\phi$	s_u	$\frac{s_u}{\sigma'_{v0}}$
1	Calaveras Dam	8.1	0.142	34.5	0.112
2	Fort Peck Dam	5.0	0.087	27.3	0.078
3	Lower San Fernando Dam	11.0	0.194	18.7	0.112
4	Wachusett Dam	9.5	0.167	16.0	0.106
5	Hachiro-Gata Embankment	10.6	0.187	2.0	0.062
6	Koda Numa Embankment	7.4	0.130	1.2	0.052
7	Lake Ackerman Embankment	11.5	0.203	3.9	0.076
8	Route 272 Embankment	11.0	0.194	4.8	0.097
9	Shibecha-Cho Embankment	12.0	0.213	5.6	0.086
10	Uetsu-Line Embankment	6.0	0.105	1.7	0.027

$\phi(^\circ)$, bulk friction angle; $\tan\phi$, coefficient of bulk friction; s_u, liquefied shear strength from kinetic analysis; $\frac{s_u}{\sigma'_{v0}}$, liquefied strength ratio, where σ'_{v0} is the weighted average pre-failure vertical effective stress.

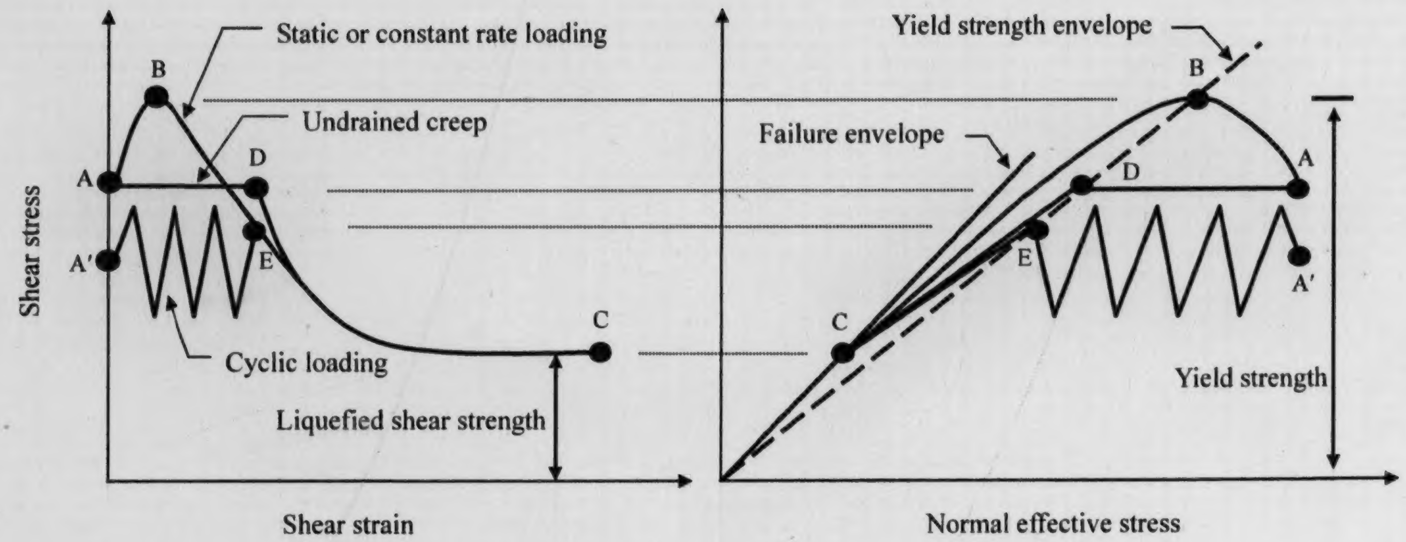
Static or constant rate loading
Undrained creep
Cyclic loading
Liquefied shear strength
Shear stress
Shear strain
A
A'
B
C
D
E
Yield strength envelope
Failure envelope
Yield strength
Normal effective stress
B
A
D
E
A'
C

Figure 6-1 Typical undrained response of loose sands in monotonic loading, creep, and cyclic loading

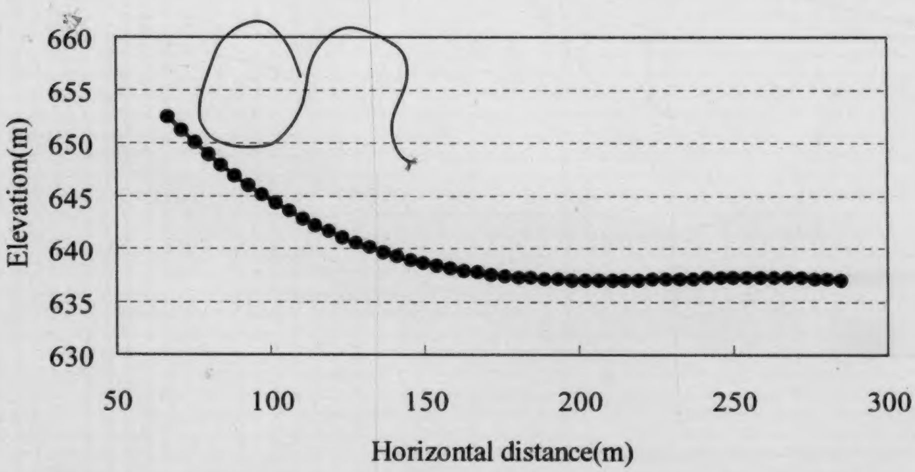

Figure 6-2 Travel path of the center of gravity in the sliding block model

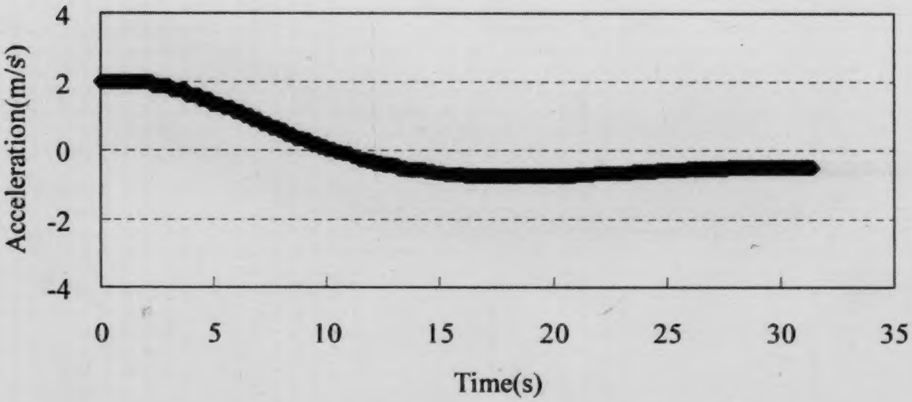

Figure 6-3 Acceleration versus time in analysis with the sliding block model

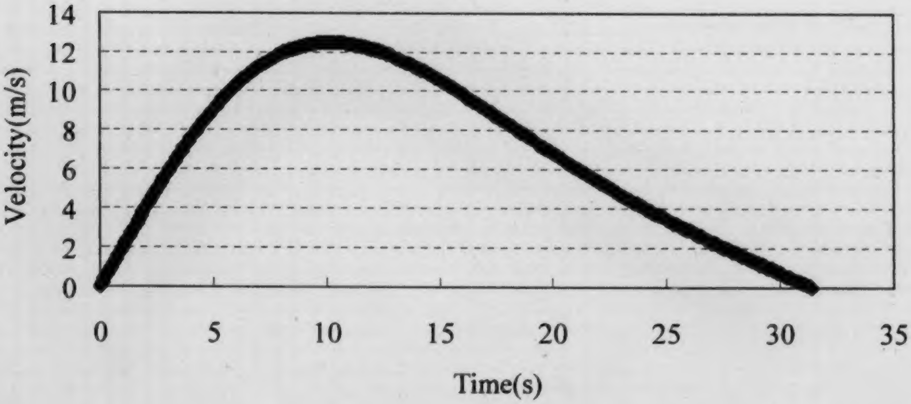

Figure 6-4 Velocity versus time in analysis with the sliding block model

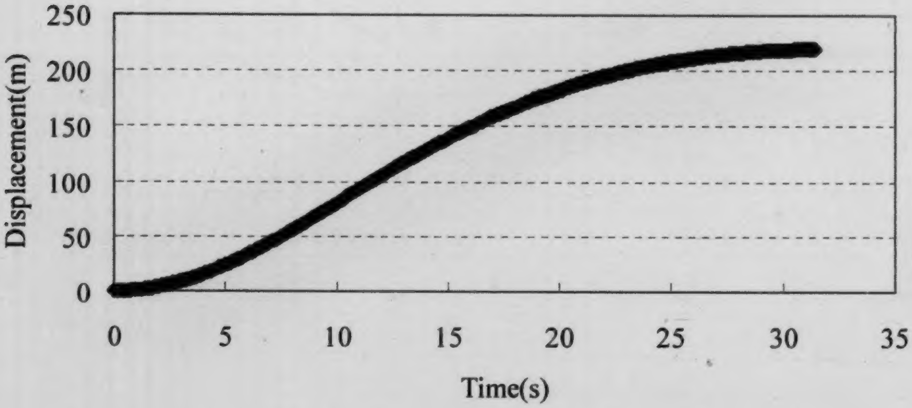

Figure 6-5 Displacement versus time in analysis with the sliding block model

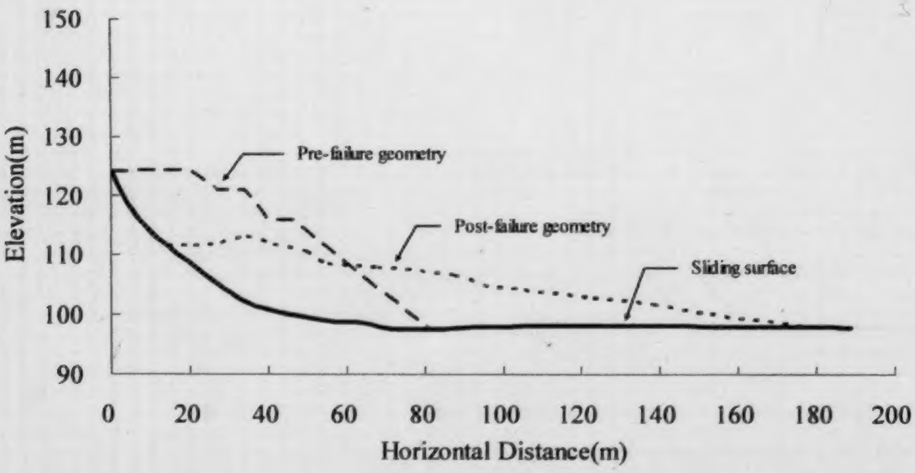

Figure 6-6 Geometries of the North Dike of the Wachusett Dam based on field observation

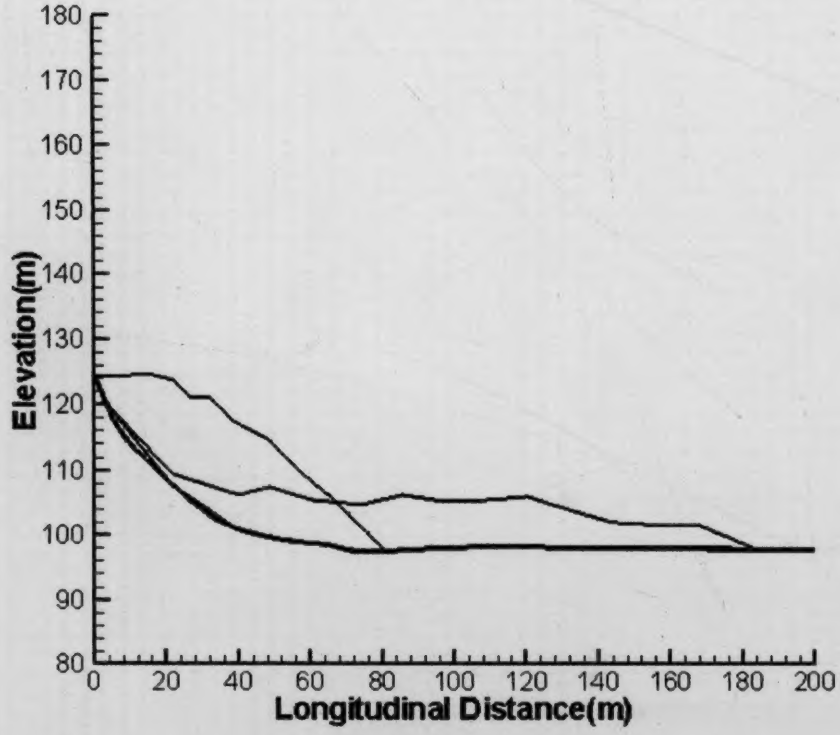

Figure 6-7 Geometries of the North Dike flow slide based on dynamic analysis with the cohesive model

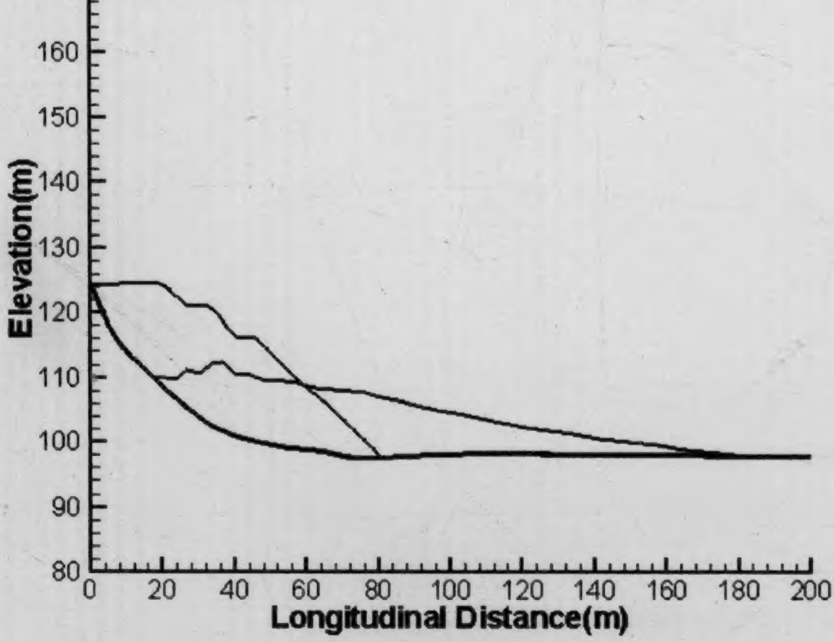

Figure 6-8 Geometries of the North Dike flow slide based on dynamic analysis with the friction model

Chapter 7

Dynamic Analysis of Debris Flows on Natural Slopes

7.1 Introduction

Debris flows on natural slopes are often mobilized from slope failures. Compared with fluid-like deformation in a debris flow, the deformation of a landslide is more rigid and often localized along a slip surface or a persistent shear zone. The transformation from landslide to debris flow involves a decrease in the strength of the sediment mass and a subsequent conversion of gravitational potential energy to kinetic energy. The increase of kinetic energy changes the style of motion from sliding along a localized failure surface to a more widespread deformation recognized as flow (Iverson et al. 1997).

Water contributes to the instability of slopes and the mobilization of debris flows from landslides. Field observations, laboratory experiments, and theoretical analyses suggest that most transformations from landslides to debris flow are related to the increase of pore-water pressures (Iverson et al. 1997; Savage and Baum 2005; Sassa 2000; Sassa and Wang 2005). The increase of pore-water pressure in a sediment mass can be the result of precipitation such as rainfall, either intense or long lasting, thaw of snow or ice, or groundwater inflow from adjacent areas. The changes of pore-pressure can also be associated with the mechanical response of loose sediments to the undrained loading, such as the collapse of contractive soils during the process of liquefaction. Iverson et al. (1997) discussed the mechanics of debris flow mobilization and indicated that landslides can transform into debris flows by three processes: widespread Coulomb failure within a soil mass, partial or complete soil liquefaction due to high pore-fluid pressure, and conversion of landslide translational energy to internal deformation energy. In most scenarios these processes operate simultaneously and contribute to the transformation of landslides to debris flows.

Debris flow can also originate from surface runoff if the sediment in the flow accumulates rapidly within a short period of time. The accumulation of sediment in a flow increases the effects of solid phase on the motion and tends to transfer the water flow into a debris flow. According to Iverson (1997) and Iverson et al. (1997), both solid and fluid forces strongly influence the motion in a debris flow, which distinguishes the debris flow from the avalanche where solid grain forces dominate the motion and from a sediment-laden water flow where viscous fluid forces dominate the motion. The sediment concentration plays a key role in differentiating debris flow from other related phenomena. The boundary of sediment concentration between sediment-laden water flows and debris flows is about 50 to 60 percent by volume (O'Brien 2003; Pierson 2005). Field observations and experiments demonstrate that bed erosion provides a major source of sediment during the development of debris flow from surface runoff (Takahashi et al. 1992). Flume tests were conducted to investigate the triggering mechanisms of debris flows developed from surface runoff (Takahashi 1978, 1980). The critical slope for the occurrence of a debris flow is proposed based on experimental results and theoretical analyses. The concept of critical slope is only applicable to debris flows originating from surface runoff. Because of high sediment concentration in debris flows, it is apparent that debris flows on natural slopes predominantly occur through the mobilization of landslides.

Debris flows on natural slopes have considerable variation in both material composition and volume. For instance, debris flows mobilized from landslides, through entrainment of water or water-rich sediments, involve not only the displaced soil mass in the source area but also the deposits accumulated along the path of travel. Composition and constitutive behavior may change dramatically with position and time of the individual flow. This chapter focuses on the dynamic analysis of debris flows on natural slopes. Only relatively simple debris flow cases are selected in this study so that the variations in material composition and mass within an individual flow are negligible. As a consequence, a specific constitutive model can be used to estimate material behavior during all stages of flow development.

7.2 Liquefaction and Debris Flow-Triggering Mechanism

Debris flow mobilization from slope failures is characterized by liquefaction-type failure. Liquefaction is a process by which an increase of pore water pressure in a loose, saturated soil results in a dramatic loss of shear strength. Liquefaction is often followed by a catastrophic failure and rapid deformation of the failure mass; in that respect debris flow is similar to liquefaction flow slides that have occurred in hydraulic fill dams (Seed et al. 1975a; Castro et al. 1989; Seed et al. 1989), flow slides in coal stockpiles and coal mine waste dumps (Eckersley 1985; Dawson et al. 1998; Hungr et al. 2002), and flow slides in subaqueous slopes (Terzaghi 1956; Morgenstern 1967; Sladen 1985b). Liquefaction can be triggered by static loading such as rainfall or cyclic loading such as earthquake. Static liquefaction often results in the initiation of debris flow on natural slopes. Flow failure associated with static liquefaction has been studied for many years (Casagrande 1936; Castro 1969; Poulos 1981; Sladen 1985a, 1985b).

7.2.1 Steady-State Line, Collapse Surface and Debris Flow Initiation

In a classic paper by Casagrande (1936), the significance of volume change during shear deformation in relation to the shear strength of soils was investigated. Based on his studies on shear resistance of sands, Casagrande concluded that during shear deformation, a cohesionless material in a loose state decreases its volume and in a dense state increases its volume. The cohesionless material tends to reach a critical void ratio in which it deforms continuously without volume change. Castro (1969) conducted a series of drained and undrained triaxial tests on sands and demonstrated that liquefaction flow failure is characterized by a constant void ratio and a constant shear resistance. Poulos (1981) presented the concept of the steady state of deformation which plays an important role in the analysis of liquefaction and related phenomena. The steady state of deformation is defined as the state in which a granular material can undergo flow deformation at constant volume, constant normal effective stress, constant shear stress, and constant velocity. The undrained steady-state shear strength is the minimum strength a saturated contractive soil can possess during undrained shear deformation and its magnitude is dependent only on the in situ void ratio of the soil. Studies on the behavior of liquefied sands by Been et al. (1991) showed that steady state and critical state are equivalent from a practical perspective and that a constant velocity in the definition of the steady-state deformation is not necessary. This conclusion agrees with findings from laboratory experiments on rapid granular flows (Hungr and Morgenstern 1984a, 1984b), which demonstrated that the constitutive behavior of a granular material is governed by the Coulomb law and independent of strain rate.

The steady-state line describes the relationship between the effective stress and the void ratio at steady state. Based on the steady-state concept, a laboratory-based procedure for estimating liquefied shear strength was proposed by Poulos et al. (1985). This method has not found much practical application because the steady-state shear strength determined from laboratory experiments shows high sensitivity to changes in the void ratio of soils. Slight error in the determination of the in situ void ratio can result in a large discrepancy between the liquefied shear strength estimated and the shear resistance mobilized in situ (Kramer and Seed 1988; Olson 2001). Recent studies on liquefaction indicate that the steady-state line based on laboratory tests on reconstituted samples can be influenced by loading system characteristics, shear mode, level confining stress, and sample preparation procedure (Yshimine et al. 1999; Vaid and Sivathayalan 2000).

Investigations on the triggering mechanism of static liquefaction flow failure have been undertaken by a number of researchers (Salden 1985a; De Matos 1988; Kramer and Seed 1988; Sasitharan 1994). Isotropically consolidated undrained triaxial tests on loose sands were conducted by Sladen et al. (1985a) to study the Nerlerk berm liquefaction flow slides. The undrained effective stress paths show that peak strengths tested for sand samples at the same void ratio but in various initial stress states fall on a straight line in the $p' - q$ (mean effective stress – deviator stress) space and that these stress paths all converge on the same steady state point, as illustrated in Figure 7-1. The line connecting the peak points of the stress paths with the steady-state point is defined as the collapse surface (Sladen et al. 1985a). The concept of the collapse surface was further examined by Alarcom-Guzman et al. (1988) and Sasitharan et al. (1993, 1994). They demonstrated that the post-peak portion of a constant void ratio stress path constitutes a state boundary that governs the initiation of liquefaction and the occurrence of flow failure of loose granular materials under undrained loading. Sasitharan (1994) showed that the post-peak strain-softening portion of undrained stress paths of sand samples at the same void ratio can be approximated by a straight line for a very loose sand. Strain softening and liquefaction failure under drained and undrained loading occur when the stress path tries to cross the state boundary surface of the sand. Constant deviator stress-drained tests were also conducted by Sasitharan (1994) to simulate the initiation of flow failure in a slope due to pore water pressure increase.

The concepts of steady state (Castro 1969; Poulos 1981) and collapse surface (Sladen 1985a; Sasitharan et al. 1993, 1994) provide a basis for understanding and predicting the undrained behavior of loose granular materials. The concepts that collapse surface provides a triggering criterion of liquefaction in loose materials, and that the steady state provide a basis for evaluating undrained resistance mobilized in a loose granular material flow (Morgenstern 2001), have been applied to explain the Nerlerk berm flow slides (Sladen et al. 1985b), the flow slides in the Fraser River Delta (Chillarige et al. 1997), and the liquefaction flowslides in coal mine waste dumps (Dawson et al. 1998).

Despite apparent differences in source material and slope geometry there are similarities in failure mechanism and post-failure deformation behavior between liquefaction flows and natural debris flows (Morgenstern 1978; Hungr et al. 2002; Fell et al. 2000; Pastor et al. 2002). Liquefaction flow slides and debris flows also have much in common during the process of initiation: a sudden loss of shear resistance associated with the undrained failure. The concepts of steady state and the collapse surface are thus applicable to the analysis of debris flows, particularly debris flows mobilized from landslides. The stress states and stress path for a rainfall-induced debris flow on a natural slope are presented in Figure 7-2 and Figure 7-3. It is evident that the field stress path is very different from the stress path in a traditional triaxial compression test in soil mechanics such as those explored by Bishop and Henkel (1962). The field stress path may actually deviate from the horizontal path because of an increase of soil weight and seepage force due to changes in the ground water condition. Field investigations indicated these effects are not significant and the horizontal field stress path provides a reasonably accurate generation of the field stress path (Anderson and Sitar 1995). The stress path in Figure 7-3 describes changes in stresses of a soil element on a slope during an intense rainfall.

As indicated by Figure 7-3, normal effective stress is reduced with an increase in pore water pressure, while deviator stress remains constant. Pore pressure causes the stress state to move to the collapse surface. When the stress state lies on or approaches the collapse surface, a slight disturbance can cause debris material strain-softening accompanied by rapid generation of excess pore pressure. The stress state will move along the state boundary surface and arrive at the steady state. If the driving shear stress in the slope is much greater than the steady state shear resistance, the debris mass can be transformed from a solid state into a fluid state and, in consequence, a debris flow has been mobilized.

Loose material often has high permeability and the stress state may be drained up to the failure point. Drained tests on very loose sands have shown that as soon as the collapse surface is reached, the pore water pressure measured in the tests increases suddenly (too rapidly for drainage to take place) and the sand sample liquefies; reduction of the rate of loading cannot avoid this phenomenon (Lindengerg and Koning 1981). Therefore, it is possible that when subjected to very slow, drained increases in shear stress, loose debris material contracts and water is expelled from the voids. When a point of inherent instability is reached, even the slightest increment of stress or strain results in such rapid generation of excess pore pressures in comparison to the drainage capacity of the debris materials, that shear strength drops rapidly to the steady state value along the state boundary. The applied stress can then no longer be sustained and rapid acceleration of a failure mass occurs. This triggering mechanism has been used to explore the initiation of laboratory debris flows (Eckersley 1990; Spence and Guymer 1997; Wang and Sassa 2001; Moriwaki et al. 2004; Ochiai et al. 2004) and debris flows on natural slopes (Kramer 1988; Anderson and Sitar 1995).

7.2.2 Natural Comminution and Sliding-Surface Liquefaction

It has been recognized that large volume rock avalanches exhibit excessive mobility and the equivalent friction coefficient (tangent of the travel angle) of rock avalanches apparently decreases as the volume of displaced materials increases (Scheidegger 1973; Hsu 1975; Davies 1982; Corominas 1996; Legros 2002). Davies and McSaveney (1999) conducted a series of experiments to explore the long runout of large rock avalanches. They found that rock avalanches with volumes less than 10^5 m^3 and those with volumes greater than 10^7 m^3 behave differently in terms of runout characteristics. The unusually long runout distance of a large rock avalanche is associated with the volume of displaced materials, and rock fragmentation has a significant effect on the mobility of rock avalanches. A fragmentation-spreading model was proposed by Davies et al. (1999) to analyze long runout rock avalanches (Davies and McSaveney 2002). The natural comminution in relation to the mobility of soil and rock avalanches was investigated by De Matos (1988). His study indicated that the comminution following a slope failure is influenced by a number of factors, including applied energy (height of fall), stress level (thickness of debris), duration of the avalanche, characteristics of the slope, and the properties of displaced materials. The percentage of fines within a rock avalanche has a tendency to increase with thickness and depth of displaced materials. For a large volume rock avalanche, potential energy and stress states are conducive to the occurrence of rock fragmentation and natural comminution. The increase of fines as a result of particle breakage and comminution leads to an increased susceptibility of displaced materials to liquefaction under undrained loading produced by the self weight of the debris. High pore pressure can build up and may account for a significant decrease in bulk frictional resistance and high mobility of the avalanche. This conclusion has been confirmed by field observations of many avalanche deposits (Davies et al. 1999). Locat et al. (2006) estimated the fragmentation energy for nine rock avalanches from the European Alps and Canadian Rocky Mountains and concluded that the fragmentation energy is approximately 20 percent of the potential energy for the cases studied.

In relation to debris flow initiation, grain crushing and fragmentation during shear deformation causes liquefaction characterized by a loss of strength resulting from the generation of excess pore water pressures due to the increase of fine grained materials. Sliding-surface liquefaction has been proposed to describe this type of phenomena (Sassa 1996, 2000; Sassa and Wang 2005). De Matos (1988) conducted isotropically-consolidated undrained triaxial tests to investigate the influence of grain size distribution on the steady state of granular materials. The test results for soils with the same type of grains, as shown in Figure 7-4, indicated that soils with different grain size distributions have different steady-state lines and the susceptibility of soils to liquefaction increases with the coefficient of uniformity. The work by De Matos (1988) provides a theoretical basis for the concept of sliding-surface liquefaction (Sassa 1996, 2000) and has been used to explain the liquefaction of granular soils with medium and high densities (Sassa 1996).

As illustrated in Figure 7-5, if a soil consolidated to the void ratio and normal stress represented by point A in the contractant zone is sheared with no volume change, positive pore pressure will be generated during the liquefaction process (effective stress is reduced from point A in the contractant zone to point B on the steady state line SSL1). Under undrained conditions, a soil with void ratio and normal stress represented by point C in the dilatant zone (relative to SSL1) generates negative pore pressure and in consequence results in an increase in strength when effective stress increases from point C to point D. If particle breakage and comminution take place, the increase in fine-grained materials changes the grain size distribution of the soil. The steady state line SSL1 of the soil with initial coefficient of uniformity moves left to the steady state line SSL2 with an increased coefficient of uniformity. Point C in relation to the steady state line SSL2 is in the contractant zone and liquefaction occurs corresponding to the variation of the effective stress from point C to point E under undrained conditions.

A series of ring-shear tests were carried out to investigate the sliding-surface liquefaction and related debris flows (Sassa 1996; Wang and Sassa 2002; Sassa et al. 2004). These experiments indicate that grain crushing during shear deformation plays an important role in triggering sliding-surface liquefaction, as shown in Figure 7-6 and Figure 7-7. Typical cases of debris flows related to sliding-surface liquefaction have been explored by Sassa (2000) and Sassa and Wang (2005).

7.3 Dynamic Analysis of the Tsukidate Landslide

On May 26, 2003, an earthquake with a moment magnitude of 7.0 occurred in northern Japan. The earthquake triggered a number of landslides. One of the earthquake-induced large landslides is located in the Tsukidate area (Figure 7-8). Field observations indicated that the Tsukidate landslide showed typical debris flow characteristics. Fukuoka et al. (2004) investigated triggering mechanisms of the landslide using undrained ring-shear tests. In this study a dynamic analysis of the Tsukidate landslide is presented. The following descriptions of the Tsukidate landslide are summarized from work by Fukuoka et al. (2004), Wang et al. (2005), and Uzuoka et al. (2005).

7.3.1 Field and Experimental Investigations of the Tsukidate Landslide

The Tsukidate landslide originated from a failure in a gentle natural slope with an inclination of approximately 13.5°. It was estimated that the volume of landslide was about 8,100 m^3. The source area was about 40 m wide and 80 m long, with a maximum depth of about 5 m. After movements stopped, the final failure materials ware spread on a horizontal rice paddy. The deposition area was about 50 m wide and 120 m long.

The uppermost scarp of the landslide was about 25 m high and 180 m long from the outermost edge of landslide deposits on the rice field. Figure 7-9 shows photos of the Tsukidate landslide. Photos of the front and side views of the landslide were taken just after the earthquake. The photo of the landslide toe was taken four days after the event. As shown in the photos, the landslide material from the source area traveled a significant distance along a gentle slope before coming to rest on a paddy field. Bamboo growths originally on the source area were transported with the landslide mass and stood almost vertically on the rice paddy after the long traveling distance (Figure 7-9 (c)).

Field investigation indicated that the soils in the source area were composed mainly of pyroclastic deposits. Soil samples were taken from the source area and deposition area of the landslide after the earthquake. The configuration of displaced materials and sampling sites is shown in Figure 7-10. The grain size distribution of soil samples taken from the landslide is presented in Figure 7-11. The figure indicates that soil samples have similar grain size distributions: gravel about 20 percent, sand about 50 percent, silt about 20 percent, and clay about 10 percent. Gravel in soil samples consists entirely of pumice. Regarding soil classification, the pyroclastic deposits involved in the Tsukidate landslide can be categorized as silty sand with pumice. The physical properties of soil samples are summarized in Table 7-1. The dry density measured for undisturbed samples is about 1.1 g/cm^3. The solid concentration for displaced materials in a flowing state estimated from Table 7-1 is greater than 50 percent by volume. Field investigations indicate that the Tsukidate landslide is essentially a debris flow, according to the classification by Hungr et al. (2001).

Undrained cyclic ring-shear tests were conducted on samples from the landslide source area to simulate the triggering process involved in the Tsukidate landslide. The tests revealed that soils in the Tsukidate landslide were highly liquefiable and the bulk friction angle of liquefied soils was about 7.5°. The failure of the slope was the result of high pore-water pressures generated by seismic loading during the earthquake. After the original slope failure, persistent high pore water pressure due to widespread shear deformation within the soils resulted in the lower resistance and high mobility of the landslide.

7.3.2 Numerical Modeling of the Tsukidate Landslide

A detailed contour map of the Tsukidate landslide area after the earthquake is shown in Figure 7-12. The central longitudinal section of the landslide from the source area to the deposition area (the line A-A' in Figure 7-12) is used to obtain the sliding surface and pre-failure geometry in the dynamic analysis, as presented in the Figure 7-14. The motion of the landslide was simulated using the analytical model based on the energy consideration. The frictional model is used as the constitutive law to calculate flow resistance. Figure 7-15 is the final profile of mass distribution simulated by the dynamic analysis. The front velocities calculated are shown in Figure 7-16.

The front runout distance calculated from the dynamic analysis is about 136 m, which is very close to the observed runout distance 135 m. The mass distribution estimated by dynamic analysis reasonably matches that observed in the field, although the deposition of a small amount of sliding mass on the upper slope was predicted in the dynamic analysis. The back-calculated friction angle is about 7.9°. This value shows an excellent match with the bulk frictional angle of 7.5° measured in the undrained ring-shear tests. There are no velocity records for the Tsukidate landslide. According to local residents, the landslide movement lasted about 60 to 90 seconds. The velocity at the center of the landslide was estimated to be about 6 to 7m/s (Uzuoka et al. 2005). The velocity profile (Figure 7-16) based on the dynamic analysis provides a very reasonable estimation.

7.4 Dynamic Analysis of the Takarazuka Landslide

The Takarazuka landslide was triggered by the Hyogoken-Nambu earthquake in Japan in 1995. The landslide occurred on a slope of 19° and traveled on the very smooth ground of a golf course with a slope of 5–6°. The landslide moved smoothly with a forest standing on it. The plan view of the Takarazuka landslide is show in

Figure 7-17. Soils involved in the Takarazuka landslide are angular sandy soils with weathered granite. The long runout distance and high solid concentration indicated that the landslide behaved as a debris flow after failure of the slope.

Undrained ring-shear tests were performed on samples from the Takarazuka landslide (Sassa et al. 1995) to examine the high mobility of the landslide. The tests revealed that the bulk friction angle of soils in the Takarazuka landslide was about 8.9°. The residual friction angle obtained from drained unloading tests was 28.8°. Experimental results indicated that the high mobility of the Takarazuka landslide was the result of sliding-surface liquefaction (Sassa et al. 1995; Sassa 2000).

The bulk friction angle mobilized in the Takarazuka landslide is back-calculated from dynamic analysis using the new analytical model. The initial slope geometry, as shown in Figure 7-18, is determined based on the longitudinal cross section (the line A-A' in Figure 7-17) of the Takarazuka landslide. To simulate the sliding-surface liquefaction in the Takarazuka landslide, the residual friction angle of 28.8° is used as the internal friction angle for calculating the coefficients of lateral stress and the internal energy dissipation in the dynamic analysis. The bulk friction angle along the sliding surface of the landslide is determined when the simulated runout distance is in good agreement with field observations.

The post-failure profile and front velocities of the Takarazuka landslide based on dynamic analysis are presented in Figure 7-19 and Figure 7-20, respectively. The front runout distance calculated from dynamic analysis is about 130 m, which is close to the runout distance of 133 m from field observations. To match the runout distance, the bulk friction angle back-calculated is about 11°, which is in good agreement with the bulk frictional angle of 8.9° measured from the shear-ring tests (Sassa et al. 1995; Sassa 2000).

7.5 Dynamic Analysis of the Hiegaesi Landslide

The Hiegaesi landslide was triggered by heavy rainfall in August 1988 at Hiegaesi in Otakura, Japan. The source area of the landslide was about 23 m wide and 28 m long and the maximum thickness of displaced soil was about 2.5 m. The volume of the displaced mass was estimated to be 1200 m^3. The angle of the sliding surface in the source area was about 25°. The failed soil mass was deposited on a rice paddy in a three-lobed shape, as shown in Figure 7-21. Based on field observations, the long runout distance of about 70 m and low bulk friction angle of about 11° indicate that the Hiegaesi landslide experienced flow-type motion (Sassa 2000; Wang et al. 2002; Wang et al. 2003).

Field investigations showed that soils involved in the Hiegaesi landslide can be classified as silty sand with gravel. A series of drained and undrained ring-shear tests were conducted to investigate the high mobility of the Hiegaesi landslide. Locations of soil samples taken from both source and deposition areas are presented in Figure 7-21. The results of ring-shear tests and field observations indicated that the high mobility of the Hiegaesi landslide resulted from sliding-surface liquefaction. Figure 7-22 shows the results of the grain-size distribution analysis on soil samples taken from the sliding zone (S1) and from the displaced materials (S2) overlying the sliding zone in the Hiegaesi landslide. Compared with samples of displaced materials (S2), the sample from the sliding zone (S1) consists of more fines and suggests grain crushing occurred along the sliding surface. The residual friction angle and bulk friction angle measured from the ring-shear tests are 41° and 8°, respectively.

Dynamic analysis using the new analytical model was carried out to simulate the Hiegaesi landslide. Based on the longitudinal cross section in Figure 7-21 (c), the sliding surface and the initial slope geometry used for the dynamic analysis are determined and presented in Figure 7-23. The residual shear friction angle measured from the ring-shear tests is used as the internal friction angle to calculate the coefficients of lateral stress and the internal energy dissipation in the dynamic analysis. The bulk friction angle is then back-calculated from the dynamic analysis.

The post-failure geometry and front velocities of the Hiegaesi landslide based on dynamic analysis are presented in Figure 7-24 and Figure 7-25, respectively. The runout distance calculated from dynamic analysis is about 70 m, which is the same as the runout distance from field observations. To match the runout distance, the bulk friction angle back-calculated is about 10.4°, which is in reasonable agreement with the bulk frictional angle of 8° measured from shear-ring tests (Sassa et al. 1995; Sassa 2000; Wang et al. 2002).

7.6 Conclusions

Mobilization of debris flows from landslides on natural slopes is investigated in terms of liquefaction. The concepts of steady state of deformation, collapse surface, and sliding-surface liquefaction are used to interpret post-failure deformation behavior of rapid landslides and their high mobility. Effects of grain size distribution on the steady states of granular materials are investigated in relation to the sliding-surface liquefaction concept. Debris flows mobilized from landslides on natural slopes have been analyzed using the dynamic model based on energy consideration. Field observations and experimental studies indicate that the high mobility of rapid landslides is a result of liquefaction of displaced materials or shear zone along the sliding surface. The bulk friction angle back-calculated from dynamic analysis is in general agreement with the results from ring-shear tests. Comparison with field observations indicates that the new analytical model provides a reasonable estimate of material distribution and velocity profiles for debris flows on natural slopes.

Table 7-1 Properties of soil sample from source area of the Tsukidate landslide

Sample Sites	Water Content $w(\%)$	Specific Gravity G	Void Ratio e	Unit Weight $\gamma(kN/m^3)$	Degree of Saturation $S_r(\%)$	Grain Content $(\%)$			
						Gravel	**Sand**	**Silt**	**Clay**
A	26.1	2.478	—	—	—	17	53	22	8
B	28.0	—	1.175	14.30	59.0	—	—	—	—
C	30.6	2.400	—	—	—	18	50	23	9
D	55.7	2.313	—	—	—	15	54	23	8
E	38.6	—	0.909	17.36	103.6	—	—	—	—
F	31.8	2.438	—	—	—	17	53	20	10
G	40.9	2.428	—	—	—	18	50	20	12
H	42.6	2.442	1.159	15.82	89.8	—	—	—	—
I	39.1	2.354	1.098	15.30	83.8	20	48	24	8
J	29.8	2.447	—	—	—	14	53	25	8

Note: —, data not available.

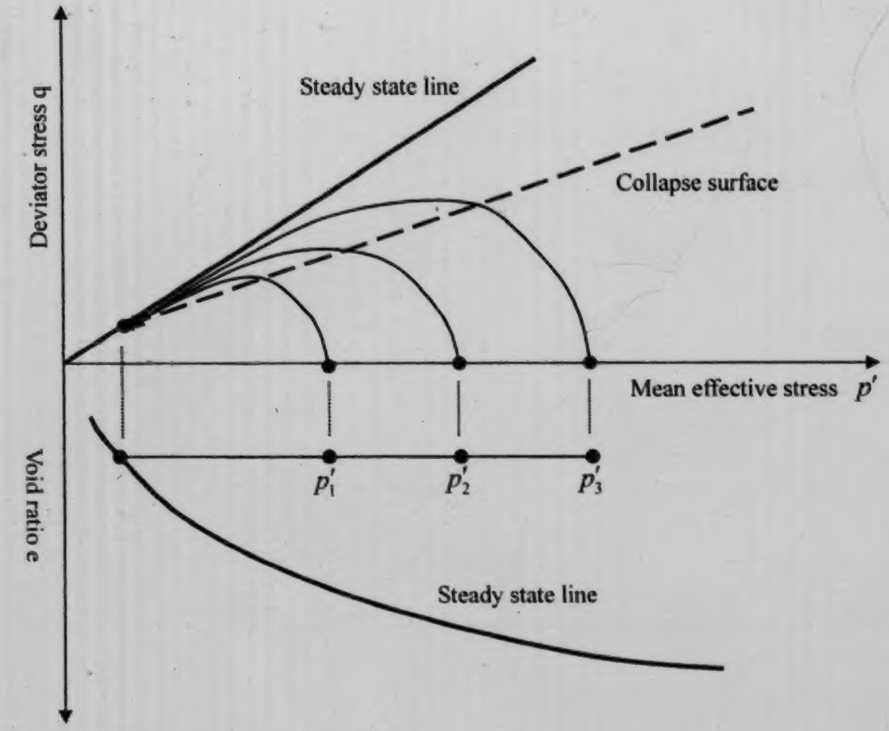
Deviator stress q
Steady state line
Collapse surface
Mean effective stress p'
Void ratio e
p'_1
p'_2
p'_3
Steady state line

Figure 7-1 Typical isotropically consolidated undrained test on loose sand (Modified from Sladen et al. 1985a)

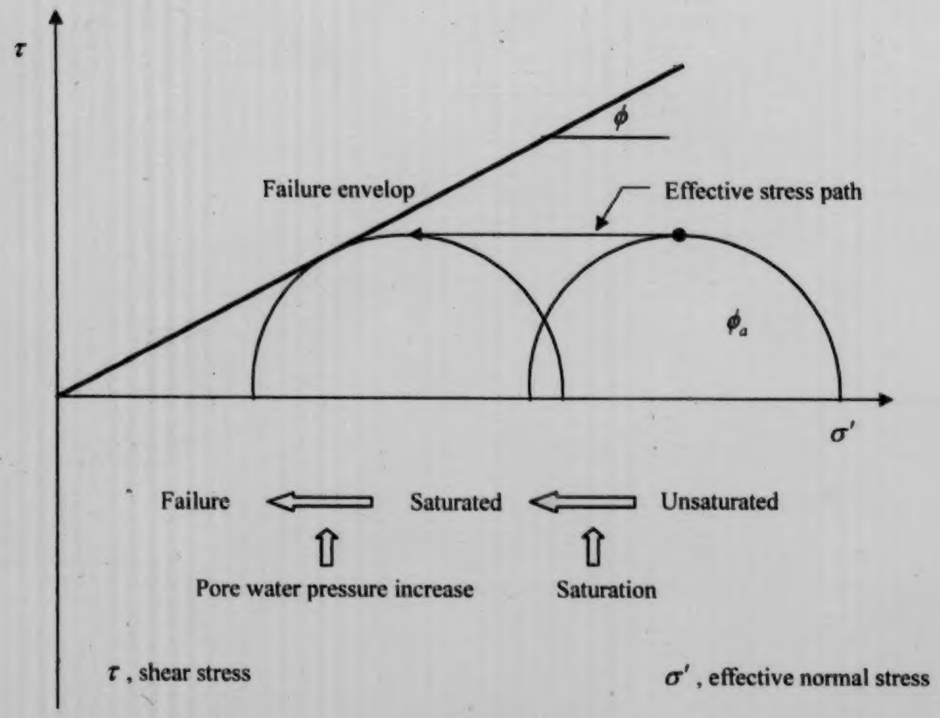
τ
ϕ
Failure envelop
Effective stress path
ϕ_a
σ'
Failure
Saturated
Unsaturated
Pore water pressure increase
Saturation
τ , shear stress
σ' , effective normal stress

Figure 7-2 Mohr circles for rainfall-induced debris flows (Modified from Anderson and Sitar 1995)

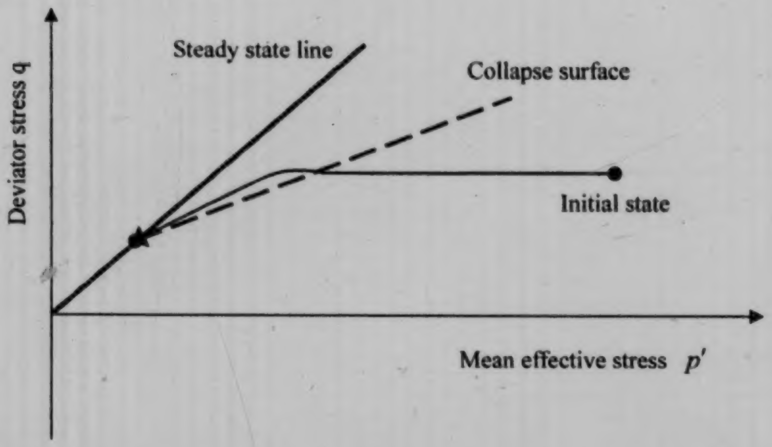
Deviator stress q
Steady state line
Collapse surface
Initial state
Mean effective stress p'

Figure 7-3 Field stress path in $p' - q$ plane for rainfall-induced debris flows

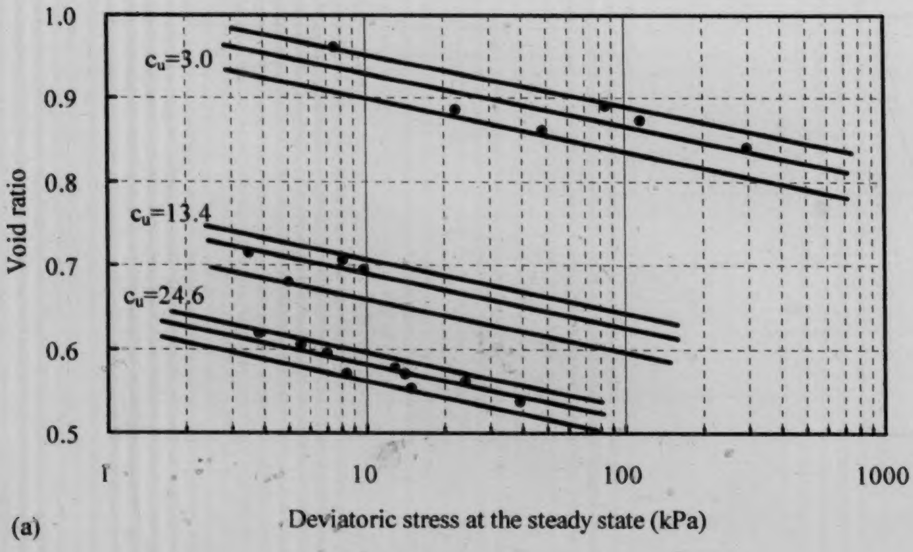

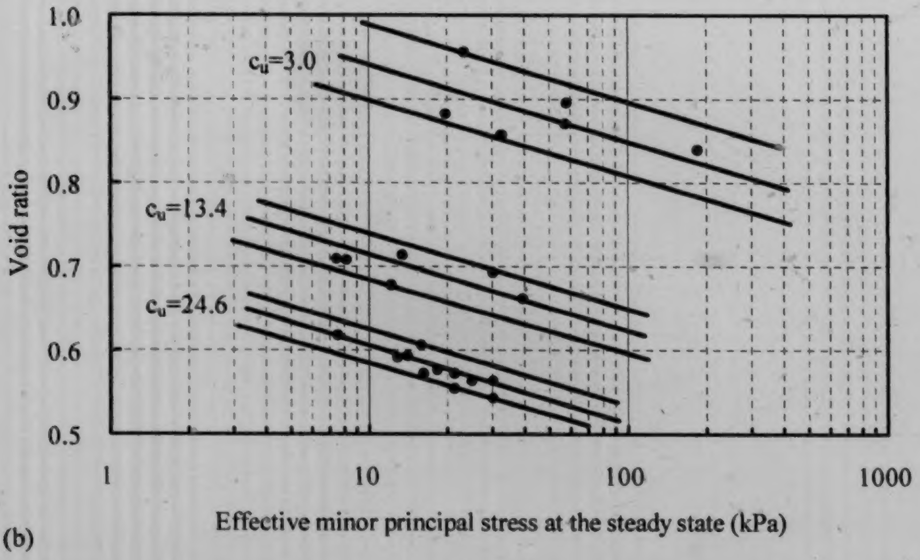

Figure 7-4 Steady-state lines for soils with different coefficients of uniformity (Modified from De Matos 1988): (a) Deviator stress versus void ratio; (b) Effective minor principal stress versus void ratio

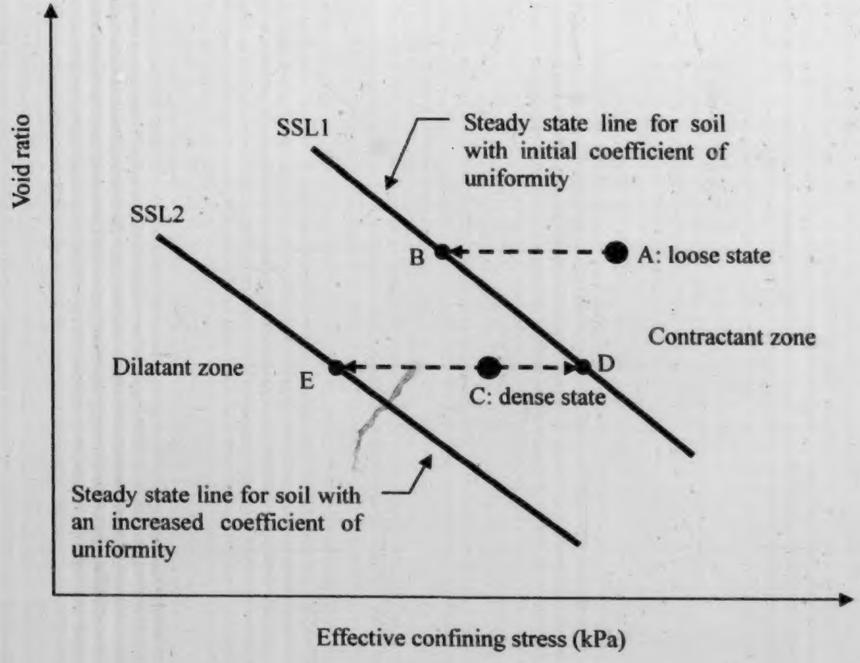
Void ratio
SSL1
Steady state line for soil with initial coefficient of uniformity
SSL2
B
A: loose state
Contractant zone
Dilatant zone
E
D
C: dense state
Steady state line for soil with an increased coefficient of uniformity
Effective confining stress (kPa)

Figure 7-5 Changes in steady-state line associated with natural comminution

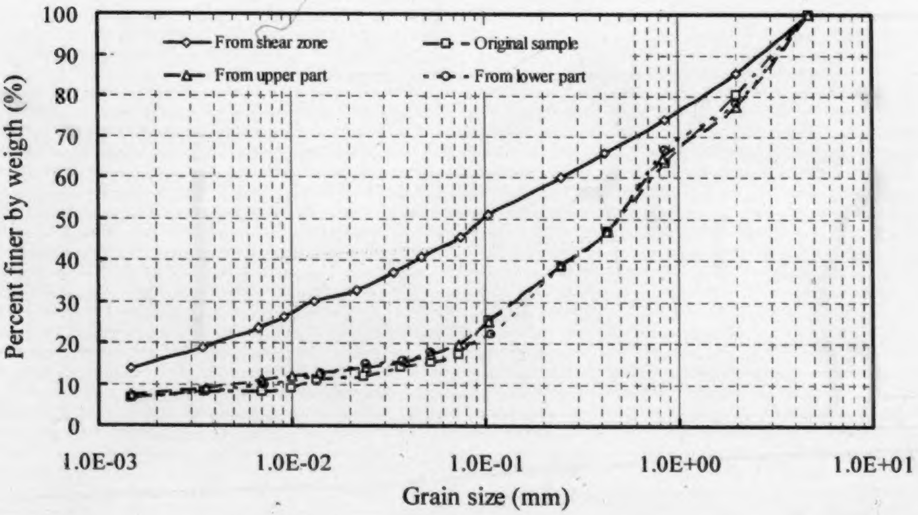

Figure 7-6 Grain size distribution for samples in shear-ring tests (Data from Sassa 2000)

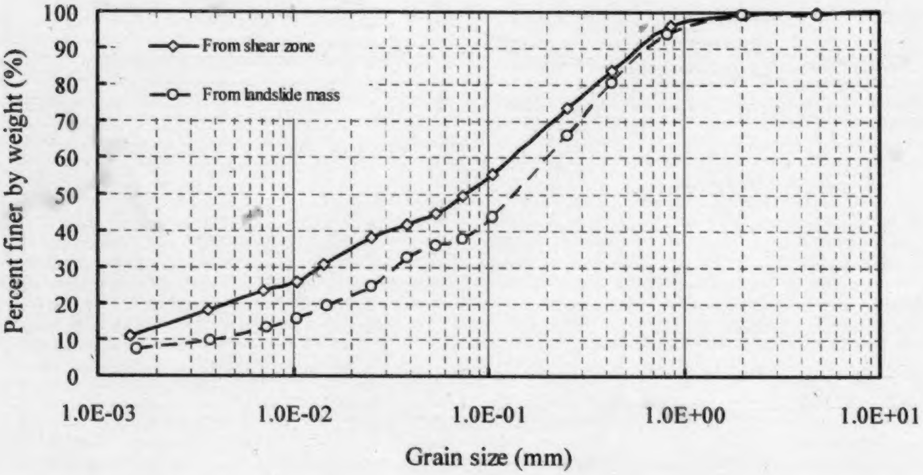

Figure 7-7 Grain size distribution for samples of a landslide associated with sliding-surface liquefaction (Data from Sassa 2000)

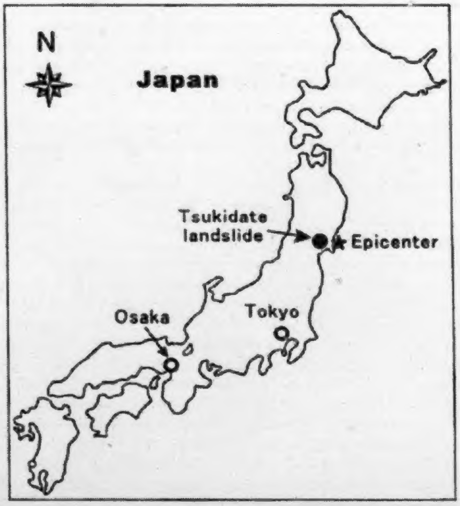
N
Japan
Tsukidate
landslide
Epicenter
Osaka
Tokyo

Figure 7-8 Location of Tsukidate landslide and the earthquake epicenter (After Wang et al. 2005)

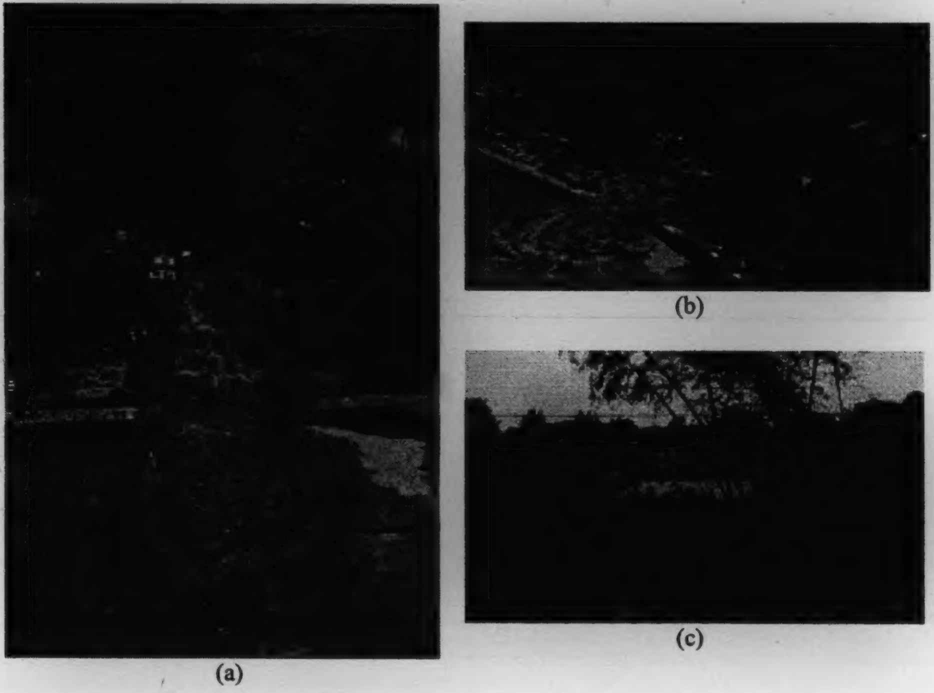

Figure 7-9 Views of the Tsukidate landslide (After Fukuoka et al. 2004): (a) Oblique front view; (b) Oblique side view; (c) View from the toe of the Tsukidate landslide

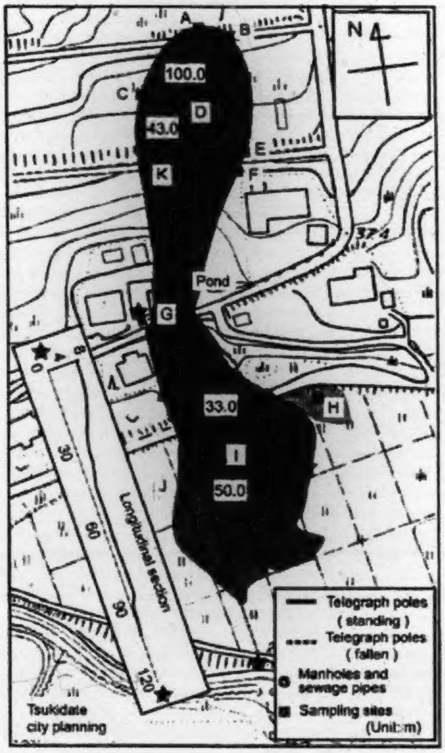
A
B
N
100.0
C
D
43.0
E
K
F
374
Pond
G
0
8
30
60
90
120
Longitudinal section
33.0
H
I
J
50.0
Telograph poles (standing)
Telegraph poles (fallen)
Manholes and sewage pipes
Sampling sites
(Unit: m)
Tsukidate city planning

Figure 7-10 Configuration of displaced materials and location of sampling sites (After Uzuoka et al. 2005)

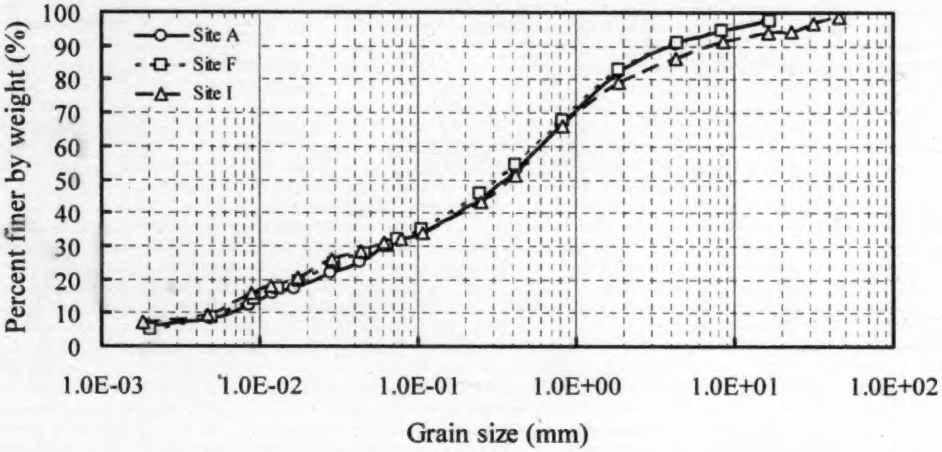

Figure 7-11 Gain-size distribution of soil samples taken from the Tsukidate landslide (Data from Uzuoka et al. 2005)

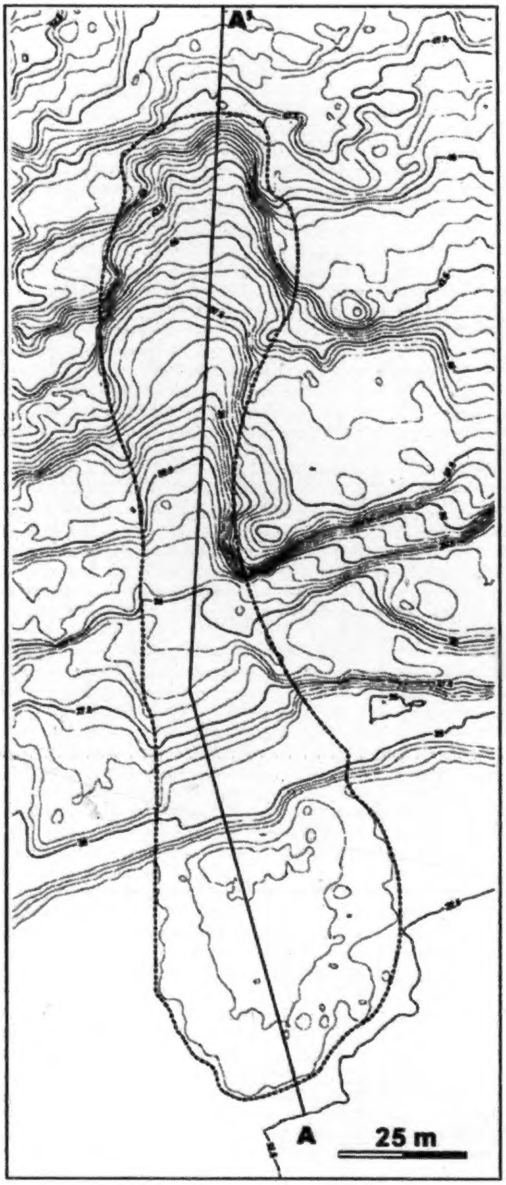

Figure 7-12 Contour map of the Tsukidate landslide area after the earthquake (After Wang et al. 2005)

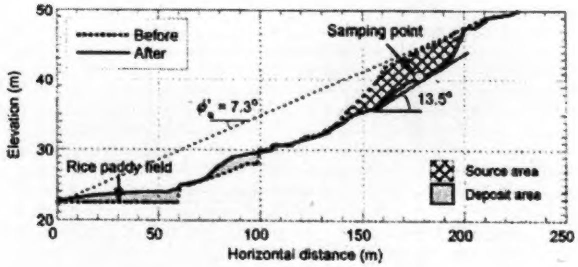

Figure 7-13 Cross section of the Tsukidate landslide along A-A' in Figure 7-12 (After Wang et al. 2005)

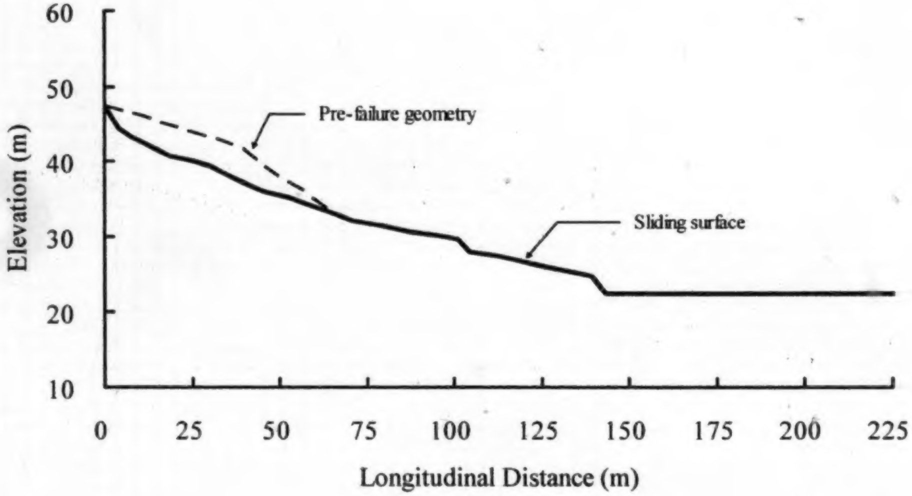

Figure 7-14 Longitudinal cross section of the Tsukidate landslide used for dynamic analysis

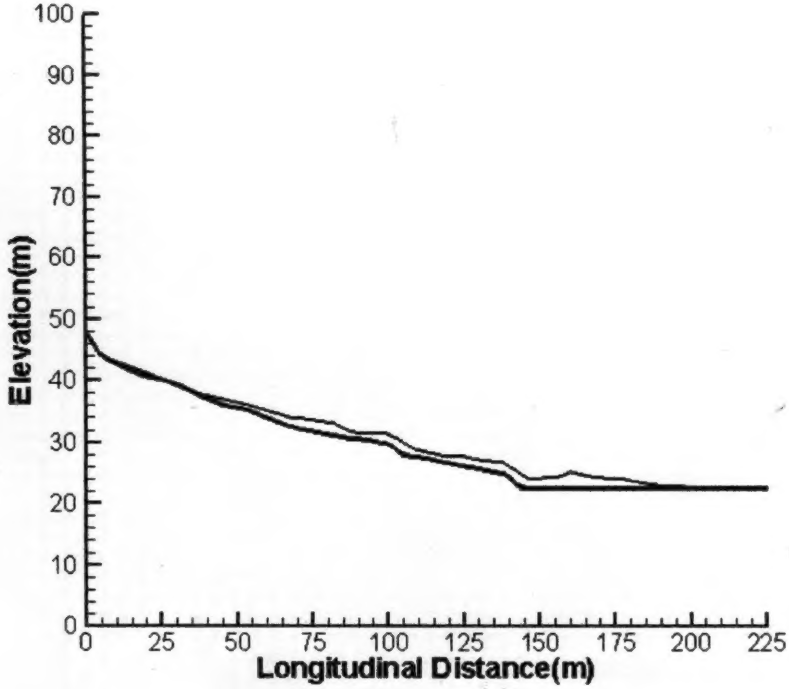

Figure 7-15 Post-failure profile of the Tsukidate landslide based on dynamic analysis

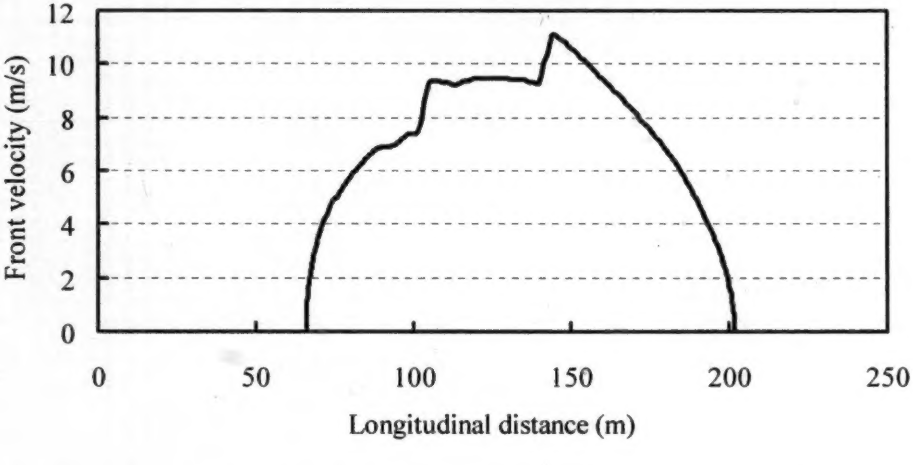

Figure 7-16 Front velocity profile of the Tsukidate landslide based on dynamic analysis

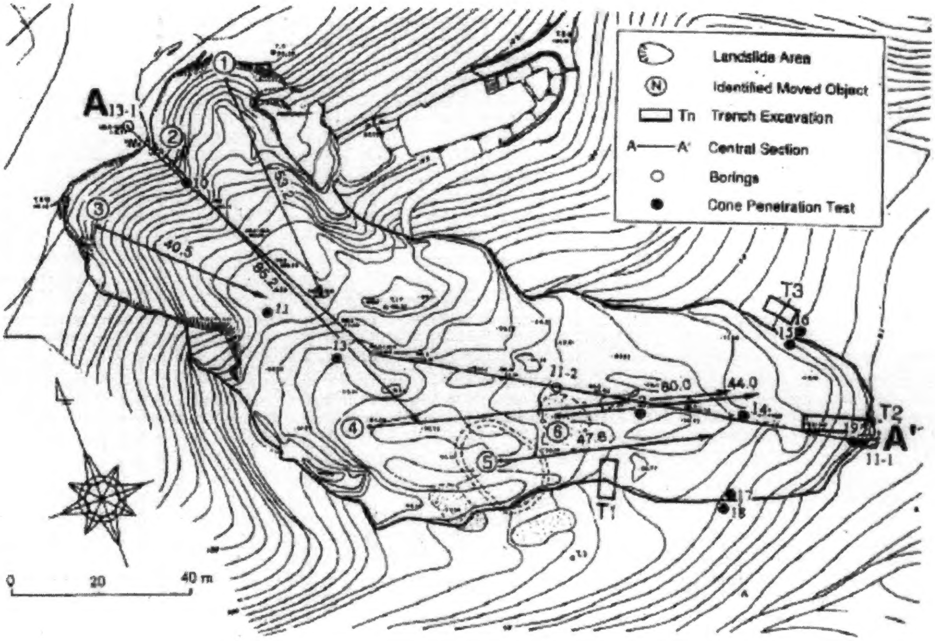
Landslide Area
Ⓝ Identified Moved Object
Tn Trench Excavation
A——A' Central Section
○ Borings
● Cone Penetration Test
A
13-1
①
②
③
④
⑤
⑥
40.5
86.2
53
80.0
44.0
47.6
19
11
13
11-2
14
15
16
17
18
T1
T2
T3
A'
11-1
0
20
40 m

Figure 7-17 Plan view of the Takarazuka landslide (After Sassa 2000)

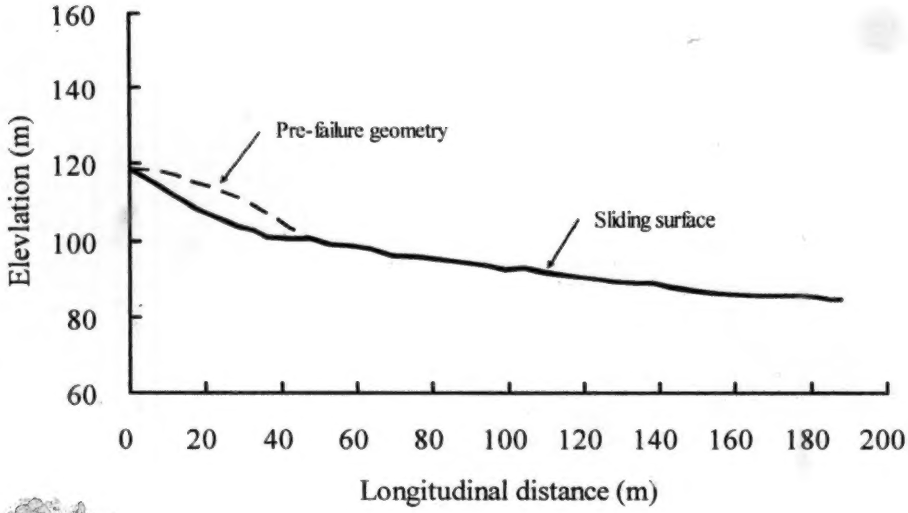

Figure 7-18 Longitudinal cross section of the Takarazuka landslide used for dynamic analysis

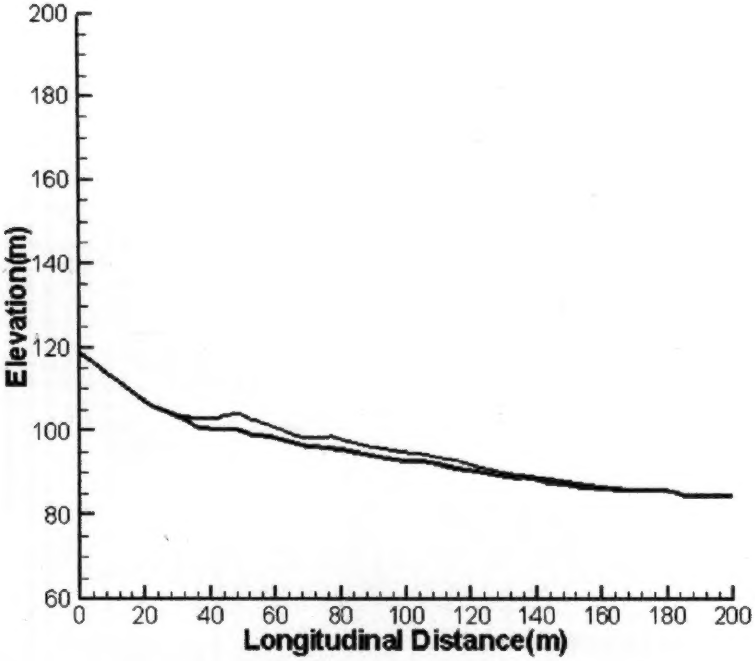

Figure 7-19 Post-failure profile of the Takarazuka landslide simulated using dynamic analysis with the friction model

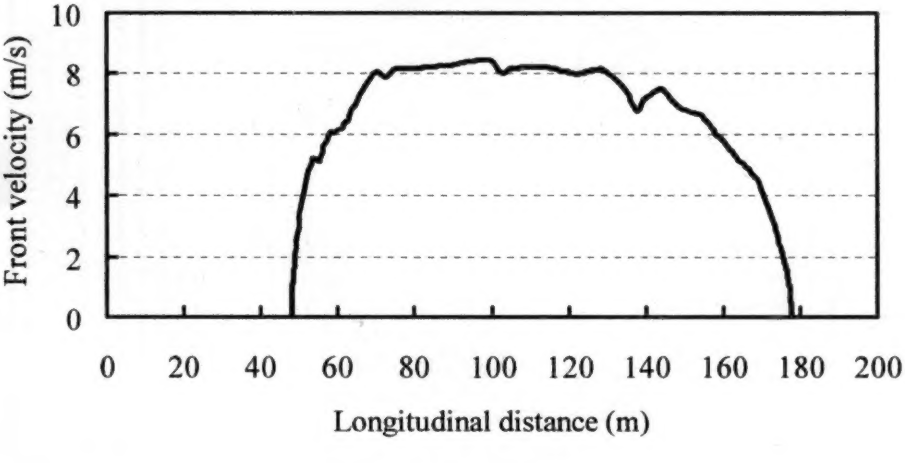

Figure 7-20 Front velocity profile of the Takarazuka landslide based on dynamic analysis

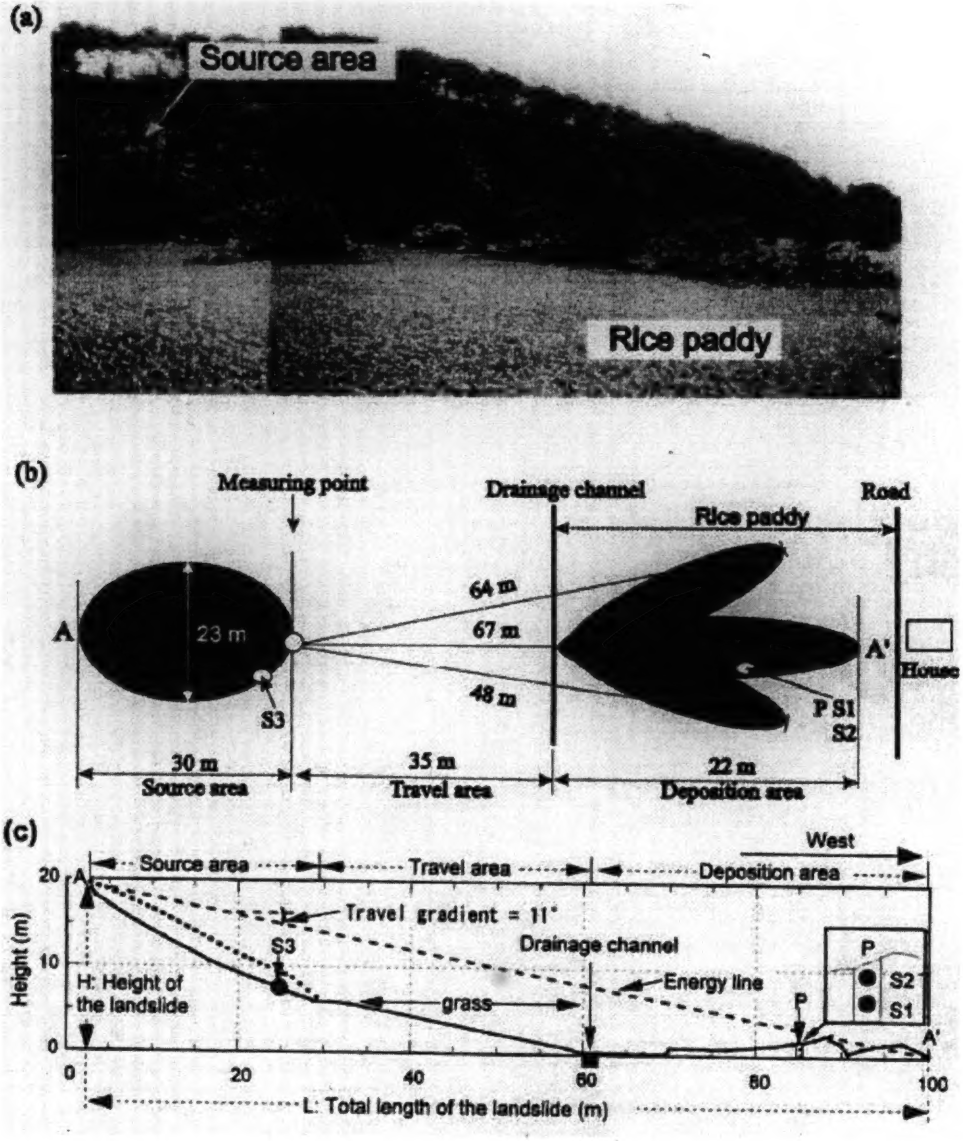
(a)
Source area
Rice paddy
(b)
Measuring point
Drainage channel
Road
Rice paddy
64 m
67 m
48 m
23 m
A
A'
House
S3
P S1
S2
30 m
Source area
35 m
Travel area
22 m
Deposition area
(c)
West
Source area
Travel area
Deposition area
Travel gradient = 11°
S3
Drainage channel
Energy line
H: Height of the landslide
grass
P
S2
S1
A
A'
Height (m)
20
10
0
0
20
40
60
80
100
L: Total length of the landslide (m)

Figure 7-21 The Hiegaesi landslide (After Sassa 2000): (a) Photograph of the landslide; (b) Sketch of the landslide in plan; (c) Longitudinal cross section of the landslide. P: observation pit; S1, S2 and S3: sampling sites.

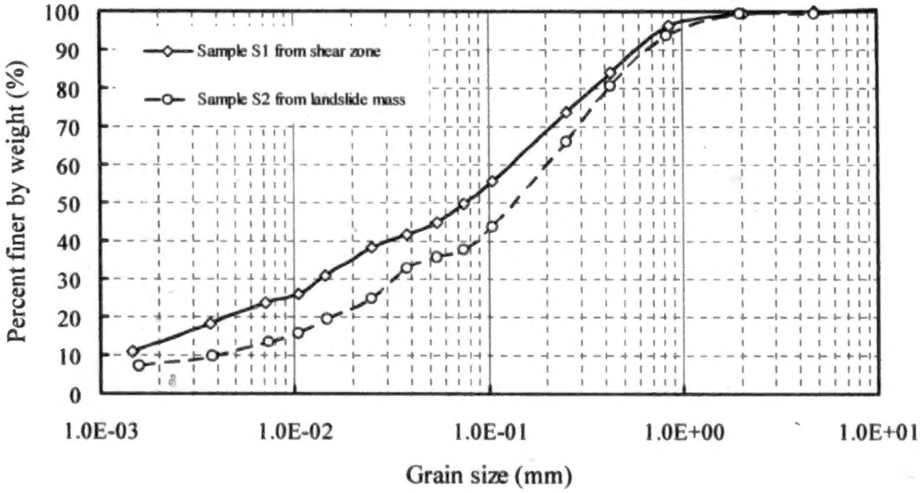

Figure 7-22 Grain size distributions of soil samples from the sliding zone and the displaced mass of the Hiegaesi landslide (Data from Sassa 2000)

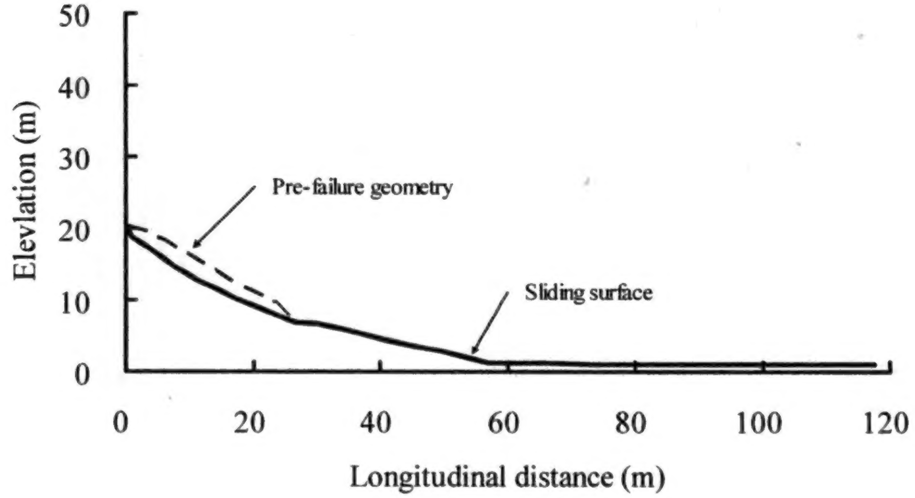

Figure 7-23 Sliding surface and pre-failure slope geometry of the Hiegaesi landslide

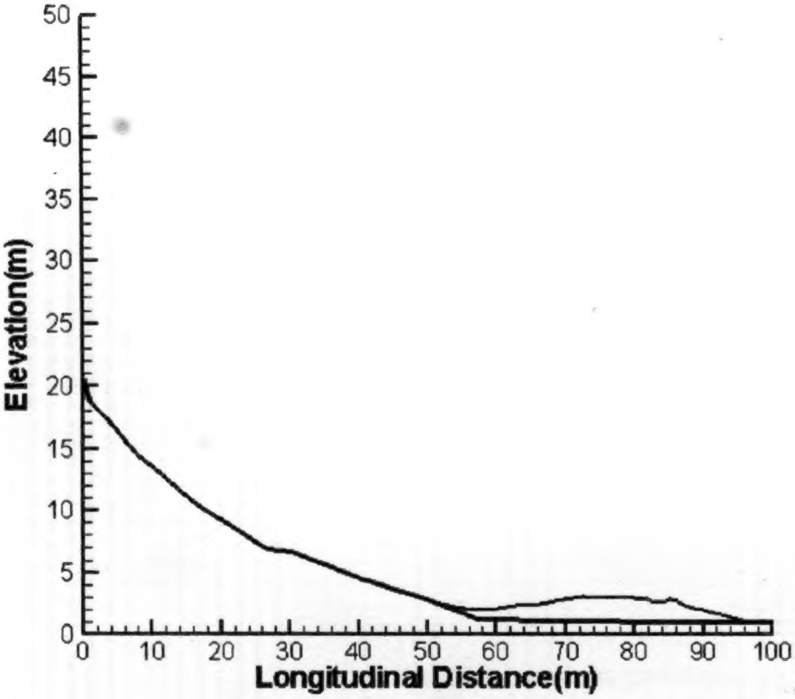

Figure 7-24 Post-failure geometry of the Hiegaesi landslide based on dynamic analysis

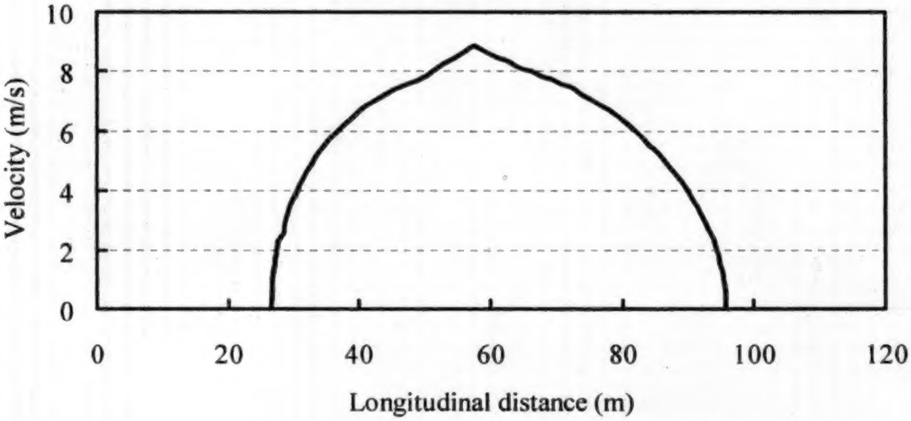

Figure 7-25 Front velocity profile of the Hiegaesi landslide based on dynamic analysis

Chapter 8

Conclusions and Recommendations

As illustrated in this thesis, debris flows incorporate a broad range of sediment-fluid flows intermediate between dry rock avalanches and hyperconcentrated flows. Debris flows and related phenomena are encountered in a variety of geological and geomorphological settings. The evolution of debris flow from the onset of motion to final deposition is a complicated process: mobilization involves surface runoff erosion and liquefaction of deposits as a result of changes in pore water pressure; transport involves complex interactions between solid and fluid phases and variations in solid and fluid constituents along the travel path; deposition involves stress redistribution and reconsolidation. These complications make analyzing debris flow and related phenomena some of most complex issues facing the geotechnical profession and pose great challenges in understanding debris flow mechanics and predicting debris flow behavior. This study provides a comprehensive examination of the state of the art in constitutive and numerical modeling of debris flows. Emphasis is placed on undrained granular deposit flows with high solid concentration (greater than 50 percent by volume). A new analytical model is proposed to improve understanding of fundamental aspects in debris flow modeling and to provide practitioners with simple, reliable predictions of the debris flow behavior.

8.1 Summary

Debris flow phenomena and the historical development of debris flow modeling are briefly reviewed in Chapter 1. The review demonstrates that debris flow modeling incorporates extremely different points of view on constitutive behavior and numerical simplification.

The term debris flow has been applied to a broad and imprecisely defined range of flow phenomena intermediate between dry rock avalanches and sediment-laden water floods. Improper uses of the definitions of debris flow in different classification systems often causes problems in understanding and communication between researchers and practitioners. An unambiguous and agreed-upon definition of debris flows is important for the communication and exchange of ideas among debris flow researchers. Chapter 2 focuses on classifications of flow-like mass movement and definitions of debris flow. Definitions of debris flow within qualitative and quantitative classification systems have been critically reviewed. Quantitative classifications are mainly based on constitutive properties of flowing masses and have not found much practical application because of difficulties obtaining parameters required by the classification systems. Qualitative classifications are based on a wide variety of factors encompassing material properties, type and rate of movement, water content, liquefaction behavior of source materials, and the presence of a confined channel. Most information required can be easily obtained in practice through geotechnical investigations and laboratory experiments. As a consequence, qualitative classification is more practical and suitable for hazard prediction and risk assessment in a debris flow-prone terrain. Among qualitative classifications, the classification presented by Hungr et al. (2001) focuses on landslides of the flow type and approaches the subject from a geotechnical perspective. This classification provides more meaningful definitions for debris flows and related phenomena compared with other classifications. The use of the classification by Hungr et al. (2001) is thus recommended for debris flow studies.

In the application of numerical methods to the analysis of debris flows, constitutive equations play a fundamental role. From a quantitative point of view, constitutive models provide the mathematical equations which define the mechanical properties of the materials. The constitutive model adopted in the analysis governs the response of the material to the applied loads. Practical implementation of numerical models must take account of the details of the constitutive equations, particularly when material behavior is characterized by strong nonlinearity, irreversibility, and path-dependence. The constitutive models for debris flow were critically examined in Chapter 3. The validity and applicability of constitutive equations are investigated in the context of debris flow modeling. A literature survey indicates that the flow resistance in a debris flow has been described by extremely different and often contradictory constitutive models. These models can be classified as the Newtonian fluid model, non-Newtonian fluid model, dilatant fluid model, Coulomb frictional model, Coulomb viscous model, and Voellmy fluid model.

On a microscopic scale, the strength of water-sediment mixtures is dependent on the viscosity of a fluid phase and on the frictional strength of a solid phase. The constitutive behavior of water-sediment mixture flows is sensitive to changes in sediment concentration, grain size, and grain-size distribution. For flows with lower solid concentration, shear resistance is strain rate dependent and often defined by a non-Newtonian fluid model such as the Bingham model, the Herschel-Bulkley model, or the quadratic model. The non-Newtonian fluid model appears to be applicable to the analysis of mud flow, peat flow, or debris flood, according to the classification by Hungr et al. (2001). If the solid concentration in a flow of sediment-water mixtures is high enough, and grains touch one another, granular friction make a significant contribution to the total flow resistance. Field observations, laboratory experiments, and theoretical analyses demonstrate that shear resistance in dense granular flows such as debris flows and rock avalanches is independent of strain rate. Compared with the frictional resistance, yield strength of the interstitial fluid is negligible in dense granular flows. Granular friction dominates flow behavior of dense granular flows. The behavior of debris flows can be represented with reasonable accuracy by the Coulomb friction model. Although the accurate lower bound of volume concentration for debris flows depends on sediment properties and interactions between solid and fluid phases, laboratory experiment and case history studies indicate that sediment-water mixtures behave like Coulomb-type materials if the solid concentration exceeds 50 to 60 percent by volume.

Empirical methods, sliding block models, and depth-averaged models have been applied to the prediction of post-failure mobility of debris flows, debris avalanches, and other types of flow-like landslides. The strengths and limitations of these methods were investigated in Chapter 4. A detailed formulation of the depth-averaged model was given in Chapter 4 to improve the understanding of this commonly used model in debris flow analyses. Empirical equations can be developed for regional and type-specified debris flows provided that a number of good-quality databases are available. Easy implementation is a conspicuous advantage of the empirical method over other approaches. However, empirical correlations are mainly based on regression analyses of the relationship between the volume of displaced materials and the mobility of debris flows. The material properties and the roughness of the sliding surface are not fully taken into account in an empirical model. As a consequence, empirical equations can be applied only to regions having geological and climatic conditions similar to the region where the empirical equations were formulated. The application of empirical equations to field data often presents considerable scatter due to the complexity of the debris flow process and uncertainty involved in the establishment of the equations. Most relationships established so far provide only an order of magnitude estimate of some debris flow parameters. Compared with analytical models, the empirical models possess limited applicability and generality in debris flow hazard assessment and protective designs.

The sliding block model simulates a debris flow as the motion of a rigid, dimensionless block representing the centroid of the displaced materials. The velocity and displacement of the block is dependent on the sum of driving force of gravity and basal resistance. Frictional and Voellmy models are the most widely used constitutive law to define the resistance in sliding block models. The sliding block model cannot account for the confinement of travel path and lateral spreading of the failure materials. Simulation with the sliding block model produces information about the centroid position only. Predictions based on the sliding block model provide a crude approximation of debris-flow mobility.

Depth-averaged models provide the most advanced analysis of debris flows. Simulation using depth-averaged equations produces estimates of velocity profiles, lateral spreading, and longitudinal runout distance of debris flows. Derivation of the depth-averaged equations is based on the assumption that the longitudinal dimension in a flow is much greater than the flow depth. Flow resistance in a depth-averaged model is dependent on constitutive equations which describe the mechanical behavior of the material. The Bingham, Herschel-Bulkley, quadratic fluid, and Coulomb frictional models are often used to describe material properties in depth-averaged models due to the simplicity of their practical implementation. A detailed formulation of depth-averaged models with different constitutive models indicates that for a non-Newtonian fluid the resistance is related to the average flow velocity, while for a Coulomb material the resistance is independent of the flow velocity.

The depth-averaging technique significantly reduces computational cost and makes possible a practical simulation of debris flows over complex topography. The depth-averaging process, however, sacrifices flow details in the dimension normal to flow direction. The accuracy of prediction using depth-averaged equations can be improved by incorporating internal deformations into debris flow analytical models.

Consumption of kinetic energy in debris flow occurs through basal sliding and internal deformation. To incorporate internal energy dissipation into debris flow analysis with the Coulomb frictional law, a slice-based analytical model was formulated in Chapter 5. Formulation of the governing equations is based on the conservation law for energy. The internal energy dissipation is approximated using the Coulomb failure criterion. For easy implementation of the new analytical model, a Lagrangian finite difference scheme was proposed to solve the governing equations.

Application of the dynamic model with internal energy dissipation in the analysis of liquefaction flows was explored in Chapter 6. Liquefied shear strengths were back-calculated for ten liquefaction flow slide cases. Cohesive and frictional models were used as constitutive laws to calculate the resistance mobilized in liquefaction flows. Simulation results indicate that the constitutive law used in a dynamic analysis has a significant influence on material distribution. Compared with the cohesive model, the friction model appears to provide a better fit between simulation and field observation in terms of deposit distribution. Kinetic analysis with the sliding block model has also been carried out in Chapter 6. Based on case history studies, values of liquefied shear strength agree broadly between kinetic analysis and dynamic analysis based on energy conservation. By using the Coulomb friction model as a constitutive law, back-analyses of case histories with the new analytical model provide a useful strength parameter for liquefaction analysis.

In Chapter 7, debris flows on natural slopes were analyzed using the dynamic model based on energy consideration. Concepts of steady state of deformation, collapse surface, and sliding surface liquefaction were used to interpret the high mobility of debris flows. Bulk friction angles back-calculated from the dynamic analyses are in broad agreement with the results from ring-shear tests. Comparison with field observations indicates that dynamic analysis with new the analytical model provides a reasonable estimate of material distribution and velocity profiles for debris flows on natural slopes.

8.2 Conclusion

This study provides a comprehensive examination of the state of the art in constitutive and numerical modeling of dense granular flows. Emphasis is placed on dense granular deposit flows with high solid concentration.

Constitutive laws widely used in debris flow modeling are critically examined with information found in the literature and data from field observations, laboratory experiments, and theoretical analyses. Based on a comprehensive review of existing analytical approaches to debris flow runout predictions, a new analytical model based on energy conservation and considering internal energy dissipation is formulated.

The post-failure deformation behavior of liquefaction flow slides is simulated using the new analytical model. Liquefied shear strengths in terms of undrained strength and bulk friction angle are back-calculated for ten flow slide cases according to cohesive and frictional soil behavior models. Results from back-analyses provide evidence that a useful strength parameter can be obtained through dynamic analysis within the framework of the Coulomb friction model.

The new analytical model is also applied to simulating debris flows mobilized from landslides on natural slopes. The analyses indicate that back-calculated bulk friction angles appear to be in agreement with the results from undrained ring-shear tests. Using the Coulomb friction model as a constitutive law, the analytical model developed in this study is capable of simulating post-failure deformation behavior of rapid landslides on natural slopes.

8.3 Recommendations for Future Studies

Within the framework of debris flow hazard and risk analysis, the following questions arise (Morgenstern 1978):

(1) How much material moves?

(2) What will be the time history of the movements in terms of velocities and accelerations?

(3) How are protective structures designed against moving masses?

From a geotechnical engineering perspective, an attempt to solve these questions involves predicting and controlling both pre-failure and post-failure deformation behaviors of a slope. In routine slope stability analysis, calculation of the factor of safety is undertaken using the limit equilibrium method. If the factor of safety of a slope is greater than unity, large movements will not occur in the slope. The actual deformation of the slope is dependent on a number of factors, including geological history, soil type, groundwater conditions, and external loading of the slope. A problem-oriented classification of soils proposed by Morgenstern (1992) has proven appropriate for slope stability analysis. A reasonably accurate prediction for pre-failure deformation of the slope can be obtained through advanced numerical simulation techniques such the finite element method and the finite difference method.

If the factor of safety is less than unity, the post-failure slope will accelerate as the result of an imbalance between driving forces and resisting forces. Large volumes of soil mass can become liquefied by virtue of energy transfer mechanisms following instability (Morgenstern 1978). The triggering mechanisms of debris flows mobilized from landslides are well understood using the concepts of steady-state line and collapse surface. Despite considerable advances in understanding post-failure movements of slopes, prediction and control of the catastrophic slope failures such as flow slides and debris flows are still extremely difficult due to the range and complexity of materials and the deformation characteristics associated with failures of natural and man-made slopes. From an engineering point of view, the dynamic model with the concept of an equivalent fluid provides the best fit for practical use in the analysis of geotechnical granular flows. An increase in the complexity of a model does not necessarily mean an increase in accuracy. Practical applications of debris flow numerical simulations require elegant simplification of the complicated behavior of debris flows. It seems unrealistic and presumptuous to seek complete generality for the dynamic model when simple materials such as rock and sand present formidable problems in geotechnical engineering. However, to improve understanding and knowledge in relation to debris flow mobility evaluation, the following areas have priority in future studies:

(1) Extension and generalization of the dynamic model to simulate debris flows on three-dimensional terrains.

(2) Formulation of a more rigorous expression for internal energy dissipation terms in the dynamic model.

(3) Development of the model for natural debris flows involving material deposition and entrainment along the travel path. The effects of mass changes on the energy transfer should be appropriately taken into account in the governing equations.

(4) Development of computer programs to simulate temporal and spatial variations during all stages of debris flow evaluation.

(5) Calibration of the dynamic model with well-documented case histories of debris flows. Model calibration on the basis of a number of field observations provides the primary means to verify theoretical formulation of dynamic analysis in debris flow studies. Results of the parameter calibration also provide important data-bases for practical applications of the dynamic model.

(6) Development of the model incorporating GIS within numerical simulations for debris flow hazard and risk analysis. Debris flows and related phenomena occur in natural slopes and man-made slopes and earth structures. Hazard and risk assessment

in a debris flow-prone region requires integrated qualitative and quantitative analyses of data from distinct disciplines including geology, hydrology, hydrogeology, geomorphology, geotechnical engineering, economy, and sociology. The success of the integrated analysis is largely dependent on an appropriate representation and articulation of the data for study areas. Geographic information systems (GIS) provide a useful tool for efficiently managing and visualizing data from various disciplines. A combination of GIS techniques with dynamic analysis allows the development of a conceptual geological model from which slope stability analysis and runout prediction can be generated. The GIS-based numerical simulation could also facilitate application of the results from dynamic analysis into hazard assessments related to debris flows.

References

Alarcon-Guzman, A., Leonards, G.A., and Chameau, J.L. 1988. Undrained monotonic and cyclic strength of sands. Journal of Geotechnical Engineering, 114(10): 1089-1109.

Anderson, S.A., and Sitar, N. 1995. Analysis of rainfall-Induced debris flows. Journal of Geotechnical Engineering, 121(7): 544-552.

Aris, R. 1962. Vectors, Tensors, and the Basic Equations of Fluid Mechanics. Dover Publications, Inc., New York.

Armanini, A., and Michiue, M. 1997. Lecture Notes in Earth Science Volume 64: Recent Developments on Debris Flows Springer-Verlag, Berlin.

Asmar, B.N., Langston, P.A., and Ergenzinger, P. 2003. The potential of the discrete element method to simulate debris flow. In Proceedings of the Third International Conference on Debris-flow Hazards Mitigation: Mechanics, Prediction, and Assessment. Edited by D. Richenmann, and Chen, C.L. Davos, Switzerland. 10-12 September 2003. Millpress, Rotterdam, Vol.1, pp. 435-445.

Ayotte, D., and Hungr, O. 1998. Runout analysis of debris flows and debris avalanches in Hong Kong. Final report prepared for the Geotechnical Engineering Office, Hong Kong.

Ayotte, D., and Hungr, O. 2000. Calibration of a runout prediction model for debris-flows and avalanches. In Proceedings of the Second International Conference on Debris-Flow Hazards Mitigation: Mechanics, Prediction, and Assessment. Edited by G.F. Wieczorek and N.D. Naeser. Taipei, Taiwan. 16-18 August 2000. A.A. Balkema, Rotterdam, pp. 505-514.

Bagnold, R.A. 1954. Experiments on gravity-free dispersion of large solid spheres in Newtonian fluid under shear. Proceedings of the Royal Society of London. Series A, Mathematical and Physical Sciences, 225(1160): 49-63.

Bartelt, P., Salm, B., and Gruber, U. 1999. Calculating dense-snow avalanche runout using a Voellmy-fluid model with active/passive longitudinal staining. Journal of Glaciology, 45: 242-254.

Barbolini, M., Gruber, U., Keylock, C.J., Naaim, M., and Savi, F. 2000. Application of statistical and hydraulic-continuum dense-snow avalanche models to five real European sites. Cold Regions Science and Technology, 31:133-149.

Been, K., Jefferies, M.G., and Hachey, J. 1991. The critical state of sands. Geotechnique, 41(3): 365-381.

Bertolo, P., and Wieczorek, G.F. 2005. Calibration of numerical models for small debris flows in Yosemite Valley, California, USA. Natural Hazards and Earth System Sciences, 5: 993-1001.

Bishop, A.W., and Henkel, D.J. 1962. The measurement of soil properties in the triaxial test. Edward Arnold (Publishers) Ltd., London.

Byrne, P.M., Imrie, A.S., and Morgenstern, N.R. 1994. Results and implications of seismic performance studies for Duncan Dam. Canadian Geotechnical Journal, 31: 979-988.

Cagnoli, B., and Manga, M. 2004. Granular mass flows and Coulomb's friction in shear cell experiments: Implication for geophysical flows. Journal of Geophysical Research - Earth Surface, 109(F04005).

Campbell, C.S., Cleary, P.W., and Hopkins, M. 1995. Large-scale landslide simulations: Global deformation, velocities and basal friction. Journal of Geophysical Research - Solid Earth, 100: 8267-8283.

Casagrande, A. 1936. Characteristics of cohesionless soils affecting the stability of slopes and earth fills. Journal of Boston Society of Civil Engineers, Reprinted in Contributions to Soil Mechanics 1925-1940, Boston Society of Civil Engineers: 257-276.

Casagrande, A. 1965. Role of the "calculated risk" in earthwork and foundation engineering. Journal of the Soil Mechanics and Foundations Division, Proceedings of the American Society of Civil Engineers, 91(SM4): 1-40.

Castro, G. 1969. Liquefaction of Sands. Ph.D. Thesis, Harvard University, Cambridge, Massachusetts.

Castro, G., Keller, T.O., and Boynton, S.S. 1989. Re-evaluation of the Lower San Fernando Dam: Report 1, an investigation of the February 9, 1971 slide. U.S. Army Corps of Engineers Contract Report GL-89-2, Vols. 1 and 2, U.S. Army Corps of Engineers Waterways Experiment Station, Vicksburg, Mississippi.

Castro, G., Poulos, S.J., and Leathers, F.D. 1985. Re-examination of slide of Lower San Fernando Dam. Journal of Geotechnical Engineering, 111(9): 1093-1107.

Castro, G., Seed, R.B., Keller, T.O., and Seed, H.B. 1992. Steady-state strength analysis of Lower San Fernando Dam slide. Journal of Geotechnical Engineering, 118(3): 406-427.

Chen, C.L. 1987. Comprehensive review of debris flow modeling concepts in Japan. In Debris Flows/Avalanches: Process, Recognition, and Mitigation. Reviews in Engineering Geology, Vol. 7. Geological Society of America. pp. 13-29.

Chen, C.L. 1988a. Generalized viscoplastic modeling of debris flow. Journal of Hydraulic Engineering, 114(3): 237-257.

Chen, C.L. 1988b. General solutions for viscoplastic debris flow. Journal of Hydraulic Engineering, 114(3): 259-282.

Chen, C.L. 1997. Debris-flow Hazards Mitigation: Mechanics, Prediction, and Assessment. American Society of Civil Engineers, New York.

Chen, C.L., and Ling, C.H. 1996. Granular-flow rheology: Role of shear-rate number in transition regime. Journal of Engineering Mechanics, 122(5): 469-480.

Chen, H., and Lee, C.F. 2000. Numerical simulation of debris flows. Canadian Geotechnical Journal, 37: 146-160.

Chen, H., and Lee, C.F. 2002. Runout analysis of slurry flows with Bingham model.

Journal of Geotechnical and Geoenvironmental Engineering, 128(12): 1032-1042.

Chillarige, A.V., Robertson, P.K., Morgenstern, N.R., and Christian, H.A. 1997. Evaluation of the in situ state of Fraser River sand. Canadian Geotechnical Journal, 34: 510-519

Chiou, M.C., Wang, Y., and Hutter, K. 2005. Influence of obstacles on rapid granular flows. Acta Mechanica, 175: 105-122.

Corominas, J. 1996. The angle of reach as a mobility index for small and large landslides. Canadian Geotechnical Journal, 33: 260-271.

Costa, J.E., and Wieczorek, G.F. 1987. Debris Flows/Avalanches: Process, Recognition, and Mitigation. Reviews in Engineering Geology, Volume VII. Geological Society of America.

Coussot, P., and Meunier, M. 1996. Recognition, classification and mechanical description of debris flows. Earth-Science Reviews, 40: 209-227.

Coussot, P., Laigle, D., Arattano, M., Deganutti, A., and Marchi, L. 1998. Direct determination of rheological characteristics of debris flow. Journal of Hydraulic Engineering, 124(8): 865-868.

Crosta, G.B., Imposimato, S., and Roddeman, D.G. 2003. Numerical modelling of large landslides stability and runout. Natural Hazards and Earth System Sciences, 3(3): 523-538.

Crosta, G.B., Imposimato, S., Roddeman, D., Chiesa, S., and Moia, F. 2005. Small fast-moving flow-like landslides in volcanic deposits: The 2001 Las Colinas Landslide (El Salvador). Engineering Geology, 79: 185-214.

Cruden, D.M., and Varnes, D.J. 1996. Landslide types and processes. In Landslide Investigation and Mitigation. Transportation Research Board, U.S. National Research Council, Special Report 247, Washington, D.C. pp. 36-75.

Davies, T.R.H. 1982. Spreading of rock avalanche debris by mechanical fluidization.

Rock Mechanics, 15: 9-24.

Davies, T.R., and McSaveney, M.J. 1999. Runout of dry granular avalanches. Canadian Geotechnical Journal, 36: 313-320.

Davies, T.R., and McSaveney, M.J. 2002. Dynamic simulation of the motion of fragmenting rock avalanches. Canadian Geotechnical Journal, 39: 789-798.

Davies, T.R., and McSaveney, M.J., and Hodgson, K.A. 1999. A fragmentation-spreading model for long-runout rock avalanches. Canadian Geotechnical Journal, 36: 1096-1110.

Davis, A.P., Poulos, S.J., and Castro, G. 1988. Strengths backfigured from liquefaction case histories. In Proceedings of Second International Conference on Case Histories in Geotechnique Engineering. St. Louis, MO. 1-5 June 1988, pp. 1693-1701.

Dawson, R.F., Morgenstern, N.R., and Stokes, A.W. 1998. Liquefaction flowslides in rocky mountain coal mine waste dumps. Canadian Geotechnical Journal, 35: 328-343.

De Matos, M.M. 1988. Mobility of Soil and Rock Avalanches. Ph.D. thesis, University of Alberta, Edmonton, Alberta.

Denlinger, R.P., and Iverson, R.M. 2001. Flow of variably fluidized granular masses across three-dimensional terrain 2. Numerical predictions and experimental tests. Journal of Geophysical Research - Solid Earth, 106: 553-566.

Denlinger, R.P., and Iverson, R.M. 2004. Granular avalanches across irregular three-dimensional terrain: 1. Theory and computation. Journal of Geophysical Research - Earth Surface, 109: F01014.

Dickau, R., Brunsden, D., Schrott, L., and Ibsen, M.L. 1996. Landslide Recognition. John Wiley & Sons, Chichester.

Eckersley, J.D. 1985. Flowslides in stockpiled coal. Engineering Geology, 22: 13-22.

Eckersley, D. 1990. Instrumented laboratory flowslides. Geotechnique, 40(3):

489-502.

Evans, S.G., Hungr, O., and Clague, J.J. 2001. Dynamics of the 1984 rock avalanche and associated distal debris flow on Mount Cayley, British Columbia, Canada; implications for landslide hazard assessment on dissected volcanoes. Engineering Geology, 61: 29-51.

Fannin, R.J., and Wise, M.P. 2001. An empirical-statistical model for debris flow travel distance. Canadian Geotechnical Journal, 38: 982-994.

Fear, C.E. 1996. In-situ testing for liquefaction evaluation of sandy soils. Ph.D. thesis, University of Alberta, Edmonton, Alberta.

Fear, C.E., and Robertson, P.K. 1995. Estimating the undrained shear strength of sand: a theoretical framework. Canadian Geotechnical Journal, 32(859-870).

Fell, R., Hungr, O., Leroueil, S., and Riemer, W. 2000. Keynote Lecture - Geotechnical engineering of the stability of natural slopes, and cuts and fills in soil. In GeoEng 2000: An International Conference on Geotechnical and Geological Engineering. Melbourne, Australia. 19-24 November 2000. Technomic Publishing Company, Inc., Lancaster, Pennsylvania, Vol.1: Invited Papers, pp. 21-120.

Finlay, P.J., Mostyn, G.R., and Fell, R. 1999. Landslide risk assessment: prediction of travel distance. Canadian Geotechnical Journal, 36: 556-562.

Fukuoka, H., Wang, G., Sassa, K., Wang, F., and Matsumoto, T. 2004. Earthquake-induced rapid long-traveling flow phenomenon: May 2003 Tsukidate landslide in Japan. Landslides, 1(2): 151-155.

Golder Associates Ltd. 1992. Runout characteristics of debris from dump failures in mountainous terrain, Stage 1: data collection. Report to Supply and Services Canada, Contract No. 23440-0-9198/01-X8G.

Golder Associates Ltd. 1995. Runout characteristics of debris from dump failures in mountainous terrain, Stage 2: analysis, modeling and prediction. Report to Supply and Services Canada, Contract No. 23440-0-9198/01-X8G.

Gray, J.M.N.T., Wieland, M., and Hutter, K. 1999. Gravity-driven free surface flow of granular avalanches over complex basal topography. Proceedings of the Royal Society A: Mathematical, Physical and Engineering Sciences, 455: 1841-1874.

Greve, R., and Hutter, K. 1993. Motion of a granular avalanche in a convex and concave curved chute: experiments and theoretical predictions. Philosophical Transactions of the Royal Society A: Physical Sciences and Engineering, 342(1666): 573-600.

Greve, R., Koch, T., and Hutter, K. 1994. Unconfined flow of granular avalanches along a partly curved surface. I. Theory. Proceedings of the Royal Society A: Mathematical, Physical and Engineering Sciences, 445(1924): 399-413.

Han, G., and Wang, D. 1996. Numerical modeling of Anhui debris flow. Journal of Hydraulic Engineering, 122(5): 262-265.

Hazen, A. 1918. A study of the slip in the Calaveras dam. Engineering News - Record, 81(26): 1158-1164.

Hazen, A. 1920. Hydraulic-fill dams. Transactions of the American Society of Civil Engineers, 83(No.1458): 1713-1821.

Hildebrand, F.B. 1976. Advanced calculus for applications. Prentice-Hall, Englewood Cliffs, New Jersey.

Hryciw, R.D., Vitton, S., and Thomann, T.G. 1990. Liquefaction and flow failure during seismic exploration. Journal of Geotechnical Engineering, 116(12): 1881-1899.

Hsu, K.J. 1975. Catastrophic debris streams (Sturzstroms) generated by rockfalls. Geological Society of America Bulletin, 86: 129-140.

Huang, X., and Garcia, M.H. 1997. A perturbation solution for Bingham-plastic mudflows. Journal of Hydraulic Engineering, 123(11): 986-994.

Hungr, O. 2003. User's Manual of DAN-W: Dynamic Analysis of Landslides.

Hungr, O. 2000. Analysis of debris flow surges using the theory of uniformly progressive flow. Earth Surface Processes and Landforms, 25: 483-495.

Hungr, O. 1995. A model for the runout analysis of rapid flow slides, debris flows, and avalanches. Canadian Geotechnical Journal, 32: 610-623.

Hungr, O. 1998. Mobility of landslides in Hong Kong: pilot analysis using a numerical model. Report prepared for the Geotechnical Engineering Office, Hong Kong.

Hungr, O., and Evans, S.G. 1996. Rock avalanche runout prediction using a dynamic model. In Proceedings of the Seventh International Symposium on Landslides. Edited by K. Senneset. Trondheim. 17-21 June 1996. A.A.Balkema, Rotterdam, Vol.1, pp. 233-238.

Hungr, O., and Evans, S.G. 1997. A dynamic model for landslides with changing mass. In Proceedings of IAEG International Symposium on Engineering Geology and Environment. Edited by P.G. Marinos, G.C. Koukis, G.C. Tsiambaos, and G.C. Stournaras. Athens. June 1997. A.A.Balkema, Rotterdam, pp. 719-724.

Hungr, O., and Evans, S.G. 2004. Entrainment of debris in rock avalanches: An analysis of a long run-out mechanism. Geological Society of America Bulletin, 116: 1240-1252.

Hungr, O., and Morgenstern, N.R. 1984a. Experiments on the flow behaviour of granular materials at high velocity in an open channel. Geotechnique, 34(3): 405-413.

Hungr, O., and Morgenstern, N.R. 1984b. High velocity ring shear tests on sand. Geotechnique, 34(3): 415-421.

Hungr, O., Corominas, J., and Eherhardt, E. 2005. Estimating landslide motion mechanism, travel distance and velocity. In Proceedings on International Conference on Landslide Risk Management. Edited by O. Hungr, R. Fell, R. Couture, and E. Eberhardt. Taylor & Francis Group, pp. 99-128.

Hungr, O., Evans, S.G., Bovis, M., and Hutchinson, J.N. 2001. A review of the classification of landslides of the flow type. Environmental & Engineering

Geoscience, 7(3): 221-238.

Hungr, O., Dawson, R.F., Kent, A., Campbell, D., and Morgenstern, N.R. 2002. Rapid flow slides of coal-mine waste in British Columbia, Canada. In Catastrophic landslides: Effects, occurrence and mechanisms. Reviews in Engineering Geology, Vol. 15. Geological Society of America. pp. 191-208.

Hunt, B. 1994. Newtonian fluid mechanics treatment of debris flows and avalanches. Journal of Hydraulic Engineering, 120: 1350-1363.

Hunt, M.L., Zenit, R., Campbell, C.S., and Brennen, C.E. 2002. Revisiting the 1954 suspension experiments of R.A. Bagnold. Journal of Fluid Mechanics, 452: 1-24.

Hunter, G., and Fell, R. 2003. Travel distance angle for "rapid" landslide in constructed and natural soil slopes. Canadian Geotechnical Journal, 40: 1123-1141.

Hutchinson, J.N. 1986. A sliding-consolidation model for flow slides. Canadian Geotechnical Journal, 23: 115-126.

Hutchinson, J.N. 1988. Morphological and geotechnical parameters of landslides in relation to geology and hydrogeology. In Proceedings of the Fifth International Symposium on Landslides. Edited by C. Bonnard. Lausanne, Switzerland. 10-15 July 1988. A.A.Balkma, Vol.1, pp. 3-35.

Hutter, K. 2005. Geophysical granular and particle-laden flows: review of the field. Philosophical Transactions of the Royal Society A: Mathematical, Physical and Engineering Sciences, 363(1832): 1497-1505.

Hutter, K., and Koch, T. 1991. Motion of a granular avalanche in an exponentially curved chute: experiments and theoretical predictions. Philosophical Transactions of the Royal Society A: Physical Sciences and Engineering, 334(1633): 93-138.

Hutter, K., Koch, T., and Savage, S.B. 1995. The dynamics of avalanches of granular materials from initiation to runout. Part II. Experiments. Acta Mechanica, 109: 127-165.

Imran, J., Parker, G., Locat, J., and Lee, H. 2001. 1D numerical model of muddy subaqueous and subaerial debris flows. Journal of Hydraulic Engineering, 127(11): 959-968.

Ishihara, K. 1993. Liquefaction and flow failure during earthquakes. Geotechnique, 43: 349-416.

Iverson, R.M. 1997. The physics of debris flows. Reviews of Geophysics, 35(3): 245-296.

Iverson, R.M. 2003. The debris-flow rheology myth. In Proceedings of the Third International Conference on Debris-flow Hazards Mitigation: Mechanics, Prediction, and Assessment. Edited by D. Richenmann, and Chen, C.L. Davos, Switzerland. 10-12 September 2003. Millpress, Rotterdam, Vol.1, pp. 303-314.

Iverson, R.M., and Denlinger, R.P. 2001. Flow of variably fluidized granular masses across three-dimensional terrain 1. Coulomb mixture theory. Journal of Geophysical Research - Solid Earth, 106: 537-552.

Iverson, R.M., and Vallance, J.W. 2001. New views of granular mass flows. Geology, 29(2): 115-118.

Iverson, R.M., Logan, M., and Denlinger, R.P. 2004. Granular avalanches across irregular three-dimensional terrain: 2. Experimental tests. Journal of Geophysical Research - Earth Surface, 109: F01015.

Iverson, R.M., Reid, M.E., and LaHusen, R.G. 1997. Debris-flow mobilization from landslides. Annual Review of Earth and Planetary Sciences, 25:85-138.

Jakob, M. 2005. A size classification for debris flows. Engineering Geology, 79: 151-161.

Jakob, M., and Hungr, O. 2005. Debris-flow Hazards and Related Phenomena. Praxis Publishing Ltd, Chichester.

Jan, C.D., and Shen, H.W. 1997. Review dynamic modeling of debris flows. In Lecture Notes in Earth Sciences 64: Recent Developments on Debris Flows. Springer, Berlin. pp. 93-116.

Jefferies, M., and Been, K. 2006. Soil Liquefaction: A critical state approach. Taylor & Francis, New York.

Jeyapalan, J.K., Duncan, M., and Seed, H.B. 1983a. Analysis of flow failures of mine tailings dams. Journal of Geotechnical Engineering, 109(2): 150-171.

Jeyapalan, J.K., Duncan, M., and Seed, H.B. 1983b. Investigation of flow failures of tailings dams. Journal of Geotechnical Engineering, 109(2): 172-189.

Jin, M., and Fread, D.L. 1999. 1D modeling of mud/debris unsteady flows. Journal of Hydraulic Engineering, 125(8): 827-834.

Johnson, A.M. 1970. Physical Processes in Geology. Freeman, Cooper & Company, San Francisco.

Johnson, A.M. 1996. A model for grain flow and debris flow. U.S. Geological Survey Open-File Report 96-728.

Johnson, A.M., and Rodine, J.R. 1984. Debris flow. In Slope Instability. John Wiley & Sons, Chichester. pp. 257-361.

Julien, P.Y., and Lan, Y. 1991. Rheology of hyperconcentrations. Journal of Hydraulic Engineering, 117(3): 346-353.

Kelfoun, K., and Druitt, T.H. 2005. Numerical modeling of the emplacement of Socompa rock avalanche, Chile. Journal of Geophysical Research - Solid Earth, 110: B12202.

Kern, M.A., Tiefenbacher, F., and McElwaine, J.N. 2004. The rheology of snow in large chute flows. Cold Regions Science and Technology, 39: 181-192.

Konrad, J.M., and Watts, B.D. 1995. Undrained shear strength for liquefaction flow failure analysis. Canadian Geotechnical Journal, 32: 783-794.

Korner, H.J. 1980. The energy-line method in the mechanics of avalanches. Journal of Glaciology, 26: 501-505.

Kramer, S.L. 1988. Triggering of liquefaction flow slides in coastal soil deposits.

Engineering Geology, 26: 17-31.

Kramer, S.L., and Seed, H.B. 1988. Initiation of soils liquefaction under static loading conditions. Journal of Geotechnical Engineering, 114(4): 412-430.

Kwan, J.S.H., and Sun, H.W. 2006. An improved landslide mobility model. Canadian Geotechnical Journal, 43: 531-539.

Laigle, D., and Coussot, P. 1997. Numerical modeling of mudflows. Journal of Hydraulic Engineering, 123(7): 617-623.

Lang, R.E., Nakamura, T., Dent J.D., and Martinelli, M. 1985. Avalanche flow dynamics with material locking. Annals of Glaciology, 6: 5-8.

Legros, F. 2002. The mobility of long-runout landslides. Engineering Geology, 63: 301-331.

Lajeunesse, E., Monnier, J.B., and Homsy, G.M. 2005. Granular slumping on a horizontal surface. Physics of Fluids, 17: 103302.

Lindenberg, J., and Koning, H.L. 1981. Critical density of sand. Geotechnique, 31(2): 231-245.

Lo, K.H., and Chau, K.T. 2003. Debris-flow simulations for Tsing Shan in Hong Kong. In Proceedings of the Third International Conference on Debris-flow Hazards Mitigation: Mechanics, Prediction, and Assessment. Edited by D. Richenmann and C.L. Chen. Davos, Switzerland. 10-12 September 2003. Millpress, Rotterdam, Vol.1, pp. 577-588.

Locat, P., Couture, R., Leroueil, S., Locat, J., and Jaboyedoff, M. 2006. Fragmentation energy in rock avalanches. Canadian Geotechnical Journal, 43: 830-851.

Lucia, P.C. 1981. Review of Experiences with Flow Failures of Tailings Dams and Waste Impoundments. Ph.D. Thesis, University of California, Berkeley.

Major, J.J. 1997. Depositional processes in large-scale debris-flow experiments. The Journal of Geology, 105: 345-365.

Major, J.J. 2000. Gravity-driven consolidation of granular slurries - implications for debris-flow deposition and deposit characteristics. Journal of Sedimentary Research, 70(1): 64-83.

Major, J.J., and Iverson, R.M. 1999. Debris-flow deposition: Effects of pore-fluid pressure and friction concentrated at flow margins. Geological Society of America Bulletin, 111(10): 1424-1434.

Major, J.J., and Pierson, T.C. 1992. Debris flow rheology: experimental analysis of fine-grained slurries. Water Resources Research, 28(3): 841-857.

McClung, D.M. 1983. Derivation of Voellmy's maximum speed and run-out estimates from a center-of-mass model. Journal of Glaciology, 29: 350-352.

McDougall, S., and Hungr, O. 2004. A model for the analysis of rapid landslide motion across three-dimensional terrain. Canadian Geotechnical Journal, 41: 1084-1097.

McDougall, S., and Hungr, O. 2005. Dynamic modelling of entrainment in rapid landslides. Canadian Geotechnical Journal, 42: 1437-1448.

McDougall, S., Boultbee, N., Hungr, O., Stead, D., and Schwab, J.W. 2006. The Zymoetz River landslide, British Columbia, Canada: description and dynamic analysis of a rock slide-debris flow. Landslides, 3: 195-204.

Mei, C.C., and Yuhi, M. 2001. Slow flow of a Bingham fluid in a shallow channel of finite width. Journal of Fluid Mechanics, 431: 135-159.

Miao, T., Liu, Z., Niu, Y., and Ma, C. 2001. A sliding block model for the runout prediction of high-speed landslides. Canadian Geotechnical Journal, 38: 217-226.

Middlebrooks, T.A. 1942. Fort Peck slide. Transactions of the American Society of Civil Engineers, 107(Paper No. 2144): 723-764.

Mikos, M., Fazarinc, R., Majes, B., Rajar, R., Zagar, D., Krzyk, M., Hojnik, T., and Cetina, M. 2006. Numerical simulation of debris flows triggered from the Strug rock fall source area, W Slovenia. Natural Hazards and Earth System Sciences, 6: 261-270.

Mishima, S., and Kimura, H. 1970. Characteristics of landslides and embankment failures during the Tokachoki earthquake. Soils and Foundations, 10(2): 39-51.

Miura, K., Yoshida, N., and Wakamatsu, K. 1995. Damage to fill embankment during 1993 Kushiro-Oki earthquake. In Proceedings of the First International Conference on Earthquake Geotechnical Engineering. Edited by K. Ishihara. Tokyo. A.A. Balkema, Vol.2, pp. 1057-1062.

Miura, K., Yoshida, N., Nishimura, M., and Wakamatsu, K. 1998. Stability analysis of the fill embankment damaged by recent two major earthquakes in Hokkaido, Japan. In Proceedings of a Specialty Conference on Geotechnical Earthquake Engineering and Soil Dynamics III, Geotechnical Special Publication No. 75. Edited by P. Dakoulas, M. Yegian, and B. Holtz. University of Washington, Seattle, Washington. 3-6 August 1998. American Society of Civil Engineers, Vol.2, pp. 926-937.

Monaghan, J.J. 1992. Smoothed particle hydrodynamics. Annual Review of Astronomy and Astrophysics, 30: 543-574.

Morgenstern, N.R. 1967. Submarine slumping and the initiation of turbidity currents. In Proceedings of the International Research Conference on Marine Geotechnique. Edited by A.F. Richards. Monticello, Illinois. University of Illinois Press, pp. 189-220.

Morgenstern, N.R. 1978. Mobile soil and rock flows. Geotechnical Engineering, 9: 123-141.

Morgenstern, N.R. 1992. The evaluation of slope stability: A 25 year perspective. In Stability and Performance of Slope and Embankments II, Geotechnical Special Publication No. 31. American Society of Civil Engineers.

Morgenstern, N.R. 2001. Terzaghi and liquefaction flow slides. In Reports on Geotechnical Engineering, Soil Mechanics and Rock Engineering. Vienna Technical University, pp. 64-72.

Moriwaki, H., Takashi, I., Hattanji, T., Sassa, K., Ochiai, H., and Wang, G. 2004.

Failure process in a full-scale landslide experiment using a rainfall simulator. Landslides, 1(4): 277-288.

Naef, D., Rickenmann, D., Rutschmann, P., and McArdell, B.W. 2006. Comparison of flow resistance relations for debris flows using a one-dimensional finite element simulation model. Natural Hazards and Earth System Sciences, 6: 155-165.

O'Brien, J.S. 2003. FLO-2D Users Manual, Version 2003. FLO-2D Software, Inc.

O'Brien, J.S., and Julien, P.Y. 1985. Physical properties and mechanics of hyperconcentrated sediment flows. In Proceedings of the Specialty Conference on Delineation of Landslides, Flash Flood and Debris Flow Hazards in Utah. Edited by D.S. Bowles. Logan, Utah. June 1984, pp. 260-279.

O'Brien, J.S., and Julien, P.Y. 1988. Laboratory analysis of mudflow properties. Journal of Hydraulic Engineering, 114(8): 877-887.

O'Brien, J.S., Julien, P.Y., and Fullerton, W.T. 1993. Two-dimensional water flood and mudflow simulation. Journal of Hydraulic Engineering, 119(2): 244-261.

Ochiai, H., Okada, Y., Furuya, G., Okura, Y., Matsui, T., Sammori, T., Terajima, T., and Sassa, K. 2004. A fluidized landslide on a natural slope by artificial rainfall. Landslides, 1(3): 211-219.

Okura, Y., Kitahara, H., and Sammori, T. 2000a. Fluidization in dry landslide. Engineering Geology, 56: 347-360.

Okura, Y., Kitahara, H., Sammori, T., and Kawanami, A. 2000b. The effects of rockfall volume on runout distance. Engineering Geology, 58: 109-124.

Olson, S.M. 2001. Liquefaction Analysis of Level and Sloping Ground Using Field Case Histories and Penetration Resistance. Ph.D. thesis, University of Illinois at Urbana-Champaign, Urbana, Illinois.

Olson, S.M. 2004. Personal communication.

Olson, S.M., and Stark, T.D. 2002. Liquefied strength ratio from liquefaction flow failure case histories. Canadian Geotechnical Journal, 39: 629-647.

Olson, S.M., Stark, T.D., Walton, W.H., and Castro, G. 2000. 1907 static liquefaction flow failure of the North Dike of Wachusett Dam. Journal of Geotechnical and Geoenvironmental Engineering, 126(12): 1184-1193.

Parsons, J.D., Whipple, K.X., and Simoni, A. 2001. Experimental study of grain-flow, fluid-mud transition in debris flows. The Journal of Geology, 109: 427-447.

Pastor, M., Quecedo, M., Fernandez Merodo, J.A., Herreros, M.I., Gonzalez, E., and Mira, P. 2002. Modelling tailings dams and mine waste dumps failures. Geotechnique, 52(8): 579-591.

Pastor, M., Quecedo, M., Gonzalez, E., Herreros, M.I., Fernandez Merodo, J.A., and Mira, P. 2004. Simple approximation to bottom friction for Bingham fluid depth integrated models. Journal of Hydraulic Engineering, 130(2): 149-155.

Perla, R., Cheng, T.T., and McClung, D.M. 1980. A two-parameter model of snow-avalanche motion. Journal of Glaciology, 26: 197-207.

Phillips, C.J., and Davies, T.R.H. 1991. Determining rheological parameters of debris flow material. Geomorphology, 4: 101-110.

Pierson, T.C. 2005. Hyperconcentrated flow - transitional process between water flow and debris flow. In Debris-flow Hazards and Related Phenomena. Praxis Publishing Ltd, Chichester. pp. 159-202.

Pierson, T.C., and Costa, J.E. 1987. A rheologic classification of subaerial sediment-water flows. In Debris Flows/Avalanches: Process, Recognition, and Mitigation. Reviews in Engineering Geology, Vol. 7. Geological Society of America. pp. 1-12.

Pitman, E.B., and Le, L. 2005. A two-fluid model for avalanche and debris flows. Philosophical Transactions of the Royal Society A: Mathematical, Physical and Engineering Sciences, 363(1832): 1573-1601.

Poulos, S.J. 1981. The steady state of deformation. Journal of the Geotechnical Engineering Division, Proceedings of the American Society of Civil Engineers, 107(GT5): 553-562.

Poulos, S.J. 1988. Liquefaction and related phenomena. In Advanced Dam Engineering for Design, Construction, and Rehabilitation. Van Nostrand Reinhold, New York. pp. 292-320.

Poulos, S.J., Castro, G., and France, J.W. 1985. Liquefaction evaluation procedure. Journal of Geotechnical Engineering, 111(6): 772-792.

Pudasaini, S.P., and Hutter, K. 2003. Rapid shear flows of dry granular masses down curved and twisted channels. Journal of Fluid Mechanics, 495: 193-208.

Pudasaini, S.P., Wang, Y., and Hutter, K. 2005a. Rapid motions of free-surface avalanches down curved and twisted channels and their numerical simulation. Philosophical Transactions of the Royal Society A: Mathematical, Physical and Engineering Sciences, 363(1832): 1551-1571.

Pudasaini, S.P., Wang, Y., and Hutter, K. 2005b. Modelling debris flows down general channels. Natural Hazards and Earth System Sciences, 5: 799-819.

Quecedo, M., and Pastor, M. 2003. Finite element modelling of free surface flows on inclined and curved beds. Journal of Computational physics, 189: 45-62.

Quecedo, M., Pastor, M., Herreros, M.I., and Fernandez Merodo, J.A. 2004. Numerical modelling of the propagation of fast landslides using the finite element method. International Journal for Numerical Methods in Engineering, 59: 755-794.

Rickenmann, D. 1991 Hyperconcentrated flow and sediment transport at steep slopes. Journal of Hydraulic Engineering, 117: 1419-1439.

Rickenmann, D. 1999. Empirical relationships for debris flows. Natural Hazards, 19: 47-77.

Rickenmann, D., and Chen, L.C. 2003. Proceedings of the Third International Conference on Debris-Flow Hazards Mitigation: Mechanics, Prediction, and Assessment. Millpress, Rotterdam.

Salm, B. 2004. A short and personal history of snow avalanche dynamics. Cold

Regions Science and Technology, 39: 83-92.

Sasaki, Y., Oshiki, H., and Nishikawa, J. 1994. Embankment failure caused by the Kushiro-Oki earthquake of January 15, 1993. In Performance of Ground and Soil Structures during Earthquakes, Proceedings of the Thirteenth International Conference on Soil Mechanics and Foundation Engineering. New Delhi. 1994. The Japanese Society of Soil Mechanics and Foundation Engineering, pp. 61-68.

Sasitharan, S. 1994. Collapse Behavior of Very Loose Sand. Ph.D. thesis, University of Alberta, Edmonton, Alberta.

Sasitharan, S., Robertson, P.K., Sego, D.C., and Morgenstern, N.R. 1993. Collapse behavior of sand. Canadian Geotechnical Journal, 30: 569-577.

Sasitharan, S., Robertson, P.K., Sego, D.C., and Morgenstern, N.R. 1994. A state boundary surface for very loose sand and its practical implications. Canadian Geotechnical Journal, 31: 321-334.

Sassa, K. 1988. Geotechnical model for the motion of landslides. In Proceedings of the Fifth International Symposium on Landslides. Edited by C. Bonnard. Lausanne, Switzerland. 10-15 July 1988. A.A.Balkema, Rotterdam, Vol.1, pp. 37-55.

Sassa, K. 1996. Prediction of earthquake induced landslides. In Proceedings of the Seventh International Symposium on Landslides. Edited by K. Senneset. Trondheim. 17-21 June 1996. A.A. Balkema, Rotterdam, Vol.1, pp. 115-132.

Sassa, K. 2000. Mechanism of flows in granular soils. In GeoEng 2000: An International Conference on Geotechnical and Geological Engineering. Melbourne, Australia. 9-24 November 2000. Technomic Publishing Company, Inc., Lancaster, Pennsylvania, Vol.1: Invited Papers, pp. 1671-1702.

Sassa, K., and Wang, G. 2005. Mechanism of landslide-triggered debris flows: Liquefaction phenomena due to the undrained loading of torrent deposits. In Debris-flow Hazards and Related Phenomena. Praxis Publishing Ltd, Chichester. pp. 81-104.

Sassa, K., Fukuoka, H., Scarascia-Mugnozza, G., and Evans, S.G. 1995. Long-runout Takarazuka landslide. Landslide News, 9: 9-11.

Sassa, K., Fukuoka, H., Wang, G., and Ishikawa, T. 2004. Undrained dynamic-loading ring-shear apparatus and its application to landslide dynamics. Landslides, 1(1): 7-19.

Savage, S.B., and Hutter, K. 1989. The motion of a finite mass of granular material down a rough incline. Journal of Fluid Mechanics, 199: 177-215.

Savage, S.B., and Hutter, K. 1991. The dynamics of avalanches of granular materials from initiation to runout. Part I. Analysis. Acta Mechanica, 86: 201-223.

Savage, S.B., and Iverson, R.M. 2003. Surge dynamics coupled to pore-pressure evolution in debris flows. In Proceedings of the Third International Conference on Debris-flow Hazards Mitigation: Mechanics, Prediction, and Assessment. Edited by D. Richenmann and C.L. Chen. Davos, Switzerland. 10-12 September 2003. Millpress, Rotterdam, Vol.1, pp. 503-514.

Savage, W., and Baum, R. 2005. Instability of steep slopes. In Debris-flow Hazards and Related Phenomena. Praxis Publishing Ltd, Chichester. pp. 53-79.

Scheidegger, A.E. 1973. On the prediction of the reach and velocity of catastrophic landslides. Rock Mechanics, 5: 231-236.

Seed, H.B. 1968. Landslides during earthquakes due to soil liquefaction. Journal of the Soil Mechanics and Foundations Division, Proceedings of the American Society of Civil Engineers, 94(SM5): 193-261.

Seed, H.B. 1987. Design problems in soil liquefaction. Journal of Geotechnical Engineering, 113(8): 827-845.

Seed, H.B., Lee, K.L., Idriss, I.M., and Makdisi, F.I. 1975a. The slides in the San Fernando Dams during the earthquake of February 9, 1971. Journal of the Geotechnical Engineering Division, Proceedings of the American Society of Civil Engineers, 101(GT7): 651-688.

Seed, H.B., Idriss, I.M., Lee, K.L., and Makdisi, F.I. 1975b. Dynamic analysis of the slide in the Lower San Fernando Dam during the earthquake of February 9, 1971. Journal of the Geotechnical Engineering Division, Proceedings of the American Society of Civil Engineers, 101(GT9): 889-911.

Seed, H.B., Seed, R.B., Harder, L.F., and Jong, H.-L. 1989. Re-evaluation of the Lower San Fernando Dam: Report 2, examination of the post-earthquake slide of February 9, 1971. U.S. Army Corps of Engineers Contract Report GL-89-2, U.S. Army Corps of Engineers Waterways Experiment Station, Vicksburg, Mississippi.

Seed, R.B., and Harder, L.F., Jr. 1990. SPT-based analysis of cyclic pore pressure generation and undrained residual strength. In Proceedings of the H.B. Seed Memorial Symposium, Bi-Tech Publishing Ltd., Vol. 2, pp. 351-376.

Sharpe, C.F.S. 1938. Landslides and Related Phenomena. Columbia University Press, New York.

Siviglia, A., and Cantelli, A. 2005. Effect of bottom curvature on mudflow dynamics: theory and experiments. Water Resources Research, 41 (W11423).

Sladen, J.A., D'Hollander, R.D., and Krahn, J. 1985a. The liquefaction of sands, a collapse surface approach. Canadian Geotechnical Journal, 22: 564-578.

Sladen, J.A., D'Hollander, R.D., Krahn, J., and Mitchell, D.E. 1985b. Back analysis of the Nerlerk berm liquefaction slides. Canadian Geotechnical Journal, 22: 579-588.

Spence, K.J., and Guymer, I. 1997. Small-scale laboratory flowslides. Geotechnique, 47(5): 915-932.

Stark, T.D., and Mesri, G. 1992. Undrained shear strength of liquefied sands for stability analysis. Journal of the Geotechnical Engineering, 118(11): 1727-1747.

Steffler, P.M., and Jin, Y.-C. 1993. Depth-averaged and moment equations for moderately shallow free surface flow. Journal of Hydraulic Research, 31(1): 5-17.

Tai, Y.C., Noelle, S., Gray, J.M.N.T., and Hutter, K. 2002. Shock-capturing and front-tracking methods for granular avalanches. Journal of Computational physics, 175: 239-301.

Takahashi, T. 1978. Mechanical characteristics of debris flow. Journal of the Hydraulics Division, Proceedings of the American Society of Civil Engineers, 104(HY8): 1153-1169.

Takahashi, T. 1980. Debris flow on prismatic open channel. Journal of the Hydraulics Division, Proceedings of the American Society of Civil Engineers, 106(HY3): 381-396.

Takahashi, T. 1991. Debris Flow. A.A. Balkema, Rotterdam.

Takahashi, T., Nakagawa, H., Tarada, T., and Yamashike, Y. 1992. Routing debris flows with particle segregation. Journal of Hydraulic Engineering, 118(11): 1490-1507.

Terzaghi, K. 1943. Theoretical Soil Mechanics. John Wiley and Sons, Inc., New York.

Terzaghi, K. 1956. Varieties of submarine slope failures. In Proceedings of the Eighth Texas Conference on Soil Mechanics and Foundation Engineering, University of Texas, Austin, pp. 1-41.

Tinti, S., Bortolucci, E., and Vannini, C. 1997. A block-based theoretical model suited to gravitational sliding. Natural Hazards, 16: 1-28.

Uzuoka, R., Sento, N., Kazama, M., and Unno, T. 2005. Landslides during the earthquake on May 26 and July 26, 2003 in Miyagi, Japan. Soils and Foundations, 45(4): 149-163.

Vaid, Y.P. and Sivathayalan, S. 2000. Fundamental factors affecting liquefaction susceptibility of sands. Canadian Geotechnical Journal, 37: 592-606.

Valentino, R., Barla, G., and Montrasio, L. 2004. DEM simulation of dry granular flow in laboratory flume tests. In Proceedings of the Ninth International Symposium on Landslides. Edited by W.A. Lacerda, M. Ehrlich, S.A.B. Fontoura, and A.S.F. Sayao. Roe de Janeiro, Rrazil. 28 June to 2 July 2004. Taylor & Francis Group, London, Vol.2, pp. 1489-1495.

Varnes, D.J. 1978. Slope movement types and processes. In Landslides Analysis and Control. Special Report 176, Transportation Research Board, National Academy of Sciences, Washington, D.C., pp. 11-33.

Wang, F., Sassa, K., and Wang, G. 2002. Mechanism of a long-runout landslide triggered by the August 1998 heavy rainfall in Fukushima Prefecture, Japan. Engineering Geology, 63: 169-185.

Wang, G., and Sassa, K. 2001. Factors affecting rainfall-induced flowslides in laboratory flume tests. Geotechnique, 51(7): 587-599.

Wang, G., and Sassa, K. 2002. Post-failure mobility of saturated sands in undrained load-controlled ring shear tests. Canadian Geotechnical Journal, 39: 821-837.

Wang, G., Sassa, K., and Fukuoka, H. 2003. Downslope volume enlargement of a debris slide-debris flow in the 1999 Hiroshima, Japan, rainstorm. Engineering Geology, 69: 309-330.

Wang, G., Sassa, K., and Fukuoka, H. 2005. Seismic behavior of saturated sandy soils: case study for the May 2003 Tsukidate landslide in Japan. In Landslides - Risk Analysis and Sustainable Disaster Management. Springer-Verlag. pp. 157-164.

Wang, Y., Hutter, K., and Pudasaini, S.P. 2004. The Savage-Hutter theory: A system of partial differential equations for avalanche flows of snow, debris, and mud. ZAMM - Journal of Applied Mathematics and Mechanics, 84: 507-527.

Wang, Z., and Shen, H.T. 1999. Lagrangian simulation of one-dimensional dam-break flow. Journal of Hydraulic Engineering, 125(11): 1217-1220.

Whipple, K.X. 1997. Open-channel flow of Bingham fluids: Applications in debris-flow research. The Journal of Geology, 105: 243-262.

Wieczorek, G.F., and Naeser, N.D. 2000. Proceedings of the Second International Conference on Debris-Flow Hazards Mitigation: Mechanics, Prediction, and Assessment. A.A. Balkema, Rotterdam.

Wieland, M., Gray, J.M.N.T., and Hutter, K. 1999. Channelized free-surface flow of cohesionless granular avalanches in a chute with shallow lateral curvature. Journal of Fluid Mechanics, 392: 73-100.

Wride, C.E., McRoberts, E.C., and Robertson, P.K. 1999. Reconsideration of case histories for estimating undrained shear strength in sandy soils. Canadian Geotechnical Journal, 36: 907-933.

Yamada, G. 1966. Damage to earth structures and foundations by the Niigata earthquake June 16, 1964. in JNR. Soils and Foundations, 6(1): 1-13.

Yoshimine, M., Robertson, P.K., and Wride, C.E. 1999. Undrained shear strength of clean sands to trigger flow liquefaction. Canadian Geotechnical Journal, 36: 891-906.

Appendix A

Numerical Algorithm and Model Verification

A.1 Numerical Algorithm

The analytical model based on energy conservation in Chapter 5 is used in this study for debris-flow runout analysis. A computer program is developed for implementation of the dynamic analysis. Solution of the governing equation of the dynamic model is based on the Lagrangian finite difference approach proposed by Savage and Hutter (1989) and Hungr (1995). As shown in Figure A.1, a dynamic analysis of debris flows using the slice-based model with internal energy dissipation can be undertaken using the following procedures:

(1) Preparation of sliding surface and initial slope profile. The initial profile of a slope is obtained by comprehensive studies of site geology and construction history of the slope. The sliding surface is mainly determined by stability analysis of the pre-failure slope geometry and field investigations of the configuration of the post-failure slope.

(2) Discretization of the flow domain. A rectangular Cartesian or curvilinear coordinate system can be used in a dynamic analysis. Studies indicate that the normal slices generated in the curvilinear coordinate system tend to overlap when the slice number is greater than 15 for most liquefaction flow slide analyses. The rectangular Cartesian coordinate system is thus used in this study.

(3) At the beginning, i.e., $t = 0$, initial velocities and kinetic energy of slices are equal to zero. The initial acceleration of each slice is determined from the momentum conservation equations.

(4) At time step n after the slope movement is initiated, coefficients of lateral

stress are calculated during each time step based on deformation of the slices. The rates of the work done by interslice force, basal resistance, and gravity force are calculated. The deformation work rate (internal energy dissipation) is also computed. The velocity of each slice at time step $n+1$ is then used to determine changes in the kinetic energy of each individual slice.

(5) If the calculated kinetic energy of a slice is close to zero, the force balance is examined. If there exists an imbalance in terms of forces for a slice, the slice will accelerate according to the momentum conservation equation.

(6) The computation proceeds until the maximum velocity of the slice is less than a threshold of velocity.

(7) The back-calculated shear strength is obtained when simulating reasonably fit field observations in terms of runout distance and material distributions.

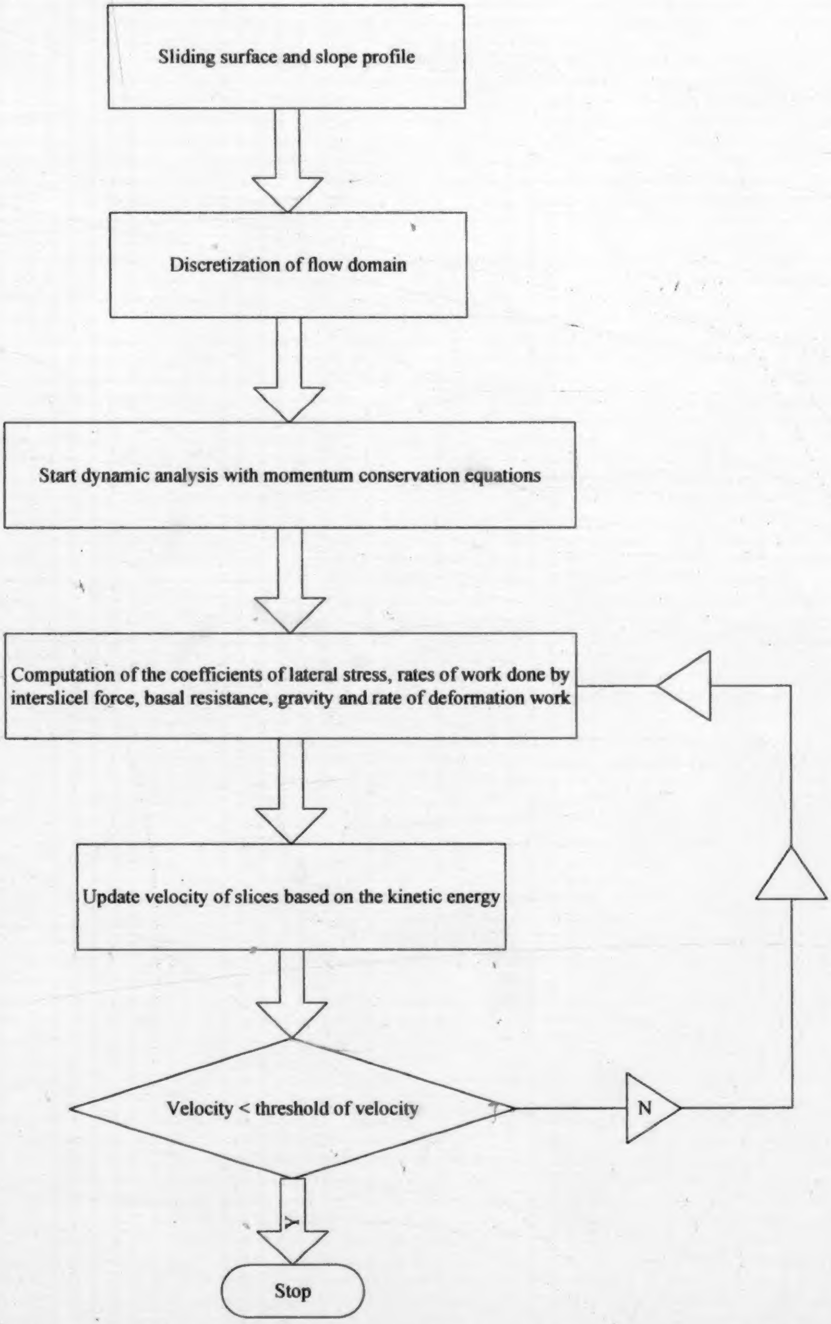
Sliding surface and slope profile
Discretization of flow domain
Start dynamic analysis with momentum conservation equations
Computation of the coefficients of lateral stress, rates of work done by interslicel force, basal resistance, gravity and rate of deformation work
Update velocity of slices based on the kinetic energy
Velocity < threshold of velocity
N
Y
Stop

Figure A.1 Flow chart of dynamic analysis based on energy consideration

A.2 Code Verification

Hand calculation of simple debris flow case has been carried out to test against computer code. The geometry of the slope is shown in Figure A.2. The sliding path consists of an inclined section connected to a horizontal surface. The inclination of the sliding path is 30°. The initial geometry of the sliding mass consists of a horizontal section of 1.5 m followed by an inclined surface with a slope of about 66.5°. The initial sliding mass is divided into 4 slices with uniform width of 0.5 m.

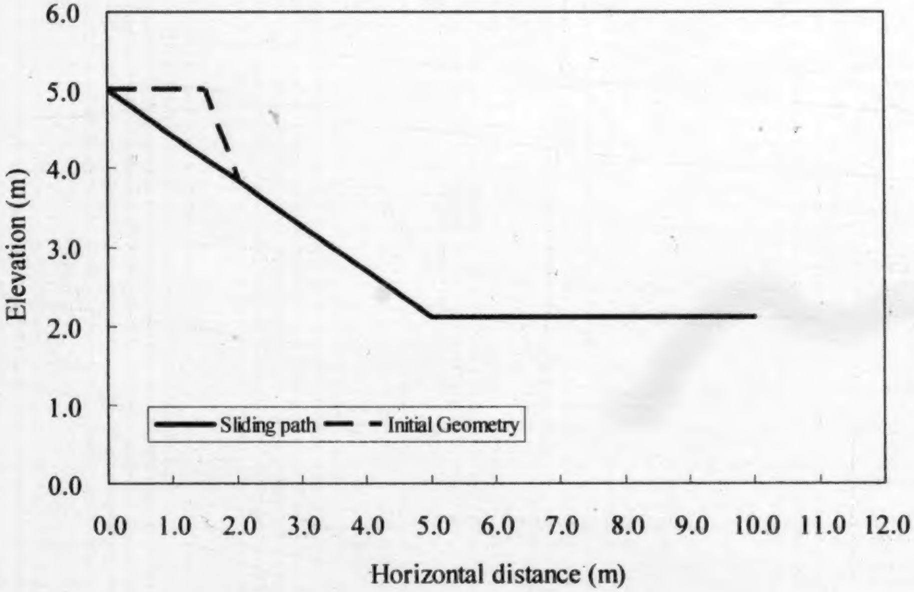

Figure A.2 Simple debris flow case for code verification

At time $t = 0$, the momentum equation is used to calculate the acceleration, velocity, and displacement of the slices.

$$m_k \frac{d\bar{u}_k}{dt} = m_k g \sin\theta_k - T_k + \left(P_{kl} - P_{kr}\right)\cos\theta_k$$

After time $t = 0$, the equations based on the energy conservation in Chapter 5 of the thesis are used to calculate the velocities and displacements of the slices.

The net work rate is calculated by summing the work rate done by gravity, lateral forces, basal resistance, and internal deformation:

$$\dot{W}_k = m_k g \overline{u}_k \sin\theta_k + \frac{1}{2} m_k g h_k \left(e_{zz}\right)_k + \left(P_l \overline{u}_l \cos\theta_l\right)_k - \left(P_r \overline{u}_r \cos\theta_r\right)_k - T_k \overline{u}_k - \int_{V_k} \tau_{ij} e_{ij} dV$$

Kinetic energy of slice k at time $t+\Delta t$:

$$E_k^{t+\Delta t} = E_k^t + \dot{W}_k^t \Delta t$$

$$E_k^t = \frac{1}{2} m_k \overline{u}_k^2$$

The center velocity of a slice at time $t+\Delta t$ is:

$$\left(u_c\right)_k^{t+\Delta t} = \sqrt{\frac{2E_k^{t+\Delta t}}{m_k}}$$

The boundary velocity is approximated as:

$$\left(u_b\right)_k^{t+\Delta t} = \frac{\left(u_c\right)_{k-1}^{t+\Delta t} + \left(u_c\right)_k^{t+\Delta t}}{2}$$

Displacement of slice boundary is:

$$\left(x_b\right)_k^{t+\Delta t} = \left(x_b\right)_k^t + \frac{\left(u_b\right)_k^t \cos\theta_k^t + \left(u_b\right)_k^{t+\Delta t} \cos\theta_k^{t+\Delta t}}{2} \Delta t$$

where $\left(x_b\right)_k^t$ and $\left(x_b\right)_k^{t+\Delta t}$ are x coordinates of boundaries of slice k at times t and $t+\Delta t$, respectively.

The height of slice k at $t+\Delta t$ is computed by:

$$\left(h_c\right)_k^{t+\Delta t} = \frac{V_k}{\left[\left(x_b\right)_{k+1}^{t+\Delta t} - \left(x_b\right)_k^{t+\Delta t}\right]}, \quad \left(h_b\right)_k^{t+\Delta t} = \frac{\left(h_c\right)_{k-1}^{t+\Delta t} + \left(h_c\right)_k^{t+\Delta t}}{2}$$

$$\left(h_b\right)_0^{t+\Delta t} = 0, \quad \left(h_b\right)_n^{t+\Delta t} = 0$$

where V_k is the volume of slice k, $\left(h_b\right)_k^{t+\Delta t}$ is the height of the left boundary of slice k at $t+\Delta t$, and $\left(h_c\right)_k^{t+\Delta t}$ is the central height of slice k at $t+\Delta t$.

Comparison between hand calculation and computer simulation has been carried out for the first 10 time steps. The size of time step for hand calculation and computer simulation is 0.1 s. The flow profiles based on hand calculation and computer simulation are presented in Figure A.3 and Figure A.4. The velocity, displacement, and height of boundary 2, 3, and 4 are shown in the Figure A.5, Figure A.6, and Figure A.7 respectively. The comprehensive comparison shown in Figures A.3 to A.7 suggests that simulation results based on computer code and hand calculation are in good agreement.

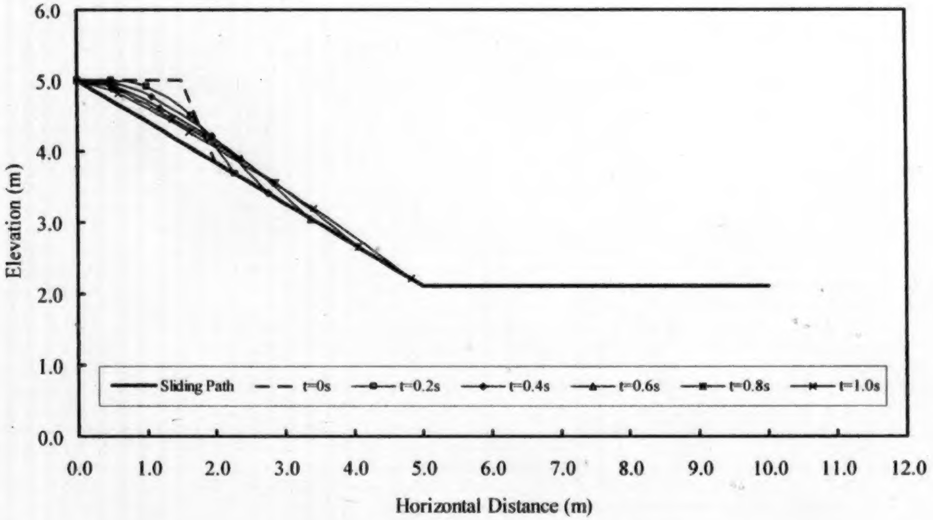

Figure A.3 Flow profiles at 0.2 s interval from hand calculation

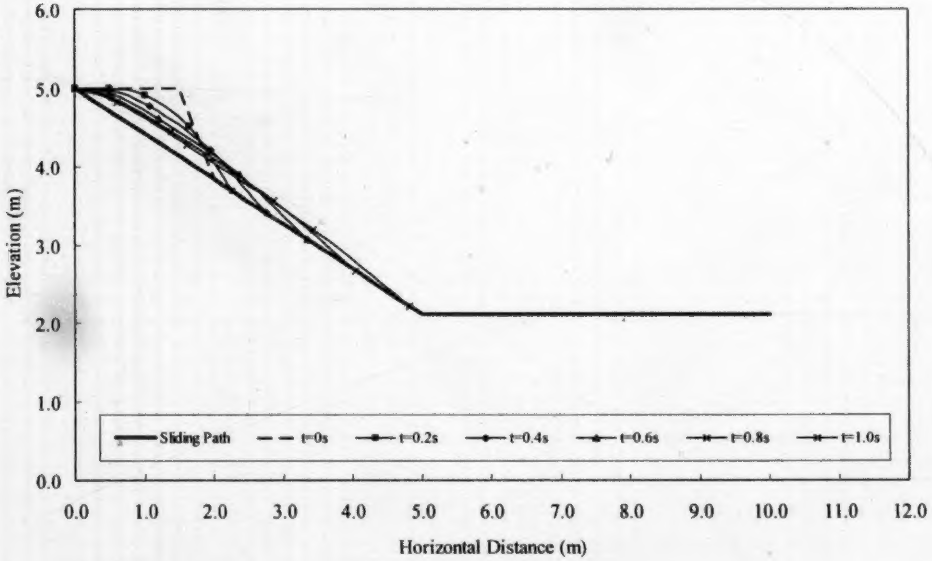

Figure A.4 Flow profiles at 0.2 s interval from computer simulation

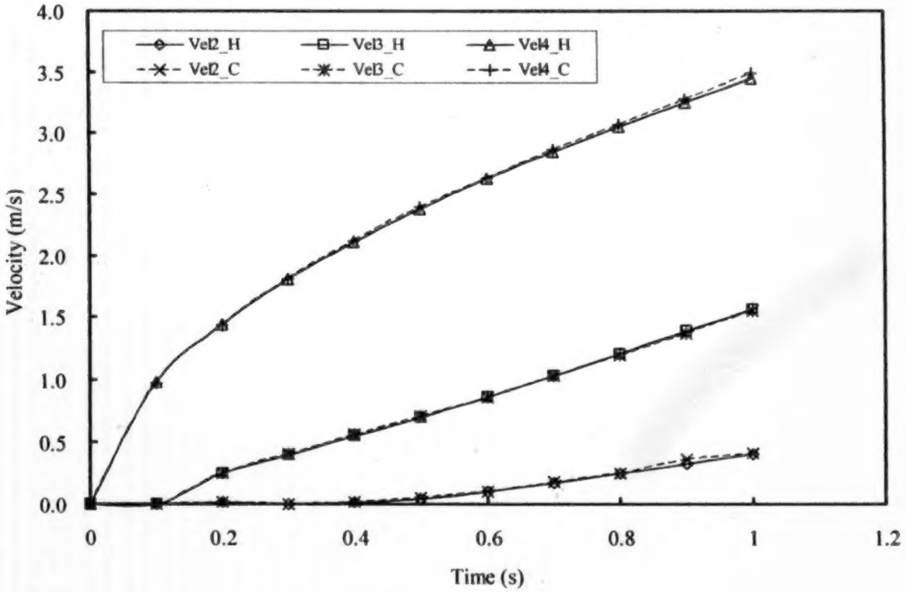

Figure A.5 Velocities on boundary 2, 3, and 4 from hand calculation (_H) and computer simulation (_C)

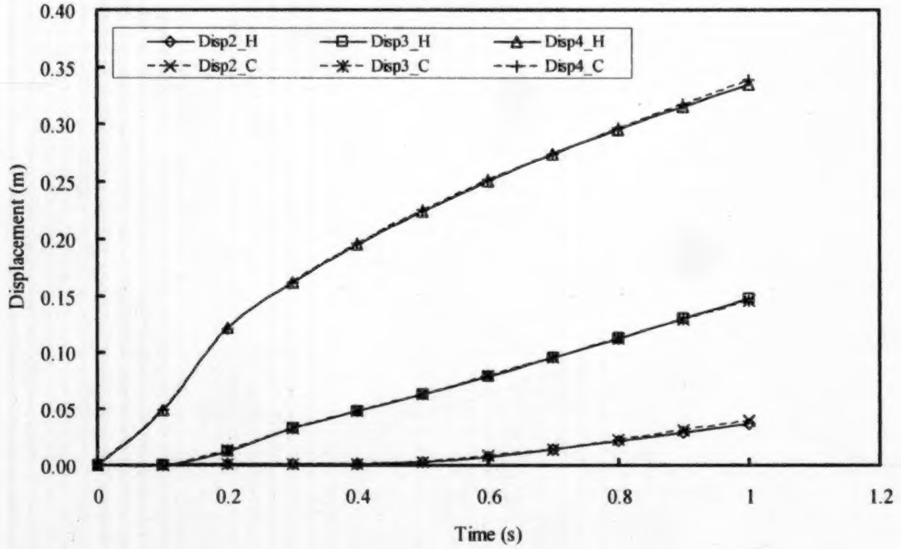

Figure A.6 Displacements on boundary 2, 3, and 4 from hand calculation (_H) and computer simulation (_C)

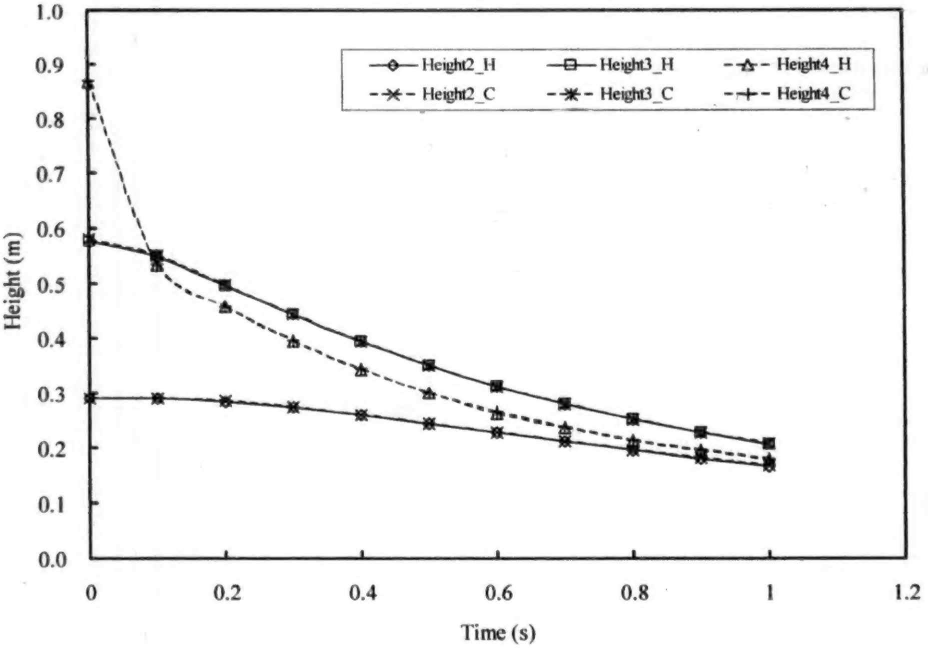

Figure A.7 Heights on boundary 2, 3, and 4 from hand calculation (_H) and computer simulation (_C)

A.3 Model Verification

A.3.1 Dam-Break Sand Flow

Dam-break sand flow has been simulated using the analytical model developed in the thesis. The initial depth of sand is taken as 10 m. Sand flow is triggered by a sudden removal of a dam. The initial geometry for dam-break case is shown in Figure A.8. The friction model is used in the dynamic analyses to compute basal resistance and internal energy dissipation. The same value is used as internal and basal friction angles in each simulation. Figure A.9 to Figure A.11 shows final geometries based on the dynamic analyses with different material strengths. Table A.1 lists the friction angle used in the simulation and average deposit angle after the dam-break induced sand flow comes to a stop. The definition of the mean deposit angle is shown in Figure A.12

Figure A.9 to Figure A.11 and Table A.1 indicate that the mean deposit angle simulated is reasonably close to the friction angle or the angle of repose.

Table A.1 Material strength and mean deposit angle

Internal Friction Angle (ϕ)	**Basal Friction Angle (ϕ_b)**	**Mean Deposit Angle**
30°	30°	32°
20°	20°	18°
10°	10°	7.5°

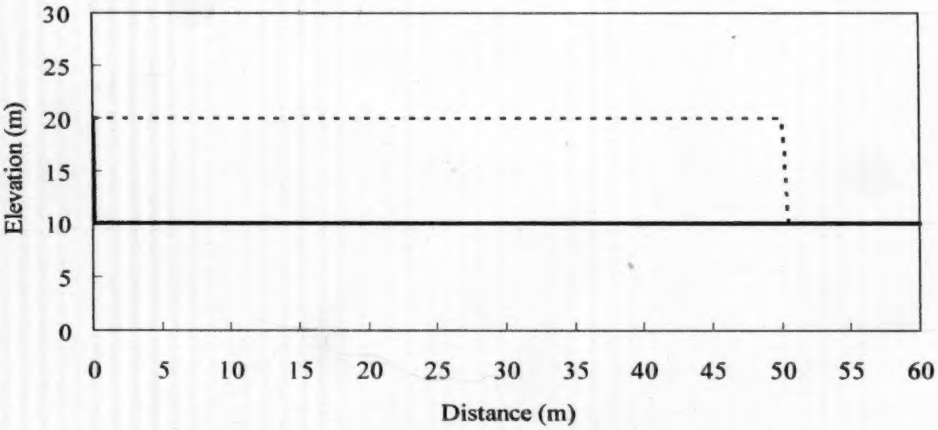

Figure A.8 Initial geometry of dam break problem

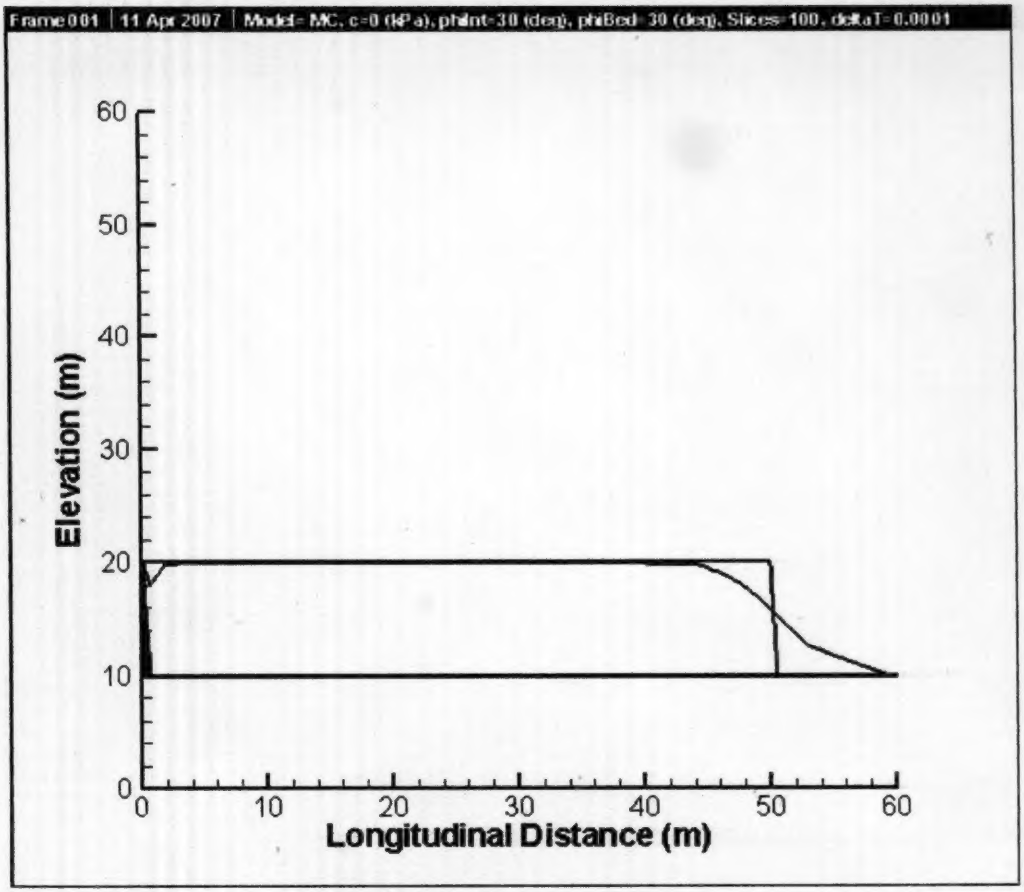

Figure A.9 Simulation of dam-break sand flow with friction model ($\phi = \phi_b = 30^\circ$)

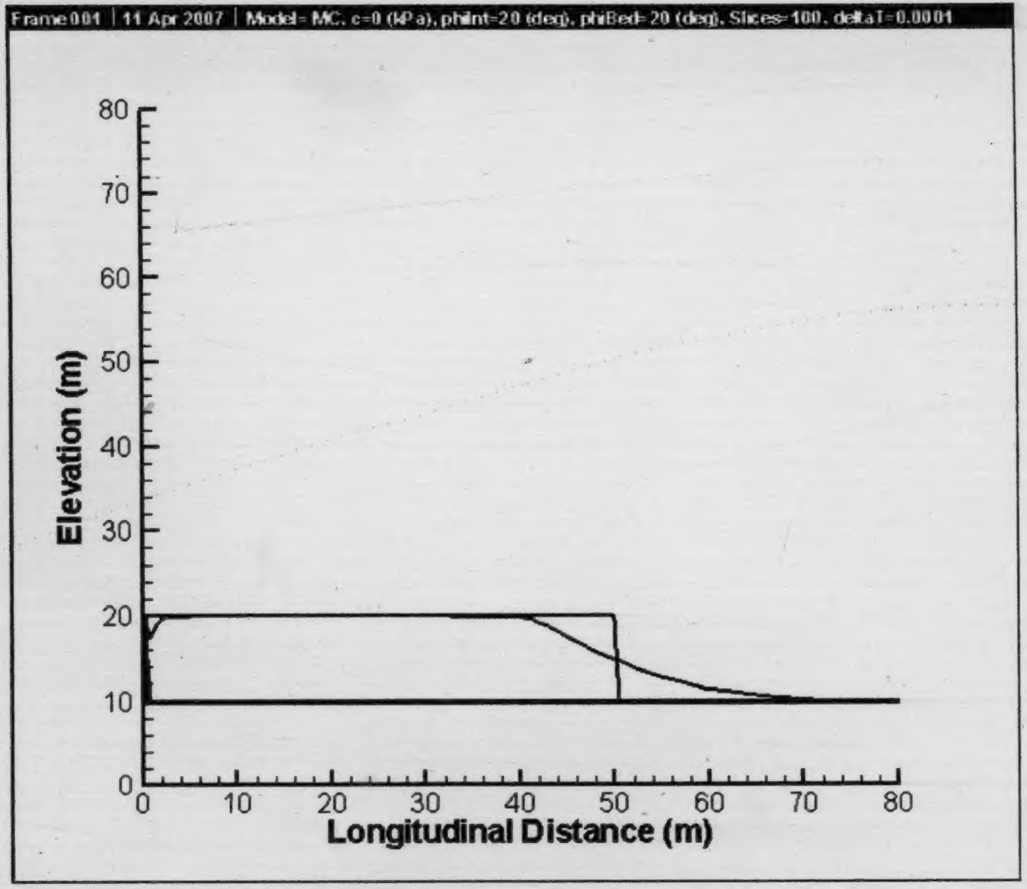

Figure A.10 Simulation of dam-break sand flow with friction model ($\phi = \phi_b = 20^\circ$)

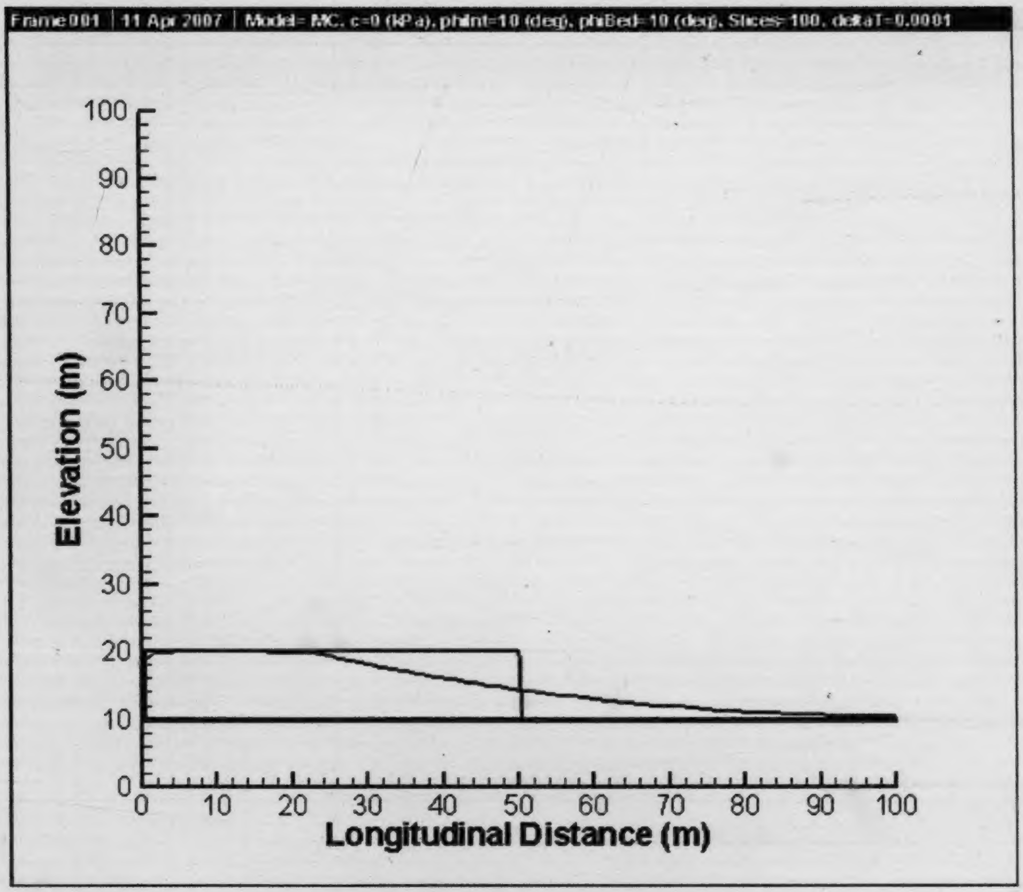

Figure A.11 Simulation of dam-break sand flow with friction model ($\phi = \phi_b = 10^\circ$)

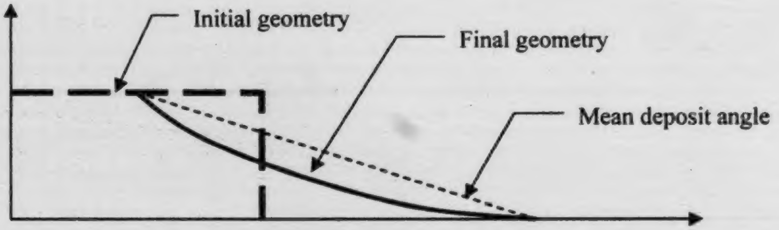
Initial geometry
Final geometry
Mean deposit angle

Figure A.12 Definition of the mean angle of dispose

A.3.2 Simulation of granular slumping on a horizontal plane

Flows induced by the collapse of initially static columns of sand over a horizontal surface were investigated experimentally by Lajeunesse et al. (2005). Effects of the initial column geometry on the flow runout behavior and internal flow structure were explored in the experiments. Granular materials used in the experiments are glass beads of diameters of 1.15 mm or 3 mm. Granular materials were initially contained within a cylinder or rectangular tank. Axisymmetric or two-dimensional granular flows were created by quickly raising the cylinder or removing the gate. The experimental observation demonstrated that the flow dynamics and final deposit depends on the initial aspect ratio of the granular column. The initial aspect ratio is defined as the ratio of the initial height to horizontal extent of the column.

Numerical simulations of the spreading of granular columns on a horizontal plane have been conducted using the dynamic model formulated in Chapter 5. The value of the internal and basal friction angles used in the analysis is 25°, which is the average of values reported by Lajeunesse et al. (2005). Figure A.13, Figure A.14, and Figure A.15 show the dynamic simulations of the granular slumping with the same initial aspect ratio of 3.2. Figure A.16 presents the normalized final profiles of simulations and experimental observations of the spreading of columns with the same initial aspect ratio but with different granular mass. The comparison of theoretical and experimental final profiles in Figure A.16 indicates that the dynamic analysis provides reasonable prediction of the runout distance for flows induced by the collapse of granular columns over a horizontal plane.

It has been observed that the granular slumping involves following two processes: (1) collapse and fall of the column, and (2) spreading of the granular mass on a horizontal plane until it comes to rest. During these processes, the initial potential energy in the tall column is converted into kinetic energy and is also dissipated because of internal deformation and basal friction. The complexity of the collective dynamics of momentum transfer and lost involved in granular slumping highlights the difficulties in modeling this class of problems within the framework of classical shallow water equations. To simulate the spreading granular mass, it appears that a model should be capable of accounting for vertical momentum transfer associated with the fall of the column and also capturing the features of the subsequent horizontal motion. It is possible to apply depth-aveaged model to modeling sideways flow of a granular mass. Unfortunately, the initial vertical column collapse and momentum transfer intrinsically violate the shallow water assumptions and can not be accounted for by shallow water approaches. It is evident that the theoretical predications are far from describing the whole process of the granular slumping and there are still many open questions to be resolved. However, it has been surprinsingly observed that the simulations carried out by using the new analytical model are able to reproduce many features of spreading of a granular mass. The model based on energy consideration provides new insights into the approaches investigating granular flows.

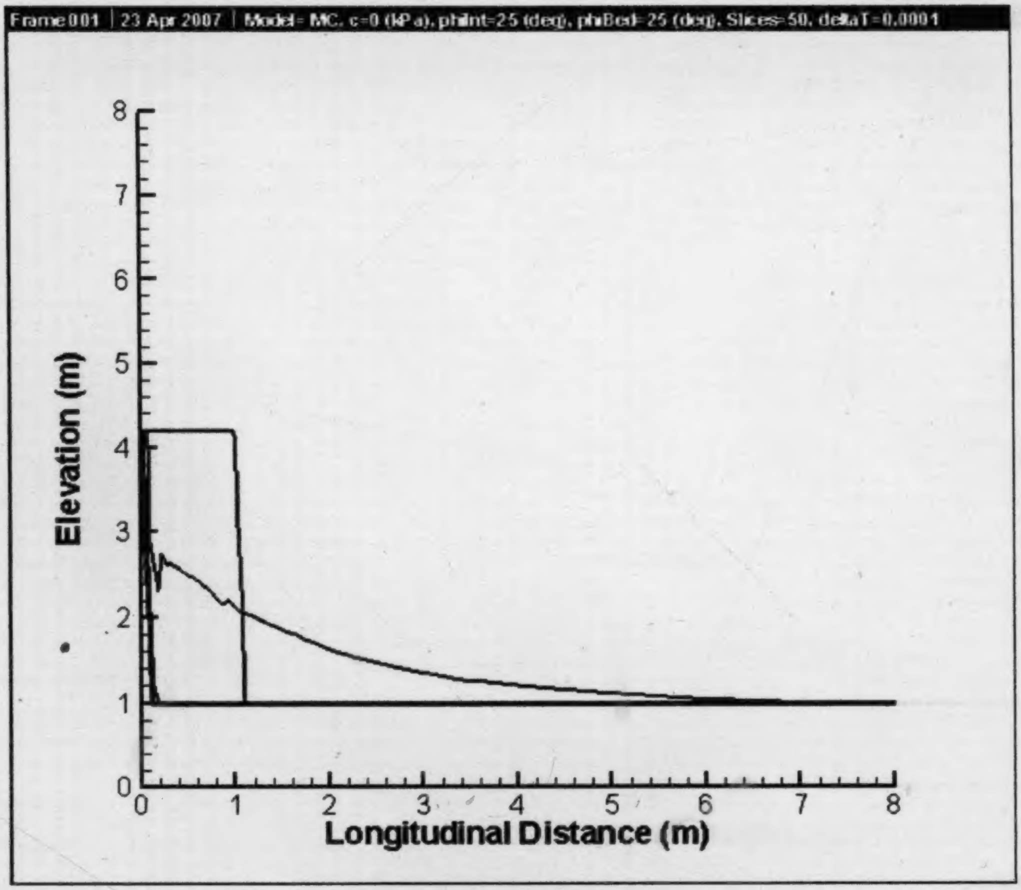

Figure A.13 Simulation of granular spreading mass with initial aspect ratio of 3.2 and height of 3.2 m

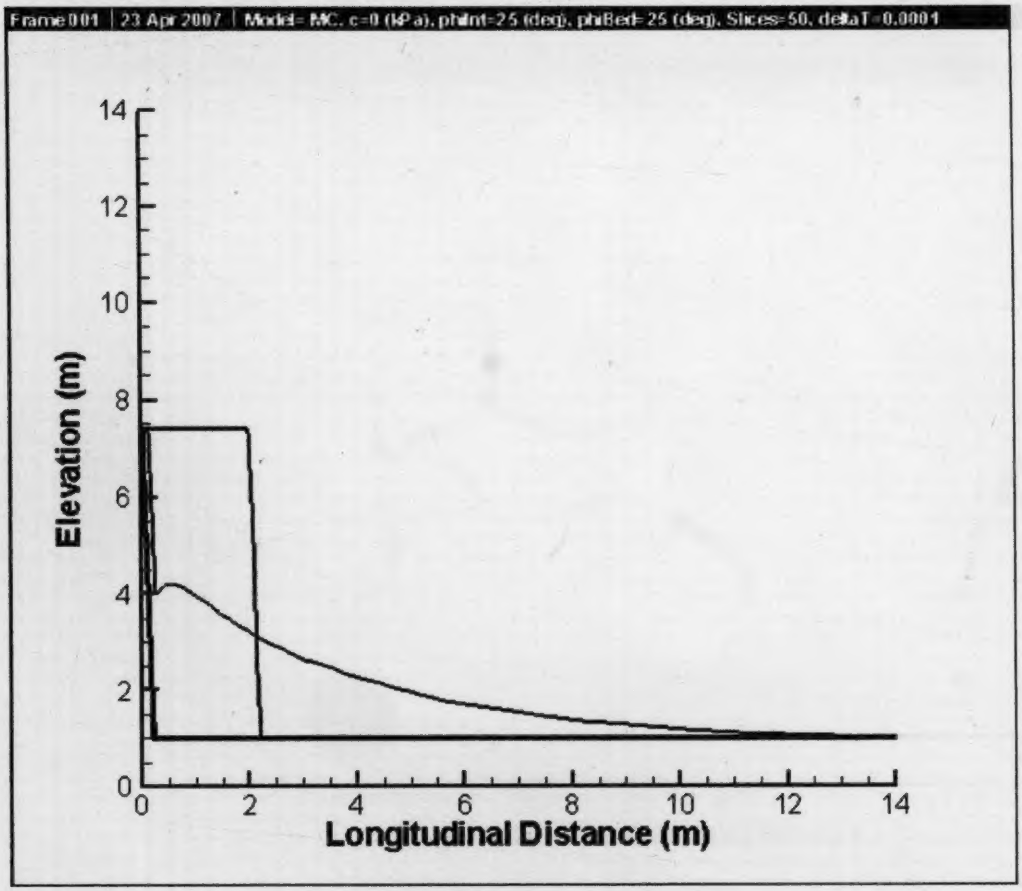

Figure A.14 Simulation of granular spreading mass with initial aspect ratio of 3.2 and height of 6.4 m

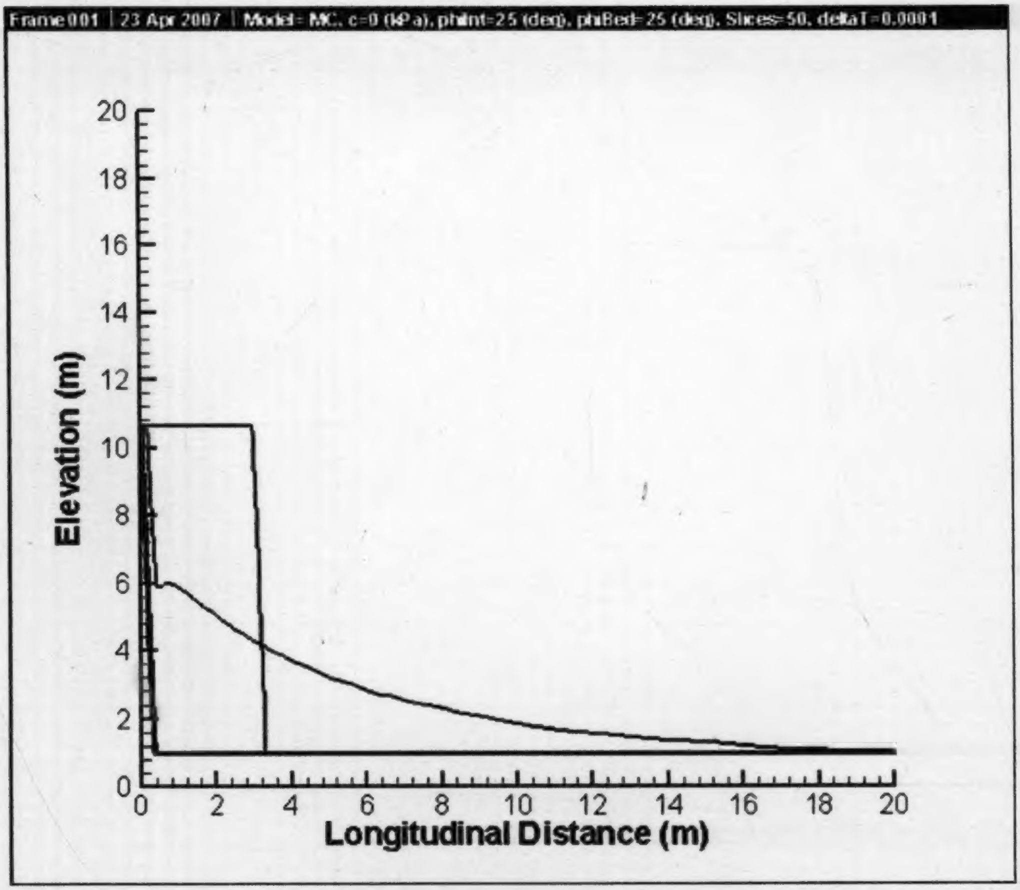

Figure A.15 Simulation of granular spreading mass with initial aspect ratio of 3.2 and height of 9.6 m

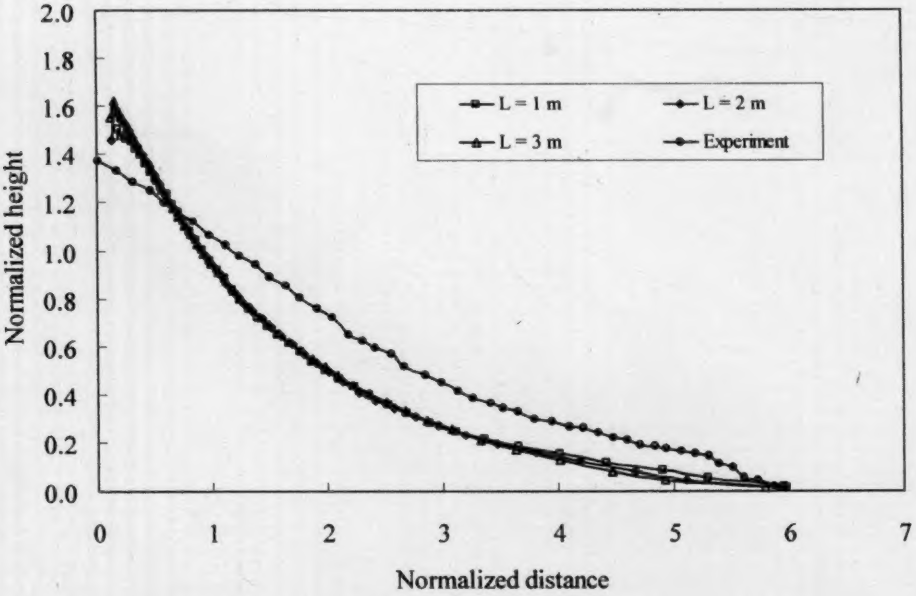

Figure A.16 Nondimensional final profiles of granular slumps with the same initial aspect ratio of 3.2 (normalized with respect to L)

A.3.2 Runout Analysis of Tailing Dam Break

Bryant et al. (1983) and Hungr (1995) analyzed a tailing dam break caused by liquefaction failure. The idealized tailing dam is 30.5 m high and 305 m long on a horizontal plane. The dam is assumed to be liquefied suddenly and flow on a horizontal surface. The liquefied shear strength of tailing materials used by Bryant et al. (1983) and Hungr (1995) is 2.39 kPa and the unit weight of tailing is 18 kN/m^3.

The idealized tailing dam break has also been back-analyzed using the new analytical model. A purely cohesive model with shear strength of 2.4 kPa and unit weight of 18 kN/m^3 is used in the analysis. Pre- and post-failure geometries of the tailing dam are shown in Figure A.17. The runout distance calculated is approximately 1500 m and the maximum velocity is about 28 m/s. The runout distance is in good agreement with the Hungr's results based on energy conservation principle (1995).

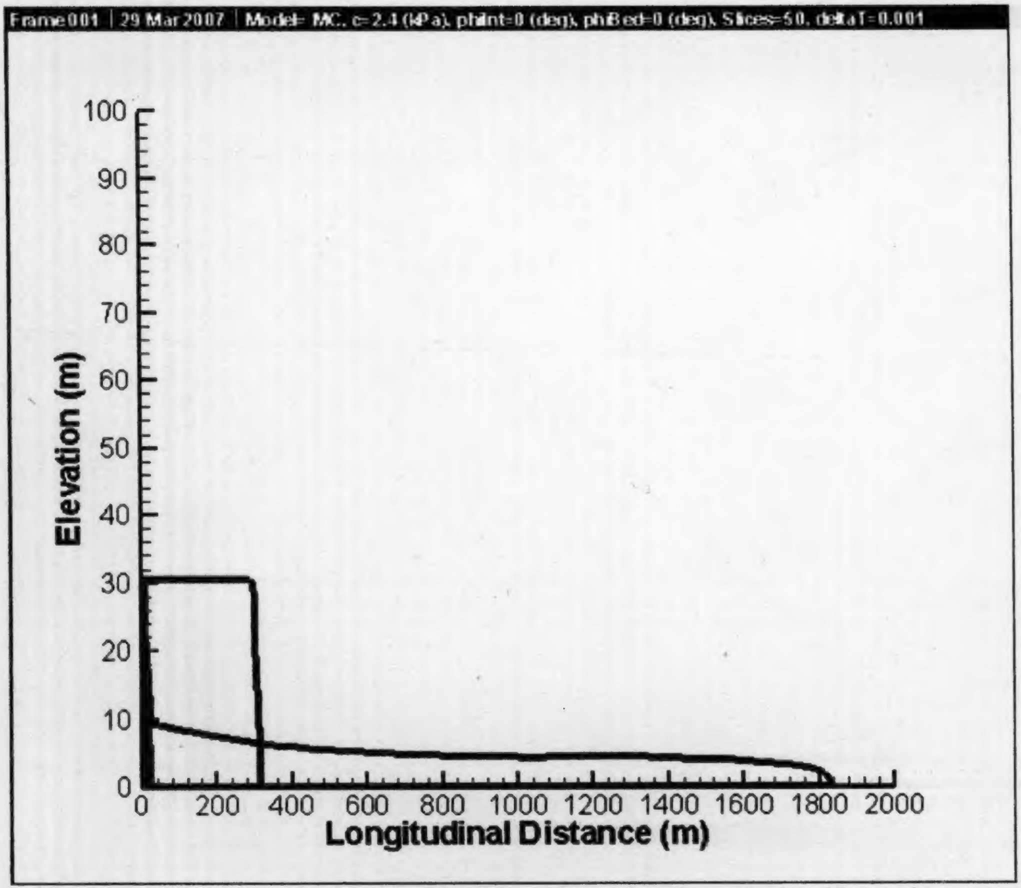

Figure A.17 Tailing dam break analysis based on dynamic analysis with purely cohesive model

Appendix B

Case Histories of Liquefaction Flow Slides and Dynamic Analyses

B.1 A Flow Slide in the Lower San Fernando Dam

B.1.1 Historical Information of the Lower San Fernando Flow Slide

A major slide occurred in the upstream slope of the Lower San Fernando Dam (LSFD) as a result of the 1971 San Fernando earthquake. The slide movement nearly caused the failure of the Lower Dam and an uncontrolled, catastrophic release of the reservoir which contained 12,300,000 m^3 of water over a heavily populated urban residential area. Following the failure of the upstream slope, comprehensive studies of site geology, construction history, and earthquake effects on the dam were undertaken by a number of investigators (e.g., Seed et al. 1975a; Castro et al. 1989; Seed et al. 1989). These studies indicated that liquefaction of hydraulic sand fill following the San Fernando earthquake caused failure of the upstream slope of the dam. Because of detailed, high quality data available from previous investigations, the LSFD flow slide is by far the most studied and best-defined liquefaction flow slide case available in the literature. The LSFD case has been analyzed by numerous investigators (e.g. Seed et al. 1975b; Davis et al. 1988; Castro et al. 1992; Olson 2001) and has proved to be the most important case for studying liquefaction flow slides.

The main body of the Lower San Fernando Dam consists of hydraulic fill constructed between 1912 and 1915. The embankment was underlain by an alluvium foundation consisting primarily of stiff clay with layers of sand and gravel with a relative density of about 65–70 percent. Initial fill placement consisted of the construction of the upstream and downstream starter dikes. The hydraulic fill was then sluiced from the floor of the reservoir and placed between starter dikes from the upstream and downstream edges of the embankment. A puddle core was maintained in the center of the dam to sediment the clay portion of the slurry. As the fill level rose, the discharge pipes were redirected and new starter dikes constructed. The upstream and downstream hydraulic fills were raised symmetrically and constructed in a similar manner. The resulting fill is a series of alluvial fans grading from coarse material near the starter dikes to clayey material in the core. The shells of embankment consist primarily of stratified sand and silty sand and the core consists primarily of clayey soils. Field investigation and laboratory testing indicated that the relative density of upstream hydraulic fill was on the order of 40–50 percent prior to the earthquake.

The flow slide of the San Fernando Dam and triggering mechanisms associated with the failure were described in detail by Seed et al. (1975a). The representative cross sections after and prior to liquefaction flow of the Lower San Fernando Dam is presented in Figure B.1 and Figure B.2, respectively. Seismoscope records at the Lower San Fernando Dam indicated that the dam was subjected to strong shaking with peak ground acceleration of about 0.55 g and 0.5 g on the abutment and crest during the earthquake. The major slide occurred approximately between 20 and 40 seconds after the earthquake had stopped (Seed 1975a). The slide movements in the upstream slope of the Lower Dam developed in the absence of earthquake loads and were driven only by the shear stress due to gravity loading of the materials in the embankment (Castro et al. 1985). Field observations and stability analyses suggested the following mechanism of failure of the upstream slope of the Lower San Fernando Dam (Seed et al. 1975a): After the earthquake shaking, very high pore-water pressures developed in the hydraulic fill near the base of the upstream slope of the dam. Increases of pore-water pressure caused some loss of strength and liquefaction of the hydraulic fill near the base of upstream shell. As a consequence, the shear resistance of the embankment soils in the upstream shell could not withstand the gravity loading caused by the embankment and slide movement developed.

As Figure B.1 illustrates, the slide occurred in the upstream direction and the deformations were concentrated in the lower part of the hydraulic fill shell consisting of saturated silty sand. Overlying materials were broken into blocks of intact soils as the movement developed. The large blocks of embankment soils moved into the reservoir floating over the liquefied hydraulic sand fill after flow was initiated. At the moment that the liquefaction flow came to rest, liquefied soil had moved as much as 61 m beyond the toe of the dam, and the soil block with the original toe of the dam moved about 46 m into the reservoir. The liquefaction zone shown in Figure B.1 and Figure B.2 indicates that not all blocks are involved in liquefaction flow. The movements of blocks 1, 2, 3, and 4 were associated with the failure of the clay core of the Lower San Fernando Dam, which are probably due to secondary sliding or slumping caused by the removal of support from the clay core resulting from the upstream slides. Therefore, the slides of blocks 1, 2, 3, and 4 are discounted in the dynamic analysis (Seed et al. 1975a; Davis et al. 1988; Olson 2001).

B.1.2 Stability Analyses of the Lower San Fernando Flow Slide

Estimates of the value of liquefied shear strength at the base of the Lower San Fernando Dam hydraulic fill have been carried out by various investigators using limit equilibrium analysis or methods incorporating momentum effects (Seed 1987; Davis et al. 1988; Poulos 1988; Castro et al. 1992; Stark and Mesri 1992; Olson 2001). Seed (1987) estimated a liquefied shear strength of 750 psf (35.9 kPa) from the stability analysis of the pre-failure slope configuration of the Lower San Fernando Dam. The calculation was based on the assumption that a driving force causing the slide is equal to the combination of the strength mobilized in the nonliquefied soil near the toe and the crest and the liquefied shear strength of the hydraulic fill near the base of the upstream slope. Castro et al. (1992) evaluated the liquefied shear strength of the hydraulic fill by means of laboratory testing of high quality undisturbed samples. The steady-state line was determined from a plot of void ratio versus undrained steady-state strength for reconstituted samples of hydraulic fill from the critical zone of the Lower San Fernando Dam. The in situ void ratio of hydraulic fill in the critical zone prior to the slide was estimated based on test results of the samples on the downstream side. Appropriate corrections were made to account for the volume changes caused by sampling, testing, earthquake and groundwater lowering, and the difference between upstream and downstream conditions. The undrained steady-state strengths for undisturbed specimens could then be determined by combining the in situ void ratio and the steady-state line. The resulting analysis based on steady-state concepts gave a range of average values of the liquefied shear strength of the hydraulic fill between 610 psf (29.2 kPa) and 810 psf (38.8 kPa). To provide good agreement with the liquefied strength estimated from the extent of the observed slide movement, a conservative to very conservative interpretation of the laboratory tests was recommended (Castro et al. 1992). Liquefied shear strength based on the conservative interpretation was about 490 psf (23.5 kPa).

Davis et al. (1988) incorporated the effects of the dynamics of failure into the estimation of liquefied shear strength and calculated the mobilized shear strength in the critical zone of hydraulic fill of the Lower San Fernando Dam. The estimated liquefied shear strength was 510 psf (24.4 kPa). Back-analyses by Poulos (1988), who also incorporated the effects of the energy and dynamics of the failure into the calculations, indicated that the liquefied shear strength mobilized in the hydraulic fill zone is in the range of 500 to 1000 psf (23.9 to 47.9 kPa). The recommended value was 750 psf (35.9 kPa). Using stability analysis and considering the kinetics of failure mass movements, Olson (2001) determined the value of liquefied shear strength for hydraulic fill of the Lower San Fernando Dam to range from 15.8 to 21.8kPa, with a best estimate of liquefied shear strength of 18.7 kPa.

Considering the significant uncertainties involved in estimating the liquefied shear strength from case histories, many investigators recommended a more conservative interpretation of the back-calculated results. Seed et al. (1989) reevaluated the slide in the Lower San Fernando Dam and suggested that the liquefied shear strength determined from the post-failure configuration was 400 ± 100 psf

(19.2 ± 4.8 kPa). Based on the findings of Seed et al. (1989), Stark and Mesri (1992) assigned a liquefied shear strength of 400 ± 100 psf (19.2 ± 4.8 kPa) as the value back-calculated from the liquefaction flow in the Lower San Fernando Dam for establishing the standard penetration test (SPT) based chart. Wride et al. (1999) reexamined the original database of case histories used for establishing the SPT based chart (Seed 1987; Stark and Mesri 1992). It is found that the original conservative interpretations of case histories are considered by many workers and regulatory agencies as the most authoritative measure of the liquefied shear strength. As a consequence, less conservative approaches are generally viewed in an unfavorable light.

B.1.3 Dynamic Analysis of the Lower San Fernando Flow Slide

Based on Figure B.1 and Figure B.2, the sliding path and pre-failure geometry used in dynamic analysis are determined and presented in Figure B.3. The post-failure geometry based on field observation is also included in Figure B.3 for testing the results of the dynamic analysis. Following the procedures described in Chapter 6, analysis of the Lower San Fernando Dam liquefaction flow was carried out using a slice-based model with consideration of internal energy dissipation. The properties of liquefied sands are approximated by cohesive and frictional models.

The post-liquefaction geometry of the Lower San Fernando Dam flow slide shown in Figure B.4 is based on dynamic analysis using the cohesive model with internal energy dissipation considered. The runout distance calculated is approximately 46.8 m. This value is close to the observed runout distance of 45 m. The liquefied shear strength from slice-based dynamic analysis with the consideration of internal energy dissipation is 25 kPa.

The post-liquefaction geometry of the Lower San Fernando Dam flow slide shown in Figure B.5 is based on dynamic analysis using the friction model with internal energy dissipation considered. The runout distance calculated is 45.4 m from simulation and the bulk friction angle back-calculated is about 11°.

B.1.4 Kinetic Analysis of the Lower San Fernando Flow Slide

Kinetic analysis of liquefaction flow slide in the Lower San Fernando Dam with a sliding block model is introduced in this section. The friction model is used to compute shear resistance in the kinetic analysis. The travel path of the center of gravity is defined by a third order polynomial similar to that used in the kinetic analysis by Olson (2001). The travel path of the centroid, velocity, and displacement based on dynamic analysis are presented in Figure B.6 to Figure B.8. The back-calculated bulk friction angle is about 11.5°.

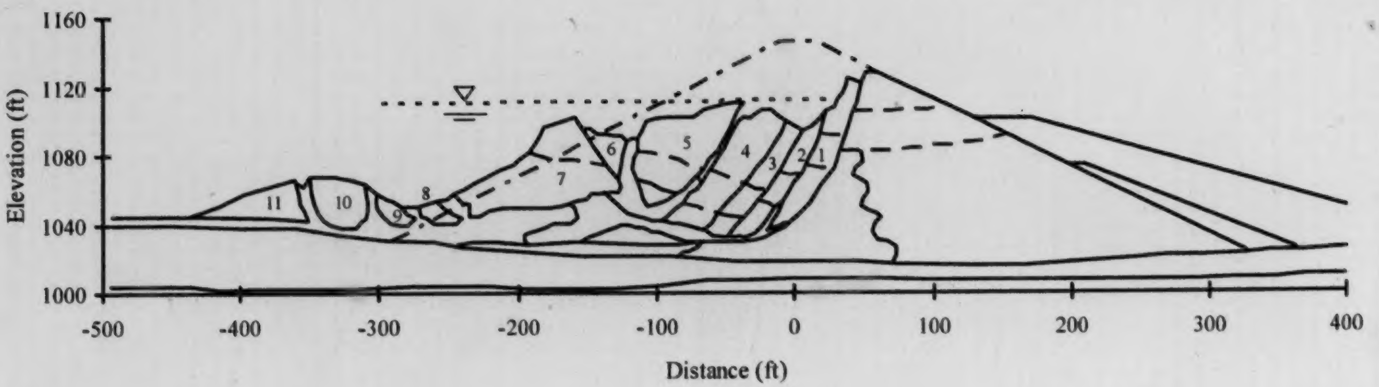
1160
1120
1080
1040
1000
Elevation (ft)
-500
-400
-300
-200
-100
0
100
200
300
400
Distance (ft)
11
10
9
8
7
6
5
4
3
2
1

Figure B.1 Cross sections of the Lower San Fernando Dam after earthquake (Modified Castro et al. 1992)

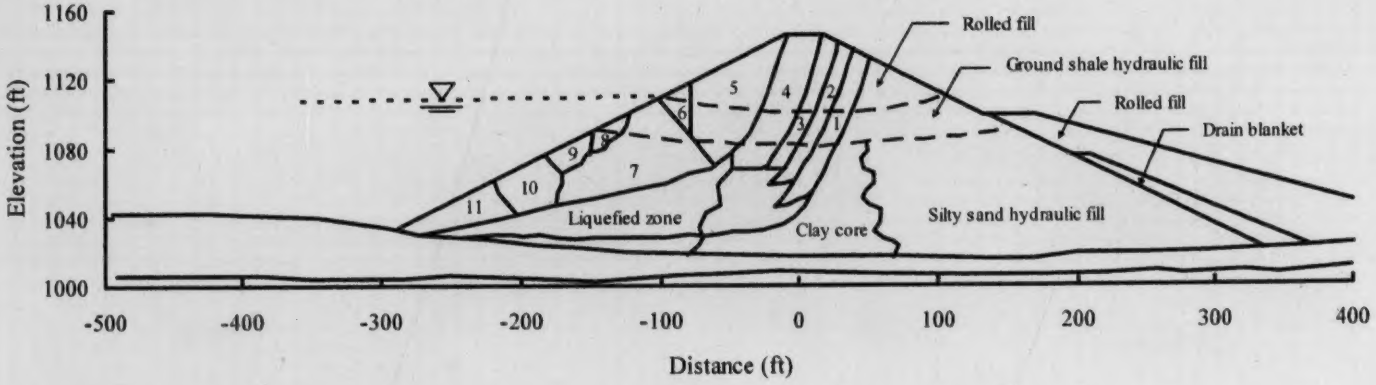
1160
1120
1080
1040
1000
Elevation (ft)
-500
-400
-300
-200
-100
0
100
200
300
400
Distance (ft)
Rolled fill
Ground shale hydraulic fill
Rolled fill
Drain blanket
1
2
3
4
5
6
7
8
9
10
11
Liquefied zone
Clay core
Silty sand hydraulic fill

Figure B.2 Schematic reconstruction of failed cross section of the Lower San Fernando Dam (Modified Castro et al. 1992)

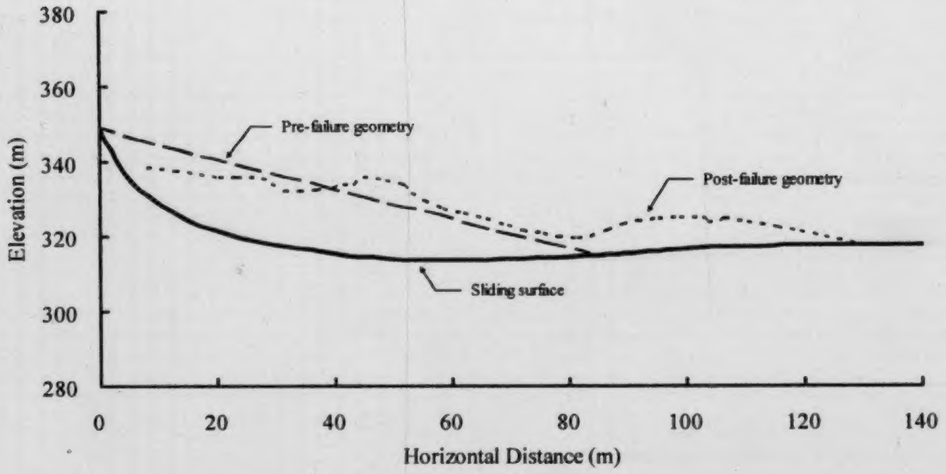

Figure B.3 Geometries of the Lower San Fernando flow slide based on field observations

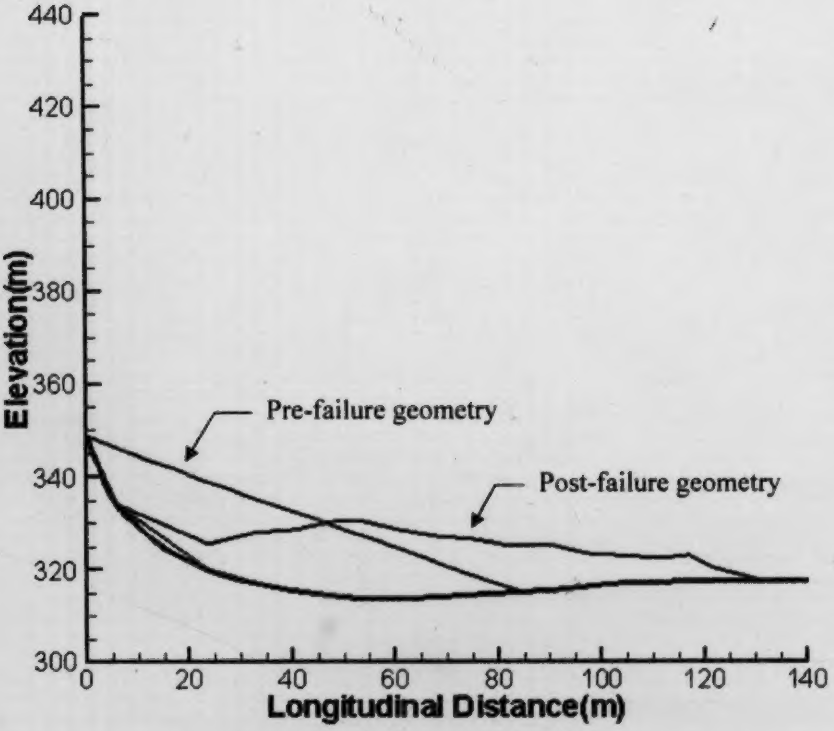

Figure B.4 Geometries of the Lower San Fernando flow slide based on dynamic analysis with the cohesive model

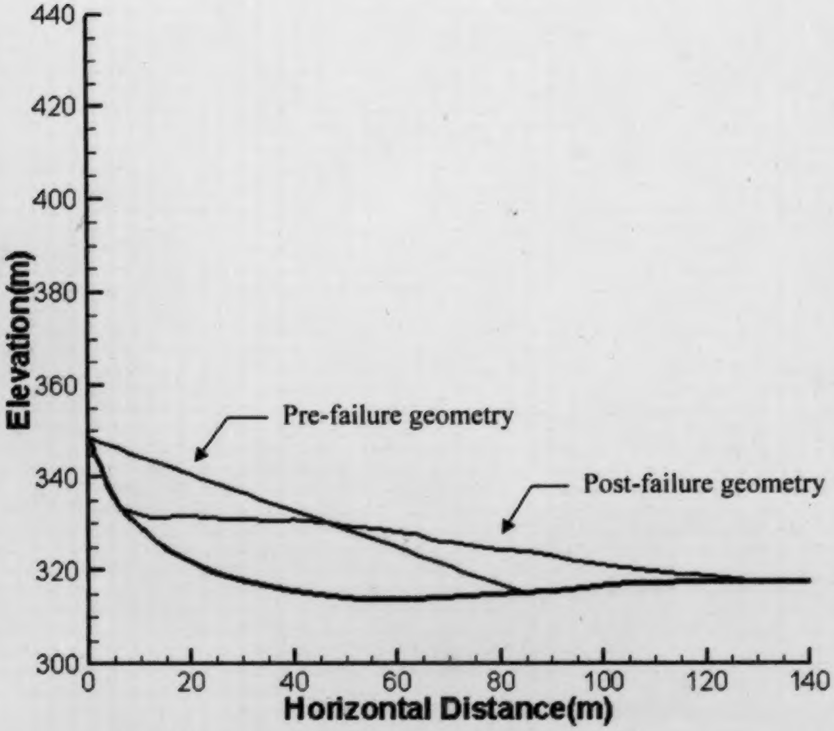

Figure B.5 Geometries of the Lower San Fernando flow slide based on dynamic analysis with the friction model

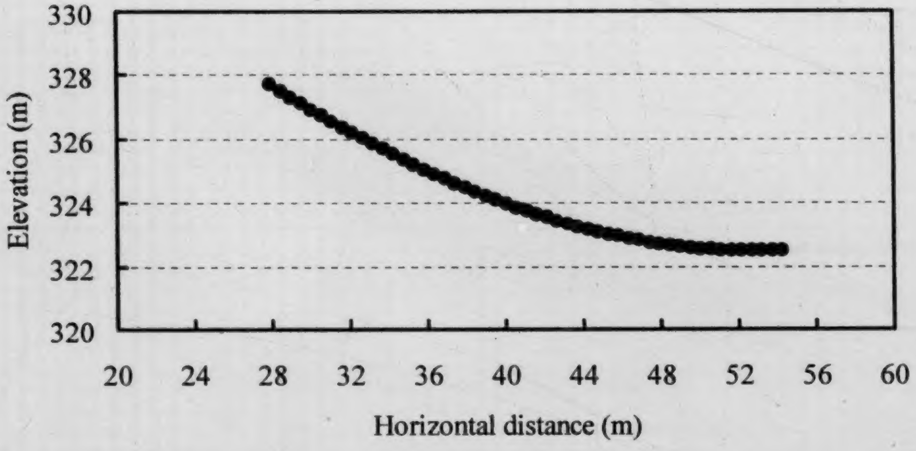

Figure B.6 Travel path of the centroid of the Lower San Fernando flow slide

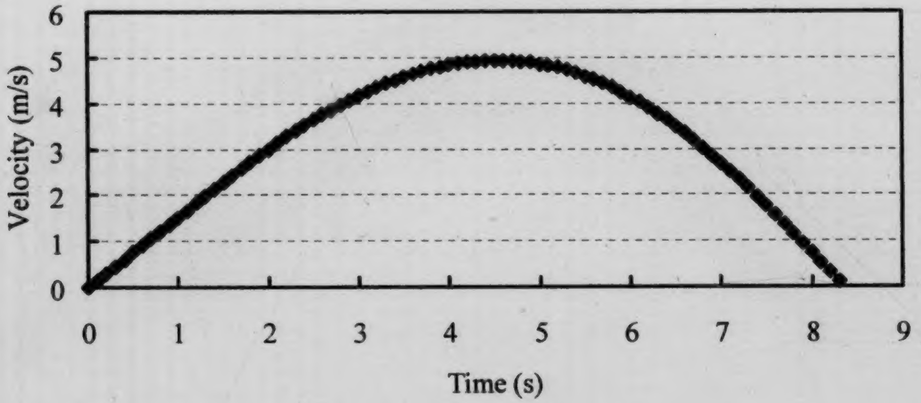

Figure B.7 Centroid velocity versus time for the Lower San Fernando flow slide

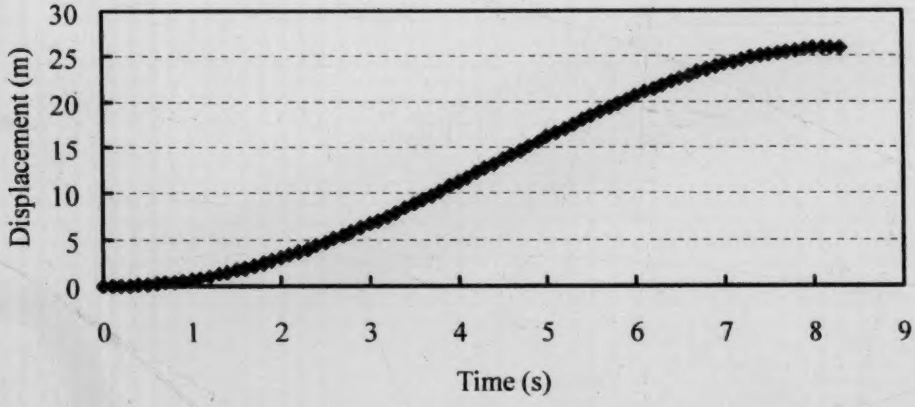

Figure B.8 Centroid displacement versus time for the Lower San Fernando flow slide

B.2 A Flow Slide in the North Dike of the Wachusett Dam

B.2.1 Historical Information of the Wachusett Flow Slide

The flow slide of the upstream slope of the North Dike of the Wachusett Dam occurred on April 11, 1907 during the first reservoir filling in 1907. The failure involved approximately 46,500 m^3 of materials. The failure mass flowed into the reservoir and showed high mobility: a maximum runout distance of approximately 100 m and a maximum vertical drop of the crest of approximately 12.2 m. Comprehensive studies indicate that that the slope failure in the Wachusett Dam occurred as a result of the static liquefaction of the loose sandy hydraulic fill in the upstream shell. Olson et al. (2000) and Olson (2001) investigated site geology and construction history of the Wachusett Dam and conducted stability analysis of the North Dike of the Dam. The following descriptions are summarized from these sources.

The Wachusett Dam and Reservoir is located in the South Branch of the Nashua River in Clinton, Massachusetts, approximately 48 km west of Boston. The main dam is a stone masonry, gravity structure, 43 m high and 259 m long with a crest elevation of 126.7 m. The North and South Dikes are zoned earth fill structures consisting of sandy silt to silty sand cores and supporting shells comprised mainly of fine sand. The construction of the 3200 m North Dike began in 1898 and completed in 1904. The construction of the North Dike was carried out using controlled placement and compaction for the cut-off and core of the dike and an uncontrolled fill method for the supporting shells. The core materials consist primarily of sandy silt to silty sand with saturated unit weight in the range of 18.9 to 20.4 kN/m^3. The upstream and downstream shell fills consist of sand to silty sand with some gravel. During the construction, the downstream fills were placed in 2.3m lifts and compacted by flooding while the upstream fill received no compaction and saturation. The geometry of the North Dike is presented in Figure B.9.

The slope failure of the North Dike occurred in 1907 at the time when the reservoir was being filled. Field investigation indicated that the failure was centered over the former river channel where the dike had a maximum height of 24.4 m. At the time of failure the water level of the reservoir was 12.8 m deep, about half of the dike height. After the failure, the displaced materials flowed into the reservoir with a maximum horizontal distance of approximately 100 m and came to rest at an angle of approximately 5° to 6°.

The failure of the North Dike appears to be the result of the static liquefaction of the upper stream sandy fills. The construction of the dike was completed in 1904, three years prior to the slope failure. The flow slide of the North Dike developed in the absence of seismic or dynamic activity and the flow of displaced materials was solely driven by the shear stress due to gravity loading of the upstream fills. Examinations of the construction history of the North Dike and filling of the Wachusett Dam indicated that loading of the North Dike probably was fully drained (Olson et al. 2000). Field investigations and analysis of the loading conditions of the North Dike suggested the following triggering mechanisms for the liquefaction flow slide:

The normal effective stress in sandy fills reduces due to the increase in pore water pressure as a result of reservoir filling, while deviator stress remains constant. The pore pressure causes the stress state to move to the collapse surface. When the stress state lies on or approaches the collapse surface, a slight disturbance can cause upstream fill sands strain-softening, accompanied by rapid generation of excess pore pressure. The stress state will move along the state boundary surface and arrive at steady state. Because driving shear stress in the upstream slope is much greater than the steady-state shear resistance, the liquefied sand transformed from a solid state into a fluid state and resulted in a flow slide. Identical stress paths associated with static liquefaction have been simulated in the laboratory (Sasitharan et al. 1994).

B.2.2 Stability Analysis of the Wachusett Flow Slide

Stability analyses for the liquefaction flow slide of the North Dike were described by Olson et al. (2000) and Olson (2001). The cross section used in the analyses is presented in Figure B.10. The pre-failure geometry was analyzed to obtain yield shear strength at the onset of failure. Sands above the phreatic surface were assigned a friction angle with a range of 30° to 35°. The yield shear strength was estimated to be in the range of 37.6 to 41.9 kPa. Stability analysis of the post-failure geometry was conducted to obtain a lower bound liquefied shear strength. The lower bound of liquefied shear strength was estimated to be 3.8 kPa. Olson et al. (2000) illustrated that the stability analysis should take account of the failure kinetics in order to provide a best estimate of liquefied shear strength mobilized after the liquefaction has been triggered. Kinetic analysis of the liquefaction flow slide of the North Dike yielded the best estimate of liquefied shear strength—16.0 kPa, with a range of 10.4 to 19.1 kPa.

B.2.3 Dynamic Analysis of the Wachusett Flow Slide

Based on Figure B.10, the geometries used for dynamic analysis of the liquefaction flow slide of the North Dike of the Wachusett Dam are obtained, as shown in Figure B.11. Cohesive and friction models are used as constitutive laws in the dynamic analyses.

The post-liquefaction geometry of the North Dike flow slide shown in Figure B.12 is based on dynamic analysis using the cohesive model with internal energy dissipation considered. The runout distance calculated is approximately 102.8 m, which is close to the observed runout distance of 97.5 m. The liquefied shear strength from slice-based dynamic analysis with the consideration of internal energy dissipation is 16.2 kPa.

The post-liquefaction geometry of the North Dike flow slide shown in Figure B.13 is based on dynamic analysis using the friction model with internal energy dissipation considered. The runout distance calculated is 101.8 m from simulation and the bulk friction angle back-calculated is about 9.5°.

B.2.4 Kinetic Analysis of the Wachusett Flow Slide

Kinetic analysis of liquefaction flow slide of the North Dike with a sliding block model is carried out. The friction model is used to calculate the shear resistance mobilized in the kinetic analysis. The travel path of the center of gravity is defined by a third order polynomial similar to that used in the kinetic analysis by Olson (2001). The travel path of the centroid, velocity, and displacement based on dynamic analysis are presented in Figure B.14 to Figure B.16. The back-calculated bulk friction angle is about 10.4°.

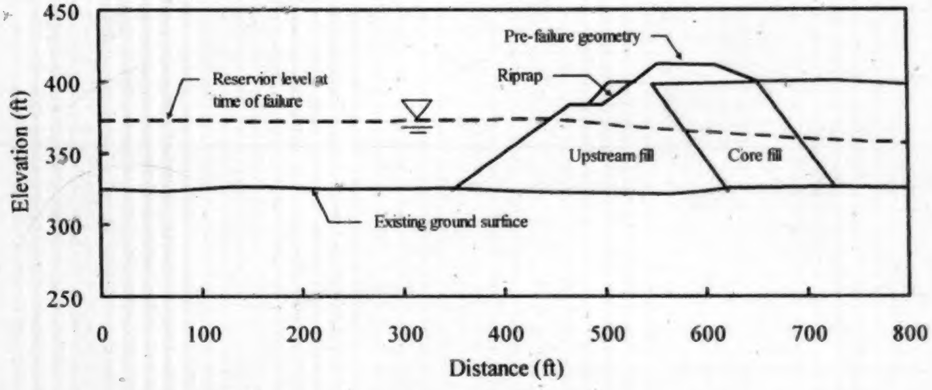

Figure B.9 Pre-failure cross section of the North Dike of the Wachusett Dam (Modified from Olson et al. 2000)

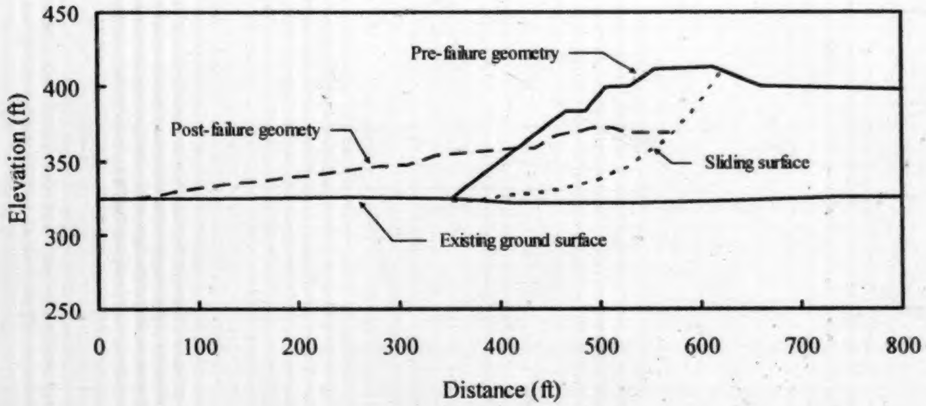

Figure B.10 Pre- and post-failure geometries of the North Dike of the Wachusett Dam (Modified from Olson et al. 2000)

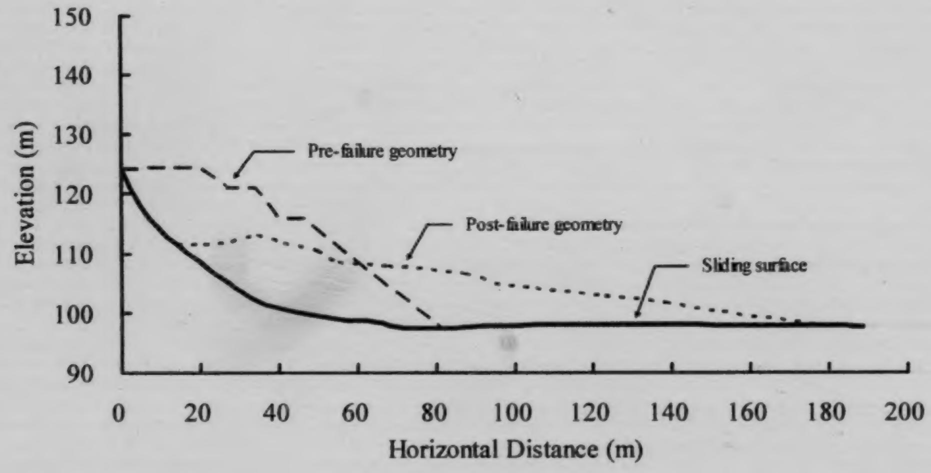

Figure B.11 Geometries of the North Dike of the Wachusett Dam based on field observation

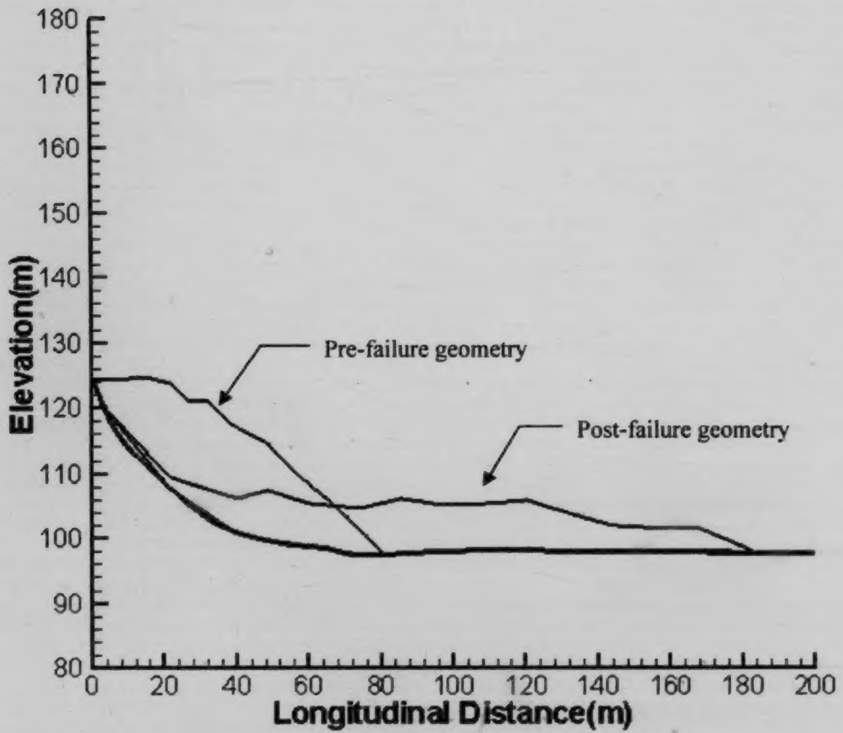

Figure B.12 Geometries of the Wachusett flow slide based on dynamic analysis with the cohesive model

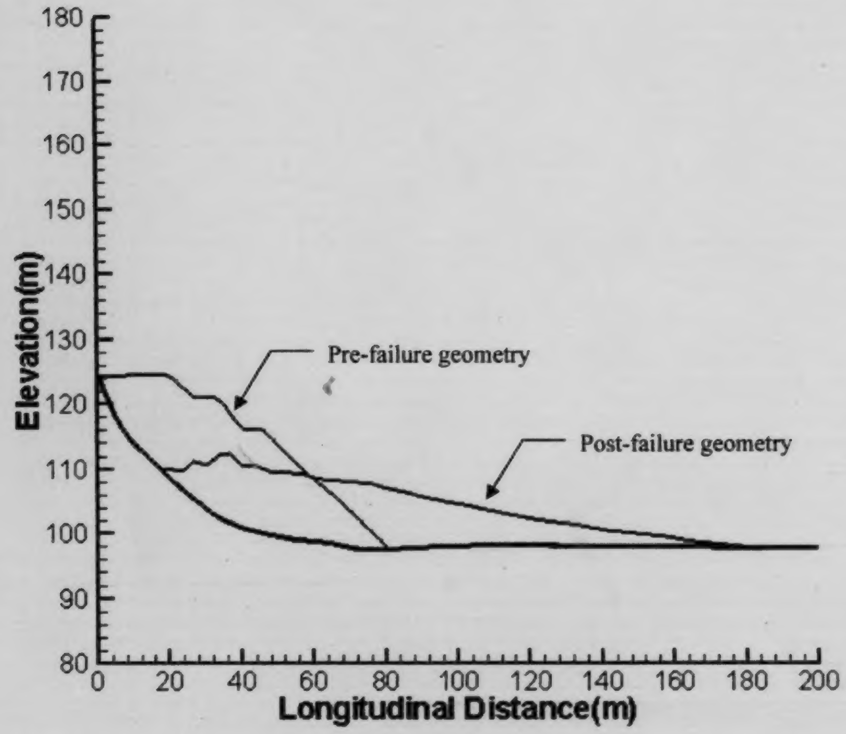

Figure B.13 Geometries of the Wachusett flow slide based on dynamic analysis with the friction model

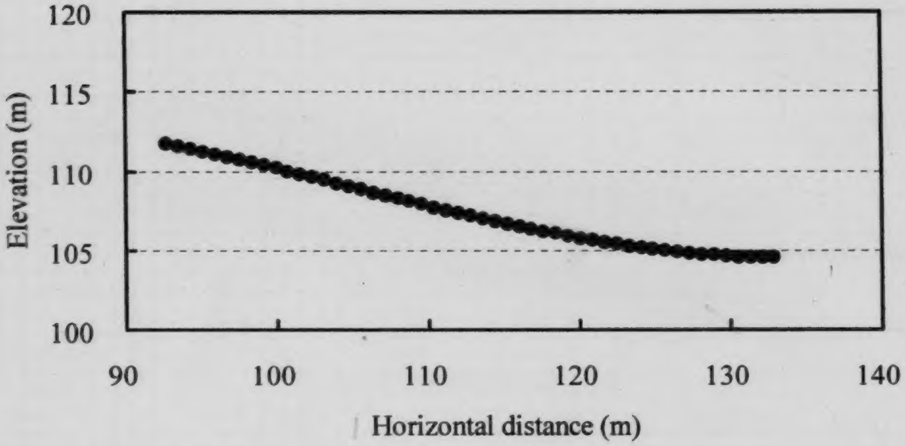

Figure B.14 Travel path of the centroid of the Wachusett flow slide

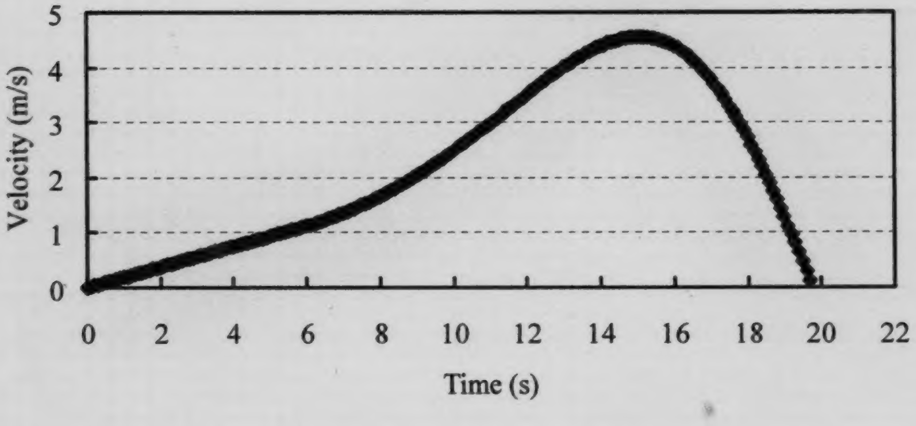

Figure B.15 Centroid velocity versus time for the Wachusett flow slide

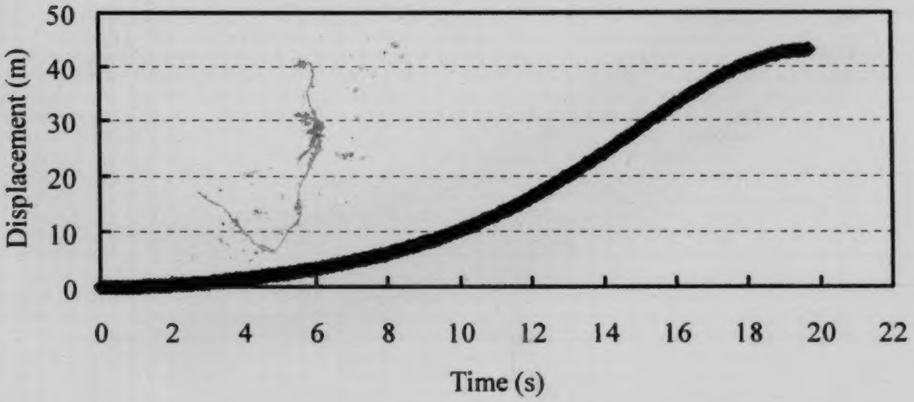

Figure B.16 Centroid displacement versus time for the Wachusett flow slide

B.3 A Flow Slide in the Calaveras Dam

B.3.1 Historical Information of the Calaveras Flow Slide

The Calaveras Dam was a hydraulic fill structure which failed during construction in 1918. The construction of the dam started in 1914. The core of the Calaveras Dam and interior portions of the shells were constructed using hydraulic fill and a majority of upstream and downstream shells were constructed using un-compacted steam-shovel fills. A liquefaction flow slide occurred in the upstream shell of the dam on March 24, 1918. At the time of failure the dam was under construction, approaching a height of 61 m with an upstream slope angle of approximately 18°. Over 600,000 m^3 of materials was involved in the failure. After the failure, the displaced materials flowed into the reservoir with a maximum horizontal distance of approximately 200 m, a maximum vertical drop of approximately 30 m, and a post-failure slope angle of approximately 6°. Hazen (1918, 1920), Davis et al. (1988), Olson (2001), and Jefferies and Been (2006) presented detailed descriptions of the construction and failure of the Calaveras Dam. The descriptions herein are based on these sources.

The Calaveras Dam was constructed using hydraulic fills and un-compacted stream-shovel fills. The fill material was obtained from weathered sandstone and comprised of granular deposits with a large range of grain sizes from clay to coarse sand. The majority of the upstream shell was uncompacted and consisted primarily of silty sand to sand with some gravels. It was observed that the fill in the starter dikes was placed in layers 4 to 5 feet thick without moisture control and that only the upper 6 to 8 inches were compacted. Davis et al. (1988) indicated that the percent compaction of fill placed in the starter dikes was below 85 percent. When the fill contains fines, the percent compaction should be as low as 75 percent. The saturated unit weight of the sandy fill varied from 17.3 kN/m^3 near the top of the dam to 18.9 kN/m^3 near the bottom of the dam. The dam core consisted of sluiced clayey fill with a grain size range of 0.002 to 0.02 mm and a unit weight of approximately 15.7 kN/m^3 (Olson 2001).

Field observations and comprehensive studies following the slope failure of the Calaveras Dam indicate that the failure of the dam was static liquefaction of sandy hydraulic fills due to saturation of the upstream shell as the reservoir rose, combined with seepage forces and the weight of fill placed during the hydraulic filling operation. The triggering mechanisms are similar to those for the flow slide of the North Dike of the Wachusett Dam (Olson 2001). The failure mechanisms have been studied experimentally by Sasitharan et al. (1994).

B.3.2 Stability Analysis of the Calaveras Flow Slide

Stability analyses of the flow slide of the Calaveras Dam have been conducted by a number of investigators to estimate the liquefied shear strength (Seed 1987; Davis et al. 1988; Poulos 1988; Olson 2001). The cross section used in the analyses is presented in Figure B.17. Based on the post-failure configuration of the slide mass, the liquefied shear strength was estimated to be 750 psf (35.9 kPa) by Seed (1987). Poulos (1988) and Davis et al. (1988) back-calculated liquefied shear strength incorporating effects of the dynamics of the failure. The estimated driving shear stresses before and after the flow slide are 1500 psf (71.8 kPa) and 250 psf (12.0 kPa), corresponding to pre- and post-failure geometries, respectively. The best estimate of the liquefied shear strength mobilized during flow was approximately 700 psf (33.5 kPa).

Olson (2001) reexamined the slope failure of the Calaveras Dam and carried out a series of stability analyses of the slope before and after the flow slide. The non-liquefied soils were assigned a friction angle with a range of 30° to 35°. The best estimate of yield shear strength was 76.6 kPa with a range of 71.8 to 80.7 kPa from stability analysis of the pre-failure slope. The back-calculated shear strength was approximately 3.6 kPa with a range of 2.2 to 10.5 kPa, based on stability analysis of the post-failure geometry of the slide mass. The best estimate of the liquefied shear strength was 34.5 kPa with a range of 28.7 to 37.8 kPa using kinetic analysis.

B.3.3 Dynamic Analysis of the Calaveras Flow Slide

Based on Figure B.17, the geometries used for dynamic analysis of the liquefaction flow slide of the North Dike of the Wachusett Dam are obtained, as shown in Figure B.18. Cohesive and friction models are used as constitutive laws in the dynamic analyses.

The post-liquefaction geometry of the Calaveras Dam flow slide shown in Figure B.19 is based on dynamic analysis using the cohesive model with internal energy dissipation incorporated. The runout distance calculated is approximately 202.6 m, which is close to the observed runout distance of 205.8 m. The liquefied shear strength from slice-based dynamic analysis with the consideration of internal energy dissipation is 32.6 kPa.

The post-liquefaction geometry of the Calaveras Dam flow slide shown in Figure B.20 is based on dynamic analysis using the friction model with internal energy dissipation considered. The runout distance calculated is 204.3 m from simulation, and the bulk friction angle back-calculated is about 8.1°.

B.3.4 Kinetic Analysis of the Calaveras Flow Slide

Kinetic analysis of the liquefaction flow slide of the Calaveras Dam with a sliding block model is carried out. The friction model is used to calculate the shear resistance mobilized in the kinetic analysis. The travel path of the center of gravity is defined by a third order polynomial similar to the travel path used in the kinetic analysis by Olson (2001). The travel path of the centroid, velocity, and displacement based on dynamic analysis are presented in Figure B.21 to Figure B.23. The back-calculated bulk friction angle is about 8°.

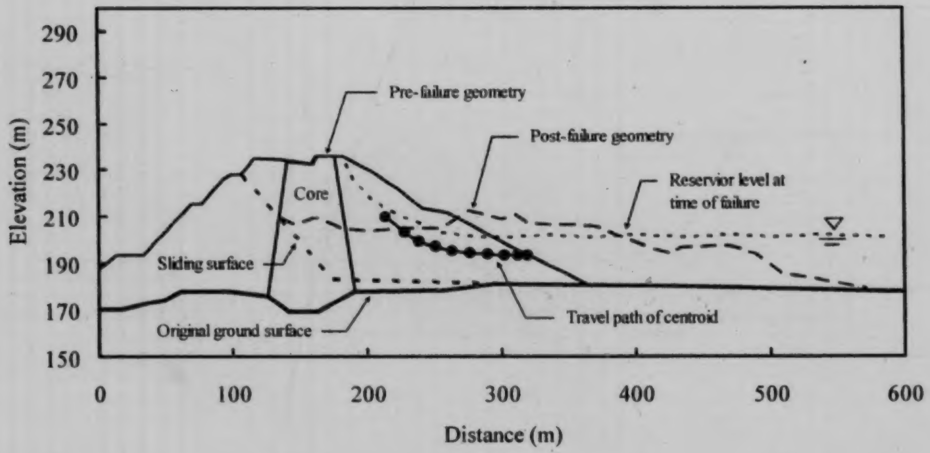

Figure B.17 Pre- and post-failure geometries of the Calaveras Dam (Modified from Olson 2001)

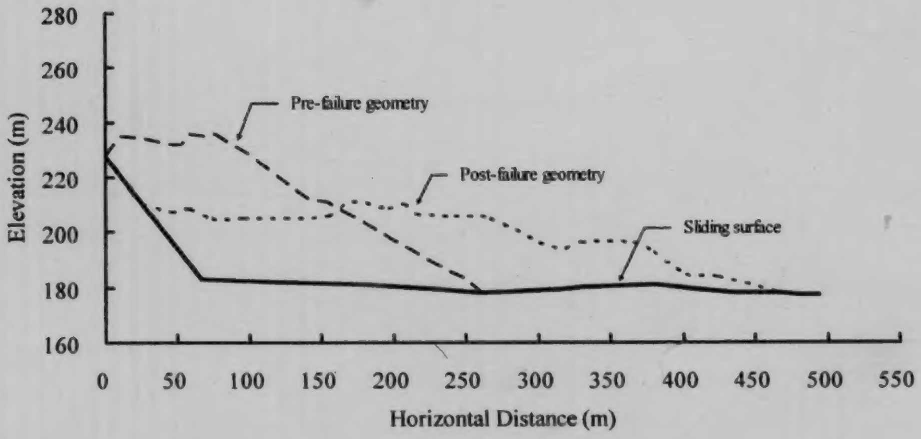

Figure B.18 Pre- and post-failure geometries of the Calaveras Dam used for dynamic analysis

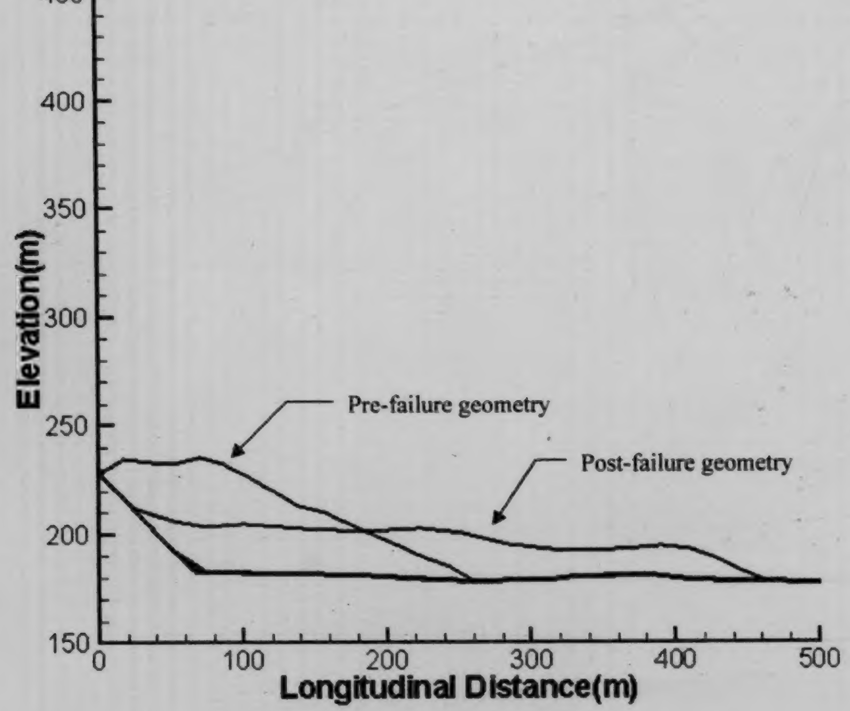

Figure B.19 Geometries of the Calaveras flow slide based on dynamic analysis with the cohesive model

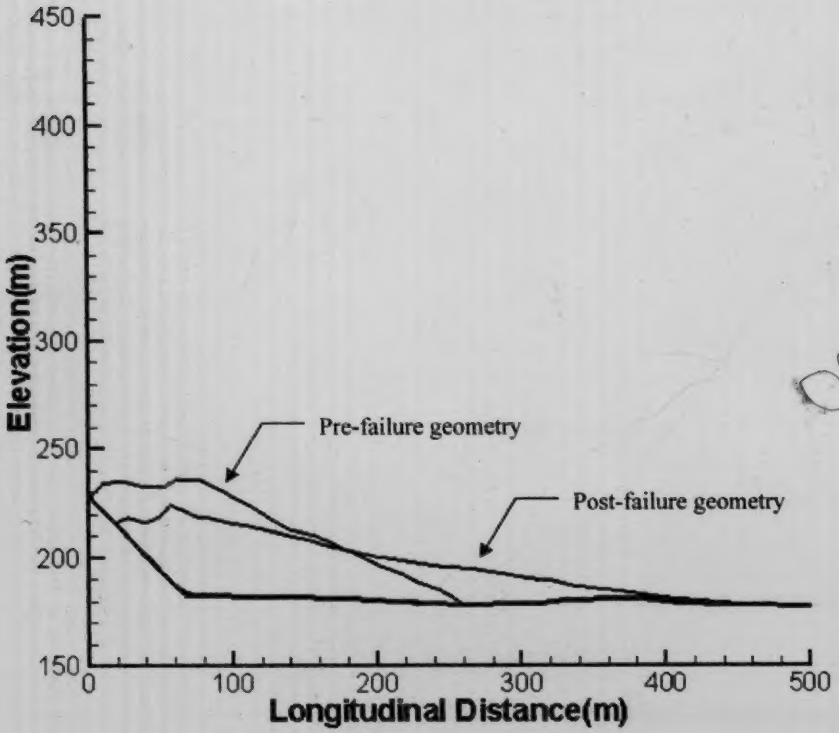

Figure B.20 Geometries of the Calaveras flow slide based on dynamic analysis with the friction model

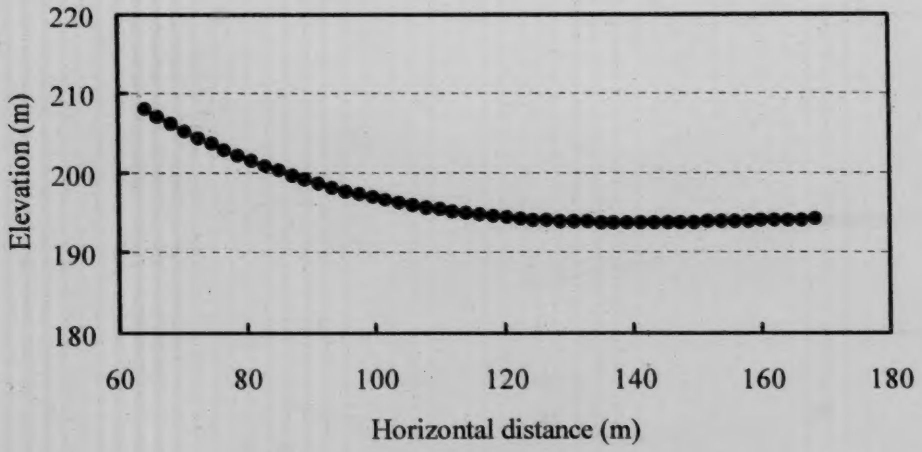

Figure B.21 Travel path of the centroid of the Calaveras flow slide

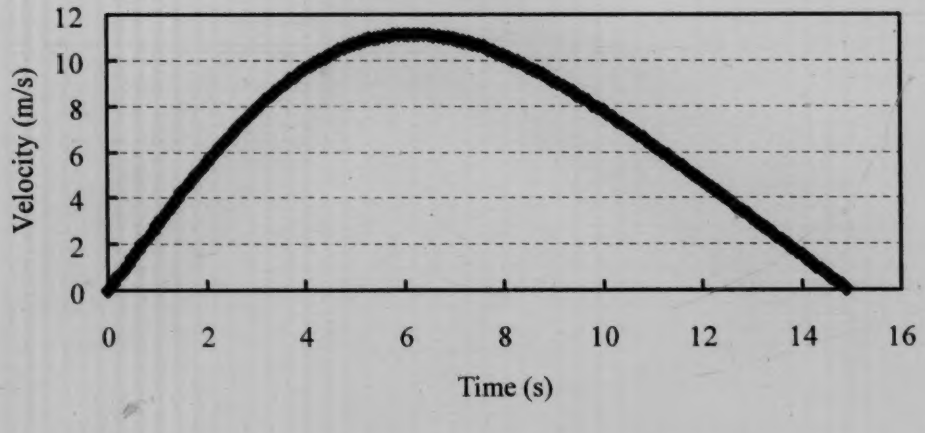

Figure B.22 Centrod velocity versus time for the Calaveras flow slide

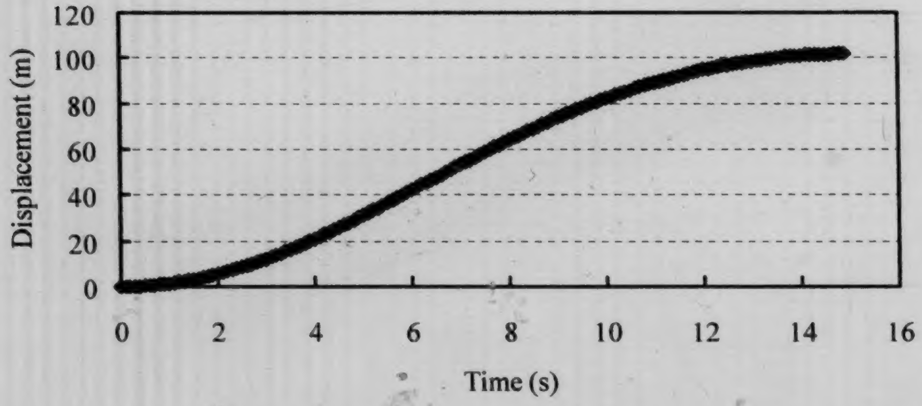

Figure B.23 Centroid displacement versus time for the Calaveras flow slide

B.4 A Flow Slide in the Fort Peck Dam

B.4.1 Historical Information of the Fort Peck Flow Slide

The Fort Peck Dam was a hydraulic fill structure on the Missouri River in northeastern Montana. A flow slide occurred in the upstream shell of the Fort Peck Dam on September 22, 1938, when the dam was nearly completed and the reservoir was partially filled. Site geology, construction history, failure, and reconstruction of the Fort Peck Dam have been studied in detail by Middlebrooks (1942), Casagrande (1965), and Olson (2001). The following descriptions are summarized from these sources.

The Fort Peck Dam was constructed of river sands and finer-grained alluvial soils using the hydraulic fill method. The foundation of the dam consisted of alluvial sands, gravel, and clays with a total thickness up to 40 m. The river alluvial materials are underlain by the Bearpaw clay-shale which contains layers of bentonite. At the time of failure, the dam was approximately 61 m high and the slope of the upstream shell was 14°. The total volume of materials involved in the slide was about 7.6 million m^3 and the volume of materials deposited outside of the original sections was about 4 million m^3. Field observations indicate that a certain amount of the sliding mass traveled a horizontal distance of 457 m beyond the original toes of the upstream slope (Casagrande 1965). The inlet channel had a major influence on the maximum runout distance. The average post-failure slope angle was about 4°, and the slope angle of the material which flowed into the inlet channel was about 2°.

After the flow slide of the Fort Peck Dam, a Board of Consultants was appointed to identify the failure mechanisms. On the basis of comprehensive field investigations and laboratory testing, diverse views of the cause of failure have been presented by the board members. A majority of the Board concluded that the slide was a result of the shear failure of the shale foundation and that excess hydrostatic pressure in the shale accounted in large part for the speed at which, and the distance to which, the slide moved (Middlebrooks 1942). A minority of Board members (including Casagrande) concluded that the high mobility of the flow slide of the Fort Peck Dam was principally caused by static liquefaction of sandy hydraulic fill and that the liquefaction was triggered by shear failure of the weak shale. Evidence supporting static liquefaction flow failure mechanisms for the slide in the Fort Peck Dam was summarized by Casagrande (1965).

B.4.2 Stability Analysis of the Fort Peck Flow Slide

Stability analyses of the flow slide of the Fort Peck Dam have been conducted by a number of investigators to estimate the liquefied shear strength (Seed 1987; Davis et al. 1988; Poulos 1988; Olson 2001). The cross section used in the analyses is presented in Figure B.24. Based on the stability analysis of the pre-failure configuration of the slide mass, the liquefied shear strength was estimated to be 700 psf (33.5 kPa) by Seed (1987) and a conservative value of 600 psf (28.7 kPa) was suggested. Poulos (1988) and Davis et al. (1988) back-calculated liquefied shear strength incorporating effects of the dynamics of the failure. The estimated driving shear stresses before and after the flow slide are 1800 psf (86.2 kPa) and 50 psf (2.4 kPa), corresponding to pre- and post-failure geometries, respectively. The best estimate of the liquefied shear strength mobilized during flow was approximately 700 psf (33.5 kPa).

Olson (2001) reexamined the slope failure of the Fort Peck Dam and carried out a series of stability analyses of the slope before and after the flow slide. The non-liquefied soils were assigned a friction angle with a range of 30° to 35°. The best estimate of yield shear strength was 82.9 kPa with a range of 69.9 to 89.6 kPa from stability analysis of the pre-failure slope. The back-calculated shear strength was approximately 3.8 kPa with a range of 0.7 to 15.1 kPa, based on stability analysis of the post-failure geometry of the slide mass. The best estimate of the liquefied shear strength was 27.3 kPa with a range of 16.8 to 34.0 kPa using kinetic analysis.

B.4.3 Dynamic Analysis of the Fort Peck Flow Slide

Based on Figure B.24, the geometries used for dynamic analysis of the liquefaction flow slide of the Fort Peck Dam are obtained, as shown in Figure B.25. Cohesive and friction models are used as constitutive laws in the dynamic analyses.

The post-liquefaction geometry of the Fort Peck Dam flow slide shown in Figure B.26 is based on dynamic analysis using the cohesive model with internal energy dissipation incorporated. The runout distance calculated is approximately 509.9 m, which is close to the observed runout distance of 508.4 m. The liquefied shear strength from slice-based dynamic analysis with consideration of internal energy dissipation is 24.5 kPa.

The post-liquefaction geometry of the Fort Peck Dam flow slide shown in Figure B.27 is based on dynamic analysis using the friction model with internal energy dissipation considered. The runout distance calculated is 509.2 m from simulation and the bulk friction angle back-calculated is about 5.0°.

B.4.4 Kinetic Analysis of the Fort Peck Flow Slide

Kinetic analysis of the liquefaction flow slide of the Fort Peck Dam with a sliding block model is carried out. The friction model is used to calculate the shear resistance mobilized in the kinetic analysis. The travel path of the center of gravity is defined by a third order polynomial similar to the travel path used in the kinetic analysis by Olson (2001). The travel path of the centroid, velocity, and displacement based on the dynamic analysis are presented in Figure B.28 to Figure B.30. The back-calculated bulk friction angle is about 4.0°.

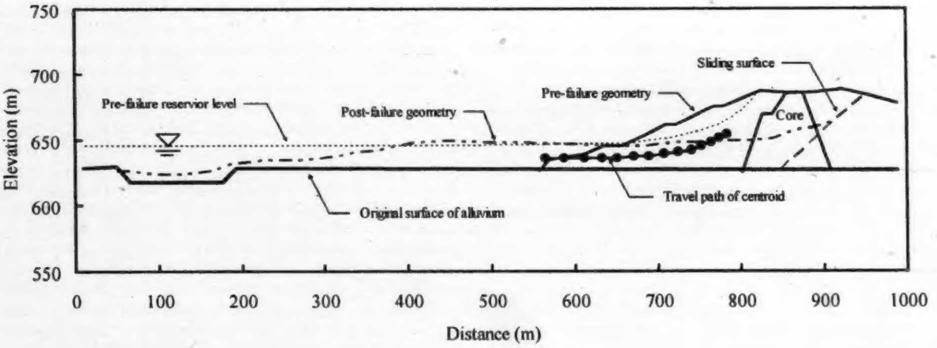

Figure B.24 Pre- and post-failure geometries of the Fort Peck Dam (Modified from Olson 2001)

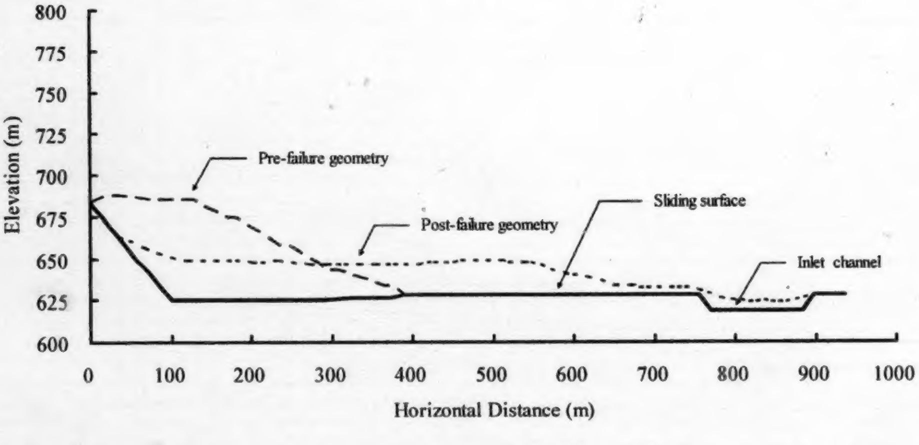

Figure B.25 Pre- and post-failure geometries of the Fort Peck Dam used for dynamic analysis

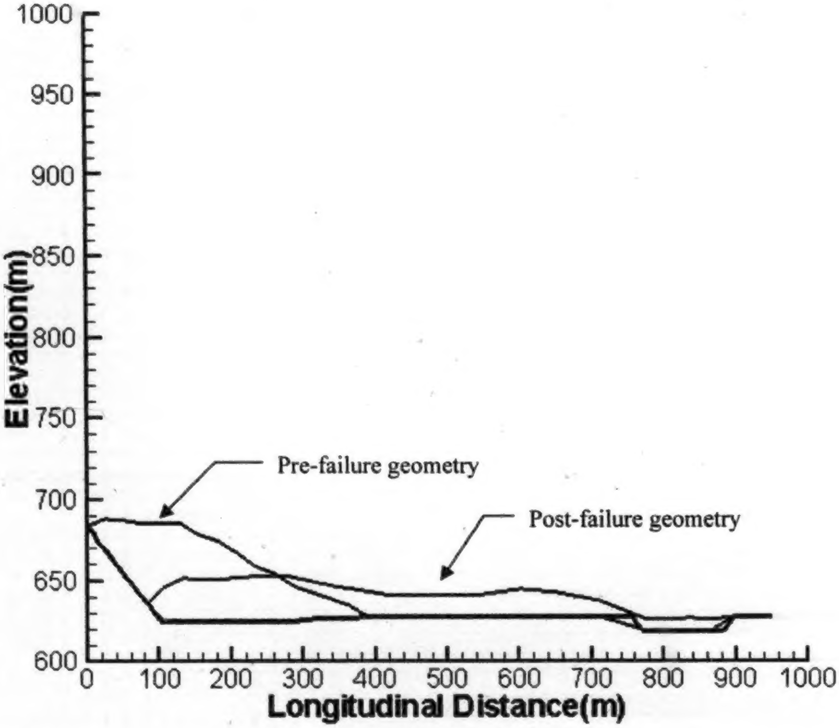

Figure B.26 Geometries of the Fort Peck flow slide based on dynamic analysis with the cohesive model

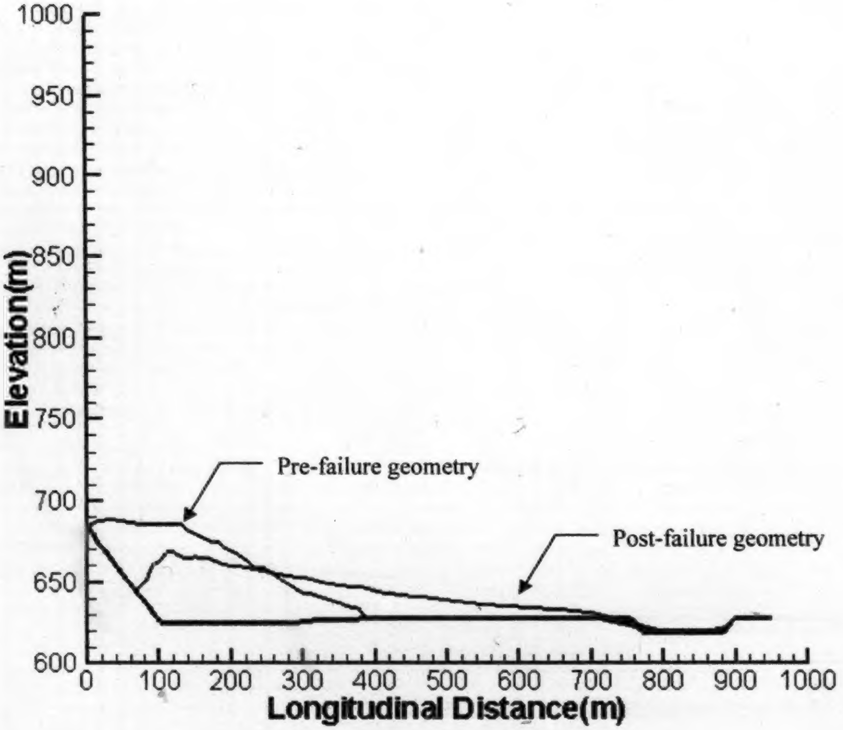

Figure B.27 Geometries of the Port Peck flow slide based on dynamic analysis with the friction model

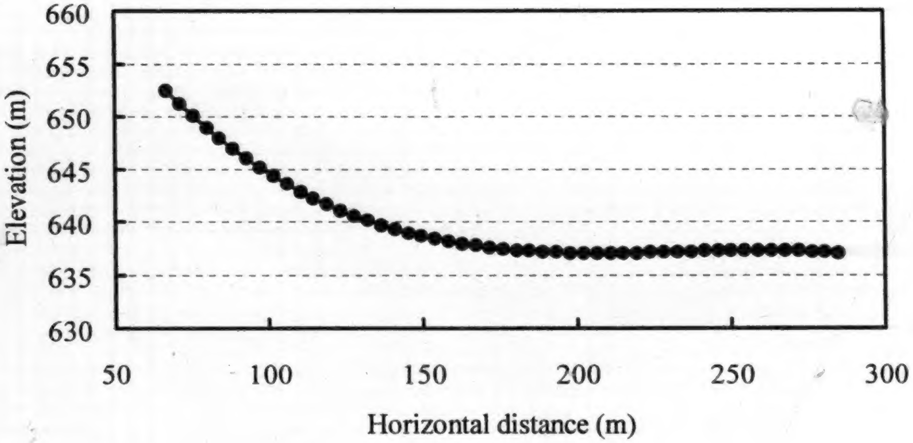

Figure B.28 Travel path of the centroid of the Fort Peck flow slide

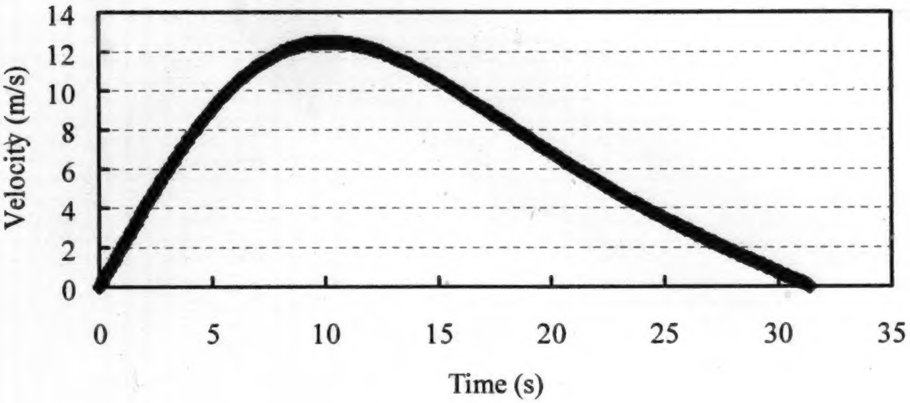

Figure B.29 Centroid velocity versus time for the Fort Peck flow slide

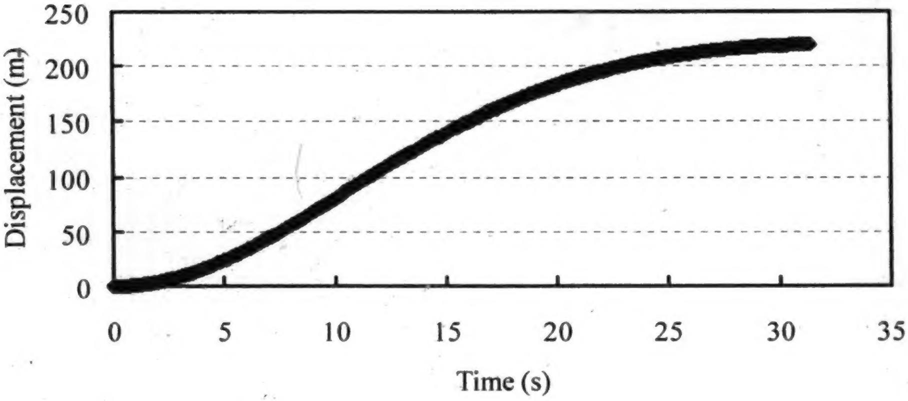

Figure B.30 Centroid displacement versus time for the Fort Peck flow slide

B.5 A Flow Slide in a Roadway Embankment on Lake Ackerman

B.5.1 Historical Information of the Lake Ackerman Flow Slide

On July 24, 1987, a flow slide occurred in the road embankment of Michigan Highway 94 on Ackerman Lake. The slide was triggered by six 196 kN trucks conducting deep seismic exploration from the road surface. The flow slide caused the collapse of a 91 m section of road embankment and generated a 4.5 m wave that crossed the 122 m lake and destroyed a boat dock. Post-failure investigations of the Lake Ackerman flow slide have been conducted by Hryciw et al. (1990), Olson (2001), and Jefferies and Been (2006). Descriptions herein are taken from their work.

The road embankment over Ackerman Lake was constructed of clean, medium to fine sand taken from adjacent roadway cuts. The embankment below water was placed by end dumping after the removal of peat and soft sediments from the original lake bottom. The thickness of removed lakebed mud was approximately 1.2 m. The fill material above the lake level was moderately compacted. The unit weight of the fill material was about 19.3 kN/m^3. The top of the embankment varied from about 1.8 m to 4.0 m above the water level. The side slopes of the embankment were 2H:1V on one side and 4H:1V on the other.

Post-failure investigations revealed that the flow slide of the Ackerman Lake road embankment was caused by liquefaction of loose hydraulic fill (Hryciw et al. 1990). The liquefaction was induced by a train of six trucks carrying out seismic surveys for exploration of oil-bearing formations. The train of six trucks was spread out over approximately 74 m along the roadway at the time of embankment collapse. The location of trucks when the slide occurred is presented in Figure B.31 and a photograph taken after the failure is shown in Figure B.32. Figure B.33 shows pre- and post-failure cross sections of the embankment. On the basis of extrapolation from post-failure geometries of the embankment, Olson (2001) indicated that during the failure the crest of the embankment dropped over 3 m vertically and the sliding mass traveled approximately 12 to 15 m horizontally beyond the toe of the slope (Olson 2001).

B.5.2 Stability Analysis of the Lake Ackerman Flow Slide

Stability analyses of the flow slide of the embankment on Ackerman Lake have been conducted to estimate the liquefied shear strength (Hryciw et al. 1990; Olson 2001). Hryciw et al. (1990) indicated that the mobilized shear strength of the liquefied soil was in the range of 170 to 260 psf (8.1 to 12.4 kPa). This result was based on stability analyses of the pre-failure geometries of the road embankment at various stations.

Olson (2001) reexamined the Lake Ackerman embankment failure and carried out a series of stability analyses of the slope before and after the slide. The cross sections used in the stability analyses by Olson (2001) are presented in Figure B.34, Figure B.35, and Figure B.36. The nonliquefied soils were assigned a friction angle of 32°. The best estimate of yield shear strength was 10.1 kPa with a range of 8.6 to 10.5 kPa from stability analysis of the pre-failure slope. The back-calculated shear strength was approximately 3.4 kPa with a range of 2.9 to 4.8 kPa, based on stability analysis of the post-failure geometry of the slide mass. The best estimate of liquefied shear strength was 3.9 kPa with a range of 3.4 to 4.7 kPa using kinetic analysis.

B.5.3 Dynamic Analysis of the Lake Ackerman Flow Slide

Based on Figure B.36, the geometries used for dynamic analysis of the liquefaction flow slide of the Lake Ackerman embankment are obtained, as shown in Figure B.37. Cohesive and friction models are used as constitutive laws in the dynamic analyses.

The post-liquefaction geometry of the Lake Ackerman embankment flow slide shown in Figure B.38 is based on dynamic analysis using the cohesive model with internal energy dissipation incorporated. The runout distance calculated is approximately 10.4 m, which is close to the observed runout distance of 10.7 m. The liquefied shear strength from slice-based dynamic analysis with consideration of internal energy dissipation is 5.5 kPa.

The post-liquefaction geometry of the Lake Ackerman embankment flow slide shown in Figure B.39 is based on dynamic analysis using the friction model with internal energy dissipation considered. The runout distance calculated is 11.5 m from simulation and the bulk friction angle back-calculated is about 11.5°.

B.5.4 Kinetic Analysis of the Lake Ackerman Flow Slide

Kinetic analysis of the liquefaction flow slide in the Lake Ackerman embankment with a sliding block model is carried out. The friction model is used to calculate the shear resistance mobilized in the kinetic analysis. The travel path of the center of gravity is defined by a third order polynomial similar to the travel path used in the kinetic analysis by Olson (2001). The travel path of the centroid, velocity, and displacement based on dynamic analysis are presented in Figure B.40 to Figure B.42. The back-calculated bulk friction angle is about 8.3°.

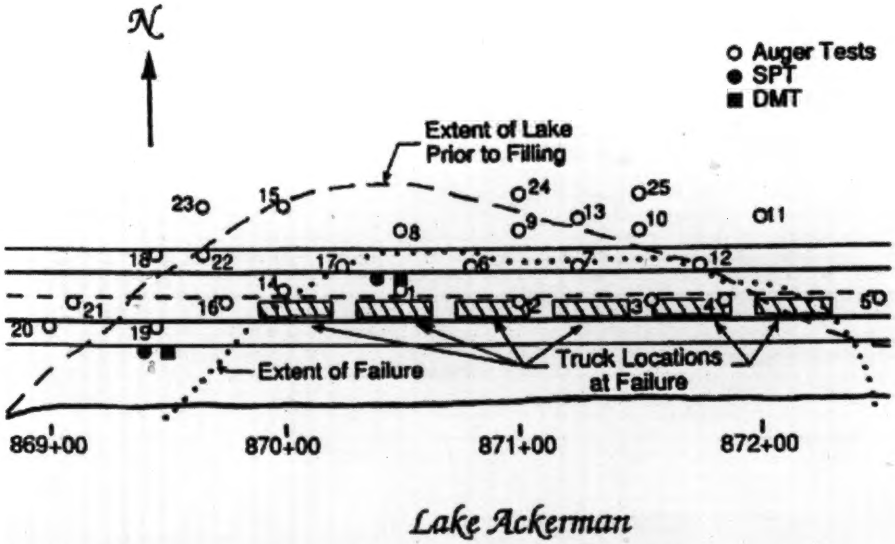
N
○ Auger Tests
● SPT
■ DMT
Extent of Lake Prior to Filling
23
15
24
25
9
13
10
11
8
18
22
17
6
7
12
14
1
2
3
4
5
21
16
20
19
Extent of Failure
Truck Locations at Failure
869+00
870+00
871+00
872+00
Lake Ackerman

Figure B.31 Location of trucks at the time of failure of the Ackerman Lake road embankment (After Hryciw et al. 1990)

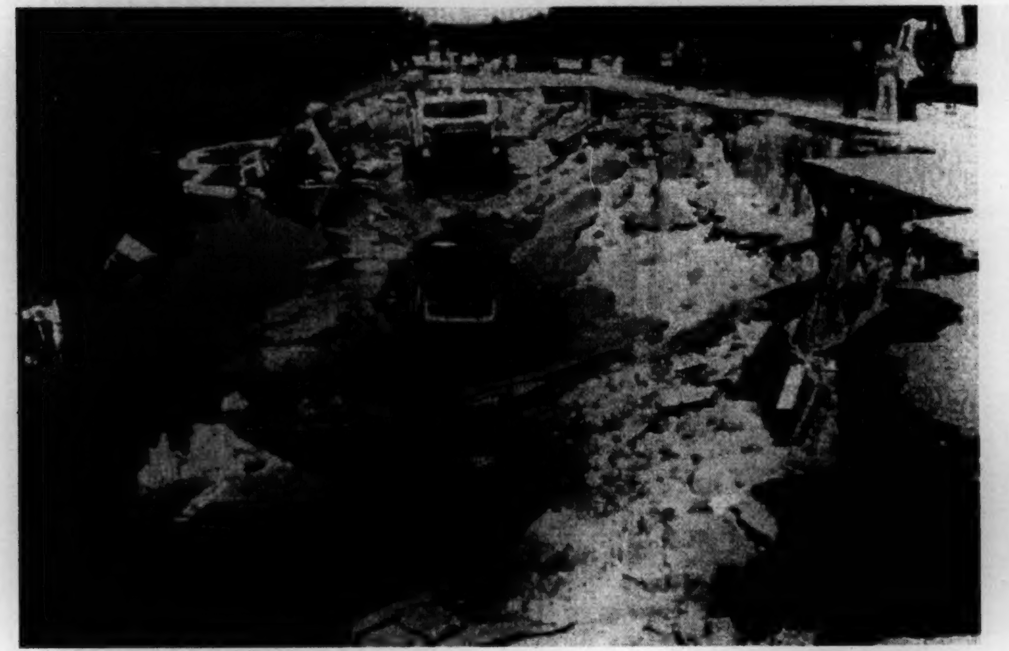

Figure B.32 Failure of the embankment on Ackerman Lake (After Hryciw et al. 1990)

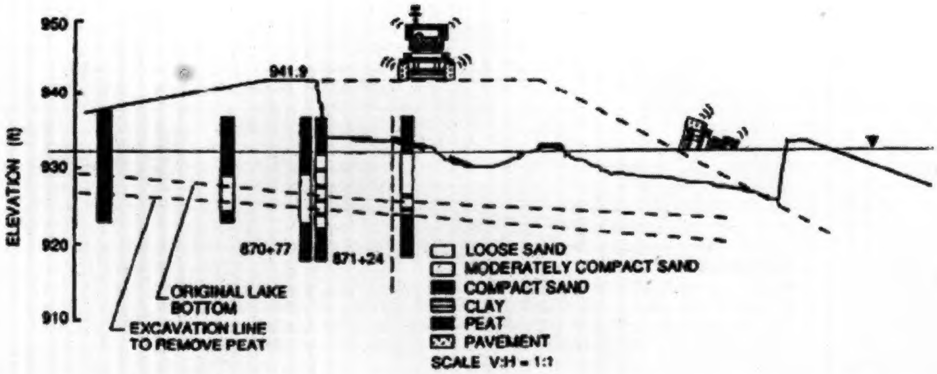
950
940
930
920
910
ELEVATION (ft)
941.9
870+77
871+24
ORIGINAL LAKE BOTTOM
EXCAVATION LINE TO REMOVE PEAT
LOOSE SAND
MODERATELY COMPACT SAND
COMPACT SAND
CLAY
PEAT
PAVEMENT
SCALE V:H = 1:1

Figure B.33 Pre- and post-failure cross section of the embankment on Ackerman Lake (After Hryciw et al. 1990)

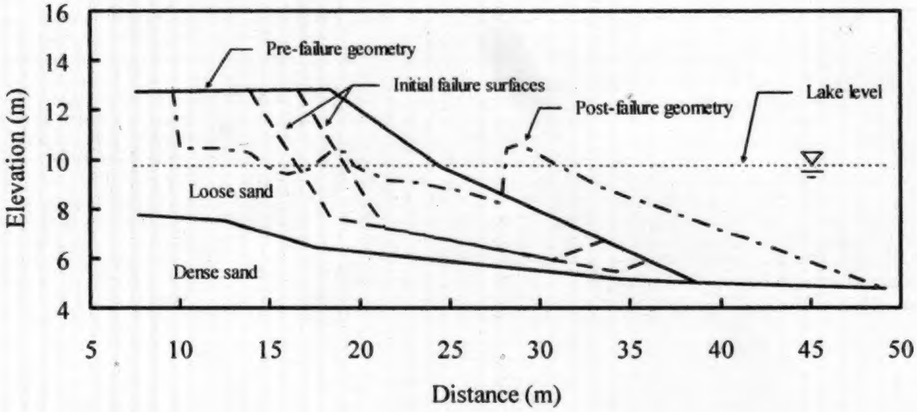

Figure B.34 Pre-failure geometries of the Lake Ackerman embankment used for yield shear strength analyses (Modified from Olson 2001)

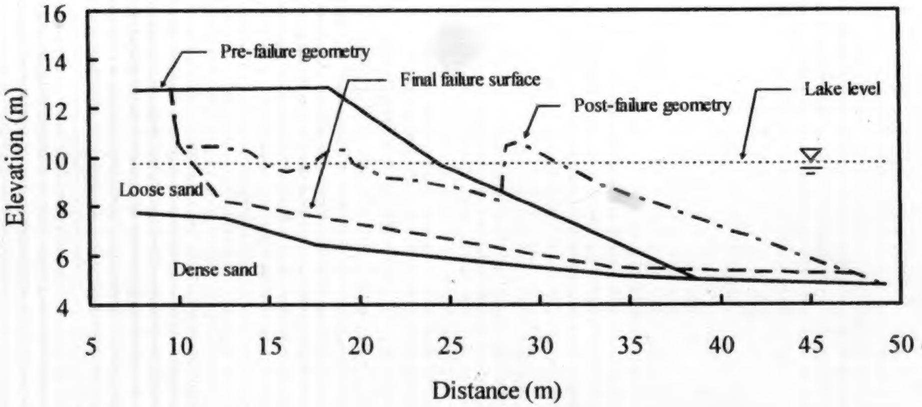

Figure B.35 Post-failure geometries of the Lake Ackerman embankment used for liquefied shear strength analyses (Modified from Olson 2001)

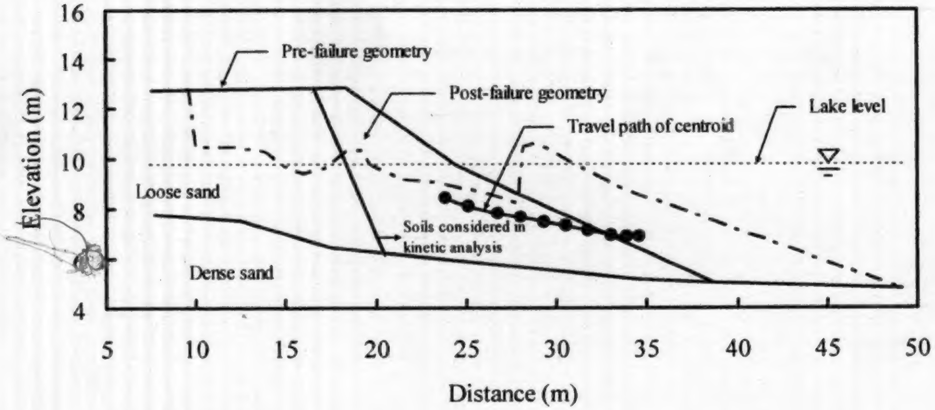

Figure B.36 Post-failure geometries of the Lake Ackerman embankment used for kinetic analysis (Modified from Olson 2001)

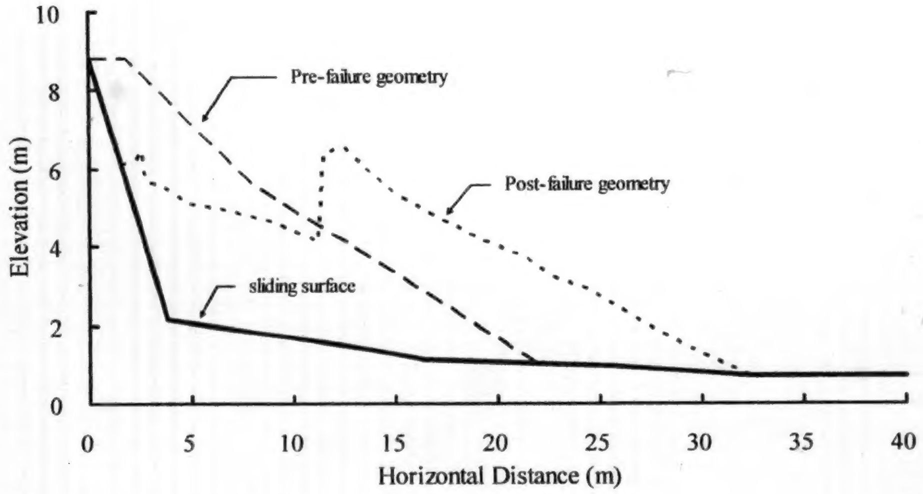

Figure B.37 Geometries of the Lake Ackerman flow slide used for dynamic analysis

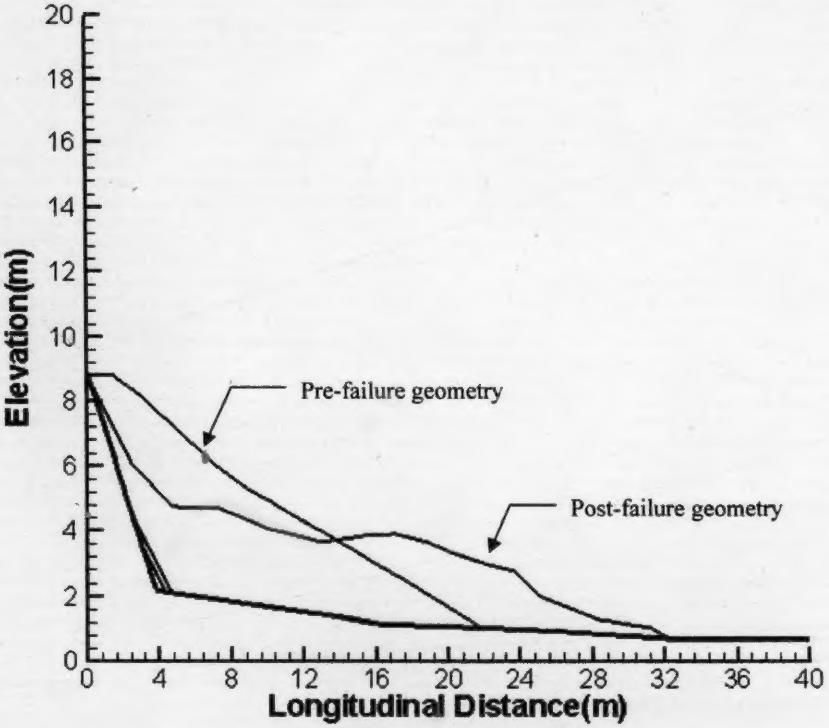

Figure B.38 Geometries of the Lake Ackerman flow slide based on dynamic analysis with the cohesive model

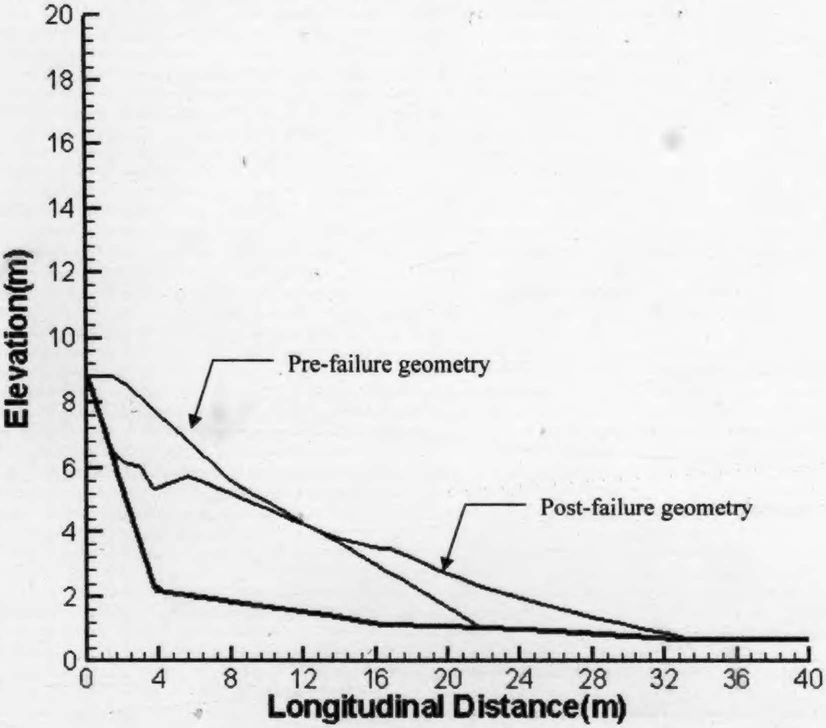

Figure B.39 Geometries of the Lake Ackerman flow slide based on dynamic analysis with the friction model

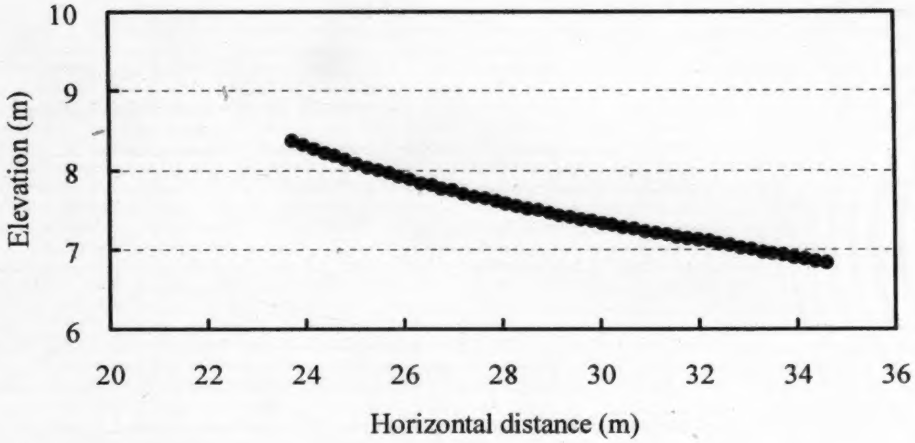

Figure B.40 Travel path of the centroid of the Lake Ackerman flow slide

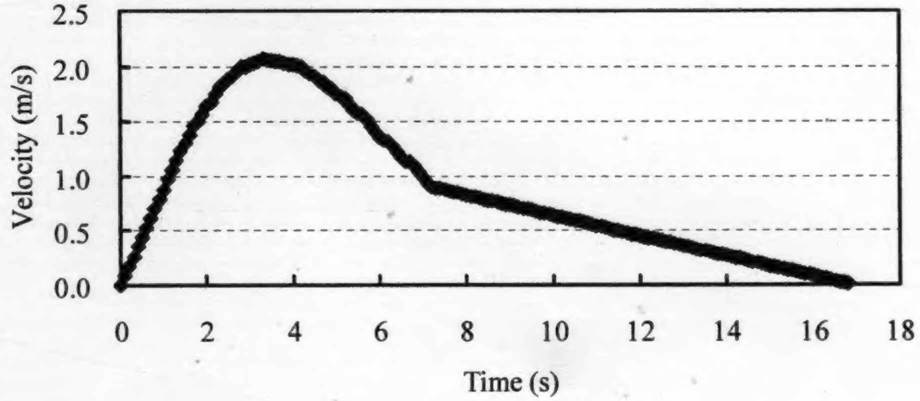

Figure B.41 Centroid velocity versus time for the Lake Ackerman flow slide

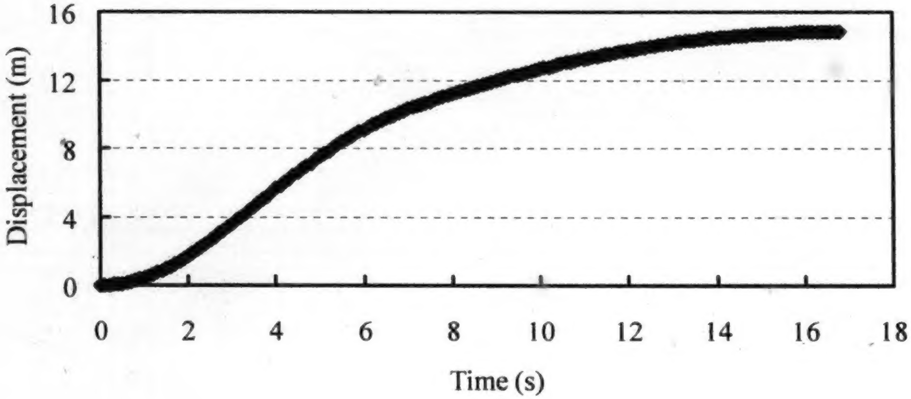

Figure B.42 Centroid displacement versus time for the Lake Ackerman flow slide

B.6 A Flow Slide in the Highway Embankment at Koda Numa

B.6.1 Historical Information of the Koda Numa Flow Slide

A flow slide in the highway embankment at Koda Numa occurred during the 1968 Tokachi-Oki earthquake in Japan. The embankment was approximately 3 m high, with a side slope angle of about 30°. The embankment consisted of a fine to medium sand. Mishima and Kimura (1970) indicated that the sand had a water content of 16.4 percent, a wet unit weight of 18.6 kN/m^3, a degree of saturation of 64.5 percent, and a void ratio of 0.7. During the earthquake the embankment sand fill liquefied and flowed in both directions from the center, as shown in Figure B.43. The embankment materials extended approximately 20 m horizontally and came to rest with a post-failure slope angle of about 4° (Seed 1987; Olson 2001).

B.6.2 Stability Analysis of the Koda Numa Flow Slide

Stability analyses of the Koda Numa flow slide have been conducted to estimate the liquefied shear strength (Seed 1987; Olson 2001). Seed (1987) estimated that the mobilized shear strength of the liquefied sand in the Koda Numa flow slide was about 50psf (24kPa). No explanations were given as to how this value was calculated.

Olson (2001) investigated the Koda Numa flow slide and carried out a series of stability analyses of the slope before and after the slide. The cross sections used in the stability analyses by Olson (2001) are presented in Figure B.44, Figure B.45, and Figure B.46. The sand above the phreatic surface was assigned a friction angle in the range of 30° to 35°. The best estimate of yield shear strength was 5.3 kPa with a range of 4.5 to 5.7 kPa from the stability analysis of the pre-failure slope. The back-calculated shear strength was approximately 1.0 kPa with a range of 0.8 to 1.9 kPa, based on stability analysis of the post-failure geometry of the slide mass. The best estimate of liquefied shear strength was 1.2 kPa by using kinetic analysis.

B.6.3 Dynamic Analysis of the Koda Numa Flow Slide

Based on Figure B.46, the geometries used for dynamic analysis of the liquefaction flow slide of the Koda Numa embankment are obtained, as shown in Figure B.47. Cohesive and friction models are used as constitutive laws in the dynamic analyses.

The post-liquefaction geometry of the Koda Numa flow slide shown in Figure B.48 is based on dynamic analysis using the cohesive model with internal energy dissipation incorporated. The runout distance calculated is approximately 19.7 m, which is close to the observed runout distance of 19.4 m. The liquefied shear strength from slice-based dynamic analysis with consideration of internal energy dissipation is 0.6 kPa.

The post-liquefaction geometry of the Koda Numa embankment flow slide shown in Figure B.49 is based on dynamic analysis using the friction model with internal energy dissipation considered. The runout distance calculated is 18.8 m from simulation and the bulk friction angle back-calculated is about 7.4°.

B.6.4 Kinetic Analysis of the Koda Numa Flow Slide

Kinetic analysis of the liquefaction flow slide in the Koda Numa embankment with a sliding block model is carried out. The friction model is used to calculate the shear resistance mobilized in the kinetic analysis. The travel path of the center of gravity is defined by a third order polynomial similar to the travel path used in the kinetic analysis by Olson (2001). The travel path of the centroid, velocity, and displacement based on dynamic analysis are presented in Figure B.50 to Figure B.52. The back-calculated bulk friction angle is about 5.0°.

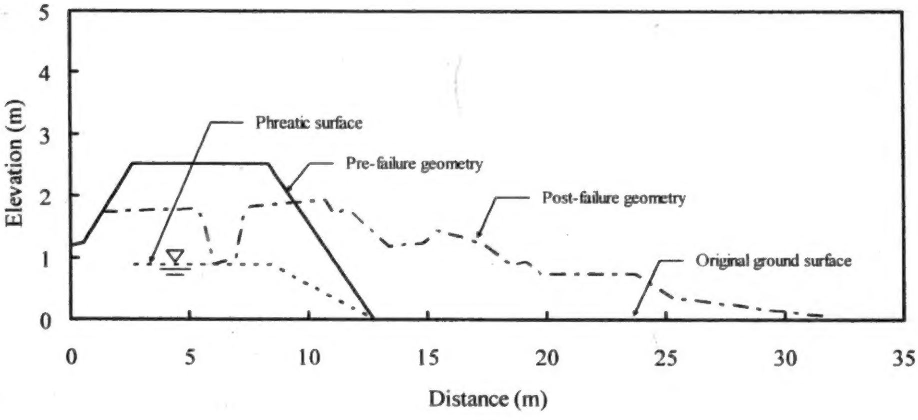

Figure B.43 Pre- and post-failure cross section of the embankment at Koda Numa (Modified from Olson 2001)

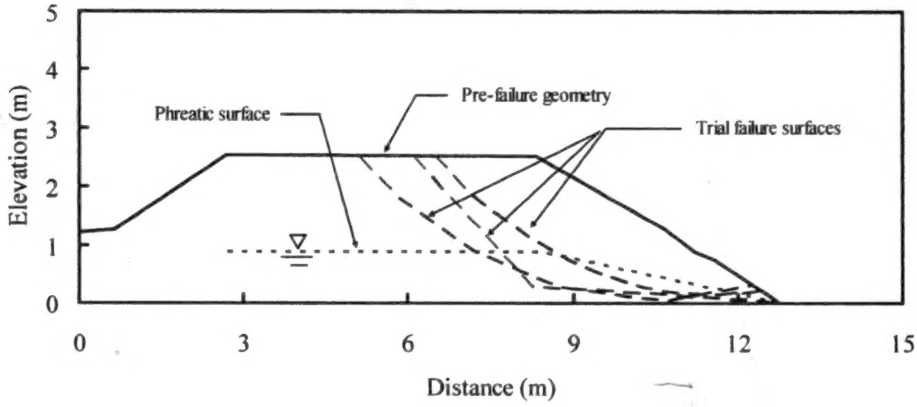

Figure B.44 Pre-failure geometries of the Koda Numa embankment used for yield shear strength analyses (Modified from Olson 2001)

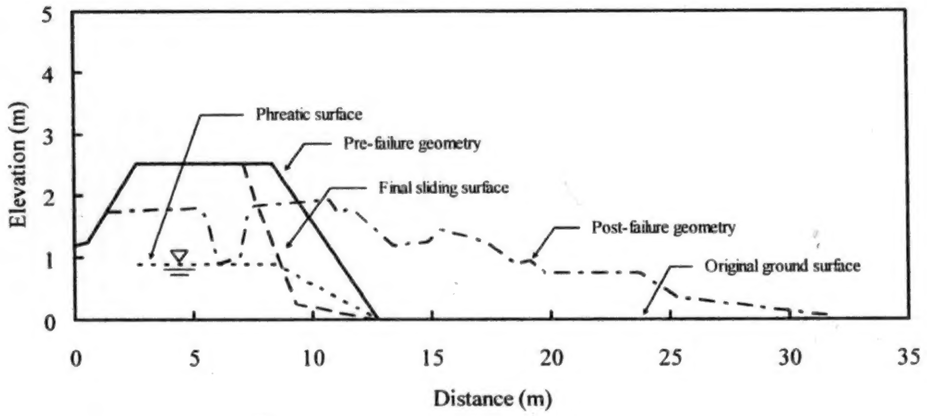

Figure B.45 Post-failure geometries of the Koda Numa embankment used for liquefied shear strength analyses (Modified from Olson 2001)

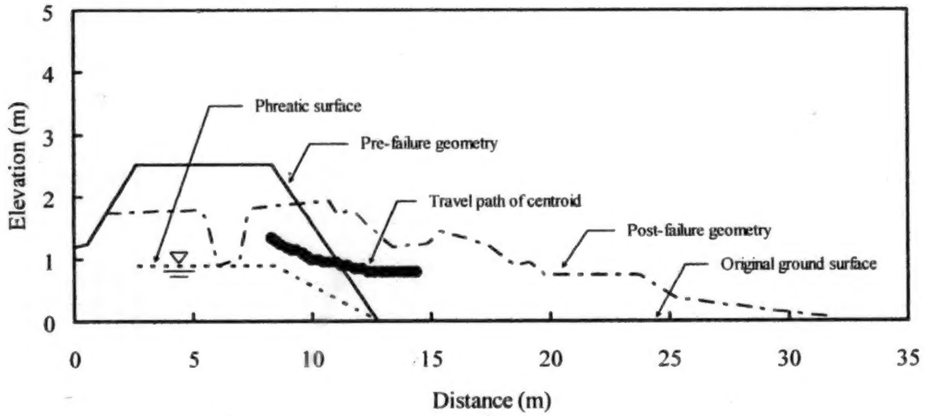

Figure B.46 Post-failure geometries of the Koda Numa embankment used for kinetic analyses (Modified from Olson 2001)

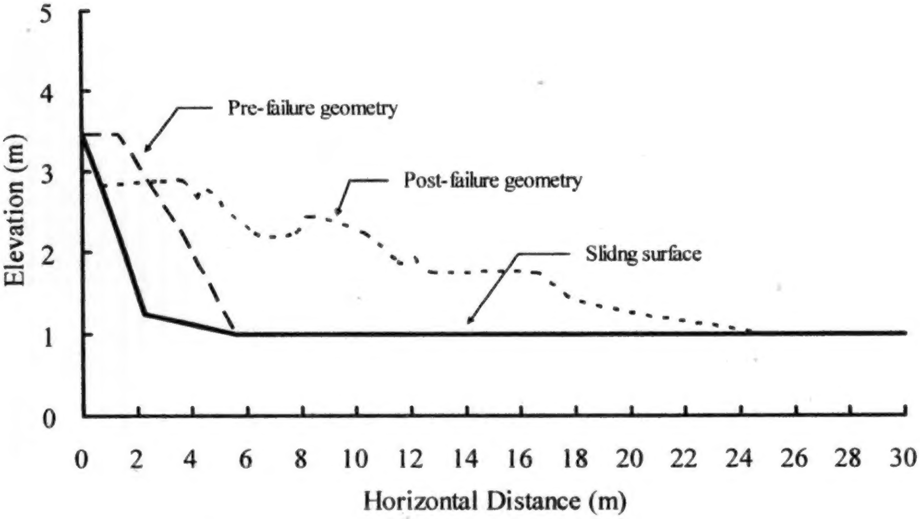

Figure B.47 Geometries of the Koda Numa flow slide used for dynamic analysis

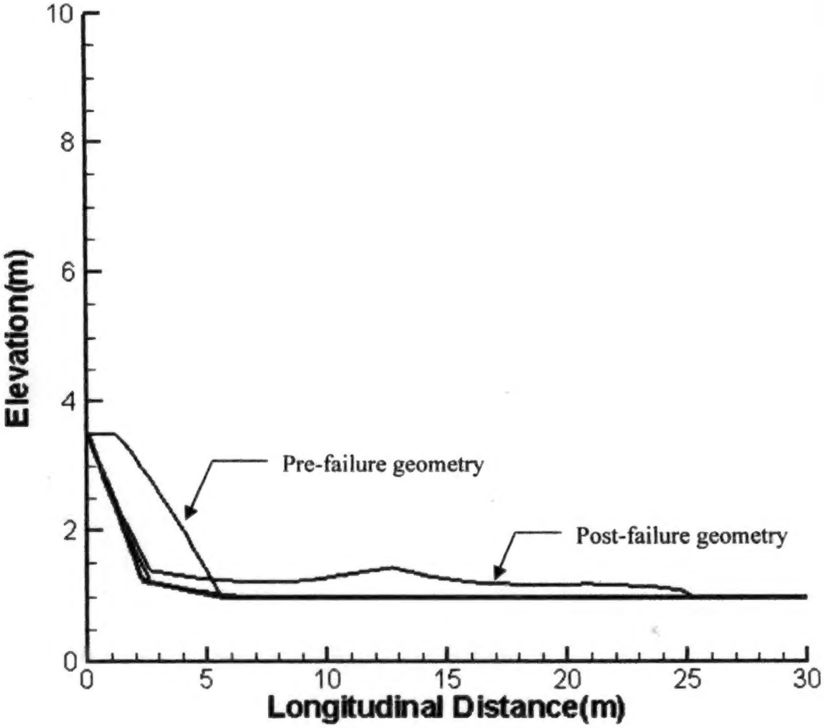

Figure B.48 Geometries of the Koda Numa flow slide based on dynamic analysis with the cohesive model

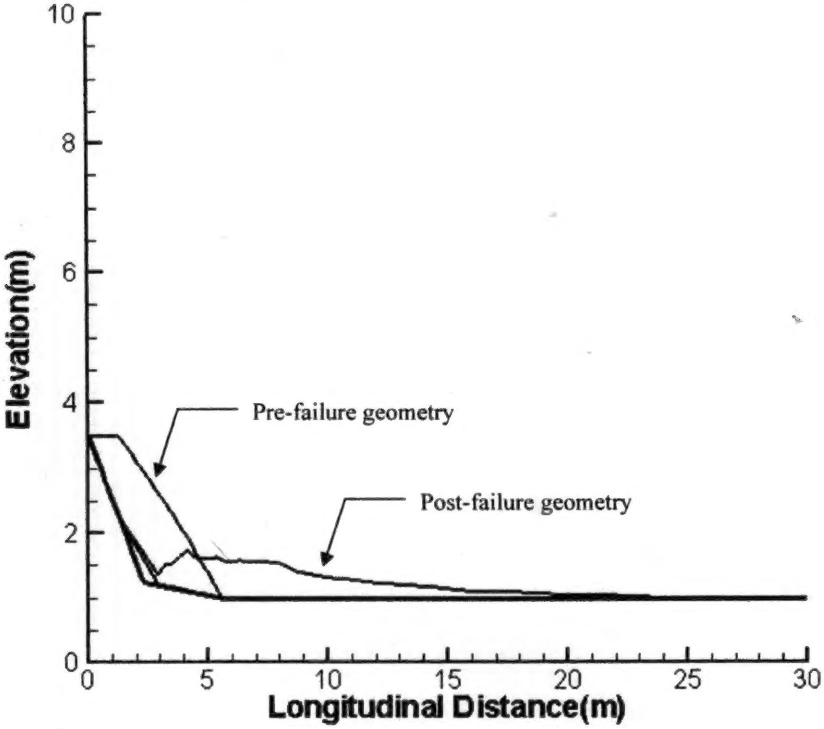

Figure B.49 Geometries of the Koda Numa flow slide based on dynamic analysis with the friction model

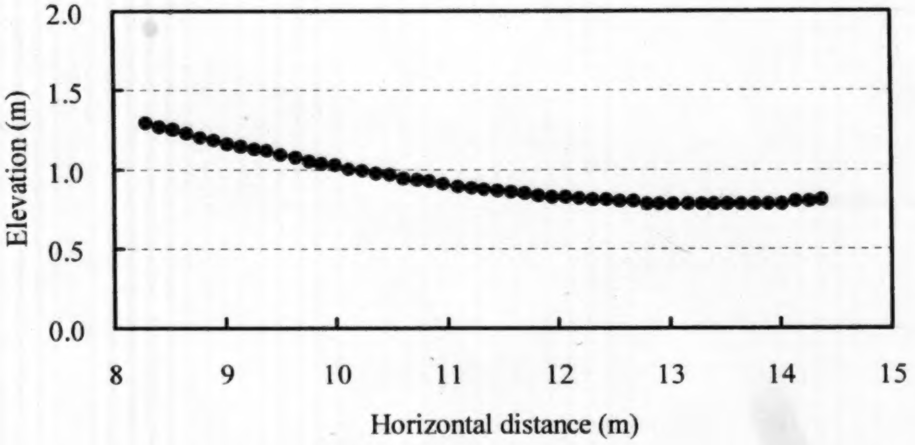

Figure B.50 Travel path of the centroid of the Koda Numa flow slide

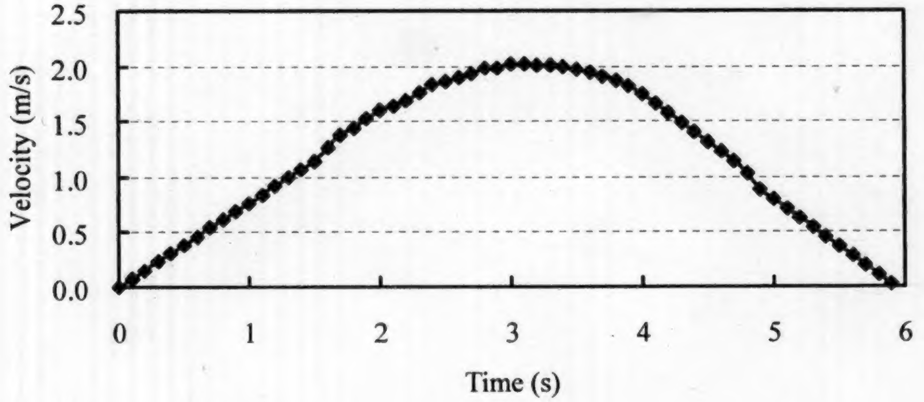

Figure B.51 Centroid velocity versus time for the Koda Numa flow slide

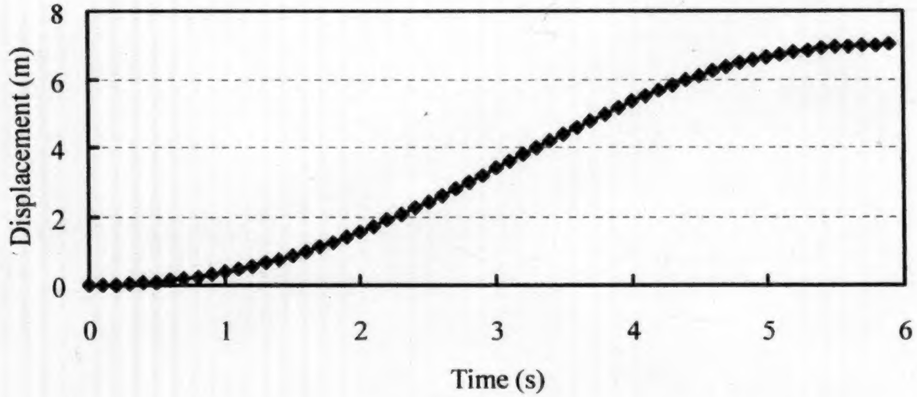

Figure B.52 Centroid displacement versus time for the Koda Numa flow slide

B.7 A Flow Slide in the Railway Embankment of the Uetsu-Line

B.7.1 Historical Information of the Uetsu-Line Flow Slide

The railway embankment between Dedo St. and Nishime St. in the Uetsu-Line failed during the 1964 Niigata earthquake in Japan. The length of the embankment involved in the failure was more than 150 m and the original height of the embankment was 7 m (Yamada 1966). The slide mass flowed about 110 m beyond the original toe of the slope, and came to rest at a post-failure slope angle of approximately 4°, as shown in Figure B.53.

The railway embankment was constructed across a rice field, which was underlain by a clay layer with sand seams. The embankment fill consisted of uniform fine sand. Comprehensive investigations indicated that the Uetsu-Line flow slide was a result of the liquefaction of loose, saturated sand triggered by the Niigata earthquake (Yamada 1966; Seed 1987; Olson 2001).

B.7.2 Stability Analysis of the Uetsu-Line Flow Slide

Stability analyses of the Uetsu-Line flow slide have been conducted to estimate the liquefied shear strength (Lucia 1981; Seed 1987; Olson 2001). Lucia (1981) and Seed (1987) estimated that the mobilized shear strength of the liquefied sand in the Uetsu-Line flow slide was about 35 psf (16.8 kPa), based on stability analysis of the post-failure geometry of the slide mass.

Olson (2001) investigated the Uetsu-Line flow slide and carried out a series of stability analyses of the slope before and after the slide. The cross sections used in the stability analyses by Olson (2001) are presented Figure B.54, Figure B.55, and Figure B.56. The sand above the phreatic surface was assigned a friction angle in the range of 30° to 35°. The best estimate of yield shear strength was 10.9 kPa with a range of 10.0

to 11.9 kPa from the stability analysis of the pre-failure slope. The back-calculated shear strength was approximately 0.6 kPa with a range of 0.3 to 1.9 kPa, based on stability analysis of the post-failure geometry of the slide mass. The best estimate of the liquefied shear strength was 1.7 kPa using kinetic analysis.

B.7.3 Dynamic Analysis of the Uetsu-Line Flow Slide

Based on Figure B.56, the geometries used for dynamic analysis of the liquefaction flow slide of the Uetsu-Line embankment are obtained, as shown in Figure B.57. Cohesive and friction models are used as constitutive laws in the dynamic analyses.

The post-liquefaction geometry of the Uetsu-Line flow slide shown in Figure B.58 is based on dynamic analysis using the cohesive model with internal energy dissipation incorporated. The runout distance calculated is approximately 98.3 m, which is close to the observed runout distance of 96.9 m. The liquefied shear strength from slice-based dynamic analysis with consideration of internal energy dissipation is 1.8 kPa.

The post-liquefaction geometry of the Uetsu-Line flow slide shown in Figure B.59 is based on dynamic analysis using the friction model with internal energy dissipation considered. The runout distance calculated is 98.6 m from simulation and the bulk friction angle back-calculated is about 6.0°.

B.7.4 Kinetic Analysis of the Uetsu-Line Flow Slide

Kinetic analysis of the liquefaction flow slide in the Uetsu-Line embankment with a sliding block model is carried out. The friction model is used to calculate the shear resistance mobilized in the kinetic analysis. The travel path of the center of gravity is defined by a third order polynomial similar to the travel path used in the kinetic analysis by Olson (2001). The travel path of the centroid, velocity, and displacement based on dynamic analysis are presented in Figure B.60 to Figure B.62. The back-calculated bulk friction angle is about 3.3°.

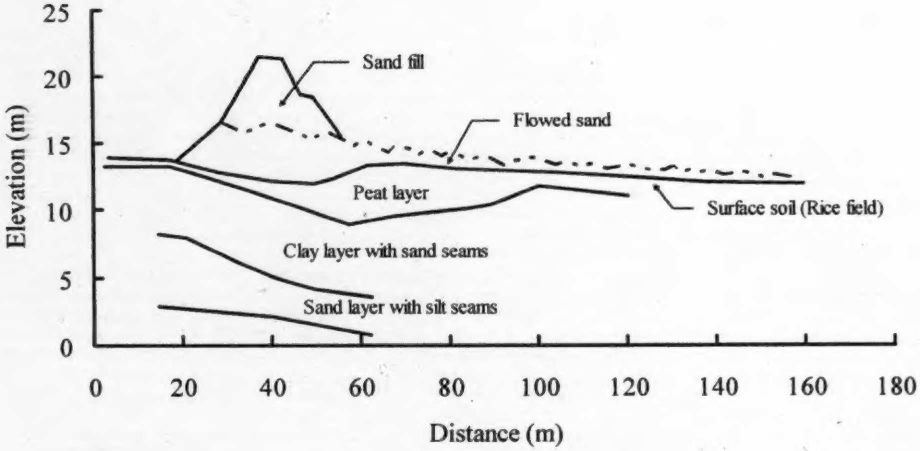

Figure B.53 Pre- and post-failure cross section of the embankment of the Uetsu-Line (Modified from Olson 2001)

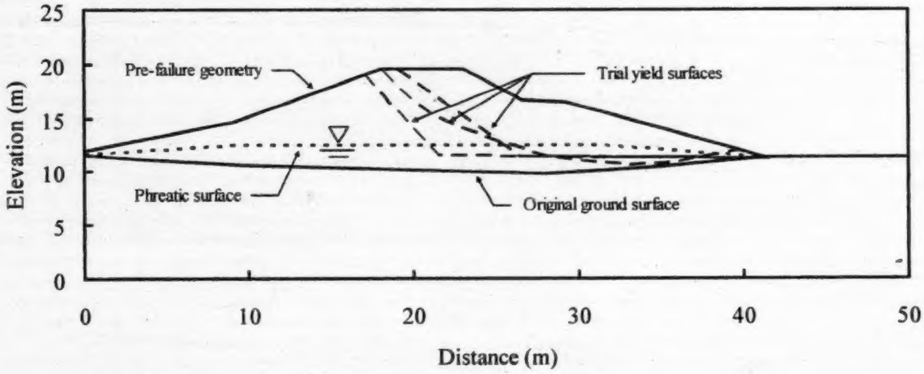

Figure B.54 Pre-failure geometries of the Uetsu-Line embankment used for yield shear strength analyses (Modified from Olson 2001)

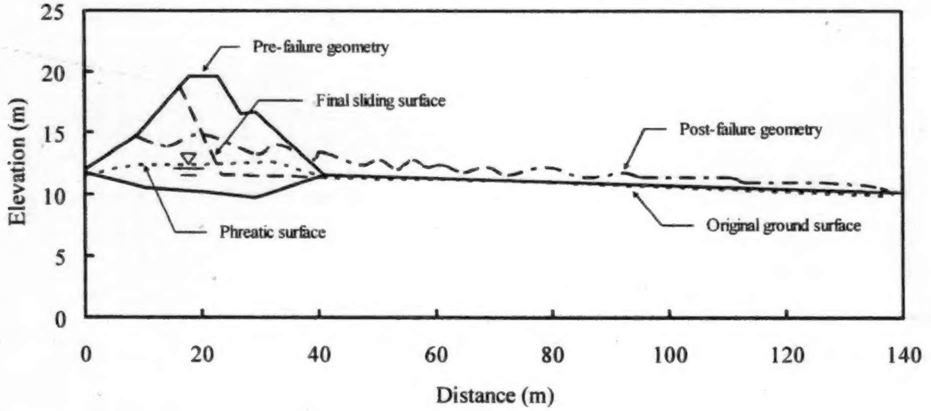

Figure B.55 Post-failure geometries of the Uetsu-Line embankment used for liquefied shear strength analyses (Modified from Olson 2001)

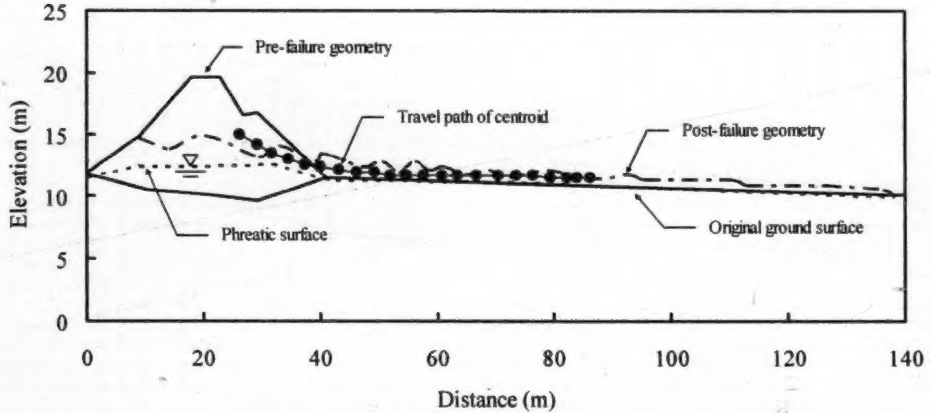

Figure B.56 Post-failure geometries of the Uetsu-Line embankment used for kinetic analyses (Modified from Olson 2001)

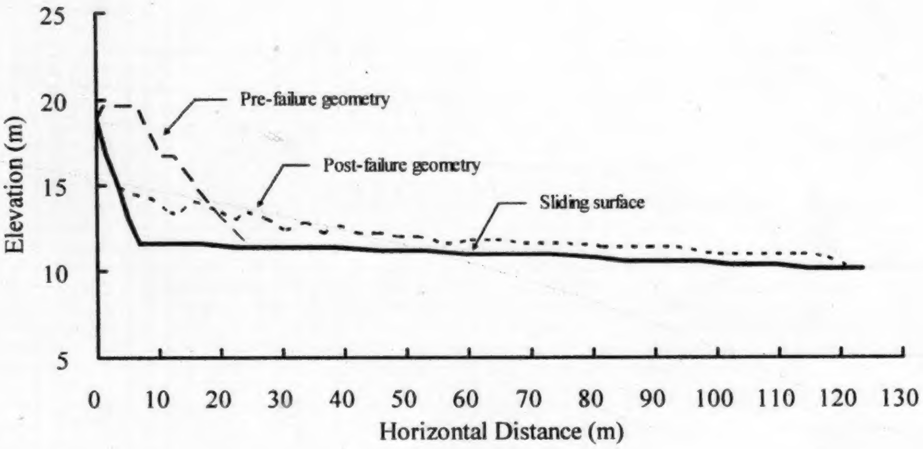

Figure B.57 Geometries of the Uetsu-Line flow slide used for dynamic analysis

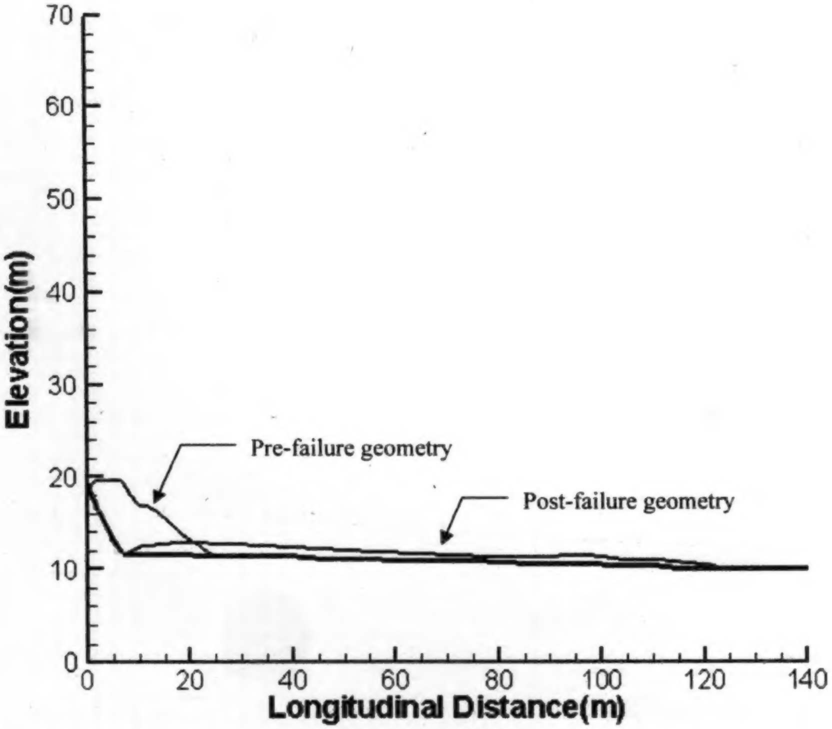

Figure B.58 Geometries of the Uetsu-Line flow slide based on dynamic analysis with the cohesive model

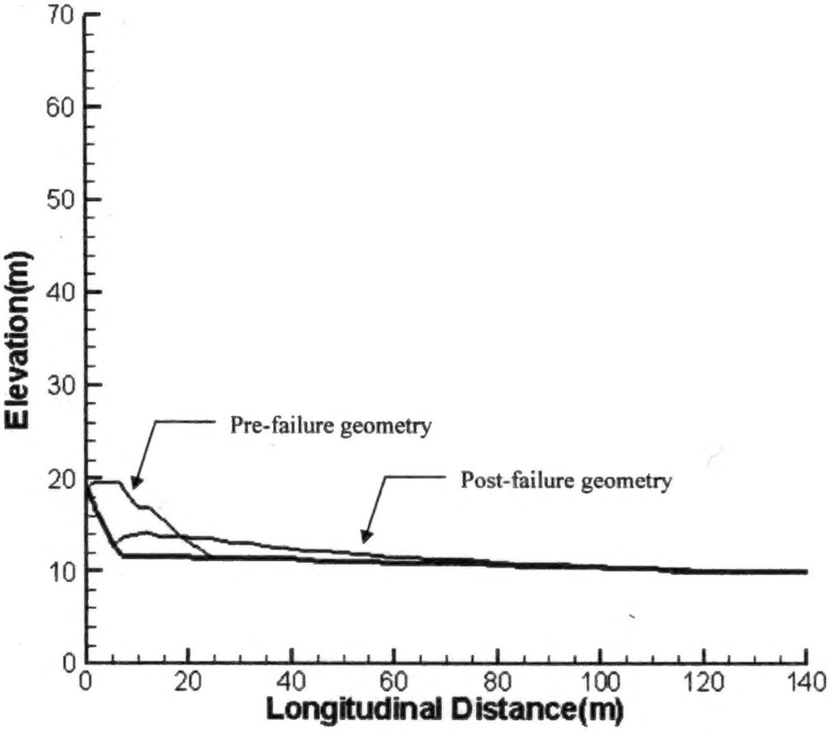

Figure B.59 Geometries of the Uetsu-Line flow slide based on dynamic analysis with the friction model

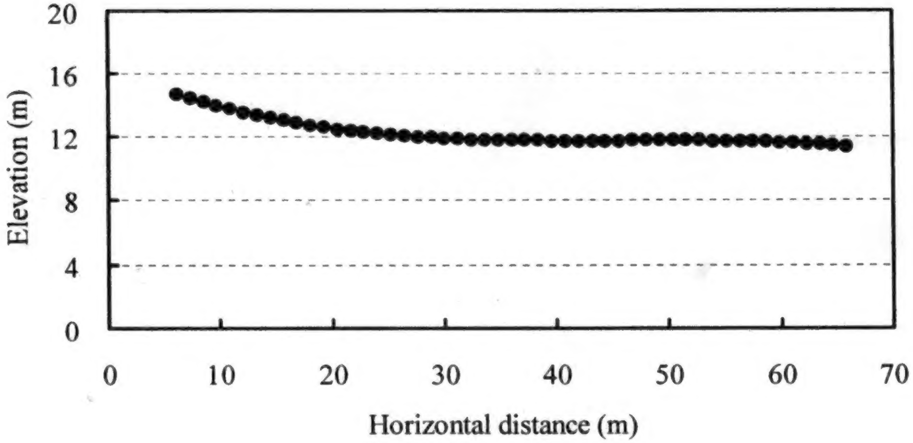

Figure B.60 Travel path of the centroid of the Uetsu-Line flow slide

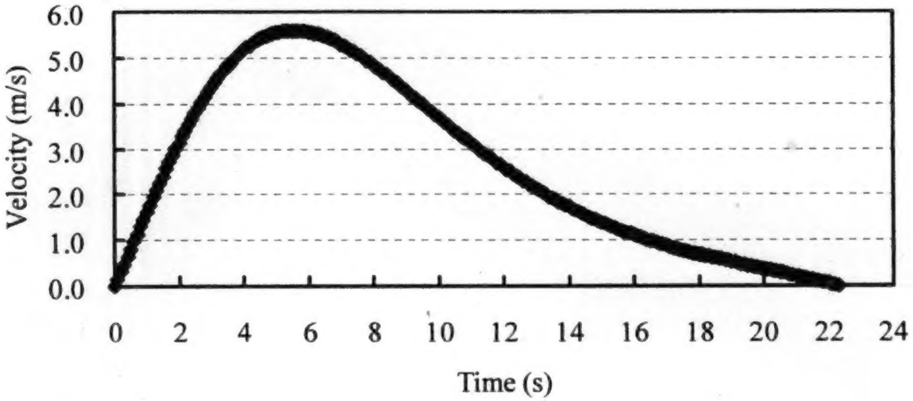

Figure B.61 Centroid velocity versus time for the Uetsu-Line flow slide

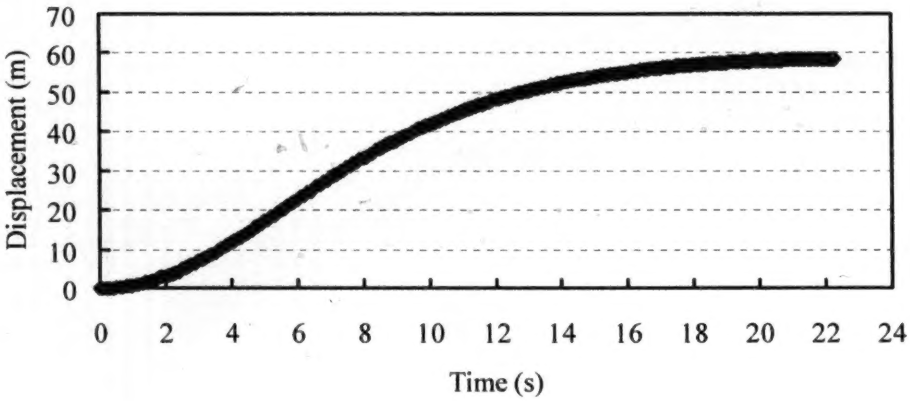

Figure B.62 Centroid displacement versus time for the Uetsu-Line flow slide

B.8 A Flow Slide in the Shibecha-Cho Embankment

B.8.1 Historical Information of the Shibecha-Cho Flow Slide

A flow slide occurred in the Shibecha-Cho embankment during the 1993 Kushiro-Oki earthquake in Japan. The length of embankment involved in the slide was over 200 m, as shown in Figure B.63 and Figure B.64. Post-failure geometry of the slide mass (cross section B-B in Figure B.64) indicated that the maximum drop of the embankment crest was approximately 5 m and the slide mass flowed about 23.5 m horizontally beyond the original embankment toe (Olson 2001).

The embankment fill consisted primarily of silty sand and was underlain by a layer of peat. Study of the construction history showed that the sandy fill received certain compaction from the construction traffic, but not in any controlled manner. The unit weight of the silty sand was approximately 15 kN/m^3. Site investigations and stability analyses (Miura et al. 1995, 1998; Olson 2001) indicated that the Shibecha-Cho flow slide was a result of the liquefaction of loose, saturated sand triggered by the Kushiro-Oki earthquake.

B.8.2 Stability Analysis of the Shibecha-Cho Flow Slide

Olson (2001) investigated the Shibecha-Cho flow slide and carried out a series of stability analyses of the slope before and after the slide. The cross sections used in the stability analyses by Olson (2001) are presented Figure B.65, Figure B.66, and Figure B.67. The sand above the phreatic surface was assigned a friction angle in the range of 30° to 35°. The best estimate of yield shear strength was 15.8 kPa with a range of 14.8 to 18.7 kPa from stability analysis of the pre-failure slope. The back-calculated shear strength was approximately 5.0 kPa with a range of 4.1 to 6.2 kPa, based on stability analysis of the post-failure geometry of the slide mass. The best estimate of the liquefied shear strength was 5.6 kPa with a range of 3.9 to 8.3 kPa using kinetic analysis.

B.8.3 Dynamic Analysis of the Shibecha-Cho Flow Slide

Based on Figure B.67, the geometries used for dynamic analysis of the liquefaction flow slide of the Shibecha-Cho embankment are obtained, as shown in Figure B.68. Cohesive and friction models are used as constitutive laws in the dynamic analyses.

The post-liquefaction geometry of the Shibecha-Cho flow slide shown in Figure B.69 is based on dynamic analysis using the cohesive model with internal energy dissipation incorporated. The runout distance calculated is approximately 22.1 m, which is close to the observed runout distance of 23.5 m. The liquefied shear strength from slice-based dynamic analysis with consideration of internal energy dissipation is 8.0 kPa.

The post-liquefaction geometry of the Shibecha-Cho flow slide shown in Figure B.70 is based on dynamic analysis using the friction model with internal energy dissipation considered. The runout distance calculated is 23.2 m from simulation and the bulk friction angle back-calculated is about 12.0°.

B.8.4 Kinetic Analysis of the Shibecha-Cho Flow Slide

Kinetic analysis of the liquefaction flow slide in the Shibecha-Cho embankment with a sliding block model is carried out. The friction model is used to calculate the shear resistance mobilized in the kinetic analysis. The travel path of the center of gravity is defined by a third order polynomial similar to the travel path used in the kinetic analysis by Olson (2001). The travel path of the centroid, velocity, and displacement based on dynamic analysis are presented in Figure B.71 to Figure B.73. The back-calculated bulk friction angle is about 15.8°.

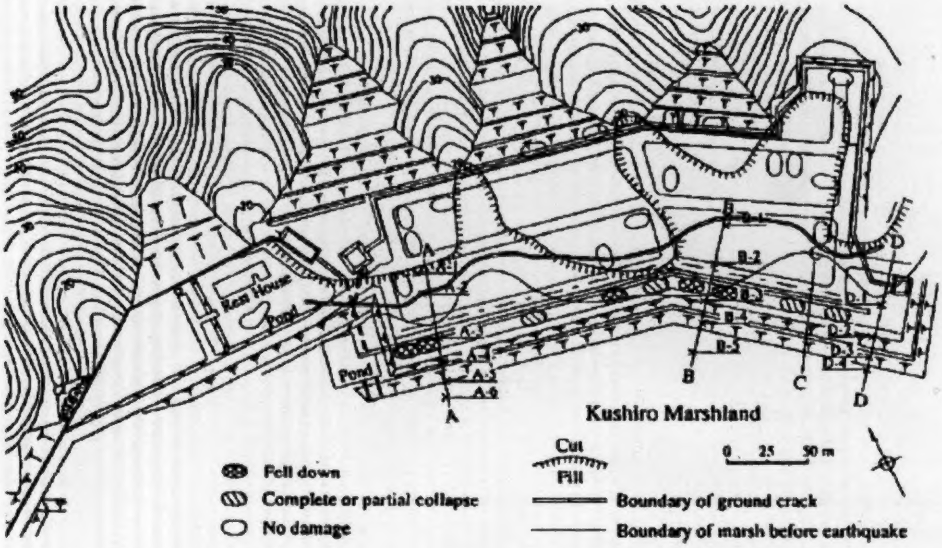
Rest House
Pond
Pond
A-1
A-2
A-3
A-5
A-6
B-1
B-2
B-3
B-4
B-5
D-1
D-2
D-3
D-4
A
B
C
D
Kushiro Marshland
Cut
Fill
0 25 50 m
Fell down
Complete or partial collapse
No damage
Boundary of ground crack
Boundary of marsh before earthquake

Figure B.63 Damage of the embankment during the Kushiro-Oki earthquake (After Olson 2001)

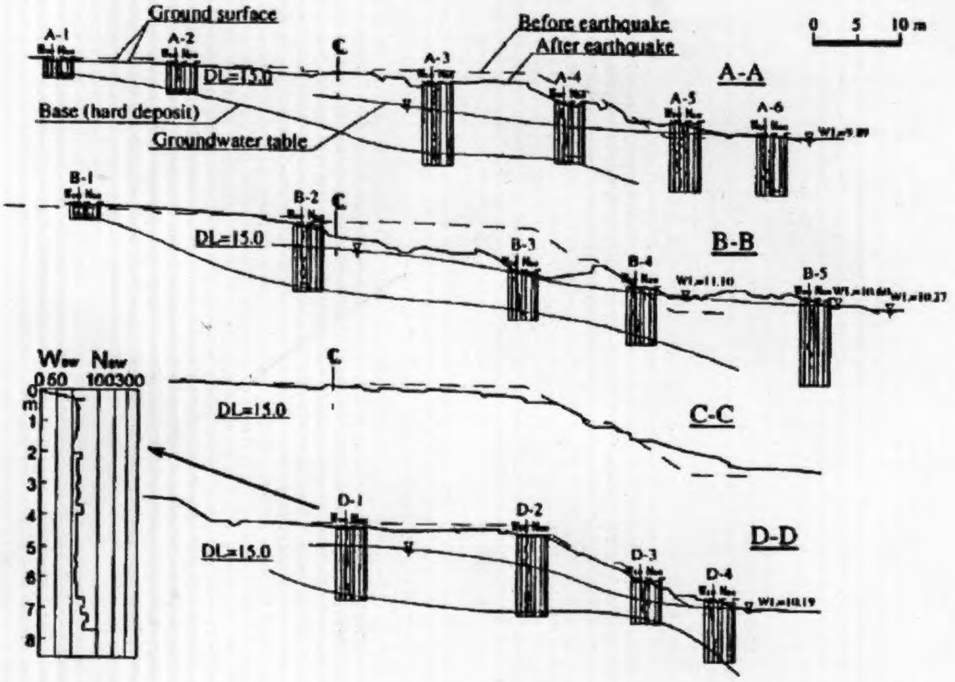
Ground surface
Before earthquake
After earthquake
0 5 10 m
A-1
A-2
A-3
A-4
A-5
A-6
DL=15.0
Base (hard deposit)
Groundwater table
A-A
B-1
B-2
B-3
B-4
B-5
DL=15.0
B-B
C-C
DL=15.0
D-1
D-2
D-3
D-4
DL=15.0
D-D
Wnw Nnw
0 60 100300
m
0
1
2
3
4
5
6
7
8

Figure B.64 Cross sections along four profiles in Figure B.63 (After Olson 2001)

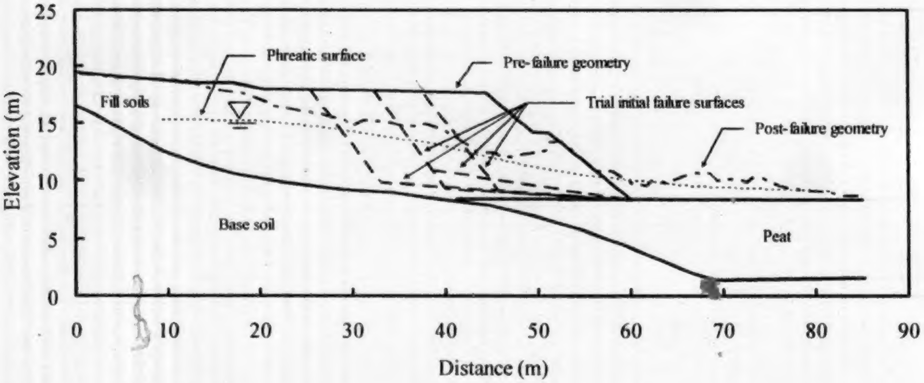

Figure B.65 Pre-failure geometries of the Shibecha-Cho embankment used for yield shear strength analyses (Modified from Olson 2001)

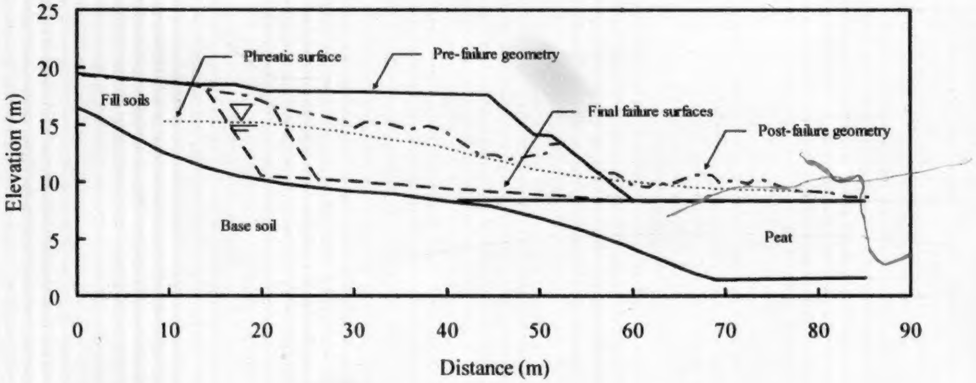

Figure B.66 Post-failure geometries of the Shibecha-Cho embankment used for liquefied shear strength analyses (Modified from Olson 2001)

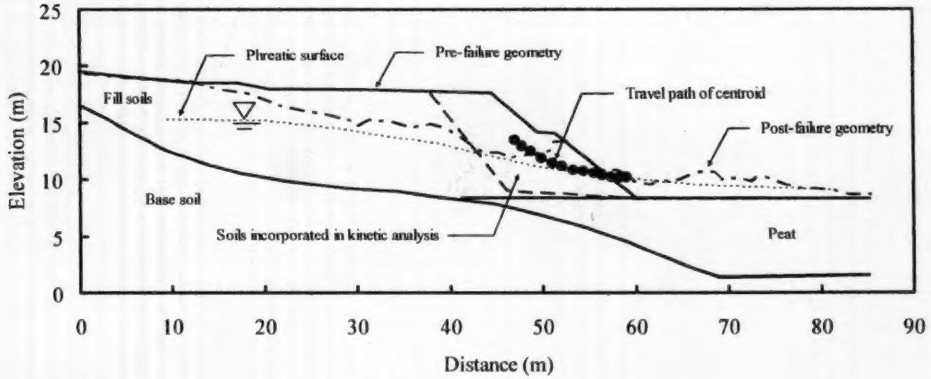

Figure B.67 Post-failure geometries of the Shibecha-Cho embankment used for kinetic analyses (Modified from Olson 2001)

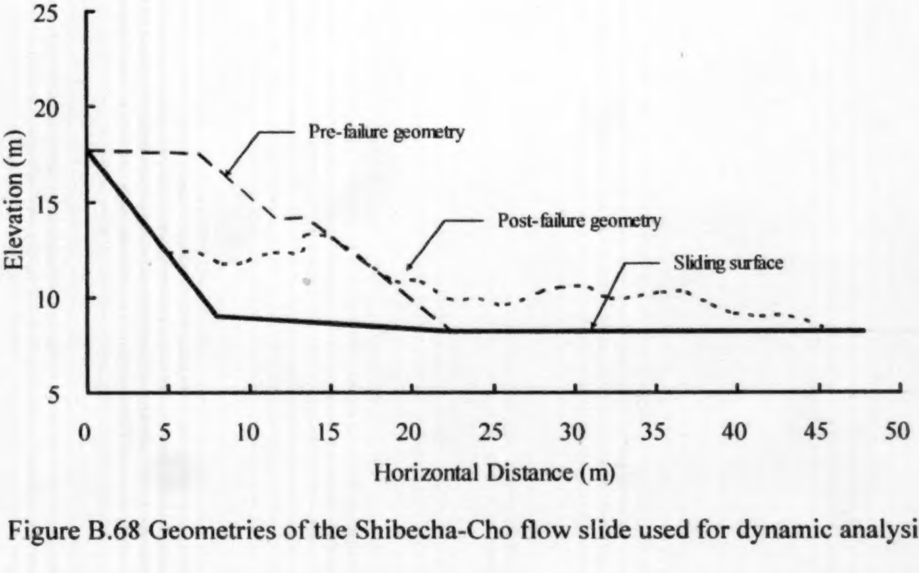

Figure B.68 Geometries of the Shibecha-Cho flow slide used for dynamic analysis

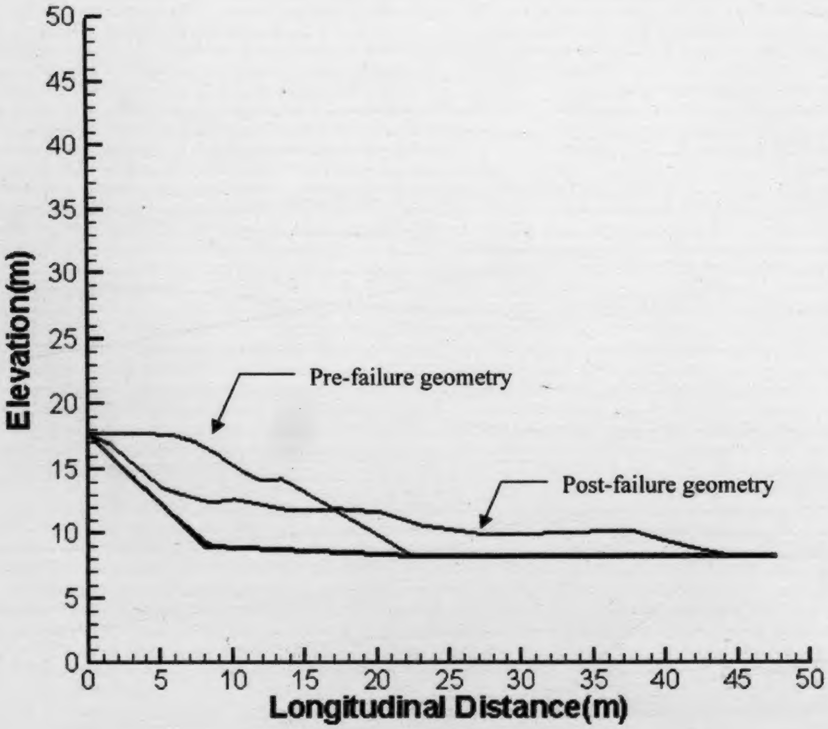

Figure B.69 Geometries of the Shibecha-Cho flow slide based on dynamic analysis with the cohesive model

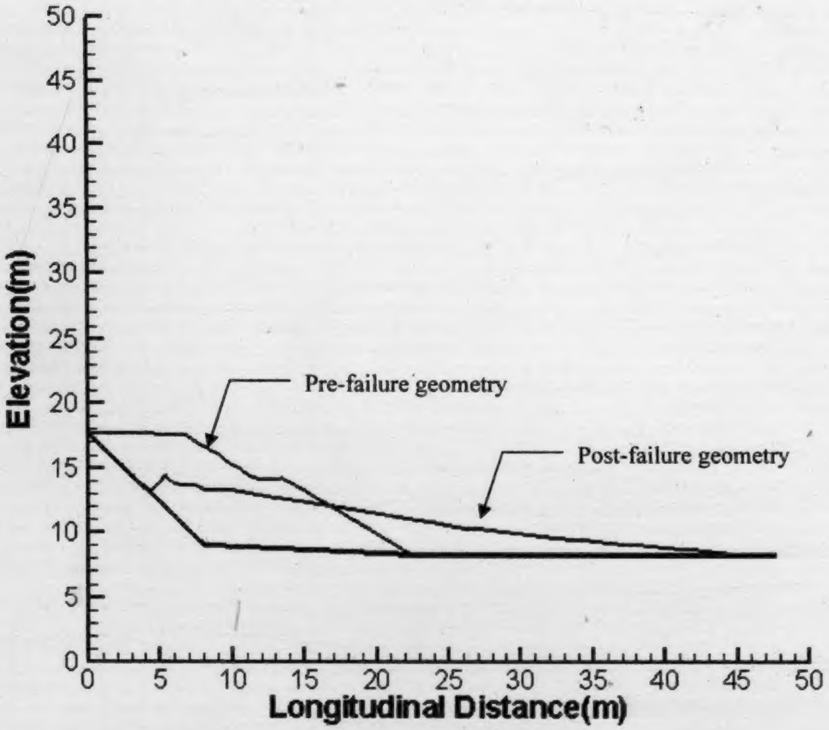

Figure B.70 Geometries of the Shibecha-Cho flow slide based on dynamic analysis with the friction model

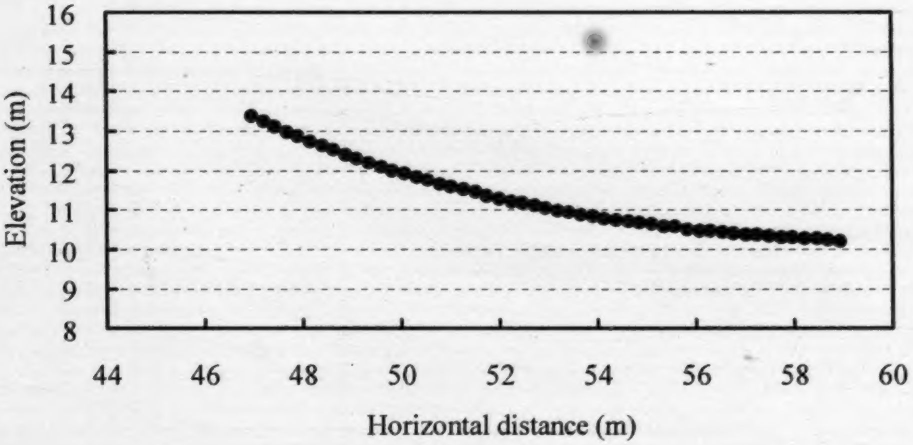

Figure B.71 Travel path of the centroid of the Shibecha-Cho flow slide

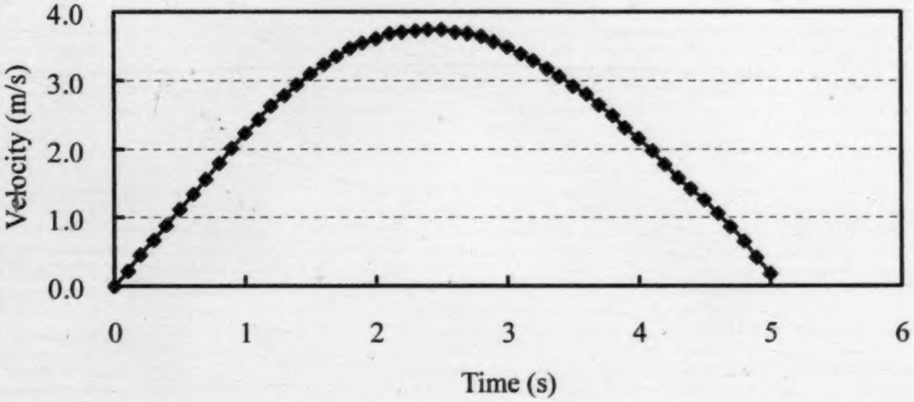

Figure B.72 Centroid velocity versus time for the Shibecha-Cho flow slide

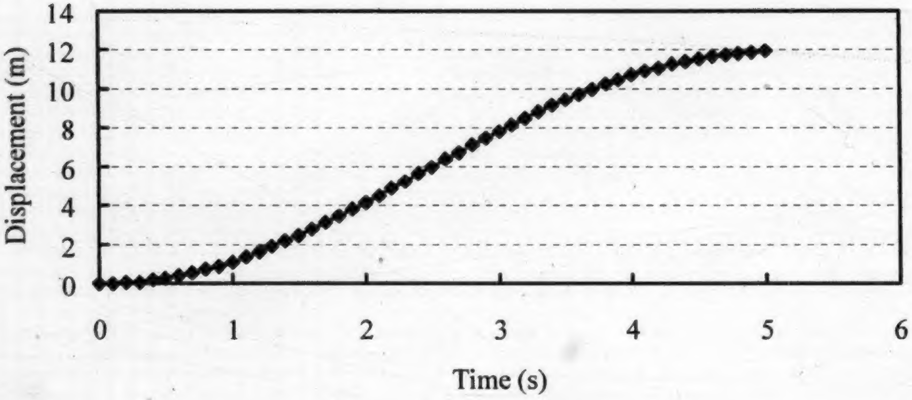

Figure B.73 Centroid displacement versus time for the Shibecha-Cho flow slide

B.9 A Flow Slide in the Route 272 Embankment

B.9.1 Historical Information of the Route 272 Flow Slide

A flow slide in the Route 272 embankment occurred during the 1993 Kushiro-Oki earthquake in Japan. The length of embankment involved in the slide was approximately 70 m. Post-failure geometry of the slide mass, as shown in Figure B.74, indicated that the maximum drop of the embankment crest was approximately 2.4 m and the slide mass flowed about 25 m horizontally beyond the original embankment toe (Olson 2001).

The embankment fill consisted primarily of silty sand and was underlain by a layer of pumice bearing volcanic sand (Sasaki et al. 1994). The unit weight of the silty sand was approximately 16.5 kN/m^3. Site investigations and stability analyses (Sasaki et al. 1994; Olson 2001) indicated that the Route 272 flow slide was a result of the liquefaction of loose saturated sandy embankment fill triggered by the Kushiro-Oki earthquake.

B.9.2 Stability Analysis of the Route 272 Flow Slide

Olson (2001) investigated the Route 272 flow slide and carried out a series of stability analyses of the slope before and after the slide. The cross sections used in the stability analyses by Olson (2001) are presented Figure B.75, Figure B.76, and Figure B.77. The sand above the phreatic surface was assigned a friction angle in the range of 30° to 35°. The best estimate of yield shear strength was 13.1 kPa with a range of 13.0 to 13.4 kPa from stability analysis of the pre-failure slope. The back-calculated shear strength was approximately 2.9 kPa with a range of 2.9 to 3.0 kPa, based on stability analysis of the post-failure geometry of the slide mass. The best estimate of liquefied shear strength was 4.8 kPa with a range of 3.0 to 5.7 kPa using kinetic analysis.

B.9.3 Dynamic Analysis of the Route 272 Flow Slide

Based on Figure B.77, the geometries used for dynamic analysis of the liquefaction flow slide of the Route 272 embankment are obtained, as shown in Figure B.78. Cohesive and friction models are used as constitutive laws in the dynamic analyses.

The post-liquefaction geometry of the Route 272 flow slide shown in Figure B.79 is based on dynamic analysis using the cohesive model with internal energy dissipation incorporated. The runout distance calculated is approximately 25.8 m, which is close to the observed runout distance of 25.6 m. The liquefied shear strength from slice-based dynamic analysis with consideration of internal energy dissipation is 5.6 kPa.

The post-liquefaction geometry of the Route 272 flow slide shown in Figure B.80 is based on dynamic analysis using the friction model with internal energy dissipation considered. The runout distance calculated is 25.8 m from simulation and the bulk friction angle back-calculated is about 11.0°.

B.9.4 Kinetic Analysis of the Route 272 Flow Slide

Kinetic analysis of the liquefaction flow slide in the Route 272 embankment with a sliding block model is carried out. The friction model is used to calculate the shear resistance mobilized in the kinetic analysis. The travel path of the center of gravity is defined by a third order polynomial similar to the travel path used in the kinetic analysis by Olson (2001). The travel path of the centroid, velocity, and displacement based on dynamic analysis are presented in Figure B.81 to Figure B.83. The back-calculated bulk friction angle is about 10.5°.

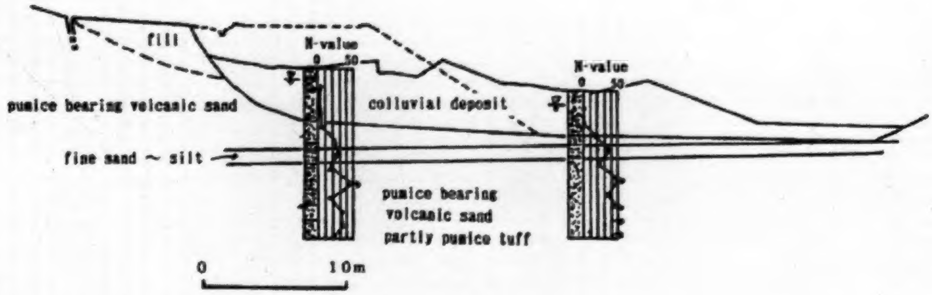
fill
N-value
0 50
N-value
0 50
pumice bearing volcanic sand
colluvial deposit
fine sand ~ silt
pumice bearing
volcanic sand
partly pumice tuff
0
10m

Figure B.74 Pre- and post-failure geometry of the Route 272 flow slide (After Olson 2001)

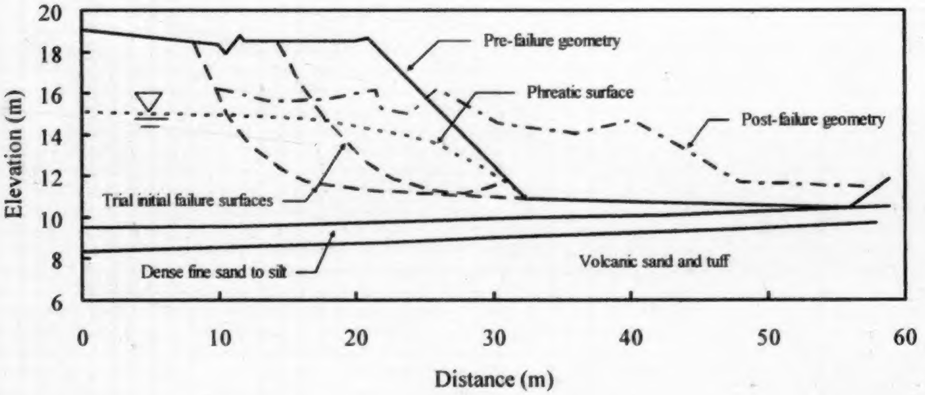

Figure B.75 Pre-failure geometries of the Route 272 embankment used for yield shear strength analyses (Modified from Olson 2001)

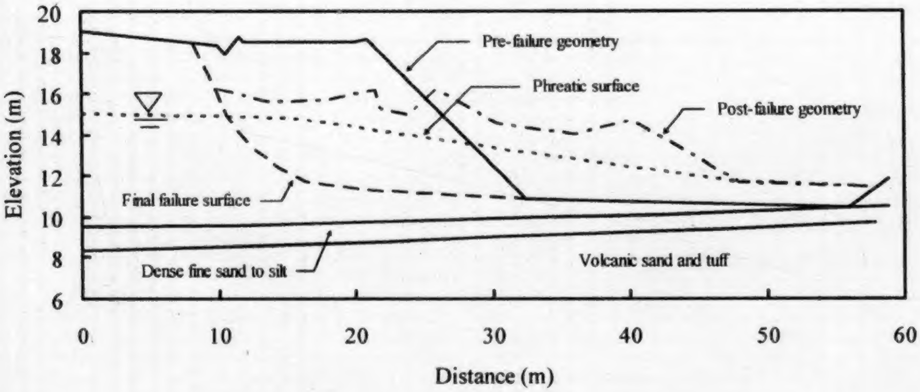

Figure B.76 Post-failure geometries of the Route 272 embankment used for liquefied shear strength analyses (Modified from Olson 2001)

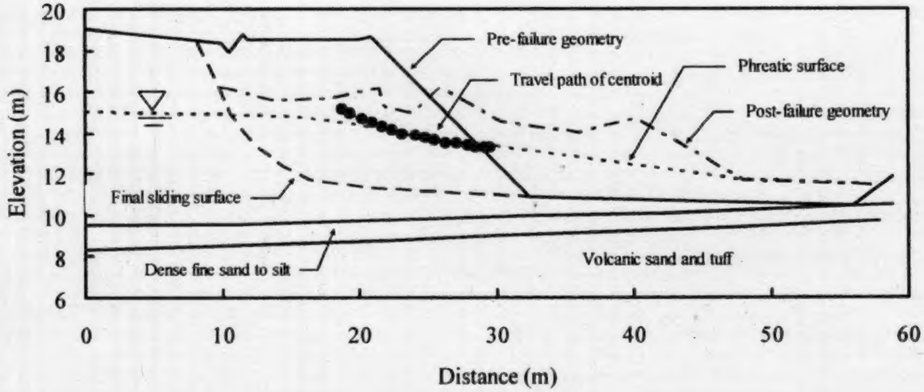

Figure B.77 Post-failure geometries of the Route 272 embankment used for kinetic analyses (Modified from Olson 2001)

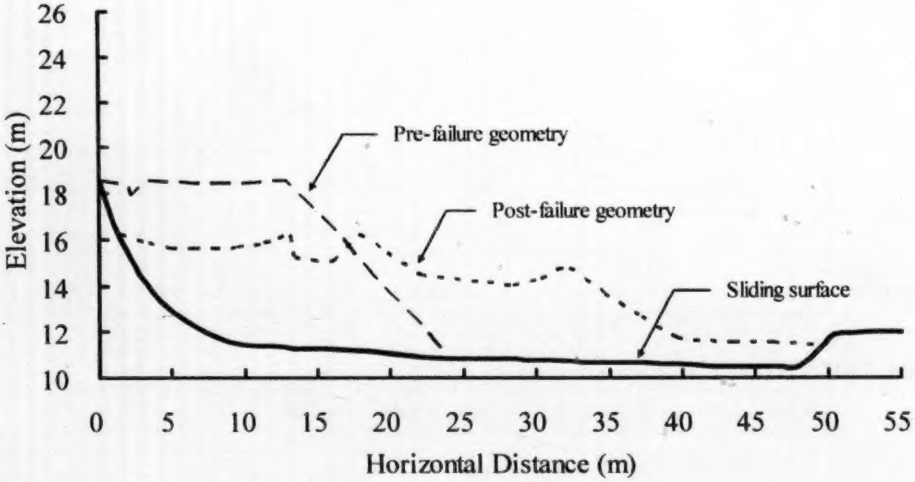

Figure B.78 Geometries of the Route 272 flow slide used for dynamic analysis

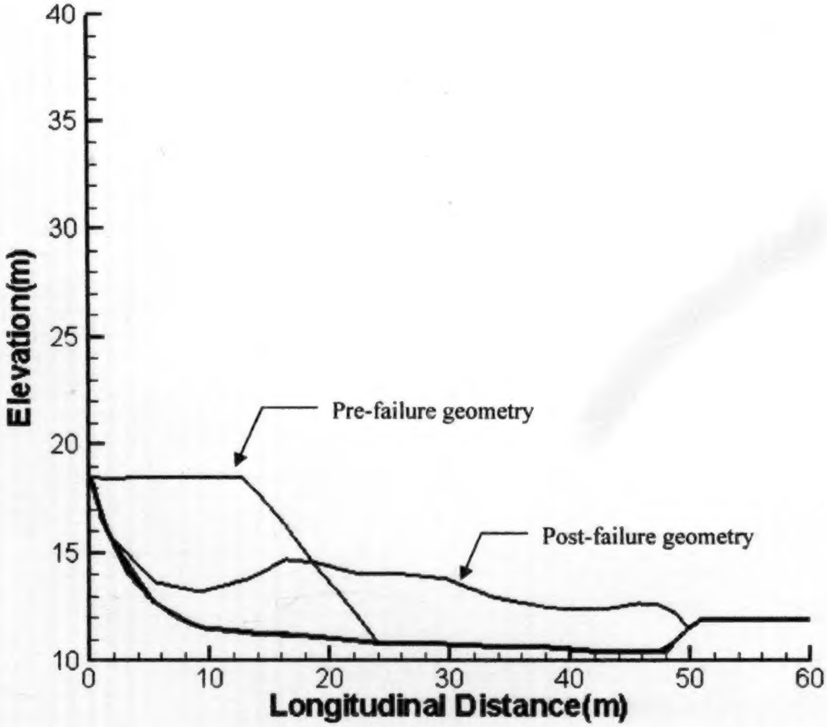

Figure B.79 Geometries of the Route 272 flow slide based on dynamic analysis with the cohesive model

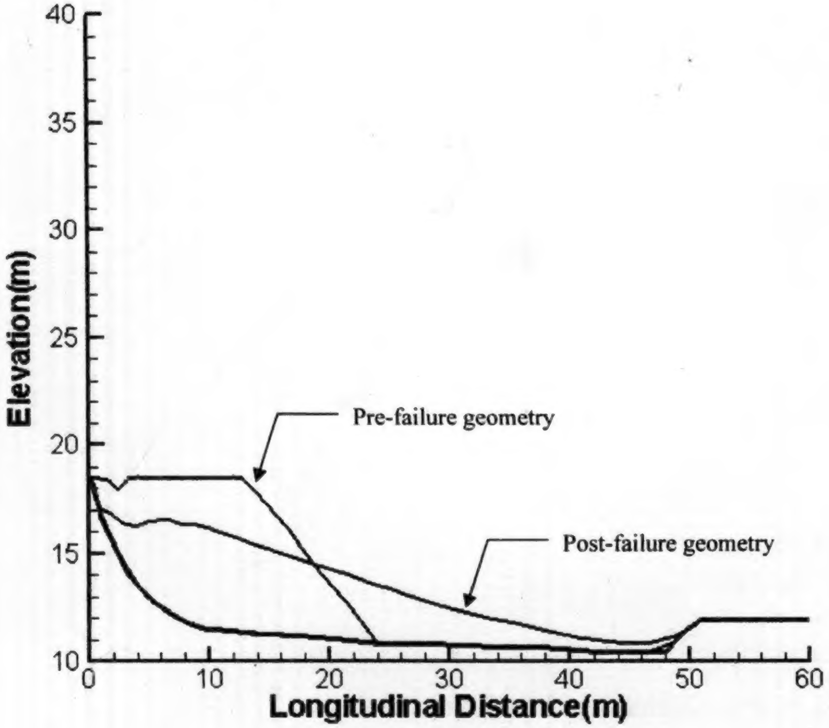

Figure B.80 Geometries of the Route 272 flow slide based on dynamic analysis with the friction model

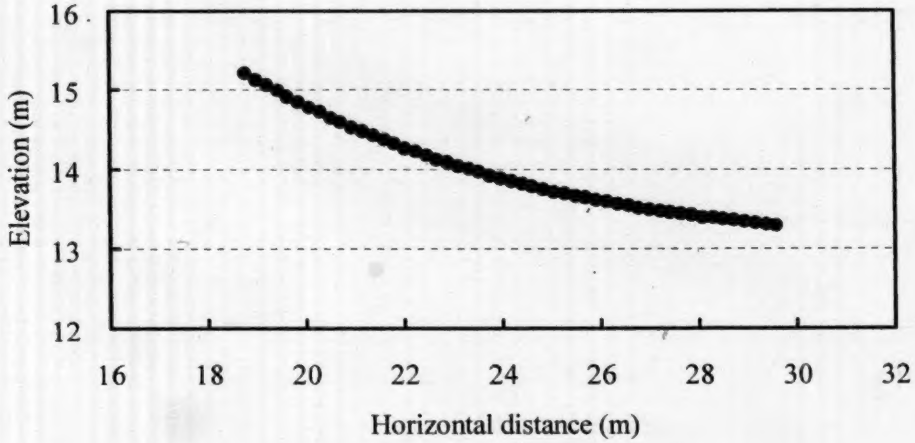

Figure B.81 Travel path of the centroid of the Route 272 flow slide

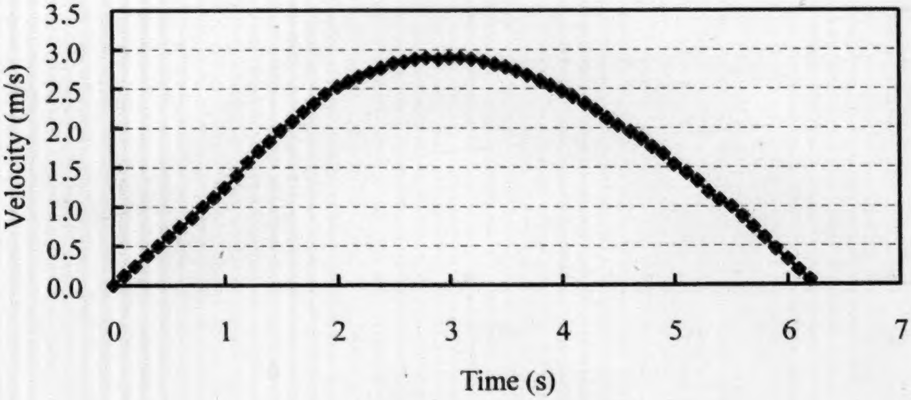

Figure B.82 Centroid velocity versus time for the Route 272 flow slide

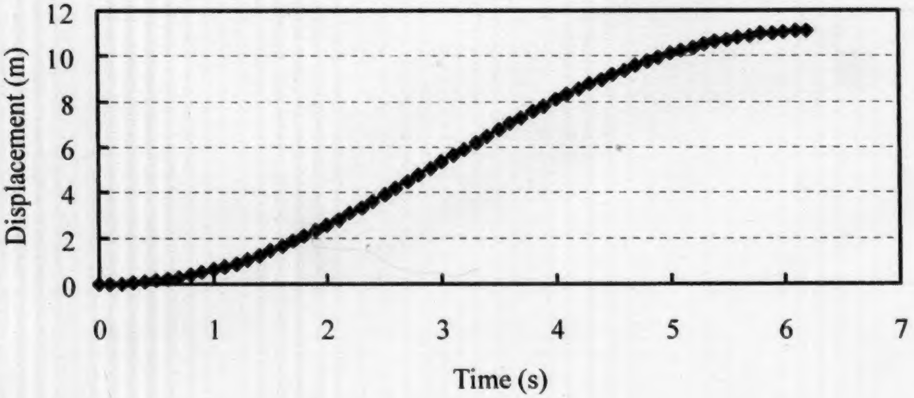

Figure B.83 Centroid displacement versus time for the Route 272 flow slide

B.10 A Flow Slide in the Hachiro-Gata Embankment

B.10.1 Historical Information of the Hachiro-Gata Flow Slide

A flow slide in the Hachiro-Gata embankment occurred during the 1993 Nihon-Kai-Chubu earthquake in Japan. The embankment failed and flowed in both directions from the centerline. Post-failure geometry of the slide mass is shown in Figure B.84. The slide on the left-hand side of the figure is analyzed in this study.

Field investigations indicated that the embankment fill consisted primarily of loose, fine sand. The embankment was underlain by a medium dense, fine sand layer of about 5 m, a dense sand layer of 6 m, and a clay layer of considerable thickness (Olson 2001). The unit weight of the silty sand was approximately 18.1 kN/m^3. Comprehensive analyses (Olson 2001) indicated that the Hachiro-Gata flow slide was a result of the liquefaction of loose embankment sand, and was triggered by the Nihon-Kai-Chubu earthquake.

B.10.2 Stability Analysis of the Hachiro-Gata Flow Slide

Olson (2001) investigated the Hachiro-Gata flow slide and carried out a series of stability analyses of the slope before and after the slide. The cross sections used in the stability analyses by Olson (2001) are presented Figure B.85, Figure B.86, and Figure B.87. The sand above the phreatic surface was assigned a friction angle of 30°. The best estimate of yield shear strength was 4.8 kPa with a range of 4.3 to 5.3 kPa from stability analysis of the pre-failure slope. The back-calculated shear strength was approximately 1.4 kPa with a range of 1.1 to 1.6 kPa, based on stability analysis of the post-failure geometry of the slide mass. The best estimate of liquefied shear strength was 2.0 kPa with a range of 1.0 to 3.2 kPa using kinetic analysis.

B.10.3 Dynamic Analysis of the Hachiro-Gata Flow Slide

Based on Figure B.87, the geometries used for dynamic analysis of the liquefaction flow slide of the Hachiro-Gata embankment are obtained, as shown in Figure B.88. Cohesive and friction models are used as constitutive laws in the dynamic analyses.

The post-liquefaction geometry of the Hachiro-Gata flow slide shown in Figure B.89 is based on dynamic analysis using the cohesive model with internal energy dissipation incorporated. The runout distance calculated is approximately 8.0 m, which is close to the observed runout distance of 8.6 m. The liquefied shear strength from slice-based dynamic analysis with consideration of internal energy dissipation is 3.0 kPa.

The post-liquefaction geometry of the Hachiro-Gata flow slide shown in Figure B.90 is based on dynamic analysis using the friction model with internal energy dissipation considered. The runout distance calculated is 9.0 m from simulation and the bulk friction angle back-calculated is about 10.6°.

B.10.4 Kinetic Analysis of the Hachiro-Gata Flow Slide

Kinetic analysis of the liquefaction flow slide in the Hachiro-Gata embankment with a sliding block model is carried out. The friction model is used to calculate the shear resistance mobilized in the kinetic analysis. The travel path of the center of gravity is defined by a third order polynomial similar to the travel path used in the kinetic analysis by Olson (2001). The travel path of the centroid, velocity, and displacement based on dynamic analysis are presented in Figure B.91 to Figure B.93. The back-calculated bulk friction angle is about 10.6°.

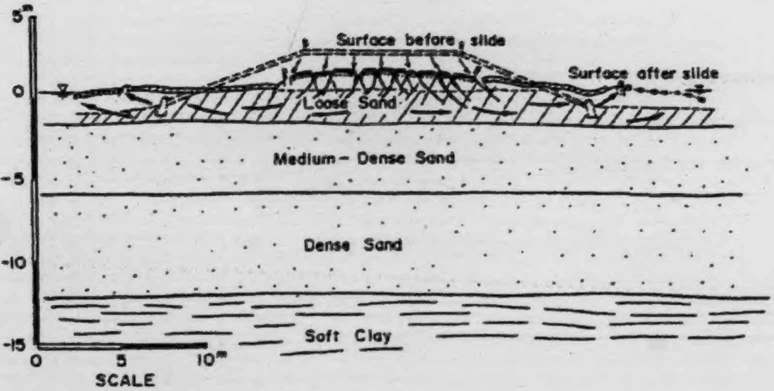
5m
0
-5
-10
-15
Surface before slide
Surface after slide
Loose Sand
Medium - Dense Sand
Dense Sand
Soft Clay
0
5
10m
SCALE

Figure B.84 Pre- and post-failure geometry of the Hachiro-Gata flow slide (After Olson 2001)

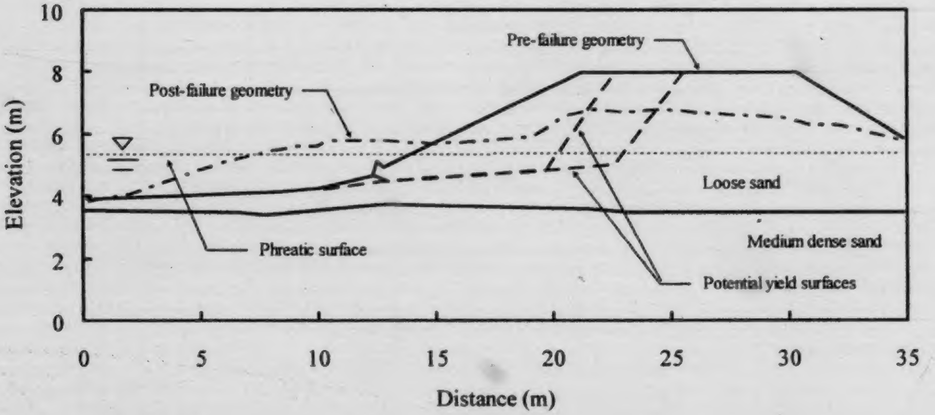

Figure B.85 Pre-failure geometries of the Hachiro-Gata embankment used for yield shear strength analyses (Modified from Olson 2001)

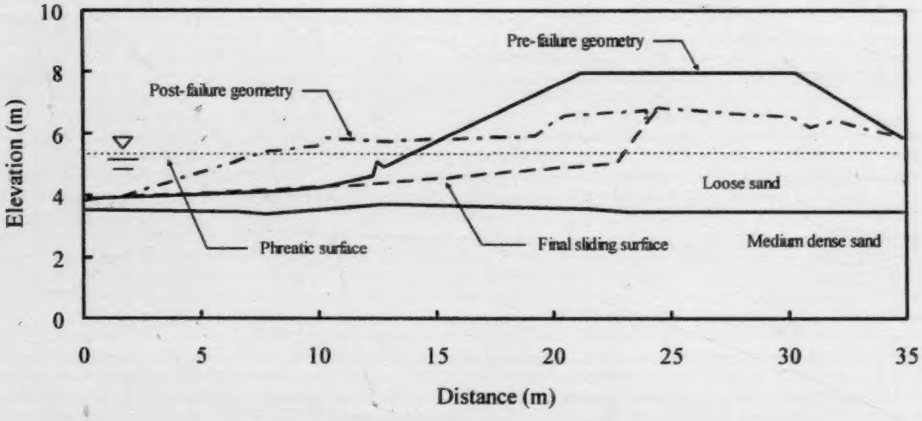

Figure B.86 Post-failure geometries of the Hachiro-Gata embankment used for liquefied shear strength analyses (Modified from Olson 2001)

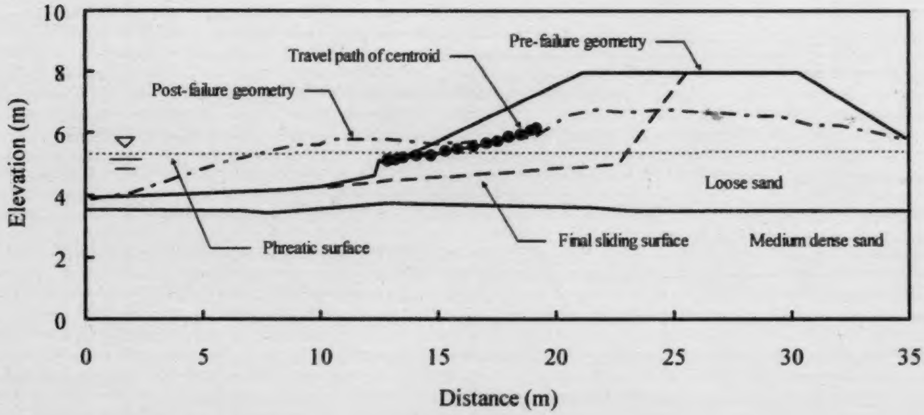

Figure B.87 Post-failure geometries of the Hachiro-Gata embankment used for kinetic analyses (Modified from Olson 2001)

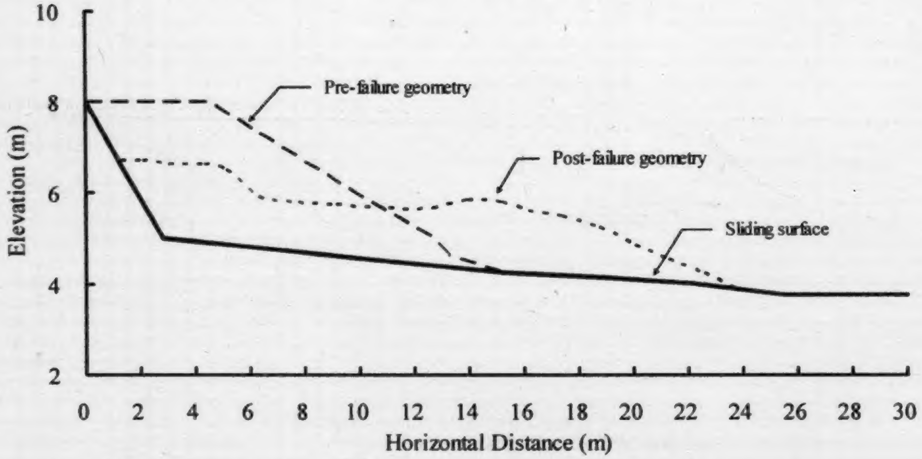

Figure B.88 Geometries of the Hachiro-Gata flow slide used for dynamic analysis

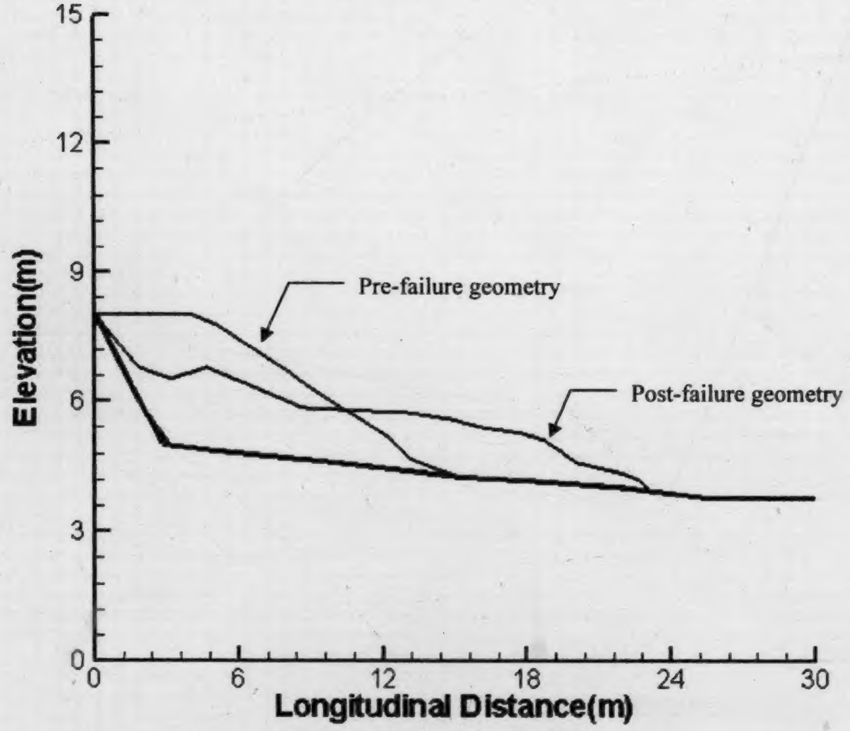

Figure B.89 Geometries of the Hachiro-Gata flow slide based on dynamic analysis with the cohesive model

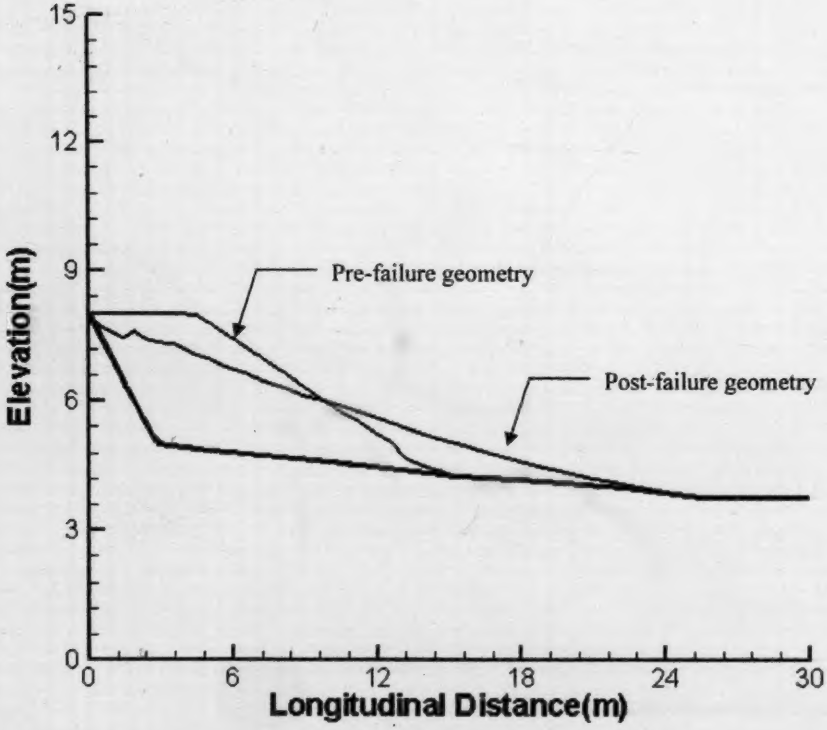

Figure B.90 Geometries of the Hachiro-Gata flow slide based on dynamic analysis with the friction model

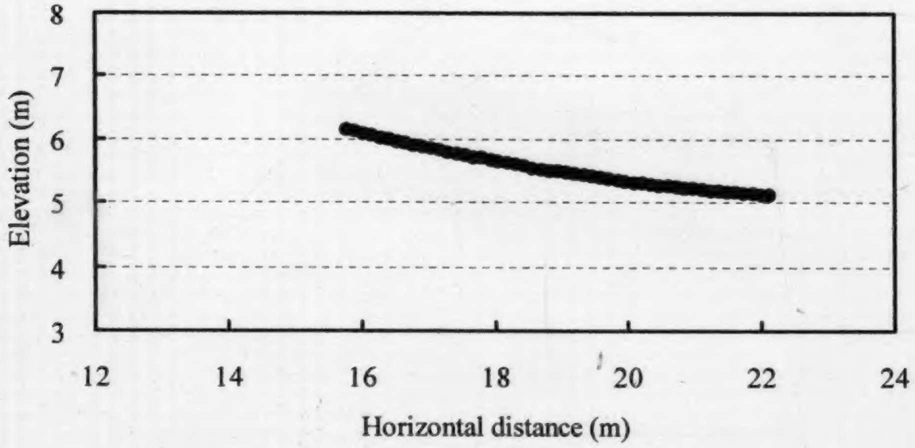

Figure B.91 Travel path of the centroid of the Hachiro-Gata flow slide

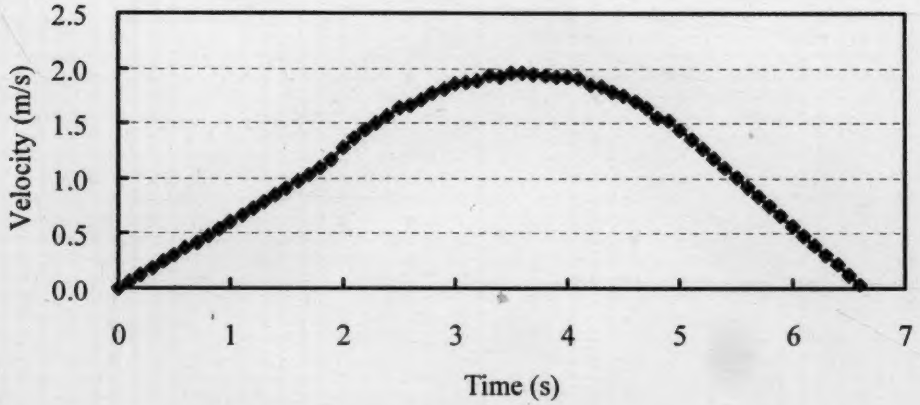

Figure B.92 Centroid velocity versus time for the Hachiro-Gata flow slide

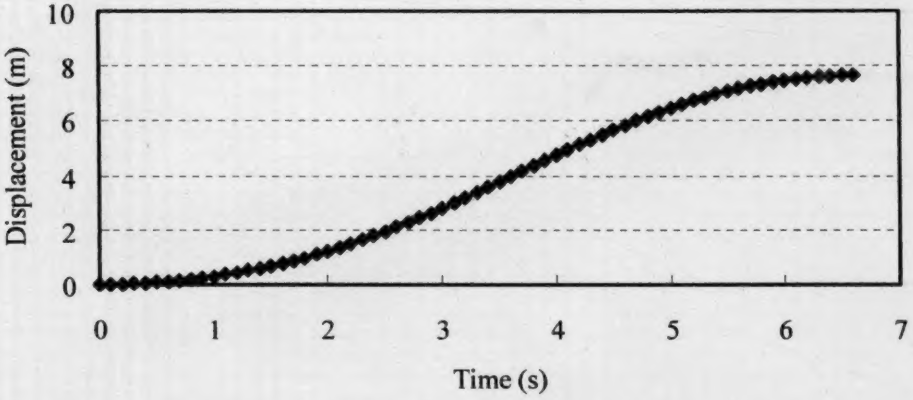

Figure B.93 Centroid displacement versus time for the Hachiro-Gata flow slide